

# **Examining effects of native microbiota on host ageing in *Caenorhabditis elegans***

Mireya Vazquez-Prada

School of Biosciences

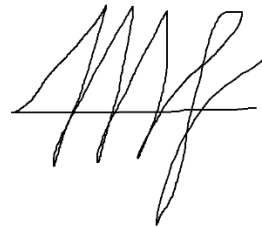
University of Kent, Canterbury, United Kingdom

Thesis submitted for the award of  
Doctor of Philosophy in Cell Biology  
August 2023

## Declaration

I, Mireya Vazquez-Prada, certify that all work presented in this thesis is my own. All information derived from other sources and data contributed by other individuals has been clearly indicated.

Signed,

A handwritten signature in black ink, consisting of stylized, overlapping letters that appear to be 'MV' followed by a flourish.

Mireya Vazquez-Prada, MRes

August 2023

## Abstract

The gut microbiome modulates many aspects of host physiology, including the ageing process. There is a pressing need for suitable, tractable models with which to investigate how host-microbe interactions affect host ageing. Studies performed in the nematode *Caenorhabditis elegans* have made significant contributions to biological research but have largely been performed outside the context of the nematode's native microbiota. A growing body of evidence has demonstrated that wild *C. elegans* harbour a rich and diverse community of commensal microorganisms. Here, we leverage the combined model system of *C. elegans* and ecologically relevant symbionts to identify the pathways underlying microbiome effects on age-related phenotypes in the host.

In this study, eleven ecologically relevant bacterial species were selected to model the native *C. elegans* microbiome. This microbial assembly, referred to as the Experimental Microbiome, was found to survive in the nematode intestine and support normal development. Colonisation with native microbiota members suppressed age-associated locomotor decline – an effect that does not involve modifications to muscle structure or function but requires the engagement of various signalling pathways in the host. The genetic components of innate immunity, iron processing, and mitochondrial homeostasis are all required for Experimental Microbiome-mediated preservation of motor function. Indeed, cultivation on the Experimental Microbiome alters mitochondrial network dynamics and occludes normal patterns of mitochondrial ageing. The Experimental Microbiome was also found to suppress age-associated proteotoxicity in a transgenic *C. elegans* strain expressing human amyloid beta, with protection provided by live bacteria as well as cell-free extracellular material. Altogether, this work highlights the

microbiome's capacity to influence host ageing by engaging host signalling pathways and illustrates the potential of targeting host-microbe interactions to extend healthspan.

## Acknowledgments

I would like to extend my utmost gratitude to all those who have supported me over the last four years – I could not have completed this project without them.

Firstly, I would like to thank the Ezcurra and Tullet labs for their expertise and friendship over the years. Thank you to Antonis, Nathan, Laura, Yasir, Sarah, Dan, Nick, Sarah, and Feng for filling every day with such fun. I miss you all dearly. Thank you to Jenny Tullet for the valued feedback I received throughout my PhD and for her continued support in the lab. I am grateful to the Kent Fungal Group for welcoming the worm labs into the department and for the sense of community they have created. Moving to Canterbury from London was daunting at first, but I found such a warm and collaborative group of scientists waiting for me. I would also like to extend special thanks to the Moore, Xue, and Labbadia labs for their collaboration on this project.

On a personal note, I would like to thank my friends and family outside of the lab environment. Thank you to Lucca, Layla, Samhita, Milou, Ruben, and Tarun for the endless laughs and the belief in my abilities. I would like to thank the forever friends who cheered me on all the way from the Philippines: Bianca, Kai, Isabel, and Nacho. Thank you to my family for always supporting my passions (even when you don't understand them). This is for you!

I would like to express my greatest appreciation to my supervisor, Marina Ezcurra. I was fortunate to receive her unwavering attentiveness and understanding, and provided with exactly the sort of support I needed every step of the way. I feel that I have grown as a scientist thanks to her

guidance, and I cannot wait to see what the future holds for the Ezcurra lab under her wing. It was an honour to have been her first PhD student and I thank her for such an invaluable opportunity.

Finally, I would like to dedicate this thesis to my grandmother, my Lola Dai, who passed away while I was in the process of completing my PhD. I miss you immeasurably, and I hope to make you proud with all that I do.

# Table of Contents

Declaration .....	2
Abstract .....	3
Acknowledgments .....	5
Table of contents .....	7
List of figures and tables .....	12
1. Introduction .....	14
1.1 Introduction to the microbiome .....	14
1.2 The microbiome and ageing .....	17
1.2.1 Hallmarks of ageing .....	17
1.2.2 Dynamism in the maturing microbiome .....	24
1.3 Existing models of microbiome study .....	26
1.4 <i>Caenorhabditis elegans</i> : A powerful genetic model system .....	28
1.5 <i>Caenorhabditis elegans</i> : An emerging model for host-microbe interactions .....	29
1.6 Concluding remarks .....	31
2. Materials and Methods .....	32
2.1 Contributors to data .....	32
2.2 Strains and reagents .....	33
2.2.1 <i>C. elegans</i> strains .....	33
2.2.2 Bacterial strains .....	34
2.2.3 Reagents and commercial kits .....	35
2.3 Methods .....	37
2.3.1 Culturing bacterial strains .....	37
2.3.2 RNA interference (RNAi) .....	38
2.3.3 Preparation of nematode growth medium (NGM) plates .....	38
2.3.4 Seeding NGM plates .....	38
2.3.5 Maintenance of <i>C. elegans</i> strains .....	39
2.3.6 Age-synchronisation of <i>C. elegans</i> populations: Egg-prep protocol .....	39
2.3.7 Age-synchronisation of <i>C. elegans</i> populations: Drop bleaching protocol .....	40
2.3.8 Lifespan/survival assay .....	40
2.3.9 Food preference assay .....	41
2.3.10 Fecundity (brood size) assay .....	41

2.3.11 Developmental timing assay .....	42
2.3.12 Body size analysis .....	42
2.3.13 Pharyngeal pumping assay .....	43
2.3.14 Defecation assay .....	43
2.3.15 Assessing two-dimensional motility in liquid media (thrashing assay) .....	44
2.3.16 Assessing two-dimensional motility on solid media .....	44
2.3.17 Assessing three-dimensional motility (burrowing assay) .....	44
2.3.18 A $\beta$ -associated paralysis assay .....	45
2.3.19 Gentle touch assay .....	45
2.3.20 Contractibility assay .....	46
2.3.21 Mounting of fluorescent <i>C. elegans</i> strains for microscopy .....	46
2.3.22 Epifluorescence microscopy .....	47
2.3.23 Scoring of mechanosensory neuron defects .....	47
2.3.24 Quantitative analysis of body wall muscle mitochondria .....	48
2.3.25 Qualitative scoring of muscular mitochondrial morphology .....	49
2.3.26 Qualitative scoring of ALM soma mitochondrial morphology .....	50
2.3.27 Gut colonisation assay .....	51
2.3.28 Sample preparation for sequencing of 16S rRNA gene .....	51
2.3.29 Sample preparation for DNA sequencing .....	52
2.3.30 DNA sequencing .....	54
2.3.31 Sample preparation for <i>C. elegans</i> RNA sequencing .....	54
2.3.32 <i>C. elegans</i> RNA sequencing .....	55
2.3.33 Expression of recombinant A $\beta$ <sub>1-42</sub> from <i>Escherichia coli</i> .....	56
2.3.34 Purification of A $\beta$ <sub>1-42</sub> monomers .....	57
2.3.35 Thioflavin T assay .....	58
2.3.36 Extraction of bioactive compounds into organic solvents .....	59
2.3.37 Statistics .....	59
3. Experimental microbiome effects on <i>C. elegans</i> healthspan and life history .....	61
3.1 Introduction .....	61
3.1.1 Healthspan and life history in <i>C. elegans</i> .....	61
3.1.2 The native microbiome of <i>C. elegans</i> .....	63
3.1.3 Native microbiota effects on gene expression .....	65
3.1.4 Investigating general experimental microbiome .....	

effects on <i>C. elegans</i> healthspan .....	66
3.2 Results .....	67
3.2.1 The experimental microbiome colonises the <i>C. elegans</i> intestine .....	67
3.2.2 The experimental microbiome sustains growth and development of <i>C. elegans</i> .....	71
3.2.3 The experimental microbiome regulates the <i>C. elegans</i> transcriptome .....	78
3.3 Discussion .....	80
3.3.1 A representative microbiome survives in the <i>C. elegans</i> intestine .....	80
3.3.2 Experimental microbiome sustains growth and development .....	82
3.3.3 Experimental microbiome alters the wildtype transcriptome .....	85
4. Experimental microbiome effects on <i>C. elegans</i> motility .....	87
4.1 Introduction .....	87
4.1.1 <i>C. elegans</i> musculature .....	87
4.1.2 Muscle and the microbiome .....	89
4.1.3 The microbiome and host immune responses .....	92
4.1.4 The p38 MAP kinase (PMK) pathway of innate immunity .....	93
4.1.5 Investigating experimental microbiome effects on <i>C. elegans</i> motility .....	95
4.2 Results .....	96
4.2.1 Experimental microbiome suppresses age-associated decline of two-dimensional motility .....	96
4.2.2 Experimental microbiome does not affect <i>C. elegans</i> gentle touch mechanosensation .....	97
4.2.3 Experimental microbiome does not alter mechanosensory neuron morphology .....	98
4.2.4 Experimental microbiome does not alter sarcomere integrity .....	101
4.2.5 Experimental microbiome suppresses age-associated decline of three-dimensional motility .....	102
4.2.6 Experimental microbiome effects on motility are not due to alterations in neuromuscular transmission .....	103
4.2.7 Experimental microbiome suppresses age-associated motility decline in a p38-dependent manner .....	106
4.3 Discussion .....	109
4.3.1 Experimental microbiome protects against age-associated	

motility decline .....	109
4.3.2 Experimental microbiome protects against locomotor decline without altering muscular structure or function .....	110
4.3.3 Experimental microbiome protects from locomotory decline via the p38 MAPK pathway .....	113
5. Experimental microbiome effects on mitochondrial homeostasis .....	115
5.1 Introduction .....	115
5.1.1 Mitochondria and the microbiome .....	115
5.1.2 Mitochondrial dynamics: A balance of fission and fusion .....	117
5.1.3 The mitochondrial unfolded protein response (UPR <sup>mt</sup> ) .....	121
5.1.4 Mitochondria and ageing in <i>C. elegans</i> .....	124
5.1.5 Investigating experimental microbiome effects on mitochondrial homeostasis ...	126
5.2 Results .....	126
5.2.1 Experimental microbiome induces mitochondrial fragmentation in body wall muscle .....	126
5.2.2 Relationship between muscular mitochondrial fragmentation and motility is lost in EM-fed worms .....	131
5.2.3 Experimental microbiome mildly induces mitochondrial fragmentation in mechanosensory neurons .....	132
5.2.4 Experimental microbiome induces nuclear localisation of DVE-1, a chaperone-binding protein involved in UPR <sup>mt</sup> .....	137
5.2.5 Experimental microbiome does not induce expression of <i>ubl-5</i> , encoding a ubiquitin-like protein involved in UPR <sup>mt</sup> .....	139
5.2.6 Experimental microbiome effect on age-associated motility decline requires genes involved in UPR <sup>mt</sup> .....	140
5.2.7 Experimental microbiome effect on age-associated motility requires expression of Mediator subunit gene <i>mdt-15</i> .....	144
5.2.8 Experimental microbiome effect on age-associated motility decline requires genes mediating mitochondrial dynamics .....	146
5.2.9 Experimental microbiome effect on mitochondrial fragmentation does not require <i>pmk-1</i> expression .....	148
5.3 Discussion .....	151
5.3.1 Experimental microbiome alters mitochondrial homeostasis .....	151

5.3.2 Mitochondrial dynamics genes are required for experimental microbiome effects on locomotion .....	153
5.3.3 Mitochondrial stress response genes are required for experimental microbiome effects on locomotion .....	155
6. Experimental microbiome effects on A $\beta$ -associated toxicity .....	160
6.1 Introduction .....	160
6.1.1 The microbiome and proteotoxic disease .....	160
6.1.2 Alzheimer's disease and iron homeostasis .....	163
6.1.3 Investigating experimental microbiome effects in human disease models .....	166
6.2 Results .....	166
6.2.1 Experimental microbiome suppresses A $\beta$ <sub>1-42</sub> -associated toxicity .....	166
6.2.2 Cell-free media from experimental microbiome partially suppresses A $\beta$ <sub>1-42</sub> -associated toxicity .....	171
6.2.3 Experimental microbiome does not suppress polyQ-mediated toxicity .....	175
6.2.4 Cell-free media from EM inhibits A $\beta$ <sub>1-42</sub> fibril formation <i>in vitro</i> .....	177
6.2.5 Active compound(s) in MYb57 extracellular material cannot be extracted into volatile solvents .....	182
6.2.6 Siderophore supplementation does not suppress A $\beta$ <sub>1-42</sub> -associated toxicity .....	185
6.2.7 Suppression of late-life motility decline by the experimental microbiome involves genes encoding ferritin .....	190
6.3 Discussion .....	193
6.3.1 Experimental microbiome suppresses A $\beta$ proteotoxicity .....	193
6.3.2 Cell-free media from experimental microbiome inhibits A $\beta$ <sub>1-42</sub> aggregation .....	195
6.3.3 Iron processing genes are required for experimental microbiome effects on locomotion .....	198
7. Concluding remarks .....	201
8. Appendix .....	207
9. Bibliography .....	224

# List of figures and tables

## 2. Materials and methods

Figure 2.1	Steps of object selection within a delineated cell	49
Table 2.1	Contributors to data within this project	32
Table 2.2	<i>C. elegans</i> strains used in this project	33
Table 2.3	Bacterial strains used in this project	34
Table 2.4	Reagents used in this project	35
Table 2.5	Commercial kits used in this project	36
Table 2.6	Descriptions of <i>C. elegans</i> developmental stages at 60h	42
Table 2.7	Motility classes used to assess movement of <i>C. elegans</i> on solid media	44
Table 2.8	Magnification objectives and exposure times used per fluorescent reporter strain imaged	47
Table 2.9	Segmentation parameters used to quantify mitochondrial objects via the SQUASSH plugin on Fiji imaging software	48
Table 2.10	Qualitative scoring paradigm for body wall muscle mitochondrial networks	50
Table 2.11	Qualitative scoring paradigm for mitochondrial networks in somata of ALM mechanosensory neurons	50

## 3. Experimental microbiome effects on *C. elegans* healthspan and life history

Figure 3.1	Experimental microbiome colonises the <i>C. elegans</i> intestine	70
Figure 3.2	Experimental microbiome affects growth and longevity but does not affect development	74
Figure 3.3	Wildtype <i>C. elegans</i> exhibit equal preference for the EM and OP50	78
Figure 3.4	Experimental microbiome strongly regulates the <i>C. elegans</i> transcriptome	80
Table 3.1	Experimental microbiome (EM) member strains	68

## 4. Experimental microbiome effects on *C. elegans* motility

Figure 4.1	<i>C. elegans</i> musculature loses integrity with advanced age	88
Figure 4.2	Experimental microbiome protects against late-life motility decline	97
Figure 4.3	Experimental microbiome does not alter mechanosensation in <i>C. elegans</i>	100
Figure 4.4	Experimental microbiome does not adversely affect sarcomere integrity or muscle function	105
Figure 4.5	The p38 MAPK (PMK) pathway is required for the protective effect of the experimental microbiome against age-associated motility decline	108

## 5. Experimental microbiome effects on mitochondrial homeostasis

Figure 5.1	Schematic diagram of mitochondrial dynamics processes	119
Figure 5.2	Schematic diagram of the mitochondrial unfolded protein response (UPR <sup>mt</sup> )	124

Figure 5.3	Experimental microbiome induces mitochondrial fragmentation in body wall muscle .....	130
Figure 5.4	Experimental microbiome induces mild mitochondrial fragmentation in mechanosensory neurons .....	136
Figure 5.5	Experimental microbiome induces nuclear translocation of chaperone-binding protein DVE-1 .....	138
Figure 5.6	Experimental microbiome induces expression of ubiquitin-like protein gene <i>ubl-5</i> .....	140
Figure 5.7	Protective effect of experimental microbiome against age-associated motility decline requires expression of UPR <sup>mt</sup> genes .....	143
Figure 5.8	Protective effect of experimental microbiome against age-associated motility decline requires expression of Mediator subunit gene <i>mdt-15</i> .....	145
Figure 5.9	Protective effect of experimental microbiome against age-associated motility decline requires expression of genes mediating mitochondrial dynamics .....	147
Figure 5.10	Experimental microbiome effect on mitochondrial dynamics in body wall muscle does not require <i>pmk-1</i> expression .....	150
6. Experimental microbiome effects on A $\beta$ -associated toxicity		
Figure 6.1	Experimental microbiome suppresses A $\beta$ <sub>1-42</sub> -associated toxicity .....	170
Figure 6.2	Cell-free media from experimental microbiome partially suppresses A $\beta$ <sub>1-42</sub> -associated toxicity .....	174
Figure 6.3	Experimental microbiome does not suppress polyQ-mediated toxicity .....	177
Figure 6.4	Cell-free media from experimental microbiome inhibits A $\beta$ <sub>1-42</sub> fibrillisation <i>in vitro</i> as detected by thioflavin T assay .....	179
Figure 6.5	Cell-free media from individual experimental microbiome member strains differentially inhibit A $\beta$ fibrillisation <i>in vitro</i> .....	181
Figure 6.6	Active compound(s) in MYb57 extracellular material cannot be extracted into ethyl acetate (EtOAc), acetonitrile (MeCN), or methanol (MeOH) .....	185
Figure 6.7	Siderophore supplementation does not suppress A $\beta$ -associated paralysis .....	190
Figure 6.8	The protective effect of the EM against age-associated motility decline requires expression of genes encoding the iron storage protein ferritin .....	192
7. Concluding remarks		
Figure 7.1	Model outlining experimental microbiome effects on <i>C. elegans</i> physiology .....	202
8. Appendix		
Figure 8.1	Experimental microbiome cultured in minimal media suppresses A $\beta$ <sub>1-42</sub> -associated toxicity .....	220
Figure 8.2	Fluorescence intensity traces from thioflavin T assay biological replicate #1 .....	221
Figure 8.3	Fluorescence intensity traces from thioflavin T assay biological replicate #2 .....	222
Figure 8.4	Secondary metabolite-encoding cluster similarity per EM member strain .....	223
Table 8.1-8.34	Statistical analyses for all relevant figures .....	207-219

# 1. Introduction

## 1.1 Introduction to the microbiome

Almost all multicellular organisms are engaged in mutualistic relationships with a diverse array of bacteria, viruses, fungi, and protozoa – altogether forming their respective microbiota. It is estimated that the adult human body contains as many bacterial cells as somatic cells, comprised of thousands of distinct species (Sender et al. 2016; Lloyd-Price et al. 2016; Qin et al. 2010). Microbiota inhabit mucosal surfaces such as the skin and oral cavity but are most densely found in the gastrointestinal tract. The collective genome of intestinal microbiota is referred to as the gut microbiome, consisting of over five million genes – two orders of magnitude greater than their human host (Consortium HMP, 2012). Higher animals are, in fact, superorganisms whose physiological functions are influenced by those of their microbial symbionts (Gill et al. 2006).

Commensal bacteria fulfil many roles underpinning host survival which can be grouped into three broad functional categories: protective (pathogen restriction), metabolic (digestion), and trophic (epithelial cell proliferation/differentiation) (Villanueva-Millán et al. 2015). Through a phenomenon known as colonisation resistance, microbiota restrict the detrimental overgrowth of endogenous bacteria and prevent colonisation by exogenous pathogens (Kim et al. 2017). Protection is partially dependent on direct action between microbes i.e., by limiting the availability of dietary carbohydrates to opportunistic species or by the production of toxic bacteriocins (Kamada et al. 2012; Cotter et al. 2012). Alternatively, colonisation resistance can be achieved indirectly through interactions with host physiology such as the engagement of innate immune receptors in the gut, inducing the production of antimicrobial peptides by epithelial and Paneth cells (Kinnebrew and Pamer, 2011; Pasparakis, 2009). Differentiating

between commensal and pathogenic bacteria relies on a precise immunosensory capacity in the gut epithelium, emphasising the importance of host-microbe communication at the mucosal surface (O'Hara and Shanahan, 2006). In terms of metabolism, gut microbiota facilitate the production of many precursors and cofactors required for host digestion. Deep sequencing of human faecal samples has revealed an overrepresentation of bacterial genes involved in amino acid metabolism and vitamin biosynthesis (Gill et al. 2006). Within the large intestine, microbiota supplement host dietary intake by synthesising water-soluble vitamins including thiamine (vitamin B<sub>1</sub>), riboflavin (vitamin B<sub>2</sub>), cobalamin (vitamin B<sub>12</sub>), and folate (Biesalski, 2016). These microbially-produced vitamins are absorbed into the colonic mucosa and serve as enzymatic cofactors for energy metabolism. Indigestible polysaccharides ingested by the host are metabolised by glycoside hydrolase and polysaccharide lyase enzymes found in intestinal microbes. The subsequent oligo- and monosaccharides are converted into short-chain fatty acids (SCFAs) which are readily absorbed by the host for the synthesis of glucose and fatty acids (Villanueva-Millán et al. 2015). Of these SCFAs, butyrate contributes to the microbiome's trophic functions, serving as the main energy source for colonic cells and stimulating the release of gastrointestinal growth factors (Guilloteau et al. 2010). Over 10% of endogenous serum metabolites in the mammalian circulatory system have been found to be bacterial in origin, underscoring the convergence of host and microbe metabolism to form a single metabolic entity known as the holobiont (Norvaisas and Cabreiro, 2018; Wikoff et al. 2009; Zilber-Rosenberg and Rosenberg, 2008).

Over the last decade, human microbiota research has benefitted from advances in large-scale sequencing and bioinformatic technology. The Human Microbiome Project (HMP) and Metagenomics of the Human Intestinal Tract (MetaHIT), hitherto the most comprehensive classification initiatives of human-associated microbial communities, have helped to define

'baseline' microbiota in healthy adult cohorts (Consortium HMP, 2012). The complementary projects have isolated over 2,200 distinct bacterial species from human subjects, with at least 160 species present per subject. Of the 12 phyla identified in the adult gut, the most abundant are Bacteroidetes and Firmicutes, accounting for over 90% of all cells, followed by Proteobacteria and Actinobacteria (Kim et al. 2017; Consortium HMP, 2012; Qin et al. 2010). Further studies have examined the variation between subjects, suggesting that an individual's microbial assembly can fall into one of three enterotypes defined by the abundance of *Bacteroides*, *Prevotella*, or *Ruminococcus* genera (Arumugam et al. 2011).

Whereas early metagenomics approaches focused on defining a core microbiome in healthy populations, more recent studies have described disturbances to normal microbiota composition – termed dysbiosis – in several disease states (Sommer and Bäckhed, 2013). Obesity, for example, has been linked to an elevated *Firmicutes/Bacteroidetes* ratio in adults and children (Bervoets et al. 2013; Ley et al. 2006). It is speculated that this shift in bacterial populations may be associated with a host response limiting energy uptake and promoting fat storage (Villanueva-Millán et al. 2015; Ley et al. 2005). Additional nutrition-associated disease states in which dysbiosis has been reported include colorectal cancer and type 2 diabetes, both of which are associated with a reduction in butyrate-producing genera (Wu et al. 2013; Qin et al. 2012). It is worth noting that the gastrointestinal tract is intimately connected to the central nervous system through nerves such as the vagus and is a major site of production for neuroactive compounds such as catecholamines, histamines, and neuropeptides (Sharon et al. 2016; Villanueva-Millán et al. 2015). Investigating gut dysbiosis in neuropsychiatric and neurodevelopmental disorders is thus an emerging area of interest. Major depression, the most prevalent mental disorder in industrialised societies, was found to be consistently associated with a depletion of butyrate-producing *Coprococcus* and *Dialister* genera (Valles-

Colomer et al. 2019). More severe depression diagnoses were also correlated with *Bacteroidetes*-dominated microbiota but an overall reduction in microbial load (Vandeputte et al. 2017, Arumugam et al. 2011). A consensus on the microbiota of autism spectrum disorder patients has yet to be reached, though several studies have converged in reporting an increased abundance of *Clostridia* species and non-spore-forming anaerobes (De Angelis et al. 2013; Finegold et al. 2010; Parracho et al. 2005). The identification of pathology-associated taxa implies that the gut microbiome may be a viable target for therapeutic intervention. However, this potential rests on the field's ability to determine if these microbial candidates are the causes or the consequences of such disorders.

## 1.2 The microbiome and ageing

### 1.2.1 Hallmarks of ageing

Due to improvements in living conditions, nutrition, and medical care, average human life expectancy has tripled over the course of human history and is only expected to increase further (Kontis et al. 2017; Wilmoth, 2000; Vaupel et al. 1998). Unfortunately, average *healthspan* – the length of an individual's healthy life – has not demonstrated a comparable increase (Crimmins, 2015). Emerging data supports the 'expansion of morbidity' hypothesis which suggests that though average life expectancy increases, individuals spend longer periods in ill health coping with age-associated comorbidities (Olshansky et al. 1991; Verbrugge, 1984; Gruenberg, 1977). The enhanced survival reported in patients suffering from chronic illnesses is therefore due to a reduction in mortality rather than a prevention of morbidity (Crimmins, 2015; Crimmins and Beltrán-Sánchez, 2011). An unhealthy ageing population increases the ratio of dependent to independent individuals and carries significant socioeconomic implications. Within the

European Union alone, a 16% drop and 77% rise in the working-age and elderly populations, respectively, are projected between 2010 and 2050 (Carone et al. 2005). Geroscience is an emerging a branch of research at the interface of ageing and chronic disease which aims to extend human healthspan, requiring identification of the genetic drivers of ageing. However, the complex nature of studying ageing has proven this to be a difficult task (Gems, 2020; Kennedy et al. 2014).

Ageing is not a single macroscopic phenomenon, as it is colloquially referred to, but a collection of genetically regulated cellular hallmarks. Invertebrate longevity mutants and genetic manipulation in mammalian models have uncovered conserved molecular pathways governing the ageing process (DiLoreto and Murphy, 2015). Experts have grouped these findings into nine aspects that together constitute the aged cellular and molecular phenotype across all organisms: (1) genomic instability, (2) telomere attrition, (3) epigenetic alternations, (4) loss of proteostasis (5) deregulated nutrient sensing, (6) mitochondrial dysfunction, (7) cellular senescence, (8) stem cell exhaustion, and (9) altered intercellular communication (López-Otín et al. 2013). Each of these hallmarks manifests during normal organismal ageing and have been shown to be experimentally ameliorated or aggravated resulting in ageing retardation or acceleration, respectively.

Genome instability refers to the loss of DNA's integrity and stability as a result of exogenous (i.e., physical, chemical, and biological agents) and endogenous (i.e., replication errors and reactive oxygen species) stressors throughout life (López-Otín et al. 2013). Progeroid (premature ageing) disorders such as Werner syndrome and Bloom syndrome characterised by increased DNA damage accumulation provide support for this

hallmark, as well as evidence that the artificial induction of DNA repair mechanisms can extend lifespan (Baker et al. 2013; Burtner and Kennedy, 2010).

Telomeres, the non-coding repetitive DNA sequences at the ends of chromosomes, shorten during successive division cycles, protecting coding regions of DNA from shortening/attrition (Heidinger et al. 2011). Upon reaching a critically diminished length, mammalian somatic cells cease division and enter a state of replicative senescence which serves as a tumour suppression mechanism (Gomes et al. 2011; Blackburn, 2005). However, telomerase – a specialised DNA polymerase – enables complete replication of telomeres. Genetic modification of telomere length in mice has been shown to alter lifespan, and telomerase deficiencies in humans have been linked to premature development of age-related diseases (Armanios and Blackburn, 2012; Armanios et al. 2009).

Epigenetic alterations that occur throughout life include DNA methylation patterns, chromatin remodelling, and post-translational histone modifications. Cells isolated from humans and mice with progeroid syndromes exhibit DNA methylation patterns akin to those in normal ageing (Osorio et al. 2010; Shumaker et al. 2006). In the fruit fly *Drosophila melanogaster*, loss- and gain-of-function mutations in heterochromatin proteins reduce and extend lifespan, respectively (Larson et al. 2012). In a similar fashion, histone deacetylation deficiencies in mice have been shown to accelerate ageing, while upregulation has been linked to lifespan extension (Kanfi et al. 2012; Mostoslavsky et al. 2006). Unlike genetic mutations, epigenetic modifications are theoretically reversible and are therefore a promising target for anti-ageing interventions (López-Otín et al. 2013).

Proteostasis, or protein homeostasis, features an array of quality control mechanisms for the stabilisation of protein structure as well as mechanisms of protein degradation (Hartl et al. 2011; Koga et al. 2011). These functions are served by two principal proteolytic systems – the autophagy-lysosomal system and the ubiquitin-proteasome system – that function in concert to restore the structure of misfolded polypeptides or to initiate their removal. In many model systems, these proteolytic pathways have been shown to depreciate with advanced age resulting in the aggregation and accumulation of damaged peptide components (Campisi et al. 2019; Tomaru et al. 2012; Rubinsztein et al. 2011; Koga et al. 2011). Many age-related diseases are thus characterised by protein misfolding, including the neurodegenerative disorders Parkinson’s disease and Alzheimer’s disease which feature the aggregation of alpha-synuclein ( $\alpha$  synuclein) and amyloid beta (A $\beta$ ) protein filaments, respectively. Indeed, even in proteotoxic disorders where a causative mutation is present ubiquitously throughout life – such as Huntington’s disease – pathogenesis is drastically influenced by ageing (Machiela et al. 2020). Animals with naturally long lifespans such as the naked mole rat have proteomes of superior stability relative to other mammals, with high levels of homeostatic proteolytic activity (Kim et al. 2011). Upregulating proteolytic activity experimentally, as has been done in transgenic nematodes and flies by overexpressing molecular chaperones, has also been shown to promote longevity (Morrow et al. 2004; Walker and Lithgow).

Organisms sense nutrients and their own nutritional status through evolutionarily conserved intracellular pathways. The insulin and insulin/insulin-like growth factor (IGF-1) signalling (IIS) pathway and its targets i.e., the FOXO family of transcription factors, constitute the most conserved ageing-controlling pathway in evolution (López-Otín et al.

2013; Kenyon 2010). Other nutrient-sensing networks include target of rapamycin (TOR), detecting high amino acid concentrations, and AMPK and sirtuins, detecting low-energy states via AMP and NAD<sup>+</sup> concentrations, respectively. Mutations that downregulate the activity of IIS pathway have been shown to promote longevity in several model organisms. Kenyon et al. (1993) famously demonstrated a doubling of lifespan in nematodes possessing a mutation in the insulin-like receptor coding gene *daf-2*. Further support for the involvement of deregulated nutrient signalling in ageing is shown by lifespan extension following dietary restriction in all investigated eukaryotic species (Fontana, 2010; Colman, 2009). In addition, pharmacological manipulations that mimic nutrient unavailability, such as rapamycin, have been shown to extend lifespan in mice (Harrison et al. 2009).

Mitochondria are membrane-bound organelles that generate a majority of the chemical energy necessary for biochemical reactions within the cell. As organisms age, mitochondrial function deteriorates. Classically, this was thought to occur due to the production of reactive oxygen species (ROS) during respiration, resulting in the accumulation of oxidative damage within cells (Harman, 1965). Although this has been demonstrated in various aged tissues and organisms, increasing mitochondrial ROS production experimentally does not accelerate ageing in mice and is even sufficient to extend lifespan in yeast and nematodes, contradicting the theory that ageing is the cumulative result of oxidative damage (Mesquita et al. 2010; Zhang et al. 2009; Doonan et al. 2008). Besides the accumulation of ROS, many other age-related phenotypes have been documented in mitochondria. A loss of mitochondrial DNA (mtDNA) integrity and stability accompany age, resulting in the introduction of mutations into mtDNA. Indeed, knock-in mice engineered to accumulate such mutations exhibit symptoms of premature ageing (Kujoth et al. 2005; Trifunovic et al. 2004). Ageing animals also display a functional

decline in mitophagy: a form of autophagy specifically directed at eliminating damaged mitochondria (Liu et al. 2020). Experimentally inhibiting mitophagy through the loss of regulatory genes amasses dysfunctional mitochondria and compromises resistance to various stressors, including oxidative stress, heat stress, and starvation (Palikaras et al. 2015). The mitochondrial unfolded protein response (UPR<sup>mt</sup>) is a proteostasis pathway in which several chaperone- and protease-encoding genes are expressed to maintain proper production, folding, and degradation of mitochondrial proteins (see section 5.1.3). As is typical of general proteostasis pathways, the UPR<sup>mt</sup> exhibits age-associated functional decline (Jensen and Jasper, 2014). Interventions that activate the UPR<sup>mt</sup> i.e., through moderate inhibition of mitochondrial translation have been shown to extend lifespan in nematodes (Houtkooper et al. 2013). There is growing interest in targeting mitochondrial function as a means of improving organismal ageing.

Cellular senescence was first described in the limited ability of human fibroblasts to divide in culture (Hayflick and Moorhead, 1961). In young organisms, cellular senescence prevents proliferation of damaged cells to maintain tissue homeostasis and prevent tumour formation (López-Otín et al. 2013). The beneficial effects of senescence entry, however, are dependent on clearance of arrested cells and rapid turnover of progenitors (discussed below). In aged organisms, this system of removal and replacement is compromised resulting in an accumulation of senescent cells (Campisi, 2013). These cells undergo a dramatic change in their secretory phenotype and begin the release of proinflammatory cytokines, inducing an age-associated chronic inflammatory state (discussed below) (Kuilman et al. 2010).

A decline in the proliferative capacity of stem cells with age has been documented in virtually all relevant mammalian niches including bone, muscle, blood, and forebrain (López-Otín et al. 2013). However, *excessive* stem cell proliferation has also been shown to accelerate ageing by prematurely exhausting reserve stem cells (Rera et al. 2011). Though seemingly counterintuitive, interventions that delay ageing onset by maintaining stem cell quiescence rather than promoting proliferation have shown promise (Chakkalakal et al. 2012).

One of the most prominent examples of impaired intercellular communication associated with age is low-grade, sterile, and chronic inflammation known as 'inflammaging' (Campisi et al. 2019). Inflammaging may emerge in response to proinflammatory tissue damage, dysfunctional pathogen clearance by immune cells, or the adoption of the senescence-associated secretory phenotype. Beyond inflammation, senescent phenotypes have been shown to spread through neighbouring cells via gap-junction-mediated cell-cell contacts *in vitro* - a potential mechanism underlying interorgan coordination of ageing (Nelson et al. 2012). Supporting this notion, lifespan-extending manipulations targeting a single tissue have been found to delay ageing onset in distal tissues (Durieux et al. 2011).

These nine traits were collated as they occur during normal ageing, accelerate ageing when experimentally aggravated, and retard ageing when ameliorated (López-Otín et al. 2013). Even with defined criteria, however, it is difficult to delineate ageing hallmarks as they have been found to exacerbate one another. For example, decreases in cell-cycle activity of hematopoietic and epidermal stem cells have been found to correlate with DNA damage accumulation as well as telomere shortening (Rossi et al. 2007; Flores et al.

2005). The depletion of these progenitors, in turn, results in immunosenescence: a subset of cellular senescence involving reduced production of adaptive immune cells (López-Otín et al. 2013). The resultant alteration in secretory phenotype then induces low-grade inflammation, which has also been found to impede stem cell function – and so the cycle continues (Doles et al. 2012).

### 1.2.2 Dynamism in the maturing microbiome

Humans display dynamic microbial profiles over the course of a lifetime (Hayashi et al. 2003). The gut microbiome is established shortly after birth as pioneer microbes from the mother's vaginal canal, gut, and breast milk colonise the neonatal gastrointestinal tract (Duranti et al. 2017). The developing microbiome, dominated by the genus *Bifidobacterium*, retains its relative simplicity into early infancy but is soon diversified by the consumption of solid foods. The transition to adult-like microbiota is a non-random process in which shifts in signature bacterial taxa can be seen at distinct developmental stages. Neonates primarily harbour aerobic gut flora while four-month-old infants possess genera facilitating lactic acid production suited to a diet rich in milk. At 12 months of age, bacteria associated with earlier stages are retained, with the addition of genera supporting the degradation of dietary fibre and production of SCFAs, suggesting an increased capacity for carbohydrate digestion (Bäckhed et al. 2015).

A stable microbial profile resembling that of a healthy adult is established by the age of three and generally maintained until old age (Bäckhed et al. 2015; Turrone et al. 2012; Yatsunen et al. 2012). Younger adults' guts are sufficiently similar between individuals such that a core microbiome of 66 operational taxonomic units (OTUs) can be defined,

dominated by the phylum *Firmicutes* (Tap et al. 2009). By contrast, the elderly microbial profile exhibits interindividual variability but is commonly enriched in Bacteroidetes members and *Clostridium* species (Claesson et al. 2011; Mariat et al. 2009). This disparity between age groups is magnified in centenarians with decreases in butyrate-producing *Clostridium* clusters and an enrichment in pathological Proteobacteria (Biagi et al. 2010). These ‘pathobionts’ are facultative anaerobes that are minor components of the microbiota under normal conditions but thrive in an inflamed environment (Pédron and Sansonetti, 2008). During inflammaging, these opportunistic species readily escape immune surveillance, surpass coverage of beneficial symbionts, and induce pathology.

With many studies elucidating an ‘aged’ microbial profile, researchers have attempted to manipulate microbiota composition in the elderly with the use of probiotic (live beneficial bacteria) and prebiotic (insoluble fibre supporting indigenous bacterial growth) dietary supplements. *Bifidobacterium* pro- and prebiotics have both been shown to reduce systemic proinflammatory cytokines and increase anti-inflammatory factors, suggesting an amelioration of inflammaging (Ouwehand et al. 2008). The efficacy of probiotics for disorders of the central nervous system has been demonstrated in rodent models, where *Bifidobacterium* and *Lactobacillus* probiotics were found to decrease anxiety-like behaviour and alter gamma-Aminobutyric acid (GABA) receptor expression in the brain, a receptor with a principal role in anxiety disorders (Messaoudi et al. 2011; Bravo et al. 2011). Extending these findings to elderly humans, community-dwelling subjects showed improved cognitive function and late-life depression outcomes following probiotic use (Kim et al. 2020). Many studies, however, have challenged such findings, suggesting that probiotics are shed in stool immediately following administration and are unable to colonise the gastrointestinal tract (Wang et al. 2015; Sierra et al. 2010). Others have

demonstrated successful modification of microbial community structure through probiotic treatment, but with transient and variable colonisation patterns across subjects (Zmora et al. 2018).

### 1.3 Existing models of microbiome study

As the vast majority of bacterial species in the human gut are non-cultivable, it was not until the development of next-generation sequencing that microbes could be identified and studied in their natural assemblies (Villanueva-Millán et al. 2015). Studies utilising germ-free (GF) mice, rendered axenic by rearing from birth in sterile environments, have been instrumental in elucidating the microbiome's role in host physiology (Douglas, 2018; Sommer and Bäckhed, 2013). For example, the development of the innate and adaptive immune systems is impaired in GF mice. These animals display aberrant cytokine profiles, impaired secretion of immunoglobulins, and a malformation of gut-associated lymphoid tissue (Round and Mazmanian, 2009). In addition, the absence of commensal microbes inhibits the formation of microvasculature networks in the gut thereby disrupting the integrity of the intestinal mucosa (Stappenbeck et al. 2002). The beneficial effects of microbial symbionts are also evident outside the intestine, influencing normal function of the cardiac, nervous, and reproductive systems (Tang et al. 2017; Cryan and Dinan, 2012; Shimizu et al. 1998). Moreover, GF mice can be rendered gnotobiotic – an experimental state in which all microorganisms present are clearly defined. Recolonisation of the axenic host with specific microbiota has permitted the study of the effects of individual microbes as well as synergistic/antagonistic interactions between microbes (Martín et al. 2016).

Despite the contributions of GF and gnotobiotic mice to our understanding of host-microbe interactions, the models possess certain methodological limitations. GF mice must be reared in controlled environments devoid of microorganisms and are therefore costly and labour-intensive to maintain. Data collection is a slow and low-throughput process, particularly in ageing research as laboratory mice hold an average lifespan of three years (Cho and Blaser, 2012). In addition to mice, researchers have explored the viability of fish species as a model for host-microbe interactions with a specific focus on ageing. The zebrafish (*Danio rerio*) is a favoured option considering their repertoire of genetic and genomic resources, amenable to genetic and chemical screening, and are optically transparent during development allowing *in vivo* imaging of host and microbial cells (Pham et al. 2008). However, with a lifespan like that of mice, zebrafish are also a low-throughput model with which to examine the interface of microbiota and ageing. The turquoise killifish (*Nothobranchius furzeri*) has recently been developed to circumvent this drawback due to their taxonomically diverse gut microbiota and short life cycle (Smith et al. 2017; Valenzano et al. 2017). Faecal transplants from young killifish promote youthful microbiota, both in composition and diversity, in middle-aged recipients. Older killifish recolonised with bacteria from young donors displayed lifespan extension as well as delays in age-associated behavioural decline, directly demonstrating microbial regulation of the ageing process (Smith et al. 2017). Nonetheless, GF fish require highly specialised diets to develop into adulthood and their tank-based husbandry still presents a significant cost (Pham et al. 2008). There is a pressing need to complement traditional animals with technically straightforward and inexpensive model systems amenable to the manipulation of both host and microbial genetics.

#### 1.4 *Caenorhabditis elegans*: A powerful genetic model system

The soil-dwelling nematode *Caenorhabditis elegans* has been used as a model organism for biological research since the 1970s (Brenner, 1974). Over the past 50 years, *C. elegans* has become a favoured model for studies in genetics, neuroscience, ageing, and more, due to its many inherent advantages. *C. elegans* is a bacterivore and is easily maintained in a laboratory setting without the need for specialised facilities. *C. elegans* was the first multicellular organism to have a fully sequenced and annotated genome. Genome-wide *C. elegans* RNA interference (RNAi) libraries have since been constructed, allowing for phenotypic characterisation of hundreds of genes through loss-of-function screens (Rual et al. 2004; Kamath et al. 2003). This is further complemented by a range of fluorescent reporter strains in which endogenous proteins and subcellular compartments are tagged with fluorescent proteins (Corsi et al. 2015). As the nematode possesses a transparent cuticle, visualising these reporters and examining gene expression patterns *in vivo* is relatively straightforward. Approximately 50% of *C. elegans* genes possess human orthologues, indicating a degree of evolutionary conservation that makes the nematode a compelling model for dissecting pathways central to human biology (*C. elegans* Sequencing Consortium, 1998).

The nematode has two sexes: self-fertilising hermaphrodites and males, allowing for tight genotypic control as well as genetic crosses. When cultured at 20°C, wildtype *C. elegans* exhibit a mean lifespan of 18-20 days during which time they can produce up to 300 eggs (Schaffitzel et al. 2006; Hertweck et al. 2003; Riddle, 1997). The nematode's short generation time and enhanced fecundity have made it an ideal high-throughput model for explorations into the biology of ageing (reviewed in Zhang et al. 2020). The primary ageing metric used in *C. elegans* is lifespan, now known to be determined by the activity of over 1000 genes (Tacutu

et al. 2013). Some of the most extensively characterised of these genes are located within pathways mediating stress responses and nutrient sensing, which are evolutionarily conserved in mammals (Kenyon, 2010). Inhibition of pathways such as the IIS and TOR signalling cascades have been shown to induce changes in gene expression that increase resistance to stress and extend lifespan. These independent nutrient sensing pathways also underlie lifespan extension in response to dietary restriction – a phenomenon observed in mammals and *Drosophila melanogaster* as well as in the nematode (Fontana et al. 2010).

### 1.5 *Caenorhabditis elegans*: An emerging model for host-microbe interactions

In the laboratory, *C. elegans* is reared on plates of solidified nematode growth medium (NGM). Worms are age-synchronised and sterilised through hypochlorite treatment then typically maintained on a single bacterial species: the gram-negative *Escherichia coli* B strain OP50 (Brenner, 1974). OP50 was selected not for any resemblance to the worm's native food sources but for ease of use in *C. elegans* husbandry protocols. OP50 is cultivable in the lab but is also a uracil auxotroph with a limited capacity for growth, allowing worms to be visualised on the surrounding bacterial lawn. *E. coli* bacterial libraries have since been generated in order to perform high-throughput, unbiased screens for microbial genetic pathways underlying phenotypes observed in the host. The *E. coli* K-12 Keio library, containing nearly 4,000 single gene deletion mutants, has enabled the identification of bacterial genes contributing to lifespan extension in *C. elegans* (Baba et al. 2006). Longevity-promoting bacterial genes act through a variety of molecular mechanisms including the IIS and mTOR pathways, bacterial production of the polysaccharide colonic acid, or disruption of bacterial folate synthesis (Pryor et al. 2019; Han et al. 2017; Virk et al. 2016; Cabreiro et al. 2013).

Although such studies have deepened our understanding of cross-talk between microorganisms and their host, *C. elegans* has primarily been studied outside of its native microbial ecology. In the wild, *C. elegans* feeds on decaying organic material such as rotting fruit and stems (Frézal and Félix, 2015). It was previously thought that bacteria served only as a source of nutrients for *C. elegans* and that they were unable to proliferate in the gut due to the macerating action of the worm's pharyngeal grinder (Zhang et al. 2017). For decades, this belief was largely unchallenged by the standard monoxenic conditions of *C. elegans* cultivation. Evidence from *C. elegans* harvested in their native substrates, however, suggests the nematode harbours diverse and functional microbiota. The wild *C. elegans* microbiome was first described in 2016 by three independent laboratories Dirksen et al. 2016, Samuel et al. 2016; Berg et al. 2016). Each of the studies characterised bacterial taxa using deep sequencing of the fourth variable region (V4) of the 16S rDNA gene, encoding a component of the 30S ribosomal subunit. The gene has long been a favoured marker in phylogenetic analyses due to its ubiquity, functional consistency, and variable evolutionary rates in different species, allowing for the measurement of phylogenetic relationships (Tringe and Hugenholtz, 2008. Woese, 1987). Microbial profiles of the guts of wild *C. elegans* as well as their native surroundings were obtained (Dirksen et al. 2016, Samuel et al. 2016). Unlike lab-reared nematodes, wild *C. elegans* isolates possess a diverse microbiome dominated by *Proteobacteria*, including the genera *Pseudomonas*, *Stenotrophomonas*, *Ochrobactrum*, and *Sphingomonas* (Dirksen et al. 2016; Samuel et al. 2016; Stiernagle, 2006). The microbiota of wild *C. elegans* were found to be distinct from their surrounding substrates and resembled those of other *C. elegans* isolates despite differences in their geographic origins. Interestingly, worms that were raised in artificial microcosms designed to emulate natural substrates exhibited microbiota resembling that of wild *C. elegans* isolates (Berg et al. 2016). Altogether, these complementary studies suggest the existence of a non-random, core *C. elegans* microbiota that is distinct from the animal's environment.

## 1.6 Concluding remarks

There is a large body of literature that has emphasised the role of the gut microbiota in regulating aspects of host physiology, including host ageing. Increasingly, there is evidence to suggest that microbiome-targeted interventions may improve age-related phenotypes in the host and ultimately contribute to an extension of host healthspan. The inherent complexity and heterogeneity of the microbiome in higher animals makes this relationship difficult to examine, particularly from a mechanistic or causative perspective. The overarching aim of this project is to use the bacterivore nematode *C. elegans* – with its short lifespan and available battery of genetic tools – in concert with its native microbiota to investigate microbiome effects on host physiology throughout age, all while gaining mechanistic insight into the emergence of such effects.

## 2. Materials and Methods

### 2.1 Contributors to data

Some data presented in this project was generated by associated members of the Ezcurra laboratory or by external collaborators, within or outside of the University of Kent. The identities of contributors are outlined in Table 2.1.

Data	Contributors
General <i>C. elegans</i> healthspan assays	Lifespan assay - FX Fecundity assay – LF Developmental timing assay – LF Body size analysis – FX Pharyngeal pumping assay – LF Defecation assay – MVP Food preference assay – FX
Commensal bacteria rRNA sequencing	Sample preparation and data analysis – MVP rRNA sequencing – Novogene UK
<i>C. elegans</i> RNA Sequencing	Sample preparation – MVP and ND Data analysis – ND
<i>C. elegans</i> motility assays	Thrashing assays – MVP and AK Gentle touch assay – AK Pluronic gel burrowing assay – FX and BK Contractility assay – FX Mechanosensory neuron imaging – MVP Body wall muscle imaging – MVP and FX A $\beta$ -associated paralysis assay - MVP
Electron microscopy	Sample preparation – MVP and IB Electron microscopy – IB EM micrograph image analysis – ND
Thioflavin T assay	Sample preparation and analysis – MVP and LA Size exclusion column operation and maintenance – LA and SH
<p>Contributor legend: MVP – Mireya Vazquez-Prada<sup>1</sup>, FX – Dr. Feng Xue<sup>1</sup>, AK – Antonis Karamalegos<sup>1</sup>, LF – Laura Freeman<sup>1</sup>, ND – Nathan Dennis<sup>1</sup>, BK – Brigita Kudzminskaitė<sup>1</sup>, IB – Dr. Ian Brown<sup>2</sup>, LA – Dr. Liam Aubrey<sup>3</sup>, SH – Dr. Samantha Hobbs<sup>3</sup></p> <p><sup>1</sup>Ezcurra lab, University of Kent <sup>2</sup>Kent Fungal Group, University of Kent <sup>3</sup>Xue lab, University of Kent</p>	

Table 2.1. Contributors to data within this project.

## 2.2 Strains and reagents

### 2.2.1 *C. elegans* strains

All *C. elegans* strains used in this project are listed in Table 2.2.

Strain	Genotype	Description (as used in project)	Source
AM140	<i>rmls132</i> ( <i>p<sub>unc-54</sub>::Q35::YFP</i> )	Yellow fluorescent protein (YFP) fused to 35-repeat polyglutamine (Q35) expressed in body wall muscle (Morley et al. 2002).	Labaddia lab, University College London
AU1	<i>sek-1</i> ( <i>ag1</i> )	Knockout in <i>sek-1</i> (Kim et al. 2002).	CGC, University of Minnesota
AU3	<i>nsy-1</i> ( <i>ag3</i> )	Knockout in <i>nsy-1</i> (Kim et al. 2002).	CGC, University of Minnesota
BXN723	<i>fzo-1</i> ( <i>cjn020</i> ) II	Knockout in <i>fzo-1</i> (Byrne et al. 2019).	Neumann lab, Monash University
CE541	<i>sbp-1</i> ( <i>ep79</i> )	Knockout in <i>sbp-1</i> (Liang, et al. 2010).	CGC, University of Minnesota
CU6372	<i>drp-1</i> ( <i>tm1108</i> ) IV	Knockout in <i>drp-1</i> (Breckenridge et al. 2008).	CGC, University of Minnesota
GMC101	<i>p<sub>unc-54</sub>::A<math>\beta</math><sub>1-42</sub>::unc-54</i> 3'-UTR + <i>p<sub>mll-2</sub>::GFP</i>	Full-length human A $\beta$ <sub>1-42</sub> expressed in body wall muscle. GFP expressed in intestine. (McColl et al. 2012).	CGC, University of Minnesota
GR2247	<i>mdt-15</i> ( <i>mg584</i> ) III	Gain-of-function mutation in <i>mdt-15</i> (Mao et al. 2019).	CGC, University of Minnesota
GR2249	<i>hsp-6</i> ( <i>mg585</i> )	Reduction-of-function mutation in <i>hsp-6</i> (Mao et al. 2019).	CGC, University of Minnesota
JIN1375	<i>hlh-30</i> ( <i>tm1978</i> ) IV	Knockout in <i>hlh-30</i> (Settembre et al. 2013).	CGC, University of Minnesota
KU25	<i>pmk-1</i> ( <i>km25</i> )	Knockout in <i>pmk-1</i> (Kim et al. 2004), (Matsumoto Group).	CGC, University of Minnesota
N/A	<i>jsIs609</i> ( <i>p<sub>mec-4</sub>::GFP<sup>mit</sup></i> ) X	GFP expressed in mitochondria of mechanosensory neurons (Fatouros et al. 2012).	CGC, University of Minnesota
N/A	<i>myo-3::GFP<sup>mit</sup>; pmk-1</i> ( <i>km25</i> )		This project (Genetic cross performed by AK)
N2 Bristol (Wildtype)	N/A	N/A	<i>Caenorhabditis</i> Genetic Center (CGC), University of Minnesota
QC115	<i>atfs-1</i> ( <i>et15</i> )	Gain-of-function mutation in <i>atfs-1</i> (Rauthan et al. 2013).	CGC, University of Minnesota

RB1085	<i>tir-1(ok1052)</i> III	Knockout in <i>tir-1</i> (OMRF Knockout Group).	CGC, University of Minnesota
RB2547	<i>pink-1(ok3538)</i>	Knockout in <i>pink-1</i> (OMRF Knockout Group).	CGC, University of Minnesota
RB2603	<i>ftn-1(ok3625)</i> V	Knockout in <i>ftn-1</i> (OMRF Knockout Group).	CGC, University of Minnesota
RW1596	$p_{myo-3}::GFP::myo-3 + rol-6(su1006)$ V	GFP-tagged MYO-3 protein (Meissner et al. 2009). Rollers.	CGC, University of Minnesota
SJ4103	<i>zcls14(myo-3::GFP<sup>mit</sup>)</i>	GFP expressed in mitochondria of body wall muscle (Benedetti et al. 2006).	CGC, University of Minnesota
SJ4151	$p_{ubl-5}::ubl-5::GFP$	GFP-tagged UBL-5 protein (Benedetti et al. 2006).	CGC, University of Minnesota
SJ4197	$p_{dve-1}::dve-1::GFP$	GFP-tagged DVE-1 protein (Haynes et al. 2007).	CGC, University of Minnesota
VC1518	<i>atf-7(gk715)</i>	Knockout in <i>atf-7</i> ( <i>C. elegans</i> Deletion Mutant Consortium, 2012).	CGC, University of Minnesota
VC2654	<i>ubl-5(ok3389)</i>	Knockout in <i>ubl-5</i> ( <i>C. elegans</i> Deletion Mutant Consortium, 2012).	CGC, University of Minnesota
VC3201	<i>atfs-1(gk3094)</i>	Knockout in <i>atfs-1</i> ( <i>C. elegans</i> Deletion Mutant Consortium, 2012).	CGC, University of Minnesota
XA7702	<i>mdt-15(tm2182)</i> III	Reduction-of-function mutation in <i>hsp-6</i> (possible hypomorphic allele) (Taubert et al. 2008).	CGC, University of Minnesota
ZB154	<i>zcls5(p<sub>mec-4</sub>::GFP)</i>	GFP-labelled mechanosensory neurons (Toth et al. 2012).	Driscoll lab, Rutgers University

Table 2.2 *C. elegans* strains used in this project.

## 2.2.2 Bacterial strains

All bacterial strains used in this project are listed in Table 2.3.

Bacterial ID	Species	Source
L4440	<i>E. coli</i> HT115 (DE3) harbouring empty vector plasmid pL4440	Dr. Jennifer Tullet, University of Kent, United Kingdom
MYb9	<i>Achromobacter</i> sp. F32	Dr. Hinrich Schulenberg, Christian-Albrechts-Universität zu Kiel, Germany
MYb10	<i>Acinetobacter</i> sp. LB BR12338	Dr. Hinrich Schulenberg, Christian-Albrechts-Universität zu Kiel, Germany
MYb11	<i>Pseudomonas lurida</i>	Dr. Hinrich Schulenberg, Christian-Albrechts-Universität zu Kiel, Germany

MYb27	<i>Arthrobacter aurescens</i>	Dr. Hinrich Schulenberg, Christian-Albrechts-Universität zu Kiel, Germany
MYb45	<i>Microbacterium oxydans</i>	Dr. Hinrich Schulenberg, Christian-Albrechts-Universität zu Kiel, Germany
MYb56	<i>Bacillus</i> sp. SG20	Dr. Hinrich Schulenberg, Christian-Albrechts-Universität zu Kiel, Germany
MYb57	<i>Stenotrophomonas</i> sp. R-41388	Dr. Hinrich Schulenberg, Christian-Albrechts-Universität zu Kiel, Germany
MYb71	<i>Ochrobactrum</i> sp. R-26465	Dr. Hinrich Schulenberg, Christian-Albrechts-Universität zu Kiel, Germany
MYb83	<i>Leuconostoc pseudomesenteroides</i>	Dr. Hinrich Schulenberg, Christian-Albrechts-Universität zu Kiel, Germany
MYb120	<i>Chryseobacterium</i> sp. CHNTR56	Dr. Hinrich Schulenberg, Christian-Albrechts-Universität zu Kiel, Germany
MYb218	<i>Serpens (Pseudomonas) flexibilis</i>	Dr. Hinrich Schulenberg, Christian-Albrechts-Universität zu Kiel, Germany
OP50	<i>Escherichia coli</i> OP50	CGC
PA14	<i>Pseudomonas aeruginosa</i> PA14	Dr. Gary Robinson, University of Kent, United Kingdom
pET Sac A $\beta$ <sub>1-42</sub>	BL21-DE3 <i>E. coli</i> strain containing pET-Sac A $\beta$ <sub>1-42</sub> expression plasmid	Dr. Wei-Feng Xue, University of Kent, United Kingdom
<i>spg-7</i> RNAi	<i>E. coli</i> HT115 (DE3) harbouring plasmids expressing dsRNA targeting <i>spg-7</i>	Dr. Jennifer Tullet, University of Kent, United Kingdom

Table 2.3 Bacterial strains used in this project.

### 2.2.3 Reagents and commercial kits

The reagents and commercial kits used within the scope of this project are detailed in Tables 2.4 and 2.5.

Reagent name	Source	Identifier
1-bromo-3-chloropropane (BCP)	Thermo Fisher Scientific	A11395
5% Sodium hypochlorite	Sigma-Aldrich	239305
Acetonitrile, HPLC grade	Fisher Chemical	75-05-8
Agar	Melford	A20020
Agarose	Melford	A20085
Ampicillin	Sigma-Aldrich	59349
Bacto-peptone	GIBCO	211677
Calcium chloride (CaCl <sub>2</sub> )	Sigma-Aldrich	1023921000

Chloramphenicol	Sigma-Aldrich	C0378
Cholesterol	Sigma-Aldrich	C8667
D-(+)-Glucose ≥99.5% anhydrous	Thermo Fisher Scientific	A16828.0E
DEAE sepharose	Sigma-Aldrich	DFF100
Dichloromethane, HPLC grade	Fisher Chemical	75-09-2
Disodium hydrogen phosphate (Na <sub>2</sub> HPO <sub>4</sub> )	Sigma-Aldrich	S9763
Ethyl acetate, HPLC grade	Fisher Chemical	141-78-6
Ethylenediamine tetraacetic acid (EDTA)	Sigma-Aldrich	E9884
Guanidine hydrochloride	Melford	G49000
Hydrochloric acid (HCl)	Sigma-Aldrich	320331
Isopropyl-β-D-thiogalactopyranoside (IPTG) ≥99 %	Thermo Fisher Scientific	15529019
Kanamycin sulfate	Sigma-Aldrich	K1377
Luria Bertani (LB) broth Miller	Melford	L24400
Magnesium sulphate (MgSO <sub>4</sub> )	Honeywell	7487-88-9
Methanol, HPLC grade	Fisher Chemical	67-56-1
Potassium phosphate (KH <sub>2</sub> PO <sub>4</sub> )	Sigma-Aldrich	P0662
Sodium azide	Sigma-Aldrich	S2002
Sodium chloride	Melford	S23020
Sodium phosphate dibasic heptahydrate (Na <sub>2</sub> HPO <sub>4</sub> ·7H <sub>2</sub> O)	Sigma-Aldrich	S9390
Tetramisole hydrochloride	Sigma-Aldrich	16595-80-5
Tris	Sigma-Aldrich	1185-53-1
Triton-X 100	Thermo Fisher Scientific	9002-93-1
TRIzol	Invitrogen	15-596-018
Urea	Sigma-Aldrich	U5128

Table 2.4 Reagents used in this project.

Commercial kit name	Source	Identifier
DNEasy Blood and Tissue Kit	QIAGEN	69504
RNEasy Mini Kit	QIAGEN	74104

Table 2.5 Commercial kits used in this project.

## 2.3 Methods

### 2.3.1 Culturing bacterial strains

In the laboratory, *C. elegans* are maintained on the canonical *Escherichia coli* strain OP50. Bacterial strains (Table 2.3) comprising the experimental microbiome (EM) were acquired courtesy of the Schulenberg lab at the Christian-Albrechts-Universität zu Kiel, where they were isolated from the native *C. elegans* gut and characterised by deep sequencing (Dirksen et al. 2016). All bacterial strains were stored at -80°C until use, in a 82% (v/v) preparation of bacterial culture in LB medium, with the remaining 18% composed of sterile 87% glycerol solution. Frozen stocks were streaked onto 10-cm agar plates using a sterile plastic loop and incubated at 37°C (*E. coli* OP50) or 25°C (EM strains; a lower temperature was used to emulate EM strains' native environments). Single colonies from each strain were used to inoculate 5 mL of LB medium or minimal media (100mM M9 salts, 0.4% (w/v) sterile glucose, 1mM MgSO<sub>4</sub>, 1µM CaCl<sub>2</sub>), as required. OP50 cultures were grown overnight at 37°C while EM strains were grown for 72 hours at 25°C. Prior to seeding of plates, equal volumes of each EM culture were aseptically combined.

### 2.3.2 RNA interference (RNAi)

*E. coli* HT115 (DE3) bacteria containing plasmids expressing dsRNA targeting specified genes were obtained from the Ahringer and Vidal libraries (Rual et al. 2004; Kamath et al. 2001). The empty vector plasmid pL4440 was used as a control. Bacterial cultures were grown overnight at 37°C in LB broth containing 50 µg/mL ampicillin. Ampicillin was washed from cells by centrifugation and the resulting supernatant was disposed. Cells were then resuspended in fresh LB. Cultures were seeded onto NGM plates containing 50 µg/mL carbenicillin and 1 mM isopropylthio-β-galactoside (IPTG). Nematodes were synchronised

by bleaching (see Age-synchronisation of *C. elegans*: Egg prep protocol) and cultivated on RNAi plates. If an RNAi targeted gene was developmentally lethal, nematodes were cultivated on OP50 and transferred onto RNAi plates at L4 stage.

### 2.3.3 Preparation of nematode growth medium (NGM) plates

*C. elegans* were maintained on 6-cm NGM agar plates. Dry reagents (17 g/L agar, 2.5 g/L Bacto Peptone, 3 g/L NaCl) were combined, autoclaved, and maintained in a water bath at 55°C until pouring. Filter-sterilised  $\text{H}_2\text{KPO}_4/\text{HK}_2\text{PO}_4$  pH 6.0 (to 25 mM),  $\text{CaCl}_2$  (to 1 mM),  $\text{MgSO}_4$  (to 1 mM), and cholesterol prepared in ethanol (to 1mM) were added immediately before pouring and mixed thoroughly. Ten mL of liquid NGM agar was dispensed into each plate while observing sterile technique. Plates were left to solidify/dry for at least 72 hours before seeding with the bacterial strain(s) of interest.

### 2.3.4 Seeding NGM plates

Using sterile technique, 200  $\mu\text{L}$  of bacterial culture was pipetted onto the centre of each plate and incubated at room temperature for at least 48 (OP50 condition) or 72 (EM condition) hours before use.

For experiments using cell-free media (CFM) from the combined experimental microbiome/individual strains, liquid bacterial cultures were centrifuged at 5000 rpm for 20 minutes. The resulting supernatant was then sterilised using a 0.2  $\mu\text{m}$  HPLC-grade syringe filter (Sartorius). Sterile CFM was then pipetted onto an established OP50 lawn (200  $\mu\text{L}$  of CFM added to 200- $\mu\text{L}$  OP50 lawn).

### 2.3.5 Maintenance of *C. elegans* strains

Standard *C. elegans* maintenance methodology was adhered to unless otherwise stated (Brenner, 1974). Wildtype *C. elegans* described were Bristol N2 hermaphrodites. *C. elegans* strains were maintained monoxenically on OP50-seeded NGM plates at 20°C. In order to prevent starvation, approximately five gravid adult animals were transferred onto fresh OP50 plates every three days. All maintenance and experimental work was performed aseptically using a flame-sterilised 0.3 mm platinum wire (Thermo Fisher Scientific) held within an aluminium wire-holder. To transfer a greater number of animals, small chunks of NGM were cut from densely populated plates using a flame-sterilised scalpel and placed onto fresh OP50 plates.

### 2.3.6 Age-synchronisation of *C. elegans* populations: Egg-prep protocol

Densely populated NGM plates (mixed developmental stages but consisting mainly of gravid adults) were washed with M9 buffer (3 g/L  $\text{KH}_2\text{PO}_4$ , 6 g/L  $\text{Na}_2\text{HPO}_4$ , 5 g/L NaCl, 1 mM  $\text{MgSO}_4$ ) and dislodged nematodes were collected in a 15 mL conical tube. Nematodes were gently centrifuged (one minute at 3000 rpm) and M9 was aspirated leaving 500  $\mu\text{L}$  of liquid in the tube. Approximately 300  $\mu\text{L}$  of egg preparation solution (equal volumes 4M NaOH and 5% solution sodium hypochlorite) was added to the tube and incubated until adult nematodes were mechanically disrupted (six to eight minutes), leaving the eggs in solution. The alkaline hypochlorite was neutralised with the addition of M9 buffer and eggs were pelleted by centrifugation under the same conditions. Aspiration and washing with M9, without disturbing the egg-enriched pellet, was repeated at least twice. The egg-enriched pellet was resuspended in M9 and pipetted onto seeded NGM plates for incubation at 20°C. After 72 hours of growth, required numbers of L4 larvae

were transferred onto new plates for experimentation. Larvae of the appropriate stage were selected for the appearance of a 'Christmas-tree' invagination of the vulva indicating the transition to sexual maturity (Podbilewicz, 2006). Adult animals were henceforth transferred onto fresh experimental plates every two days to avoid overgrowth of offspring and maintained at 20°C (unless otherwise specified).

#### 2.3.7 Age-synchronisation of *C. elegans* populations: Drop bleaching protocol

For age-synchronisation of smaller populations, two drops of drop bleach solution (equal volumes 1M NaOH and 5% solution sodium hypochlorite) were applied to opposing ends of a seeded NGM plate. Approximately 20 gravid adults were picked into each drop and plates were incubated at 20°C. After 72 hours of growth, required numbers of L4 larvae were transferred onto new plates for experimentation. Larvae of the appropriate stage were selected for the appearance of a 'Christmas-tree' invagination of the vulva indicating the transition to sexual maturity (Podbilewicz, 2006). Adult animals were henceforth transferred onto fresh experimental plates every two days to avoid overgrowth of offspring and maintained at 20°C (unless otherwise specified).

#### 2.3.8 Lifespan/survival assay

All survival assays were conducted manually on solid culture systems as previously described, at 20°C (Park et al. 2017, Amrit et al. 2014). To prevent detrimental effects on experimental microbiome bacterial strains, 5'-fluoro-2'-deoxyuridine (FUDR) was not used to eliminate live progeny. Instead, the adult population was transferred daily until cessation of reproduction. Results are expressed as mean percentage of initial population remaining

pooled from five independent biological replicates. Statistical significance was determined using a Log-rank (Mantel-Cox) test. Survival assays were performed by FX.

### 2.3.9 Food preference assay

Wildtype D1 nematodes cultivated on either OP50/EM were transferred into sterile M9 buffer and washed thrice to remove surface microbes. Nematodes were pipetted onto the centre of NGM plates seeded with equidistant 15  $\mu$ L lawns of both OP50 and EM. Plates were incubated at 20°C for 24h then imaged with a WormLab Imaging System (MBF Bioscience) overhead camera. The number of nematodes in each bacterial lawn at the 24h mark was recorded. Results are expressed as mean proportion of nematodes in each food source  $\pm$  standard error of the mean from three independent pools of biological replicates. Food preference assays were performed by FX.

### 2.3.10 Fecundity (brood size) assay

Wildtype L4 nematodes were individually picked onto seeded NGM plates of the specified feeding condition. Parent nematodes were transferred onto fresh plates at the same time each day and the number of viable progeny on source plates was counted. Parent nematodes were followed until D6 of adulthood. Results are expressed as mean brood size ( $n \approx 10$  per trial) per day of adulthood  $\pm$  standard error of the mean of three independent pools of biological replicates. Results are also expressed as mean total brood size per nematode  $\pm$  standard error of the mean. Brood size assays were performed by LF.

### 2.3.11 Developmental timing assay

Synchronised wildtype *C. elegans* eggs were incubated on NGM plates seeded with OP50 or the EM at 20°C. After 60h, 50 nematodes per condition were mounted as described in 'Mounting of fluorescent *C. elegans* strains for microscopy' and imaged with brightfield illumination at 40x objective. The developmental stages of each nematode were scored based on vulval structure/presence of fertilised oocytes as described previously (Mok et al. 2015):

Stage	Phenotype
L3	No apparent vulva.
Early L4	L4.1-L4.4 inclusive. All substages from formation of vulval lumen to fully distended uterine lumen.
Late L4	L4.5-L4.9 inclusive. All substages from curvature in side of vulval lumen to vulval lumen collapse.
Adult	Fertilised oocytes present.

Table 2.6. Descriptions of developmental stages at 60h.

Results are expressed as mean proportions of the population corresponding to each developmental stage  $\pm$  standard error of mean from three independent biological replicates. Developmental timing assays were performed by LF.

### 2.3.12 Body size analysis

Wildtype nematodes were individually suspended in a single drop of M9 buffer on glass slides and imaged with a WormLab Imaging System (MBF Bioscience) overhead camera. Fine focus and zoom settings were maintained across all video recording sessions. Still images from videos were processed using ImageJ software. Segmented lines were drawn from tip of nose to tapered tip of tail through the midline of the nematode. Calibrations were consistently maintained across all images. Results are expressed as mean body length  $\pm$  standard error of the mean of two independent pools of biological replicates with

three technical replicates each ( $n = 10$  per trial) on D1, D4, and D7 of adulthood. Body size analyses were performed by FX.

#### 2.3.13 Pharyngeal pumping assay

Wildtype adult nematodes of synchronised age were transferred onto fresh NGM plates consistent with the food source of their rearing and allowed to acclimate for one minute. The number of pharyngeal contractions per worm was counted by eye under maximum magnification using a Leica S6 E Stereo Zoom light microscope for 20 seconds. Results are expressed as mean pharyngeal pumps per minute  $\pm$  standard error of the mean of three independent pools of biological replicates ( $n = 15$  per trial) on D1, D4, and D7 adulthood. Pharyngeal pumping assays were performed by LF.

#### 2.3.14 Defecation assay

Wildtype adult nematodes of synchronised age were transferred onto fresh NGM plates consistent with the food source of their rearing and allowed to acclimate for five minutes. Beginning with the first peristaltic contraction of the posterior body wall muscle (pBoc, posterior body contraction), the time elapsed between four successive defecation motor programmes (DMPs) was recorded. Only nematodes in the process of feeding were assayed. If no pBoc was observed for five minutes, the nematode was listed as a non-defecator (0 DMPs per minute). Results are expressed as DMPs per minute  $\pm$  standard error of the mean of three independent pools of biological replicates ( $n = 10$  per trial) on D1, D4, and D7 adulthood.

### 2.3.15 Assessing two-dimensional motility in liquid media (thrashing assay)

Motility in liquid media was assessed on D1, D4, and D7 of adulthood via an established thrashing assay (Onken and Driscoll, 2010). *C. elegans* of specified ages were transferred onto unseeded NGM plates and permitted to roam to remove surface microbes. Worms were placed by eyebrow pick into individual wells of a 96-well plate (Greiner) containing M9 buffer and allowed to acclimate in liquid for 30 seconds. The number of complete body bends performed within a 30-second period were then counted. At least three independent trials of  $\geq 10$  worms each were performed per genetic background. Results are presented as mean thrashes per 30 seconds normalised to D1 results for each condition  $\pm$  standard error of the mean normalised to D1 from at least three independent biological replicates.

### 2.3.16 Assessing two-dimensional motility on solid media

Motility was assessed on solid NGM plates using a previously published qualitative scoring paradigm (Herndon et al. 2002). Animals were assigned to one of the following classes according to their movement ability:

Motility class	Phenotype
A	Spontaneous movement in a fluid sinusoidal manner.
B	Slow sinusoidal movement when prodded with platinum wire pick.
C	No movement (except for head) even when prodded with platinum wire pick.

Table 2.7 Motility classes used to assess movement of *C. elegans* on solid media.

### 2.3.17 Assessing three-dimensional motility (burrowing assay)

Neuromuscular health was assessed via a Pluronic gel-based burrowing assay as previously described (Lesanpezeshki et al. 2019). Wildtype nematodes of defined ages ( $n = 20$  per trial) were picked onto a solidified 10 $\mu$ L drop of Pluronic F-127 gel (Sigma) in the

centre of an empty 3-cm petri dish. The remainder of the plate was filled with liquefied Pluronic gel and allowed to set. Approximately 100µL of the selected bacterial culture was pipetted onto the solidified gel as a chemoattractant. Results are expressed as mean percentage of total animals identified in the bacterial drop at defined timepoints  $\pm$  standard error of the mean of three independent biological replicates on D1, D4, and D7 of adulthood. Pluronic gel burrowing assays were performed by FX.

#### 2.3.18 A $\beta$ -associated paralysis assay

Following synchronisation (see above), approximately 30 L4 larvae were transferred onto the appropriate NGM plates.  $p_{unc-54}::A\beta_{1-42}::unc-54$  3'-UTR +  $p_{mtl-2}::GFP$  (Strain ID: GMC101) animals carry a temperature-activated transgene, allowing the human amyloid beta (A $\beta$ ) isoform A $\beta_{1-42}$  to be expressed in body wall muscle following a shift to 25°C from 20°C. From days 1-4 of adulthood, the number of paralysed animals (relative to living animals) was recorded at approximately the same time each day. Paralysed nematodes were classified as being incapable of forward and backward movement when prodded but still alive i.e., moving nose or tail, feeding, laying eggs.

#### 2.3.19 Gentle touch assay

Gentle touch sensitivity was assessed as previously described (Chen and Chalfie, 2004). An eyebrow pick was used to stroke wildtype D1 nematodes in two locations: immediately posterior to the pharynx (to distinctly stimulate the anterior touch response) and immediately anterior to the anus (to distinctly stimulate the posterior touch response). Nematodes are said to be touch responsive if they cease movement towards /move away from the eyebrow. Each nematode ( $n = 10$  per feeding condition) was tested five times

anteriorly and five times posteriorly and the percentage of touches responded to (out of 10) was recorded. Results are expressed as mean percentage of all touches eliciting a response  $\pm$  standard error of the mean from three independent pools of biological replicates on D1, D4, D7, and D11 of adulthood. Gentle touch assays were performed by AK.

#### 2.3.20 Contractibility assay

Videos of wildtype nematodes were recorded as previously described in 'Body size assay.' Following the initial phase of recording, individual nematodes were transferred into a single drop of 200  $\mu$ M levamisole and allowed to paralyse. Still images from the videos were processed using ImageJ software. Segmented lines were drawn from the tip of nose to the tapered tip of tail through the midline of the nematode to measure body length in each animal before and after transfer into levamisole. Results are expressed as mean percentage change in body length  $\pm$  standard error of the mean of two independent pools of biological replicates with three technical replicates each ( $n = 10$  per trial) on D1, D4, and D7 of adulthood. Contractability was assessed by FX.

#### 2.3.21 Mounting of fluorescent *C. elegans* strains for microscopy

Mounting pads were formed by pipetting 30  $\mu$ L of molten 2% agarose (w/v), heated to 95°C, onto frosted microscope slides. Agarose was gently flattened with another glass slide to form a solidified mounting pad. Nematodes were transferred by eyebrow pick into a drop of 25 mM tetramisole (w/v, in M9 buffer) on each pad. Immobilised worms were gently rearranged by eyebrow pick and secured with a glass cover slide.

### 2.3.22 Epifluorescence microscopy

Fluorescent images were acquired with a Leica DMR compound epifluorescence microscope containing a GFP filter set (excitation 450-490 nm, emission 500-550 nm) connected to a High-Resolution Leica DFC camera. All images were captured using Leica Application Suite X and analysed using Fiji software (ImageJ). Objectives and exposures used per strain imaged are detailed in Table 2.8. For each strain imaged, at least three independent trials were performed with a minimum of 12 worms imaged per condition/timepoint.

Reporter strain	Objective	Exposure time (ms)
<i>myo-3::GFP<sup>mit</sup></i> (and generated cross)	63x	400
<i>p<sub>dve-1</sub>::dve-1::GFP</i>	10x	600
<i>p<sub>mec-4</sub>::GFP</i>	63x	400
<i>p<sub>myo-3</sub>::GFP::myo-3 + rol-6(su1006)</i>	63x	400
<i>p<sub>ubl-5</sub>::ubl-5::GFP</i>	10x	100

Table 2.8 Magnification objectives and exposure times used per fluorescent reporter strain imaged.

### 2.3.23 Scoring of mechanosensory neuron defects

*zdl55(p<sub>mec-4</sub>::GFP)* (strain ID: ZB154) nematodes were mounted and imaged as described in 'Mounting of fluorescent *C. elegans* strains for microscopy' and 'Epifluorescence microscopy.' Morphological abnormalities were documented in the somata and neurites of two gentle touch mechanosensory neurons: the ALM and PLM (see Figure 4.3 for diagram). The morphological abnormalities counted included blebs (triangle-shaped protrusions along neurite), waves (90° bends along neurite), and branches (novel outgrowths emanating from somata or neurite that were disparate from the primary neurite). Results are expressed as the mean number of each morphological abnormality

per ALM/PLM process  $\pm$  standard error of the mean of three independent pools of biological replicates ( $n \geq 12$  nematodes per trial) on D1, D4, and D7 of adulthood.

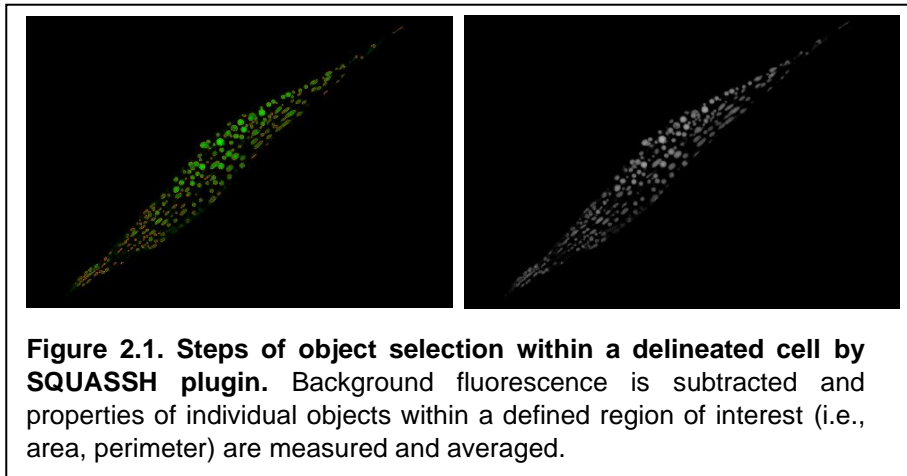
#### 2.3.24 Quantitative analysis of body wall muscle mitochondria

*zcls14(myo-3::GFP<sup>mit</sup>)* (strain ID: SJ4103) nematodes were mounted and imaged as described in 'Mounting of fluorescent *C. elegans* strains for microscopy' and 'Epifluorescence microscopy.' All images of fluorescent mitochondrial networks in muscle were processed in Fiji software (ImageJ) using the SQUASSH plugin (MOSAIC). The polygon selection tool was used to delineate individual body wall muscle cells in *zcls14(myo-3::GFP<sup>mit</sup>)* animals. For consistency, cells located halfway between the pharynx and vulva were preferentially selected. Image depth was converted to 16-bit, background was subtracted with a rolling ball window of 15 pixels, and area outside of the cell selection was cleared. Segmentation and object quantification were performed using the SQUASSH plugin (MOSAIC) with the following parameters (Byrne et al. 2019):

Parameter	Value
Regularisation, Channels 1,2	0.010
Minimum object intensity, Channels 1,2	0.100
Local intensity estimation	Automatic
Noise model	Gaussian
Standard deviation xy	0.790
Standard deviation z	0.710
Remove regions with size <	5 pixels

Table 2.9 Segmentation parameters used to quantify mitochondrial objects via the SQUASSH plugin on Fiji imaging software.

Mitochondrial morphology was evaluated both qualitatively and quantitatively using the acquired images. Mean area and perimeter values were collected on all objects within the region of interest and used to calculate circularity ( $C$ ) values between 0.0 (linear) and 1.0 (spherical) using the equation  $C = (4\pi) \times (\text{Area}/\text{Perimeter}^2)$ . Results are expressed as the mean circularity  $\pm$  standard error of the mean of three independent pools of biological replicates ( $n \geq 12$  nematodes per trial) on D1, D4, D7, and D11 of adulthood.



### 2.3.25 Qualitative scoring of muscular mitochondrial morphology

*zcls14(myo-3::GFP<sup>mit</sup>)* (strain ID: SJ4103) nematodes were mounted and imaged as described in 'Mounting of fluorescent *C. elegans* strains for microscopy' and 'Epifluorescence microscopy.' The qualitative scoring paradigm used is detailed below. Results are expressed as the mean fragmentation score  $\pm$  standard error of the mean of three independent pools of biological replicates on D1, D4, D7, and D11 of adulthood. Statistical significance was determined using a chi-square test.

Mitochondrial fragmentation score	Phenotype
0	Hyperfused; tubular networks of mitochondria are joined.
1	Linear; tubular networks of mitochondria in parallel.
2	Intermediate; both tubular and spherical mitochondria present in cell.
3	Fragmented; mostly spherical mitochondria covering majority of cell.
4	Very fragmented; large regions of cell devoid of GFP <sup>mit</sup> signal.

Table 2.10. Qualitative scoring paradigm for body wall muscle mitochondrial networks.

### 2.3.26 Qualitative scoring of ALM soma mitochondrial morphology

*jsIs609*(*p<sub>mec-4</sub>::GFP<sup>mit</sup>*) nematodes were mounted as described in ‘Mounting of fluorescent *C. elegans* strains for microscopy.’ ALM somata were imaged using the specifications described in ‘Epifluorescence microscopy.’ The qualitative scoring paradigm used is detailed below and was adapted from Morsci et al. (2016). Results are expressed as the mean fragmentation score  $\pm$  standard error of the mean of three independent pools of biological replicates on D1, D4, D7, and D11 of adulthood. Statistical significance was determined using a chi-square test.

Mitochondrial fragmentation score	Phenotype
0	Mitochondria organised into single filamentous loop around perimeter of soma.
1	Mitochondrial loop organised horizontally across centre of cell body.
2	Mitochondrial networks highly interconnected; redistributed to poles of soma.
3	Mitochondria at poles of soma; fragmentation evident.
4	Highly fragmented; short, globular mitochondria across whole soma.

Table 2.11. Qualitative scoring paradigm for mitochondrial networks in somata of ALM mechanosensory neurons.

### 2.3.27 Gut colonisation assay

Fifty synchronized adult nematodes from each bacterial feeding condition were picked and suspended in M9 buffer (Table 2.6). Animals were immobilised with 1 mM tetramisole and surface sterilised with 3% household bleach. Animals were washed at least thrice with sterile M9 buffer and centrifuged at 13,000 *g* for 60 seconds between each wash. The nematode pellet was resuspended in 1% Triton-X 100 then mechanically disrupted using a pellet pestle until a creamy suspension was obtained. The suspension was then centrifuged at 13,000 *g* for 10 minutes and the aspirated pellet was resuspended in M9. Serial dilutions ( $10^{-1}$ ,  $10^{-2}$ , and  $10^{-3}$ ) were prepared by pipetting 50  $\mu$ L of nematode suspension in 450  $\mu$ L deionised water (50  $\mu$ L was then taken from the new suspension, and so on). The dilution factor of each suspension was increased further (resulting in  $10^{-2}$ ,  $10^{-3}$ , and  $10^{-4}$  dilutions) by pipetting 50  $\mu$ L of each onto LB agar plates with sterile technique. No antibiotics were used. Bacterial plates were incubated for 24h either at 25°C (for experimental microbiome strains) or 37°C (for *E. coli* OP50). Following incubation, bacterial colonies on each plate were counted. The number of colony-forming units (CFUs) per nematode were calculated as follows:

$$\text{CFUs nematode}^{-1} = (\text{Number of colonies on plate} \times \text{Dilution factor}) / \text{Number of worms}$$

Results are expressed as mean number of CFUs per nematode  $\pm$  standard error of the mean of three independent biological replicates on D1 and D7 of adulthood.

### 2.3.28 Sample preparation for sequencing of 16S rRNA gene

Single colonies were picked from agar plates, used to inoculate 5 mL of LB media, and left to grow at 25°C for 72 hours. Bacterial DNA was extracted from 1.5 mL of culture as

described in the DNEasy Blood and Tissue Kit protocol for gram-negative bacteria (QIAGEN).

The 16S ribosomal RNA (rRNA) gene, encoding a component of the 30S prokaryotic ribosome, is an established method of reconstructing bacterial phylogenies due to a slow rate of evolution (Case et al. 2007; Woese and Fox, 1977). Samples' 16S sequences were amplified via polymerase chain reaction (PCR) in a 50 µL volume using 150 ng template DNA. GoTaq DNA Polymerase (Promega) and primers 27F (5'-AGAGTTTGATCCTGGCTCAG-3') and 1492R (5'-GGTTACCTTGTTACGACTT-3') (Eurofins) were used with the following conditions: initial denaturation at 95°C for two minutes; 30 cycles of 95°C for 30 seconds, 55°C for 30 seconds, and 72°C for 30 seconds, and final elongation at 72°C for five minutes. PCR products were purified as described in the QIAQuick PCR Purification Kit (QIAGEN) and submitted for Sanger sequencing (Source Bioscience, Cambridge, United Kingdom). The 16S rRNA sequences obtained were compared to 16S strain sequences compiled on the Ribosomal Database Project (Michigan State University, USA) and selected for highest S<sub>ab</sub> score, indicating the percentage of shared heptamers between the submitted sequence and database entries. All sequencing results obtained returned S<sub>ab</sub> scores of at least 0.8, with majority falling between 0.9 and 1.0.

### 2.3.29 Sample preparation for DNA sequencing

Genomic DNA was extracted from whole *C. elegans* and resident gut microbiota. Nematodes were age-synchronised (See 'Age-synchronisation of *C. elegans* populations: Egg-prep protocol') and transferred onto experimental plates at the L4 stage. A minimum of five experimental microbiome plates populated by animals of specified ages were

washed with M9 buffer and transferred to a 15 mL Falcon tube. Animals were pelleted by centrifugation at 2500 rpm for 30 seconds. Aspiration and washing with M9 was repeated twice, leaving 1 mL of liquid in the tube. Approximately 300  $\mu$ L of egg preparation solution was added and incubated for five minutes at room temperature. While worms were still opaque/translucent, the sterilisation step was neutralised with the addition of M9 buffer to 15 mL. A fresh agar plate was seeded with 500  $\mu$ L of supernatant and incubated overnight at 25°C to ensure sterility. Sterilised, intact worms were washed with fresh M9 thrice then resuspended in 200  $\mu$ L ATL buffer from the DNeasy Blood and Tissue kit (QIAGEN). Worms were transferred into a 1.5 mL Eppendorf tube and incubated overnight at -80°C, followed by three cycles of freezing (-20°C) and thawing (37°C). Samples were then prepared as per DNeasy Blood and Tissue kit instructions/reagents: 20  $\mu$ L of proteinase K was added followed by incubation at 56°C for three hours, vortexing in between, followed by 200  $\mu$ L of AL buffer. The samples were vortexed and incubated at 56°C for ten minutes followed by the addition of 200  $\mu$ L of absolute ethanol. Samples were mixed and pipetted into DNeasy Mini Spin Columns provided and centrifuged for one minute at 8000 rpm, discarding flow-through. Centrifugation under the same settings was repeated after the addition of 500  $\mu$ L of AW1 buffer, then 500  $\mu$ L of AW2 buffer. Columns were centrifuged at maximum speed for three minutes, transferred to a new collection tube, then spun for two minutes to dry the column membrane completely before transferring into sterile Eppendorf tubes. DNA was eluted using 50  $\mu$ L AE buffer then stored at -20°C. Purity of samples was assessed using a NanoDrop UV/Vis spectrophotometer (Thermo) while yield was determined using a Qubit Fluorometer as directed in the accompanying protocol (Invitrogen).

Samples were used to classify and quantify bacterial species in young (D1) and old (D7) wildtype worms reared on the experimental microbiome. For each aged condition, samples were collected from five independent biological replicates. Samples were shipped to Novogene UK Ltd. (Cambridge, United Kingdom) on dry ice for further processing and analysis.

### 2.3.30 DNA sequencing

Sequencing was performed by Novogene UK Ltd. (Cambridge, United Kingdom) using the 341F/806R primers to amplify region V4 of the 16S rRNA amplicon. The amplicon was sequenced on an Illumina paired-end platform to generate 250-bp paired-end raw reads. Chimeric sequences were filtered and Effective Tags were clustered with 97% identity to obtain subsequent operational taxonomic units (OTUs) identifying bacterial taxa. Results are expressed as mean proportion of each EM member strain (%) comprising total OTUs pooled from five independent biological replicates per sample type (nematode/plate).

### 2.3.31 Sample preparation for *C. elegans* RNA sequencing

RNA was extracted from whole animals using a TRIzol-1-bromo-3-chloropropane (BCP) procedure. Worms were age-synchronised (See 'Age-synchronisation of *C. elegans* populations: Egg-prep protocol') and transferred onto experimental plates at the L4 stage. For each feeding/genetic condition, at least four plates populated by animals of specified ages were washed with M9 buffer, transferring worms into a 15 mL Falcon tube. Worms were washed thrice, allowing worms to settle without centrifugation to avoid inducing stress, and transferred into an RNase-free Eppendorf tube. M9 was aspirated off and worms were resuspended in 500  $\mu$ L of TRIzol followed by ten cycles of freezing (-80°C),

thawing (37°C), and vortexing. Following the addition of 125 µL BCP, samples were incubated for three minutes then centrifuged at 12000 rpm for ten minutes at 4°C. The clear upper layer was carefully aspirated and transferred into a fresh RNase free tube. An equal volume of 70% ethanol (~300 µL) was added and mixed. Samples were transferred into a RNeasy Spin Column (QIAGEN) and purified as directed in the accompanying protocol. RNA was eluted using 35 µL of RNase free water and yield/purity analysed by NanoDrop spectrophotometer (Thermo) before storing at -20°C.

### 2.3.32 *C. elegans* RNA sequencing

RNA sequencing was performed by Glasgow Polyomics. Sequencing-ready libraries were created using the Illumina Stranded mRNA library preparation kit (Illumina) with polyA selection for mRNA enrichment. Sequencing was performed on an Illumina TruSeq 2000 sequencer using 2x75bp reads with a depth of 30M reads per sample. Raw data in FastQ format was processed by ND. Pre-processing i.e. removal of standard TruSeq adapter sequences was performed using fastP software (OpenGene). Reads were mapped to the wildtype *C. elegans* genome using the STAR software (Dobin et al. 2013) and genomic feature summarisation was performed using the featureCounts programme (Liao et al. 2014). The DESeq2 package (Love et al. 2014) was used for differential gene expression analysis of the sequencing data. Five biological replicates of two group samples (D1 nematodes reared on either OP50 or the EM) were subjected to analysis with a false discovery rate (FDR) cutoff of  $p < 0.05$ . Genes were considered differentially expressed with a logFC greater than 0.6 or less than -0.6.

### 2.3.33 Expression of recombinant A $\beta$ <sub>1-42</sub> from *Escherichia coli*

Glycerol stocks of pET Sac A $\beta$ <sub>1-42</sub> BL21 (DE3) *E. coli* cells provided by the Xue lab were streaked onto 100  $\mu$ M ampicillin, 30  $\mu$ M chloramphenicol LB-agar plates. Cultures were grown overnight at 37°C. Colonies were used to inoculate 100  $\mu$ M ampicillin, 30  $\mu$ M chloramphenicol LB media. Inoculated media was grown at 37°C overnight while shaking at 180 rpm. The following day, cultures were centrifuged at 4000 rpm for 10 minutes then resuspended in 1 L (per pellet) of 100  $\mu$ M ampicillin, 30  $\mu$ M chloramphenicol LB media made up in 2 L baffled flasks for maximum aeration. Resuspended pellets were grown at 37°C while shaking at 180 rpm until an optical density (OD<sub>600</sub>) of approximately 0.6 was reached. Cultures were induced with IPTG to obtain a final concentration of 1 mM then returned to the shaking incubator under the same conditions for four hours. Induced cultures were aliquoted as required and centrifuged for 10 minutes at 4000 rpm. After disposing of the supernatant, pellets were resuspended in a total of 200 mL 10 mM Tris, 1 mM EDTA, 20 mM NaCl pH 8.0. Resuspended cells were aliquoted into 50-mL Falcon tubes, centrifuged for 10 minutes at 4000 rpm, then frozen overnight at -80°C once supernatant had been removed.

The following day, 10 mM Tris, 1 mM EDTA pH 8.0 was added to frozen pellets. Without thawing, pellets were sonicated on ice on full power with maximum amplitude until complete dissolution. Sonicated pellets were centrifuged at maximum speed for 30 minutes then supernatant was discarded. Five mL of 10 mM Tris, 1 mM EDTA, 20 mM NaCl pH 8.0 was added to the pellet then sonicated on ice once more. Immediately, 20 mL of 10 mM Tris, 1 mM EDTA, 20 mM NaCl, 8M Urea pH 8.0 was added to the sonicated sample. The sample was then mixed with 7.5 mL of DEAE-Sepharose that had been pre-equilibrated in 10 mM Tris, 1 mM EDTA, 20 mM NaCl, 8M Urea pH 8.0. The combined

sample was gently agitated for one hour at room temperature using horizontal tube rollers then centrifuged for five minutes at 4000 rpm. After supernatant was discarded, pellets were resuspended in 1 mL of 10 mM Tris, 1 mM EDTA, 20 mM NaCl, 8M Urea pH 8.0 and transferred into disposable 0.8 cm x 4 cm Poly-Prep chromatography columns (Bio-Rad). The sample was allowed to elute by gravity flow into a sterile Falcon tube before the addition of 2.4 mL of 10 mM Tris, 1 mM EDTA, 70 mM NaCl, 8M Urea pH 8.0 to the column. The collected eluate was injected onto a 60-mL Superdex 75 size exclusion column (SEC) (Sigma-Aldrich) pre-equilibrated overnight in running buffer (10 mM Tris, 1 mM EDTA, 0.5 M NaCl, 6 M guanidine hydrochloride pH 8.0) at a flow rate of 0.1 mL/min. All buffers run through SEC columns were filtered through 0.2µm bottletop vacuum filters (Nalgene) and degassed before use. During fraction collection, running buffer was allowed to flow through the SEC column at 0.3 mL/min, generating 2 mL fractions until a total volume of 60 mL was reached. Protein-containing fractions as indicated by UV detector were aliquoted into 1.5-mL Eppendorf tubes and snap frozen using liquid nitrogen. Fractions of interest were stored at -80°C until monomer purification. Once all fractions had been collected, the SEC column was run in reverse sequence (running buffer followed by running buffer without guanidine hydrochloride) and stored in HPLC-grade ethanol.

#### 2.3.34 Purification of A $\beta$ <sub>1-42</sub> monomers

Amyloid monomers were purified using a 30-mL Superdex 75 SEC pre-equilibrated in 60 mL of HPLC-grade H<sub>2</sub>O followed by 60 mL of 20 mM sodium phosphate, 0.02% (w/v) sodium azide pH 8.5-9.0. A high pH in the running buffer ensures that amyloid monomers will not begin aggregating on the column. Protein-containing samples were removed from -80°C storage and defrosted at room temperature, with one 2-mL sample injected per trial run and 30 0.5-mL fractions subsequently collected. Amyloid-containing fractions were

immediately combined and placed on ice to prevent aggregation and used in the Thioflavin T binding assay. The concentration of A $\beta$ <sub>1-42</sub> obtained per purification trial was determined by measuring the absorbance of the combined fractions at 275 nm ( $A_{275}$ ) in a UV-Vis cuvette (BrandTech) divided by the A $\beta$ <sub>1-42</sub> extinction coefficient (Xue et al. 2017). The concentration of A $\beta$ <sub>1-42</sub> was adjusted to an optimum value of approximately 5  $\mu$ M using 20 mM sodium phosphate, 0.02% (w/v) sodium azide pH 7.4, with a lower pH promoting aggregation of amyloid fibrils in the reaction volume.

### 2.3.35 Thioflavin T assay

Amyloid fibril aggregation *in vitro* was quantified using a thioflavin T dye (ThT) fluorescence assay. Upon binding to the side chain channels along the long axis of amyloid fibrils, ThT produces a strong fluorescence signal detectable at approximately 482 nm when excited at 450 nm (Xue et al. 2017, Naiki et al. 1989). The enhancement of ThT fluorescence upon amyloid binding is attributed to a conformational change, in which the C-C bond joining the benzothiazole and aniline rings is rotationally immobilised. ThT assays were performed in clear-bottom 96-well plates (Greiner) with a ~100- $\mu$ L reaction volume per well. Each well was prepared with 1  $\mu$ L ThT, 50  $\mu$ L of experimental sample, and 50  $\mu$ L of 2-5  $\mu$ M A $\beta$ <sub>1-42</sub> pre-diluted in 20 mM sodium phosphate, 0.02% (w/v) sodium azide pH 7.4. Per trial, each condition tested was prepared in triplicate with an additional well devoid of A $\beta$ <sub>1-42</sub> (containing only 20 mM sodium phosphate, 0.02% (w/v) sodium azide pH 7.4, sample, and ThT) to be used as a baseline. Fluorescence signals from 'baseline' wells were subtracted from the corresponding signals to account for artefactual noise. Following the preparation of reaction volumes, fluorescence signals were detected using a CLARIOstar Plus plate reader (BMG Labtech).

### 2.3.36 Extraction of bioactive compounds into organic solvents

NGM plates were seeded with 400  $\mu$ L of MYb57 (*Stenotrophomonas sp. R-41388*) cultures grown in LB for 72 hours at 25°C. Bacterial lawns were allowed to proliferate at room temperature for at least 72 hours to ensure sufficient metabolite production. Bacterial lawns were scraped off of the NGM surface and NGM was chopped into 0.5 cm squares and placed into glass beakers. Within each trial, three 6-cm NGM plates were used per solvent condition. NGM chunks were covered with 14 mL of chosen solvent and allowed to incubate for one hour at room temperature. Solvents were transferred into Falcon tubes and evaporated immediately (to prevent ethyl acetate from degrading plastic) using a Rotavapor vacuum centrifuge (BUCHI). Remaining solutes were resuspended in 5 mL of ddH<sub>2</sub>O and filter sterilised before adding 200  $\mu$ L onto NGM plates seeded with OP50 for use in an amyloid-associated toxicity assay (see 'A $\beta$ -associated paralysis assay') or in a ThT binding assay. For control conditions, the procedure was repeated using NGM plates initially seeded with 400  $\mu$ L of OP50.

### 2.3.37 Statistics

Data are expressed as mean  $\pm$  standard error of the mean (SEM) unless otherwise indicated. Three independent pools of biological replicates were conducted per experimental procedure reported unless otherwise indicated. *p* values were calculated using Student's (unpaired) *t*-tests (two-tailed followed by Welch's correction) when comparing two conditions and by ANOVA (followed by Tukey's post hoc test) when comparing multiple conditions, unless otherwise indicated. Chi-square tests were used to analyse qualitative scoring of sarcomere organisation, qualitative scoring of mitochondrial morphology, and the correlation between motility and mitochondrial morphology. A Log-

rank (Mantel-Cox) test was used to analyse lifespan/survival curves. All statistical analysis was performed using GraphPad Prism V8.0.1 (GraphPad Software) and  $p$  values  $\leq 0.05$  were considered statistically significant. Summaries of statistical analyses are detailed in Section 8.1.

### 3. Experimental microbiome (EM) effects on *C. elegans* healthspan and life history

#### 3.1 Introduction

##### 3.1.1 Healthspan and life history in *Caenorhabditis elegans*

With its short lifespan and availability of molecular biology tools, *C. elegans* is an incredibly useful model system suited to ageing research (reviewed in Zhang et al. 2020). Indeed, it was in the nematode that the effects of nutrient sensing on longevity were demonstrated when a mutation in the *daf-2* insulin/IGF-1 receptor was shown to double maximal lifespan (Kenyon et al. 1993). However, the reported extension of human lifespan without an accompanying extension of healthspan – the proportion of an organism’s life spent without disease or frailty – is a major cause for concern (Crimmins, 2015). There is great social, economic, and ethical impetus to identify interventions in tractable model systems that specifically extend the duration of an organism’s *healthy* life. Several metrics for evaluating *C. elegans* healthspan have been developed, many of which assess the emergence of the nematode’s key life history traits. These include lifespan, developmental rate, and the timing and magnitude of reproduction.

One of the most straightforward metrics for assessing health is growth as indicated by body size. Growth can also be evaluated by tracking developmental timing, as the developmental programme of *C. elegans* has been extensively documented (Mok et al. 2015; Riddle et al. 1997). In favourable laboratory environments, the *C. elegans* hermaphrodite develops from embryo to gravid adult in approximately 3.5 days (Baugh and Sternberg, 2006; Cassada and Russell, 1975). Following approximately 16 hours of

embryogenesis independent of the mother, nematode larvae develop through four distinct larval stages (L1-L4) each resulting a moult. During each moult, a new stage-specific cuticle is synthesised and the previous cuticle is discarded. Approximately 12 hours after the L4 moult, adult hermaphrodites begin progeny production. The timecourse of larval development is intimately connected to nutritional availability, and worms exhibit complex responses to starvation at various stages of development. When hatched into axenic environments, larval development is arrested at the L1 stage and worms undergo a state of diapause known as dauer in which feeding is arrested indefinitely and locomotion is reduced (Baugh and Sternberg, 2006; Cassada and Russell, 1975). In less extreme conditions in which available food is limited (i.e., overcrowding), larval development is initiated as normal until diversion into a specialised dauer diapause at L3, within which the worms are able to survive starvation for several months or until the nematode again experiences favourable conditions (Cassada and Russell, 1975). Where food is available but of reduced nutritional quality, larval development is delayed (Shtonda and Avery, 2006). Like development, reproduction in *C. elegans* is actively regulated by nutritional availability. Egg-laying typically persists for three days until all self-produced spermatozoa has been utilised, with the highest amount of progeny produced on day 2 (D2) of adulthood (Byerly et al. 1976). In favourable conditions, hermaphrodites produce a brood size of up to 300 eggs (Riddle, 1997). Dietary restriction, however, results in extended periods of egg-laying and an overall reduction in brood size (Hughes et al. 2007).

Healthspan in *C. elegans* can also be assessed via changes in locomotor capacity. Like elderly humans who display evidence of sarcopenia, aged *C. elegans* exhibit a progressive deterioration of muscle tissue that can be assessed both quantitatively and qualitatively (Zembroń-Łacny et al. 2014; Herndon et al. 2002). Techniques used to judge

muscular integrity in *C. elegans* include assignment into motility classes following observation on solid media or monitoring burrowing through a semi-solid pluronic gel (Lesanpezeshki et al. 2019; Herndon et al. 2002). Alternatively, locomotion in liquid media can be measured by counting the number of rhythmic body bends performed over a defined duration – a phenomenon known as ‘thrashing’ (Onken and Driscoll, 2010).

### 3.1.2 The native microbiome of *C. elegans*

Although documented extensively in ageing worms, healthspan metrics have largely ignored *C. elegans*’ commensal microbes, which are likely to be key determinants of life history (Petersen et al. 2015). Since its introduction as an experimental system in the 1970s, *C. elegans* has largely been studied outside of the context of its natural ecology. This is mainly due to the fact that the nematode is maintained in the laboratory on a single bacterial strain, *Escherichia coli* OP50, which was selected on the basis of sustaining *C. elegans* growth and development with a limited bacterial lawn (Brenner, 1974). In addition, any other microbes persisting in the nematode gut or cuticle are eliminated by the standardised bleaching protocol used for age-synchronisation (Stiernagle, 2006). To date, only a few studies have investigated the complex interactions between nematodes and microbial species, with the majority focused on environmental microorganisms rather than those colonising the nematode host (Montalvo-Katz et al. 2013; MacNeil et al. 2013; Coolon et al. 2009; Avery and Shtonda, 2003; Venette and Ferris, 1998). In its natural environment, however, *C. elegans* harbours an extensively diverse microbiome recruited from its surrounding substrates. Three independent studies employed complementary techniques to describe the natural *C. elegans* microbiome (Berg et al. 2016; Dirksen et al. 2016; Samuel et al. 2016). These included deep sequencing of wild *C. elegans* isolates, substrates in natural *C. elegans* habitats, and laboratory *C. elegans* cultivated

on compost microcosms emulating their natural environments. These studies revealed a striking conservation in the composition of the *C. elegans* microbiome despite differences in the worms' geographic origins. The conserved core *C. elegans* microbiome was also distinct from the environmental substrates and significantly lower in microbial diversity, indicating that a defined, non-random microbial community is robustly assembled in the host gut. These results highlight the utility of *C. elegans* as a high-throughput system for studying host-microbe interactions. Combined with a range of genetic tools and annotated bacterial genomes, the tractable nematode model may aid in identifying the molecular drivers of microbial effects on host health and disease (Dirksen et al. 2020; Ezcurra 2018; Zhang et al. 2017; Cabeiro and Gems, 2013). Indeed, the first descriptions of the native *C. elegans* microbiome have already shown microbial composition to be predictive of reproductive fitness, resistance to infection, and general survival (Kissoyan et al. 2019; Samuel et al. 2016).

There is now an opportunity to colonise *C. elegans* with simplified yet ecologically relevant microbial communities to interrogate causation, rather than correlation, in host-microbe interactions. With this in mind we assembled an experimental microbiome (EM) representing the bacterial phylotypes that were most highly enriched in meta-analyses of the natural nematode microbiome and are also cultivable in a laboratory setting (Berg et al. 2016; Dirksen et al. 2016; Samuel et al. 2016). Our experimental microbiome features eleven isolates from ten distinct bacterial families including Alphaproteobacteria (*Brucellaceae*), Betaproteobacteria (*Alcaligenaceae*), Gammaproteobacteria (*Moraxellaceae*, *Pseudomonaceae*, *Xanthomonadaceae*), Actinobacteria (*Micrococcaceae*, *Microbacteriaceae*), and Firmicutes (*Bacillaceae*, *Lactobacillaceae*) (Figure 3.1A). Other research groups have also assembled representative *C. elegans* microbiomes. CeMBio, for instance, is a model microbiome selected by the Samuel group

and comprised of twelve bacterial isolates, three of which are shared with our experimental microbiome (Dirksen et al. 2020). Cultivation on CeMBio has been shown to influence fitness-affecting traits in wildtype nematodes, such as enhancing growth rate in comparison to *E. coli* OP50. Our experimental microbiome thus serves as a complement to models such as CeMBio which are designed to be tractable experimental systems while still capturing the complexity of symbiotic bacterial communities. Briefly, this project aims to identify molecular drivers of healthspan extension mediated by host-microbe interactions.

### 3.1.3 Native microbiota effects on gene expression

The profound impact that commensal microorganisms exert on host physiology has been demonstrated in various model systems, though the molecular processes underpinning this relationship remain poorly understood. Studies that have characterised the nematode's native microbiota have permitted investigations into the molecular response induced by commensal bacteria (Yang et al. 2019; Cassidy et al. 2018; Dirksen et al. 2016, Berg et al. 2016, Samuel et al. 2016). Proteomic and transcriptomic analyses have been performed in *C. elegans* cultivated on *Ochrobactrum* species – specifically *Ochrobactrum* spp. MYb71 and MYb237 – isolated from the worm's native microbiome. These bacteria were selected on the basis of their strong colonisation capacity and have been shown to colonise the nematode intestine even under adverse conditions (Dirksen et al. 2016). In comparison to controls reared on *E. coli* OP50, *Ochrobactrum*-associated nematodes displayed significant alterations in the relative abundance of 123 proteins, with 50 proteins of increased and 73 of decreased abundance (Cassidy et al. 2018). These alterations were consistent with those observed at the transcript level and a highly significant correlation between proteome and transcriptome was reported (Yang et al. 2019).

Specifically, of the differentially expressed genes and their respective protein products, 80% of those upregulated and 91.8% of those downregulated were consistent across data sets. As an example, several C-type lectin genes were differentially expressed at both transcript and protein levels. C-type lectin-like domain proteins aid in recognition of microbe-associated molecular patterns (MAMPs) and contribute to immune specificity, suggesting an important role for C-type lectins in mediating host-microbe interactions in *C. elegans* (Pees et al. 2015). Further examination of the data sets via complementary gene ontology (GO) enrichment analyses revealed an enrichment of cellular functions relating to metabolism, mitochondrial function, and oxidation-reduction, indicating a role for the microbiota in energy metabolism or, potentially, stress response (Yang et al. 2019, Cassidy et al. 2018, Yang et al. 2015). Among the overrepresented gene sets were also those related to immunity, dietary response, and ageing. Despite a promising foundation, there remains a paucity in transcriptomic data extracted from *C. elegans* associated with more complex bacterial communities.

#### 3.1.4 Investigating general experimental microbiome effects on *C. elegans* healthspan

Until now, the vast majority of healthspan-promoting interventions in *C. elegans* have been studied in the absence of the nematode's native microbiota. Similarly, though transcriptomic analyses have been performed in *C. elegans* associated with natural bacterial isolates, the assembled microbiomes used have been limited in their complexity. Considering the novelty of our microbial model system, this section of the project addresses the following aims and objectives:

1. Determine whether the Experimental Microbiome survives within and colonises the *C. elegans* intestine.
2. Establish whether the Experimental Microbiome is capable of sustaining normal *C. elegans* growth and development.
3. Characterise the transcriptomic response of *C. elegans* to the Experimental Microbiome.

As *C. elegans* and the constituents of the Experimental Microbiome have co-evolved, we predict that the nematode intestine will be a conducive environment for the survival of our microbial assembly. Noting previous reports of transcriptomic changes in response to native microbes (Yang et al. 2019; Cassidy et al. 2018), we also anticipate a range of differentially expressed genes in EM-fed animals versus OP50-fed controls, particularly gene sets serving metabolic and immune pathways.

## **3.2 Results**

### **3.2.1 Experimental microbiome colonises the *C. elegans* intestine**

To investigate host-microbe interactions in *C. elegans*, we established a simplified experimental microbiome representing the nematode's native intestinal microbiota. These bacterial species were selected from a combined data set including metagenomic sequencing of wild *C. elegans* isolates, laboratory *C. elegans* cultivated on simulated compost microcosms, and natural environmental substrates (Zhang et al. 2017, Dirksen et al. 2016, Berg et al. 2016, Samuel et al. 2016). Our experimental microbiome (EM) comprises 11 bacterial isolates of wide taxonomic diversity highly enriched in wild *C.*

*elegans* and cultivable in a laboratory setting (Table 3.1) Dirksen et al. 2016, Berg et al. 2016, Samuel et al. 2016).

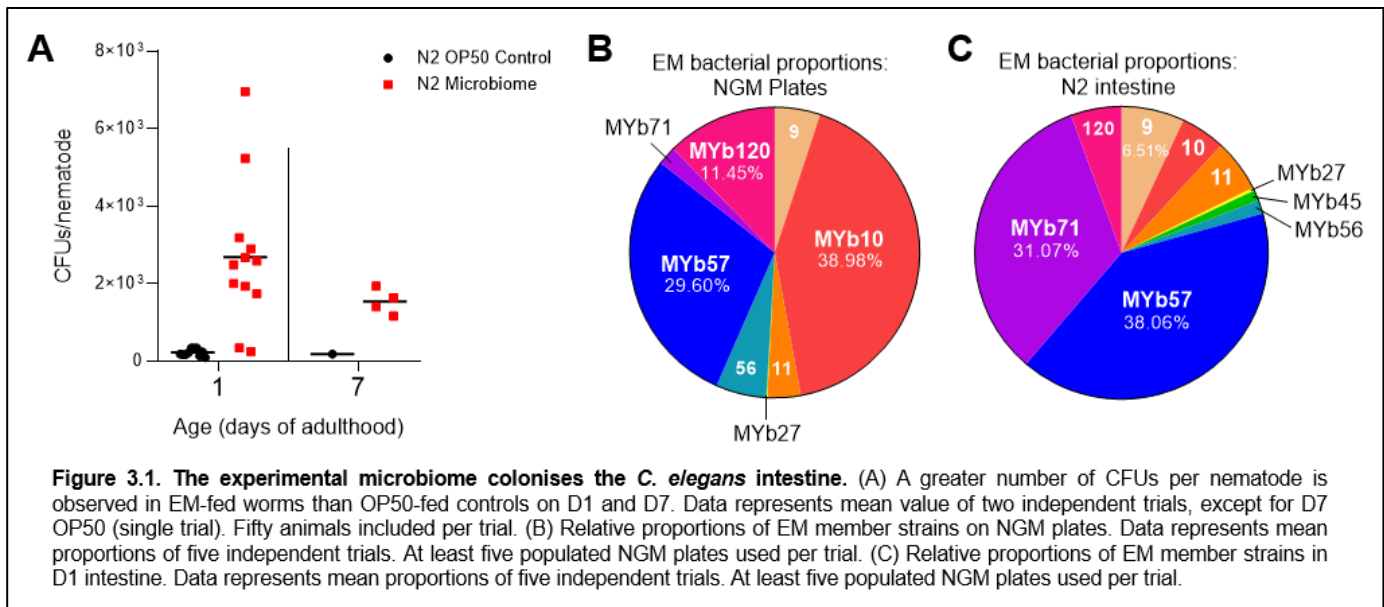
ID	Bacterial species	Phylum
MYb9	<i>Achromobacter sp.</i> F32	Proteobacteria
MYb10	<i>Acinetobacter sp.</i> LB BR12338	Proteobacteria
MYb11	<i>Pseudomonas lurida</i>	Proteobacteria
MYb27	<i>Arthrobacter aurescens</i>	Actinobacteria
MYb45	<i>Microbacterium oxydans</i>	Actinobacteria
MYb56	<i>Bacillus sp.</i> SG20	Firmicutes
MYb57	<i>Stenotrophomonas sp.</i> R-41388	Proteobacteria
MYb71	<i>Ochrobactrum sp.</i> R-26465	Proteobacteria
MYb83	<i>Leuconostoc pseudomesenteroides</i>	Firmicutes
MYb120	<i>Chryseobacterium sp.</i> CHNTR56	Bacteroidetes
MYb218	<i>Pseudomonas tuomuerensis</i>	Proteobacteria

Table 3.1. Experimental microbiome (EM) member strains.

EM strains were individually cultivated in liquid media at 25°C – a more permissive temperature to replicate their geographic origins – and combined in equal volumes before seeding onto nematode growth medium (NGM) plates. *Escherichia coli* OP50, the standard bacterial food source for laboratory-reared *C. elegans*, was used as a control (Brenner, 1974). Despite its ubiquity, OP50 has been shown to be a poor coloniser of the young intestine due to mechanical disruption of the bacteria by the nematode pharynx as well as the influence of host immunity limiting proliferation (Cabreiro and Gems, 2013; Portay-Celhay et al. 2012).

We tested whether the EM was capable of survival in the *C. elegans* intestine and compare its proliferative capacity to that of OP50. Age-synchronised wildtype nematodes were cultivated on either EM or OP50 control plates from egg stage. At day 1 (D1) of adulthood, 50 nematodes on either feeding paradigm were isolated and washed to remove surface

bacteria, allowing only intestinal microbes to persist. Following mechanical disruption of whole bodies, subsequent cells were serially diluted and plated on LB agar. We measured the number of viable bacteria (colony forming units, CFUs) recovered from the intestines of *C. elegans* reared on OP50 or EM. Wildtype D1 nematodes grown on an OP50 lawn exhibited a mean intestinal load of  $0.217 \times 10^3$  CFUs/worm compared to  $2.687 \times 10^3$  CFUs/worm in EM-fed nematodes – a 12.38-fold increase in CFUs across feeding conditions. We next tested whether this increased proliferative capacity was maintained in aged nematodes by replicating the technique in D7 adults. EM-fed D7 nematodes had a mean count of  $1.182 \times 10^3$  CFUs/worm, 6.57 times the  $0.180 \times 10^3$  CFUs/worm in aged OP50-fed controls (Figure 3.1A). Due to a limited number of successful experimental trials, we were unable to calculate descriptive statistics for these data sets. Nonetheless, the abundance of CFUs in EM-fed worms compared to OP50-fed controls on both D1 and D7 indicates enhanced survival of the EM in the wildtype *C. elegans* intestine. Although more trials are necessary, the bacterial community established in the gut by EM feeding seems to be stably maintained throughout age, providing an opportunity for direct interaction between host and microbes.



To assess the colonisation capacity of the EM, we sequenced the gut contents of EM-fed nematodes on D1 of adulthood as well as a fully-formed EM bacterial lawn. We used PCR amplification of the V4 region of the 16S ribosomal RNA (rRNA) amplicon to classify bacterial species and their relative proportions. 16S rRNA encodes the 30S small ribosomal subunit in prokaryotic cells. It is an ideal sequencing target for bacterial identification and establishing phylogenetic relationships due to its universality in microbes and the maintenance of its function in evolution (Patel 2001, Woese 1987). Sequence variations in the hypervariable regions (V1-9) of 16S rRNA are more likely to reflect random sequence changes than selective adaptations altering the molecule's function, and are therefore a more accurate measure of evolutionary time. Regions in V1-9 that are more highly conserved are correlated with higher-rank taxonomical classifications (i.e., phylum) and less conserved regions with lower ranks (i.e., genus, species) (Caporaso et al. 2011, Youssef et al. 2009). Sequence variation in the 16S gene is therefore widely used to characterise species in diverse microbial communities. The results of 16S

sequencing showed that the EM is assembled into a microbial community in the *C. elegans* intestine that is compositionally distinct from the stationary EM bacterial lawn (Figure 3.1, B,C). EM bacterial lawns are dominated by *Acinetobacter* MYb10, with a mean proportion of 38.98% of all OTUs across five replicates, followed by *Stenotrophomonas* MYb57 at 29.60%. By contrast, the D1 nematode intestine is dominated by *Stenotrophomonas* MYb57 at 38.06% followed by *Ochrobactrum* MYb71 at 31.07%. While enriched in the gut, MYb71 is present only in trace amounts (1.91%) on the EM bacterial lawn, suggesting a strong colonisation capacity in agreement with previous studies (Dirksen et al. 2016). We conclude that the EM forms a selective microbial community in the nematode intestine that is compositionally distinct from its provision as a food source.

### 3.2.2 The experimental microbiome sustains growth and development of *C. elegans*

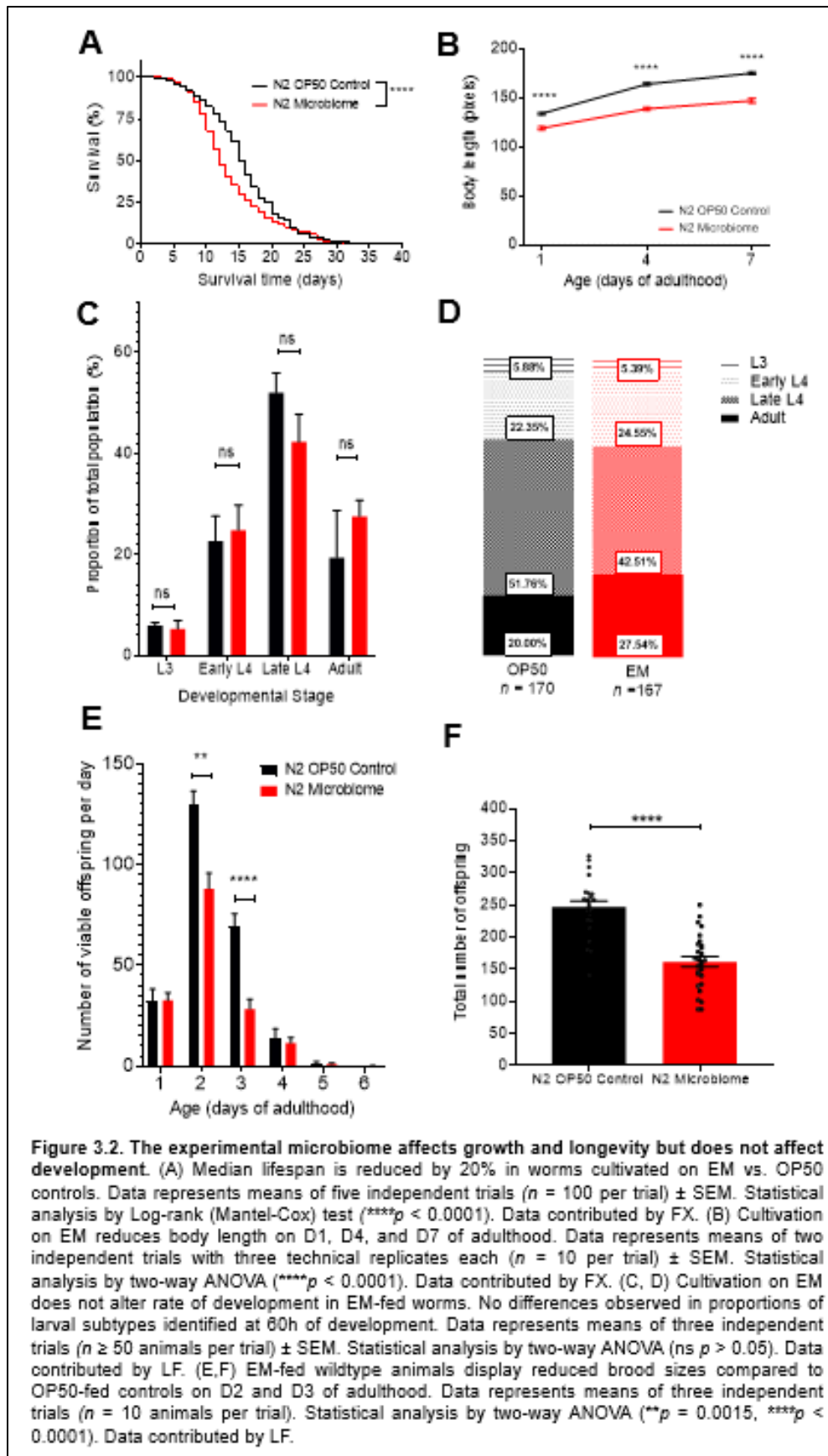
Once we had established that the EM is able to persist in the *C. elegans* intestine and has some functionality as a stable microbiome, we determined whether the EM is able to support the growth and development of the wildtype worm. We first assessed survival via a survival (lifespan) assay. Nematodes were maintained on either the EM- or OP50-seeded NGM plates from egg stage as previously described (Park et al. 2017, Amrit et al. 2014). Lifespan experiments showed that cultivation on the EM led to a 20% decrease in median lifespan compared to OP50-fed controls, with median lifespans of 12 and 15 days, respectively ( $p < 0.0001$ ).

We then compared body size in wildtype adults reared on OP50 or EM lawns. Maintaining consistent image processing calibrations, EM-fed nematodes displayed a mean length of 119.21 pixels ( $\pm 1.62$ ) compared to 134.11 pixels ( $\pm 1.00$ ) in OP50-fed controls on D1 of

adulthood (Figure 3.2B). On D4, the mean length in EM worms was 138.94 pixels ( $\pm 1.58$ ) with 164.18 pixels ( $\pm 1.22$ ) in controls, followed by 147.33 pixels ( $\pm 2.27$ ) versus 175.39 ( $\pm 1.44$ ) on D7. EM-fed nematodes were thus consistently smaller than OP50-fed controls at each of the assessed timepoints with a reduction in size of 11%, 15%, and 16% on D1, D4, and D7 of adulthood, respectively. Although the reductions in body length compared to OP50-fed controls were statistically significant (all  $p < 0.001$ ) and may reflect diminished food quality (Shtonda and Avery, 2006), they were mild and did not appear to be indicative of any form of developmental arrest. This was validated by documenting the timing of larval development in the worms during incubation of synchronised eggs for 60h at 20°C. Worms were staged based on morphological characteristics of their vulva and the presence/absence of visible oocytes as previously described (Mok et al. 2015). No significant difference in developmental rate was found between nematodes cultivated on either feeding condition (Figure 3.2C,D). At 60h of development post-bleaching, 42% ( $\pm 5\%$ ) of EM-fed nematodes had entered the L4 stage with 5% ( $\pm 2\%$ ) still classed as L3 and 28% ( $\pm 3\%$ ) progressing to young adulthood. Similarly, 52% ( $\pm 4\%$ ) of OP50-fed controls were found to have reached L4 stage at 60h with 6% ( $\pm 1\%$ ) in L3 and 19% ( $\pm 9\%$ ) classed as young adults. An expanded adult population may suggest accelerated development on the EM, but no significant difference was found in relative proportions at each of the larval substages (L3  $p > 0.999$ , Early L4  $p = 0.997$ , Late L4  $p = 0.551$ , Adult  $p = 0.698$ ). Taken together, these results indicate that the rate of development in EM-fed wildtype worms is comparable to that of OP50-fed controls. Despite differences in median lifespan and body size, the EM does not appear to be grossly nutritionally inferior to OP50.

We then investigated the effects of the EM on temporal patterns of *C. elegans* reproduction and overall fecundity. Individual nematodes were followed throughout the duration of their

reproductive period (up to D6 of adulthood) and the number of progeny produced each day were counted and subsequently summated. No difference in the number of viable progeny was identified on D1 ( $p > 0.9999$ ), D4 ( $p = 0.9995$ ), D5 ( $p = 0.9981$ ), or D6 ( $p = 0.6574$ ) of adulthood (Figure 3.2E). However, a significantly reduced number of progeny was produced in EM-fed worms compared to OP50-fed controls on D2 ( $p = 0.0015$ ) and D3 ( $p < 0.0001$ ) with a 32% and 59% decrease, respectively. This resulted in a significant 34% reduction in total brood size in nematodes cultivated on the EM versus OP50 controls ( $p < 0.0001$ ) (Figure 3.2F), contradicting the hypothesis that normal development is maintained in EM-fed animals.



Previous studies have shown that worms reared on growth-promoting bacteria display a reduced probability of leaving a food patch than those on “lower quality” bacteria (Shtonda and Avery, 2006). We were interested in whether *C. elegans* perceive the EM to be an inferior or potentially pathogenic food source. We performed a food preference assay in which D1 wildtype nematodes were washed to remove surface microbiota and positioned between equidistant OP50 and EM lawns on NGM plates (schematic in Figure 3.3A, inset). After 24h, the proportion of the population occupying either food source was determined. Wildtype *C. elegans* exhibited a preference for the food source of their first exposure upon hatching, whether OP50 or the EM. At 24h, 55.41% of OP50-reared worms were identified within the OP50 lawn, while a comparable 61.01% of EM-reared worms were identified within the EM lawn ( $p = 0.605$ ) (Figure 3.3A). Conversely, no difference was found in the proportion of worms occupying the unfamiliar food source, with 39.00% of OP50-reared worms were found on the EM lawn and a comparable 36.29% of EM-reared worms within the OP50 lawn ( $p = 0.909$ ). Neither rearing condition displayed a strong aversion to either food source.

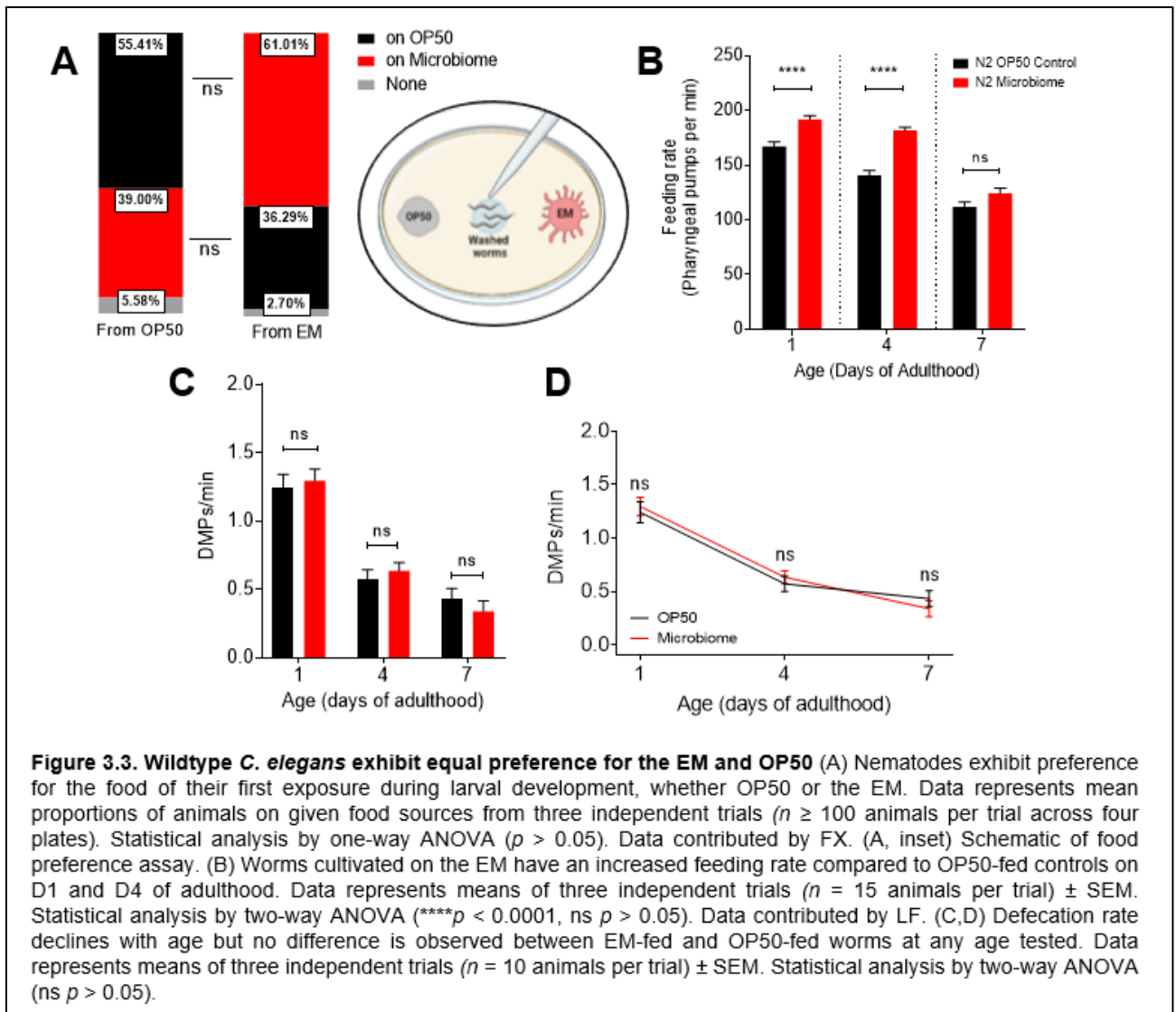
We followed the investigation of food source *preference* by assessing the *rate* of feeding on nematodes reared on the EM versus *E. coli* OP50. *C. elegans* concentrates and consumes bacteria via the rhythmic action of the pharynx, a neuromuscular pump joining the mouth and intestine. In addition to food quality, worms’ nutritional status has been shown to affect pharyngeal pumping rates. Worms subjected to periods of starvation display an enhanced pumping rate when reintroduced to food, proportional to the duration of food deprivation (Avery and Horvitz, 1990). We recorded the number of pharyngeal contractions exhibited by worms on bacterial lawns consistent with the conditions of their rearing. On D1 of adulthood, EM worms displayed a 15% elevated feeding rate versus

OP50 controls, with 191.85 pumps per min ( $\pm 3.37$ ) compared to 167.20 pumps per min ( $\pm 4.13$ ) ( $p < 0.0001$ ) (Figure 3.3B). On D4, a difference of 29% was observed with 181.80 pumps per min ( $\pm 2.806$ ) in EM worms and 140.60 pumps per min ( $\pm 4.339$ ) in controls ( $p < 0.0001$ ). No significant difference between feeding conditions ( $p = 0.11$ ) was observed on D7, with 124.20 pumps per min ( $\pm 4.83$ ) in EM worms and 111.80 pumps per min ( $\pm 4.40$ ) in controls. Wildtype *C. elegans* thus exhibit an elevated feeding rate on the EM that is lost with advanced age.

Having established that pharyngeal pumping is elevated in nematodes feeding on the EM, we asked whether this is also reflected in subsequent digestive processes, namely defecation. The *C. elegans* defecation motor programme (DMP) is a coordinated series of three muscle contractions performed approximately every 45 seconds in a D1 wildtype adult (Mahoney et al. 2008; Liu and Thomas 1994). Alternating increases and decreases in internal pressure between the posterior and anterior body-wall muscles cause intestinal contents to collect in a bolus in the preanal region, where it is later expelled by enteric muscle contraction in the anus (Riddle et al. 1997). We quantified defecation rate in wildtype animals reared on either *E. coli* OP50 or the EM from early to late adulthood. Time elapsed between four DMP events was recorded in individual worms *in situ*, providing three inter-DMP measurements per worm. Any nematode that had not defecated for over five minutes was censored as a non-defecator. Within both feeding conditions defecation rate was found to decrease with advancing age, from 1.24 DMPs/min ( $\pm 0.10$ ) on D1 to 0.43 DMPs/min ( $\pm 0.07$ ) in OP50 controls and 1.30 DMPs/min ( $\pm 0.10$ ) on D1 to 0.34 DMPs/min ( $\pm 0.08$ ) in EM nematodes (Figure 3.3C-D). However, no difference in defecation rate was observed between conditions on D1 ( $p = 0.94$ ), D4 ( $p = 0.92$ ), or D7

( $p = 0.78$ ) of adulthood, indicating comparable gut health in EM-fed nematodes versus controls.

The results of our lifespan, body size, feeding rate, and fecundity assays all indicate inferior nutritional availability in the EM. Conversely, developmental timing, food preference, and defecation rate indicate no gross nutritional deprivation in EM-fed nematodes compared to OP50 controls. Taken together, the results of these healthspan experiments reveal that while the EM has a phenotypic impact on wildtype *C. elegans*, it is able to sustain normal development and does not exhibit gross pathogenicity.

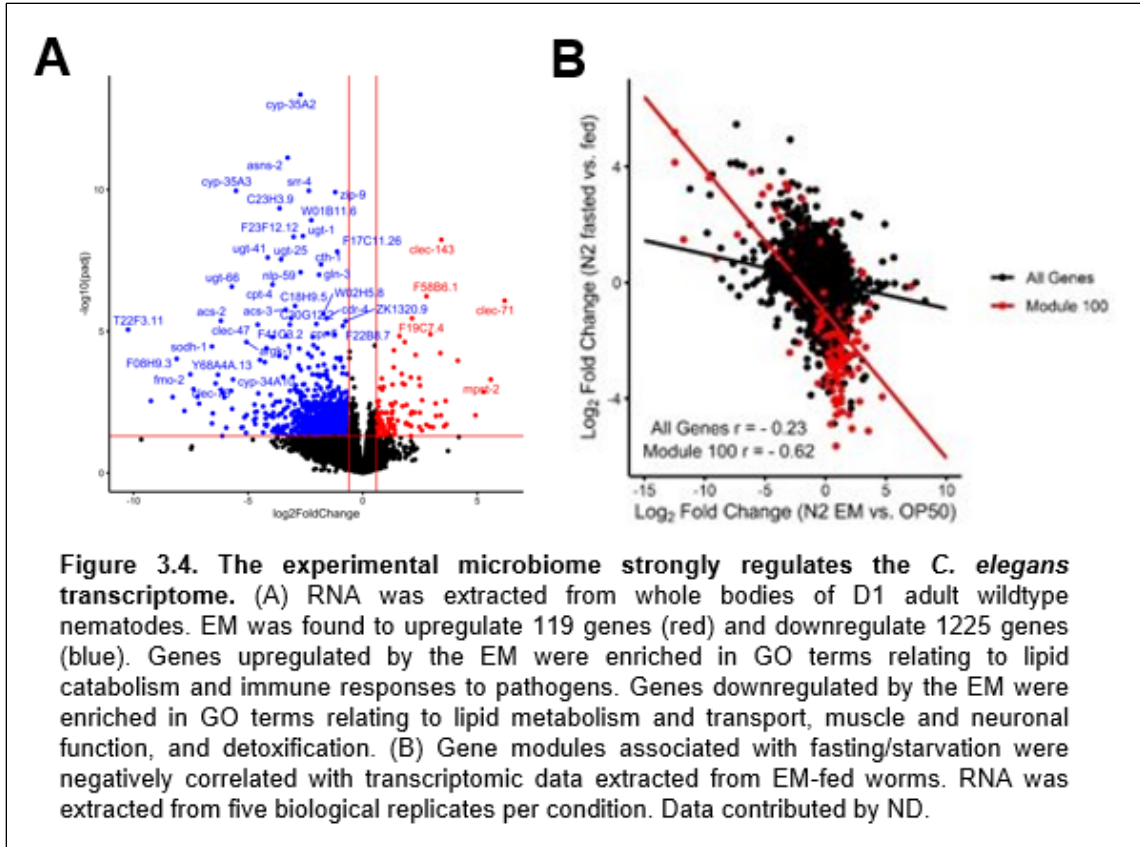


### 3.2.3 The experimental microbiome regulates the *C. elegans* transcriptome

Having identified a battery of physiological changes in the nematode host that were induced by the EM, we sought to identify the molecular bases underlying its effects. RNA sequencing was performed to identify transcriptional changes in the host that are induced by cultivation on the EM. The transcriptome of age-matched nematodes reared on *E. coli* OP50 was thereby used as a control condition. RNA was isolated from whole-body preparations of D1 adults reared on either OP50/EM from egg stage.

Cultivation on the EM had a prominent effect on gene expression in wildtype *C. elegans* with 1708 differentially expressed transcripts. Of this total, only 119 genes were found to be upregulated by the EM while a striking 1225 were downregulated (Figure 3.4A). GO enrichment analysis was performed on the resultant transcriptomic data (Ashburner et al. 2000). Downregulated genes were found to be enriched in GO terms pertaining to lipid metabolism and transport, muscle and neuronal function, and detoxification (Figure 3.4C). By contrast, upregulated gene sets were enriched in terms related to lipid catabolism and immune responses to pathogens, in concordance with previous studies utilising *Ochrobactrum* species (Figure 3.4D) (Yang et al. 2019, Cassidy et al. 2018, Yang et al. 2015).

Considering the observed reduction in brood size and increased feeding rate in nematodes cultivated on the EM, we asked whether the transcriptomic changes were indicative of inferior nutritional composition of the EM. We compared our RNA sequencing results to data extracted from *daf-2* mutants, starved, and fasted nematodes available on the GeneModules programme, which uses independent principal component analysis to organise co-expressed gene sets into functional active module (Cary et al. 2020). We found that the modules strongly activated by fasting i.e., Module 100 (m100) showed a strong negative correlation with those activated by cultivation on the EM ( $r = -0.62$ ), suggesting that the transcriptomic changes induced by the EM are distinct from those induced by starvation (Figure 3.4B). Our transcriptomic analysis illustrates the influence of the EM on *C. elegans* biology, specifically on gene sets mediating lipid metabolism and catabolism, muscular function, and host immunity – without inducing stress responses related to nutritional deprivation.



### 3.3 Discussion

#### 3.3.1 A representative microbiome survives in the *C. elegans* intestine

Many advancements in understanding host-microbe interactions have emerged from binary tests involving a host and single microbe under gnotobiotic conditions (Fischbach, 2018). While valuable, this approach likely oversimplifies the combined system and limits insights that can be derived from collaborations and competitions between microbiota. This project sought to assemble a representative microbiome that satisfied seemingly opposed criteria. The selected EM should be complex enough to be of ecological relevance to *C. elegans* and simulate community interactions between microbial species. At the same time, the EM needed to be simple enough such that subsequent phenotypes could be attributed to individual member strains, allowing the molecular drivers of host-

microbe interactions to be identified. With this in mind, eleven bacterial strains were chosen to capture the diversity of genera highly enriched in wild *C. elegans* isolates (Dirksen et al. 2016, Berg et al. 2016, Samuel et al. 2016).

Previous studies have colonised *C. elegans* using bacteria found to be highly enriched in native worm populations, although these focused on individual species rather than complex communities (Kissoyan et al. 2019; Yang et al. 2019; Zhang et al. 2017; Dirksen et al. 2016). As this project was underway, a novel *C. elegans* microbiome resource known as CeMbio was developed, comprised of twelve bacteria from nine different families (Dirksen et al. 2020). Akin to this project's assembled microbiome, CeMbio was selected to represent the core microbiome of *C. elegans* and shares three species with the EM: MYb10 (*Acinetobacter* sp. LB BR12338), MYb11 (*Pseudomonas lurida*) and MYb71 (*Ochrobactrum* sp. R-26465). The potential for CeMbio to influence *C. elegans* physiology was demonstrated via developmental timing, as growth rates were enhanced in CeMbio-reared animals compared to OP50. The impact of CeMbio on other life history traits, however, remains unreported. The work within this project represents an opportunity to examine complex interactions between microbial community members, interactions between microbiota and host, and assesses how such interactions specifically affect age-related phenotypes in the host.

We showed that the EM persists in the wildtype *C. elegans* intestine, possibly reflecting the co-evolutionary history of *C. elegans* and these microbes that are specially adapted for survival in the nematode gut. EM strains far exceed the colonisation capacity of control food *E. coli* OP50, which is unable to persist in the intestine due to mechanical breakdown by the pharynx (Darby, 2005; Tan et al. 1999). EM-reared nematodes maintain intestinal

CFU counts from early- to mid-adulthood, suggesting that rearing on the EM establishes a stable bacterial community within the worm gut. Moreover, EM composition was dynamic and subject to reassembly: although liquid cultures of each member strain were initially combined in equal volumes, the isolate MYb71 (*Ochrobactrum* sp. R-26465) was outcompeted on NGM plates, persisting only in trace amounts on the stationary EM lawn. However, MYb71 was highly enriched once taken into the intestine, demonstrating a strong colonisation capacity in agreement with previous studies (Yang et al. 2019; Dirksen et al. 2016). The results of 16S sequencing suggest that the EM is assembled into a live intestinal microbiome that is compositionally distinct from its provision on NGM plates, reflecting the varied colonisation capacities of member strains. This finding has crucial implications for all project outcomes as it suggests that subsequent EM-induced phenotypes accurately model host-microbe interactions, rather than merely reflecting an alternative food source. However, the distinction between these two possibilities is less clear in the case of bacterial species whose proportions were unchanged following ingestion. MYb57 (*Stenotrophomonas* sp. R-41388) comprised a significant proportion of the plate *and* intestinal bacterial communities, representing the second most abundant bacterial isolate in both. As the relative proportions of MYb57 were found to be similar on plates and within worms, we are unable to draw conclusions on the bacterium's colonisation capacity nor its contribution to a functional microbiome.

### 3.3.2 Experimental microbiome sustains growth and development

From a series of experiments probing healthspan and life history, we determined that the EM is capable of sustaining normal growth and development in wildtype *C. elegans* without notable adverse effects. Median lifespan was reduced by approximately 20% in EM-fed animals, possibly reflecting a pathogenic switch in late-life due to excessive

bacterial proliferation in the gut. This has previously been demonstrated in *E. coli* OP50-fed animals and is thought to be the result of a decline in innate immune function with age, resulting in reduced longevity (Portal-Celhay et al. 2012; Youngman et al. 2011). The enhanced proliferative capacity of EM member strains in the nematode intestine may indicate that this pathogenic switch occurs earlier in life than in OP50-fed controls, resulting in lifespan reduction while still preserving normal development. We validated this by examining the timing of larval development and found no differences between feeding conditions, concurrently suggesting that the EM is not nutritionally inferior to *E. coli* OP50 (Stuhr and Curran, 2020). Further support for the nutritive content of the EM was provided by the finding that nematodes displayed equal preference for the food of their first exposure during larval development, whether OP50 or the EM. Shtonda and Avery (2006) previously noted worms' ability to seek out and dwell within high-quality food and leave bacteria that is unable to support growth. They described the phenomenon of experience-dependence in which early exposure to nutritive bacteria enhances roaming behaviour away from inferior food. Comparable dietary choice behaviour between OP50-reared and EM-reared animal suggests that no significant differences in food quality are perceived. The absence of food avoidance behaviour also suggests that the EM is not perceived to be highly pathogenic. Moreover, nutritionally inferior non-pathogenic bacteria have previously been shown to extend lifespan via dietary restriction – contradicting the reduction seen in our EM survival data (Kapahi et al. 2010; Kenyon et al. 1993). No difference in defecation rate was reported between feeding conditions, suggesting that gut health is also unaffected by cultivation on the EM (Rae et al. 2012).

The remaining healthspan metrics assessed in wildtype *C. elegans*, however, undermine the hypothesis that the EM is capable of sustaining normal growth and overall fitness. In

addition to a reduction in lifespan, EM-fed worms displayed reduced body length compared to OP50-fed controls. Feeding rate, measured via rhythmic contraction of the pharynx, was elevated in EM-fed animals up to mid-adulthood suggesting that the EM may be of inferior nutritional value. Total fecundity was reduced in EM-reared worms with a significant reduction in brood size on D2 and D3 of adulthood, suggesting limited nutritional availability in the EM. This result is reminiscent of a previous study by Yang et al. (2019) who reported downregulation of genes regulating fertility when transcriptomic analysis of worms cultivated on MYb71. Whether these observed differences in *C. elegans* physiology are inherently indicative of diminished fitness is unclear. Until recently, few studies had explored interactions between *C. elegans* and wild environmental microbes, with the majority of research performed using *E. coli* OP50 as a food source (Montalvo-Katz et al. 2013; Coolon et al. 2009; Grewal, 1991). OP50 was selected for its availability in laboratory settings and bears little ecological relevance to wild *C. elegans* (Samuel et al. 2016; Brenner, 1974). Interpreting OP50-induced healthspan metrics as the organismal standard may thus be inappropriate, particularly when studying the effects of native microbiota members (Frezal and Felix, 2015). Unpublished work carried out alongside this project found sizable lipid deposits in the intestines of OP50-fed controls that were absent in age-matched EM-fed worms. These deposits, identified in cross-sectional electron micrographs, may contribute to the reported size of controls. As the reduced body size of EM-fed worms was not accompanied by a developmental delay, it is unlikely that this is truly an indicator of impaired fitness. Similarly, as pharyngeal pumping rates do not necessarily reflect the volume of bacteria consumed (Stuhr and Curran, 2020; Gomez-Amaro et al. 2015), other methods of assessing foods' nutritional quality should be considered. Quiescence behaviour – the complete cessation of feeding and moving – is rapidly induced on high quality food and can be used as a proxy for nutritional availability (You et al. 2008).

Overall, the results presented within this chapter demonstrate that the representative microbiome we have selected is able to sustain *C. elegans* throughout its life cycle without severely affecting host fitness. This has important implications for future use of the combined *C. elegans*-EM system to model host-microbe interactions throughout ageing. The project also highlights the limitations of ageing studies focused solely on lifespan extension, and expands the definition of organismal fitness in host-microbe interactions beyond mere longevity.

### 3.3.3 Experimental microbiome alters the wildtype transcriptome

Recent studies have shown that bacterial diet can alter transcriptional responses in *C. elegans* (Stuhr and Curran, 2020; Yang et al. 2019; Schumacker et al. 2019; Volkert et al. 2013). As far as we know, however, there have been no published studies that have documented *C. elegans* transcriptome changes induced by a community of multiple microbial species. This project addresses this paucity using a representative microbiome of eleven bacterial strains isolated from wild *C. elegans*. The transcriptome response to the EM was assessed in D1 wildtype adults and compared against age-matched animals cultivated on *E. coli* OP50. This analysis revealed a total of 1708 differentially regulated genes: 1225 downregulated by the EM – which were enriched in GO terms related to lipid metabolism, muscle and neuronal function, and detoxification – and a mere 119 that were upregulated – enriched in GO terms pertaining to lipid catabolism and immune responses, in agreement with previous studies using single *Ochrobactrum* species (Yang et al. 2019; Cassidy et al. 2018; Yang et al. 2015). The finding that gene sets pertaining to lipid catabolism and metabolism were up- and downregulated in EM-fed worms versus OP50-fed controls, respectively, corroborated our observation of lipid deposits in the intestines

of aged controls. The potential of the EM to alter lipid processing throughout age warrants further research, and is currently underway.

Further support for the hypothesis that the EM is a nutritionally viable food source was provided by a negative correlation between gene modules associated with starvation and our own EM-induced transcriptome data. Overall, the findings within this chapter establish the EM as a suitable microbial community for modelling host-microbe interactions and pave the way for further dissection of these relationships into advanced age.

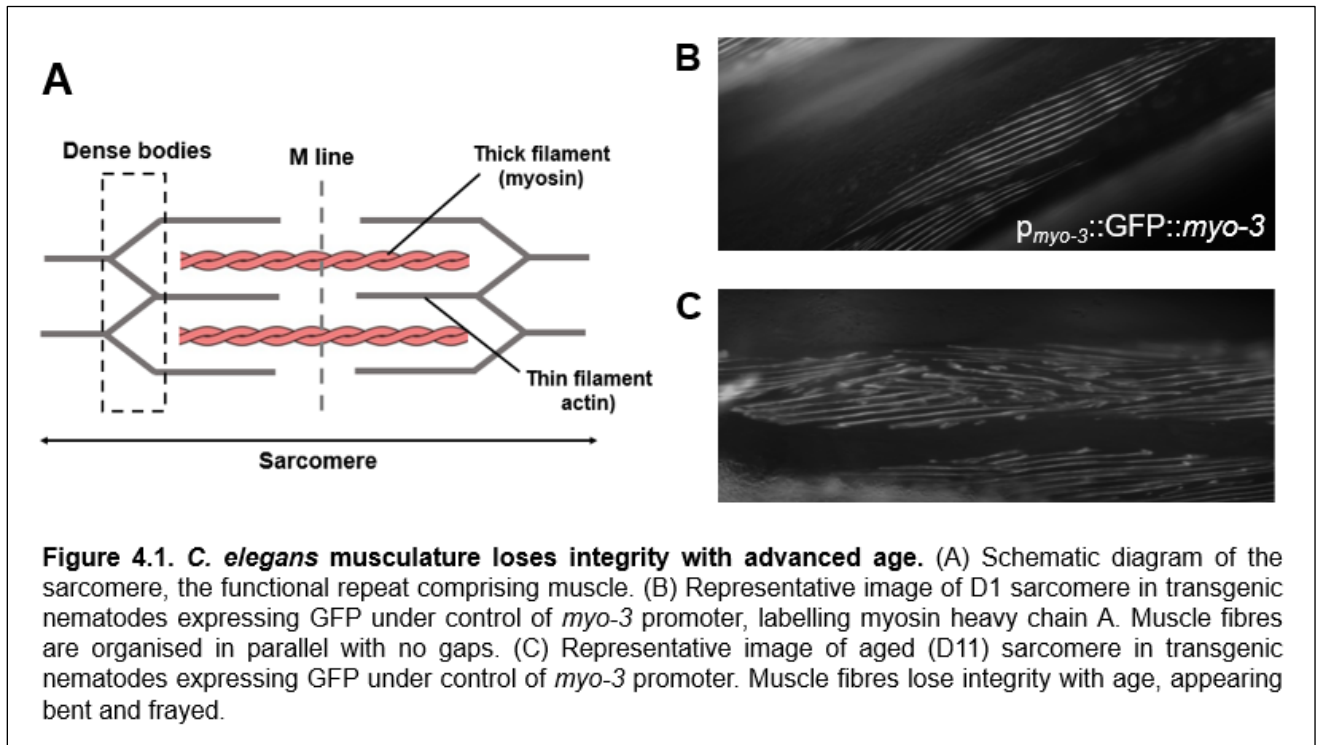
## 4. Experimental microbiome (EM) effects on *C. elegans* motility

### 4.1 Introduction

#### 4.1.1. *C. elegans* musculature

Muscle is a multifunctional and dynamic tissue that sustains coordinated functions necessary for survival, including locomotion and postural support. Defects that affect the sarcomere – the functional repeat unit underlying muscle contraction – are implicated in over 20 known human diseases (Nowak et al. 2005). Many of these conditions are age-associated and present a significant burden to an expanding ageing population. Model systems with conserved ageing pathways, short life cycles, and comparable muscle tissue to human subjects are therefore ideal candidates for identifying interventions that protect motor function. *C. elegans* meets these criteria, possessing 95 striated body wall muscle cells that are structurally similar to vertebrate skeletal muscle. As in vertebrates, *C. elegans* sarcomeres are made up of thick myosin-containing filaments interspersed between thinner filaments composed of actin. These alternating fibrils are assembled into two main attachment complexes, the M-line and dense body, which are anchored in the sarcolemma allowing the force generated by the contraction of myofibrils to be transduced to the basement membrane (Figure 4.1A). It is this extracellular transduction of force that results in coordinated, directed locomotion of the nematode (Gieseler et al. 2017; Meissner et al. 2009). *C. elegans* locomotion involves alternating ventral and dorsal turns of the musculature, contracting out of phase to generate a sinusoidal pattern of movement. The opposing contraction and relaxation of the ventral and dorsal musculature is contributed by distinct sets of motor neurons, each forming neuromuscular junctions on

the recipient tissue. As in mammals, the excitatory motor neurons of *C. elegans* that are responsible for contraction utilise the neurotransmitter acetylcholine, while the inhibitory neurotransmitters relax the opposing muscles through the action of gamma-aminobutyric acid (GABA) (Riddle et al. 1997).



Human muscle ageing is marked by sarcopenia: the progressive loss of muscle mass and composition, resulting in a reduction of overall function over time. Sarcopenia ultimately affects the ability of aged individuals to live independently and reduces their quality of life (Reid et al. 2008; Bean et al. 2003). Like humans, *C. elegans* exhibit an age-related muscular deterioration akin to sarcopenia. The sarcomeres of young nematodes are characterised by parallel, symmetric rows of myosin while those of older nematodes are increasingly disorganised and sparsely packed (Figure 4.1C-D) (Herndon et al. 2002). The progressive deterioration of muscular structure is accompanied by a decline in muscle

function, as measured by a battery of whole-organism locomotory assays. The most frequently utilised of these is a lateral swimming (“thrashing”) assay that measures locomotion in liquid (Gaffney et al. 2014; Epstein and Thomson, 1974). After a period of acclimation in physiological buffer, the number of C-shaped body bends performed by the nematode is counted. Much of what is known of the structure, differentiation, and general development of *C. elegans* muscle has been identified through forward genetic screens accompanied with thrashing assays (Gieseler et al. 2016; Gaiser et al. 2011; Epstein and Thomson, 1974). Contemporary research into neuromuscular health has supplemented thrashing assays with microfluidic pillar environments to measure muscular strength or with computer-vision analysis to map manoeuvrability (Rahman et al. 2018; Restif et al. 2014; Johari et al. 2013; Padmanabhan et al. 2012). Even still, researchers have contested the physiological relevance of two-dimensional locomotion assays. As nematodes navigating their native environments burrow in three dimensions, there has been recent incentive to design burrowing environments that more closely mimic their natural habitats of soil, fluid droplets, and rotting fruit (Lesanpezeshki et al. 2019; Lee et al. 2016). Scoring three-dimensional locomotion increases the sensitivity of neuromuscular assays, permitting the scoring of subtle motor defects that are otherwise undetectable (Beron et al. 2015).

#### 4.1.2. Muscle and the microbiome

In addition to its role in postural stabilisation and locomotion, skeletal muscle also serves as a reservoir for macronutrients, a permissive medium for the release of growth factors and cytokines, and an integral locus for glucose disposal and regulation (Lieber et al. 2017; Pedersen and Febbraio, 2008). Over the past few decades, the existence of a bidirectional ‘gut-muscle axis’ has been proposed and investigated. Although there is no

direct contact between skeletal muscle and the microbiome, muscle is subject to microbial products and secondary metabolites that are able to cross the gut barrier and influence host metabolic and immune function.

Studies involving faecal transplants from conventionally reared mice into abiotic 'germ-free' (GF) conspecifics provided some of the first evidence for cross-talk between the microbiome and skeletal muscle. Recipient mice display increased resistance to diet-induced obesity with a significant reduction in insulin sensitivity and glucose tolerance than GF controls, suggesting the microbial regulation of muscle metabolic function (Bäckhed et al. 2004). Subsequent studies which probed this superior metabolic phenotype found that microbiome-deficient mice also have an increased oxidative capacity with elevated AMP-activated protein kinase (AMPK) and carnitine palmitoyl transferase-1 (CPT-1) activity in their skeletal muscle (Bäckhed et al. 2007). Other studies have taken the investigation of the gut-muscle axis in GF mice a step further, probing the role of the microbiome in skeletal muscle adaptation to exercise. Gut microbiome dysbiosis induced through antibiotic treatment was found to impair the hypertrophic response of muscle to weighted wheel running, demonstrating that an intact gut microbiome is required for full adaptation of skeletal muscle to exercise (Valentino et al. 2021).

Much of the existing evidence supporting a gut-muscle axis in human subjects is in the form of metagenomic analyses linking gut microbial composition with muscular health (O'Toole and Jeffery, 2015). One of the first of such studies was performed in a small cohort of elderly human subjects grouped by severity of frailty. Metagenomic analysis revealed that frailty was associated with significant enrichment of bacterial species belonging to the family *Enterobacteriaceae* and a concomitant reduction in *Lactobacillus* (van Tongeren et al. 2005). The highest functioning subjects also displayed an abundance

of butyrate-producing bacteria like *Faecalibacterium prausnitzii*, spurring the hypothesis that butyrate serves a protective role against age-associated dysbiosis. It was later shown that butyrate improves the function of the intestinal barrier by strengthening tight junction assembly, preventing the translocation of endotoxins into the circulatory system and reducing overall inflammation (Peng et al. 2009; Cox et al. 2009). Such studies emphasise the contributions of live microbiota and their metabolites to muscle function and guide therapeutic interventions (i.e., dietary strategies preventing the loss of butyrate-producing bacteria). As muscle and the microbiome are both systems subjected to significant and deleterious changes with age, there has been great interest in identifying microbiome-based interventions that improve host muscular health.

GF mice that were colonised with faecal samples isolated from elderly humans displayed significant differences in muscle strength depending on the physical functioning of their donors (Fielding et al. 2019). Mice receiving transplants from high-functioning subjects (physical performance battery score was above a specified threshold) exhibited a significant increase in grip strength compared to those colonised with faeces from low-functioning donors. High-throughput sequencing of the transplanted samples revealed that high-functioning donors were enriched in genus level *Prevotella* and *Barnesiella* bacteria compared to their low-functioning counterparts, adding to a growing body of evidence that suggests bacterial involvement in mechanisms maintaining host physical function (Clarke et al. 2014). The benefit provided by these bacterial genera may be due to the production of short-chain fatty acids (SCFAs) acetate, propionate, and – once again – butyrate. Indeed, studies that have supplemented GF mice with a mixture of these SCFAs have been shown to significantly improve muscle strength (Lahiri et al. 2019). Experiments like Fielding et al. (2019), which leverage the advantages of various model

systems, help mitigate the confounds of studying the gut-muscle axis in higher animals. However, there remains a paucity of studies that directly support a causative relationship between bacterial species and a muscular phenotype.

#### 4.1.3. The microbiome and host immune responses

One physiological system that has been extensively documented in the context of dysregulated microbiota is the immune system. Extensive research in GF mice has shown that the elimination of commensal microbes disrupts immune homeostasis at the molecular, cellular, and organ levels. GF mice display defective antibody production and a reduction in intestinal lymphocyte populations (Round and Mazmanian 2014; Moreau et al. 1978). The development and maturation of intestinal organs including mesenteric lymph nodes, gut-associated lymphoid tissues, and isolated lymphoid follicles are also impaired following prolonged antibiotic treatment (Bouskra et al. 2008; Macpherson and Harris, 2004). Studies in GF animals, however, raise the important question of whether immunologic effects are truly the result of dysregulated microbial communities or if distinct antibiotic compound-related mechanisms are at work. To address this question, gnotobiotic (secondary abiotic) mice can be generated, in which sterile animals are reassociated with defined microbial species. Such studies have shown that immune cell homeostasis can be restored in GF animals through recolonisation with intestinal commensal bacterial species. However, researchers were unable to completely recapitulate the lymphocyte repertoire with transplantation, highlighting the inherent complexity of host-microbe interactions (Ekmekci et al. 2017). There is a pressing need to improve our understanding of such interactions and define causative relationships between microbial composition and host phenotype.

It is not only the adaptive immune system – responsible for mounting a cellular response that is specific to the invading pathogen – that has been shown to be stimulated by commensal microbes. Gut dysbiosis increases permeability of the intestinal barrier, permitting indiscriminate passage of endotoxins and microbial products in the circulation (Gizard et al. 2020). The presence of microbial factors in the bloodstream triggers low-grade systemic inflammation through activation of the innate immune system.

The innate immune system serves as an organism's first line of defence against pathogenic infection, providing rapid, generalised protection. Canonically, innate immune activation occurs following pathogen recognition via detection of pathogen-associated molecular patterns (PAMPs), such as structural components of bacteria, or of damage-associated molecular patterns (DAMPs), such as the release of intracellular material into extracellular space (Pukkila-Worley and Ausubel, 2012). Immune responses to pathogens are mediated by core sets of signal transduction pathways, which convert extracellular stimuli into intracellular responses and permit adaptation to environmental changes. Sequential cascades of protein kinases and phosphatases activate transcriptional regulators, resulting in protective transcriptional responses. Much of the work characterising the innate immune system has been performed in *Drosophila melanogaster* and *C. elegans*, utilising the phylogenetic conservation of this mechanism across various kingdoms and organisms (Sackton et al. 2007; Kim et al. 2002).

#### 4.1.4. The p38 MAP kinase (PMK) pathway of innate immunity

Unlike in mammals and other higher organisms, the innate immune system is *C. elegans'* sole defence against environmental pathogens and therefore serves as a simplified model

with which to study immune function. *C. elegans*' innate immune system relies heavily on mitogen-activated protein kinase (MAPK) pathways. MAPK signalling pathways are evolutionarily conserved cascades that serve a variety of essential functions in the cell including growth and proliferation, development, adaptive responses to stress, and immunity (Kim et al. 2004; Asai et al. 2002; Dong et al. 2002). One class of MAPK in particular, p38 MAPK, is a key mediator of stress and immune signalling both in mammalian organisms as well as in *C. elegans* – where many seminal experiments have been performed due to the lack of embryonic lethality in p38 MAPK mutants in nematodes as opposed to mice (Kim et al. 2004). With the use of forward genetic screens in *C. elegans*, researchers have established a cascade of kinases required for defence against pathogens. The furthest downstream of these effectors is *pmk-1*, which encodes a nematode orthologue of mammalian p38. PMK-1 is phosphorylated at conserved serine-threonine residues by the kinase encoded by *sek-1*, which is in turn phosphorylated by the product of *nsy-1*, and upstream still by the Toll and Interleukin receptor TIR-1 (see pathway diagram in Figure 4.5A) (Troemel et al. 2006; Inoue et al. 2005; Kim et al. 2002). As PMK-1 is translocated intracellularly, it phosphorylates the CREB/ATF basic-region leucine zipper bZIP transcription factor ATF-7, which constitutively functions as a transcriptional repressor. Phosphorylated ATF-7, however, directly activates transcription of PMK-1-regulated genes, inducing a concerted immune response that promotes pathogen clearance (Cheesman et al. 2016; Shivers et al. 2010). Loss-of-function mutations in any of these core kinases result in increased susceptibility to a variety of microorganisms and reduced survival (Kamaladevi and Balamurugan 2015; Pukkila-Worley et al. 2011).

Following exposure to pathogenic microbes, *C. elegans* coordinates an inducible innate immune response from intestinal epithelial cells (Pukkila-Worley et al. 2011; Shivers et al. 2009; Kim et al. 2002). It is therefore imperative that investigations featuring the nematode as a model for host-microbe interactions take into account p38 MAPK-dependent immune hyperactivation (Cheesman et al. 2016). It has also been demonstrated that an age-associated decline in p38 MAPK signalling underlies the phenomenon of innate immunosenescence in *C. elegans* (Youngman et al. 2011). With a direct link between ageing and immunity, there exists the opportunity to identify microbial interventions that benefit the aging nematode.

#### 4.1.5. Investigating experimental microbiome effects on *C. elegans* motility

A growing body of evidence suggests cross-talk between commensal microbes and host physiology; particularly skeletal muscle and its equivalents. However, current research would be benefitted by model systems that are easily colonised with simplified bacterial communities to examine causative relationships between host and microbiota. With this in mind, we evaluated frailty-associated phenotypes in *C. elegans* cultivated on the EM. We hypothesised that a functional and ecologically relevant microbiome would benefit muscular health and locomotor function in nematodes as has been shown in other animal models. In mice, for example, this has been attributed to the circulation of microbially-derived factors (Lahiri et al. 2019). We also expected that the presence of commensal microbes in the nematode intestine may initiate innate immune activation and explored this response as a candidate mechanism underlying locomotor effects. The aims of the succeeding chapter are as follows:

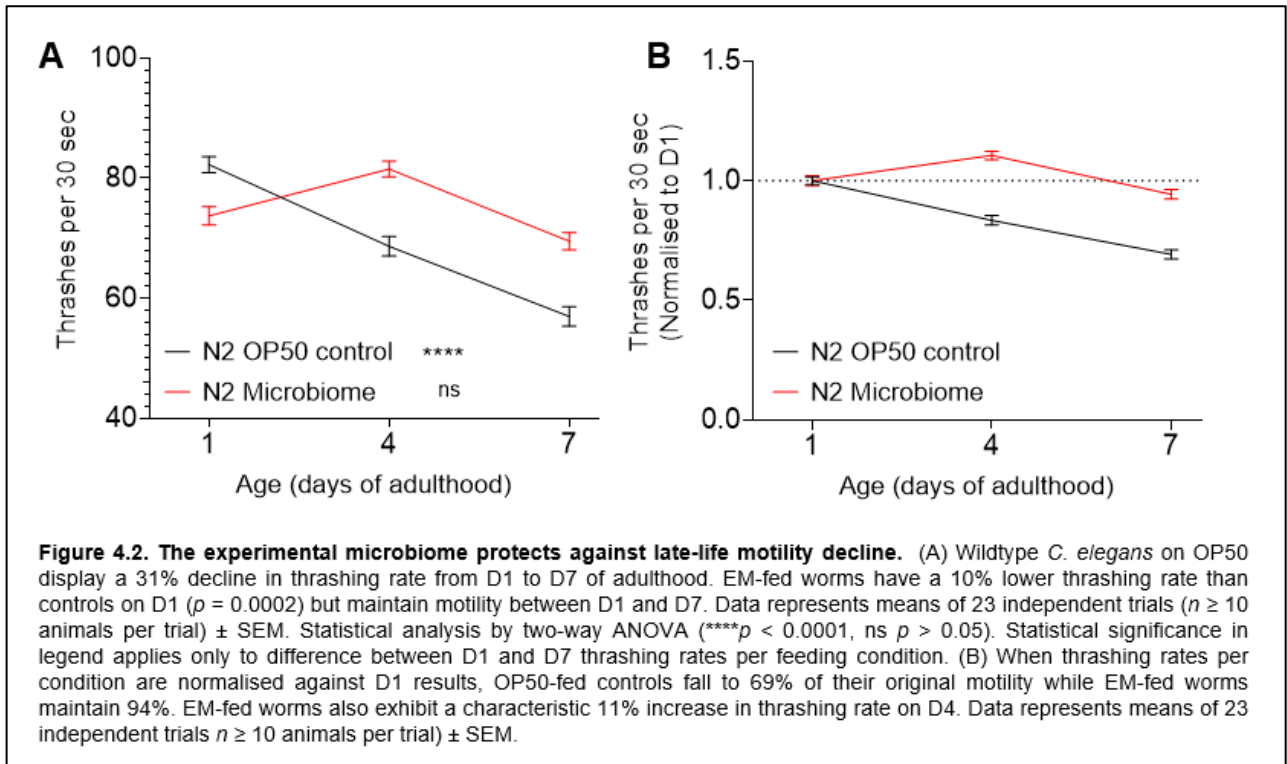
1. Assess the effects of the EM on *C. elegans* locomotion throughout ageing
2. Assess the effects of the EM on various aspects of neuromuscular health
3. Identify molecular mechanisms underlying EM effects on *C. elegans* locomotion

## 4.2 Results

### 4.2.1. Experimental microbiome suppresses age-associated decline of two-dimensional motility

We first assessed the effects of the EM on two-dimensional motility with the use of a lateral swimming (thrashing) assay, in which nematodes were transferred from solid NGM plates into M9 buffer. After a brief period of acclimation, the number of C-shaped body bends performed was manually counted. The assay was performed at 3 timepoints ranging from early to mid-adulthood: D1, D4, and D7. Wildtype control nematodes cultivated on OP50 displayed a significant 31% decline in thrashing rate from D1 to D7, from a mean rate of 82.25 ( $\pm 1.34$ ) thrashes per 30 seconds to 56.95 ( $\pm 1.61$ ) thrashes per 30 seconds ( $p < 0.0001$ ) (Figure 4.1A) – a result we had expected considering previous data on the decline of muscle function with age (Herndon et al. 2002). EM-fed nematodes thrash at a 10% lower rate compared to controls on D1 of adulthood ( $p = 0.0002$ ), with a mean 73.72 ( $\pm 1.52$ ) thrashes per 30 seconds. However, nematodes reared on the EM do not exhibit the same progressive decline in motility with age as controls and instead maintain their thrashing rate from D1 to D7 ( $p = 0.129$ ). In addition, unlike controls which display a progressive decline in thrashing rate at each successive timepoint, EM-fed worms exhibit an 11% increase in thrashing rate from D1 to D4 of adulthood ( $p = 0.0007$ ), which falls once again by D7. The suppression of motility decline by the EM is especially evident when thrashing rates were normalised against D1 values for the corresponding condition (Figure 4.1B). OP50-reared controls fall to 69% of their original motility by D7 of adulthood,

while nematodes on the EM maintain 94%. We therefore conclude that the EM protects *C. elegans* against age-related motility decline.



#### 4.2.2. Experimental microbiome does not affect *C. elegans* gentle touch mechanosensation

Following the results of the thrashing assay, we probed for major neuromuscular defects in OP50- versus EM-fed animals using gentle touch stimulation as previously described (Chen and Chalfie, 2004). The nematode's response to gentle touch is mediated by six mechanosensory neurons: the bilateral anterior lateral microtubule (ALM) and posterior lateral microtubule (PLM) neurons, as well as the singular anterior ventral microtubule (AVM) and posterior ventral microtubule (PVM) neurons (Figure 4.3B). The paired ALMs and AVM evoke a backwards escape reflex in response to light touch to the anterior body (between the nose and midbody) while the PLMs coordinate a forward escape reflex when

the nematode's posterior (between midbody and tail) is stimulated (Chalfie et al. 1985). The PVM is able to respond to gentle posterior touch but is neither required nor sufficient to coordinate touch-evoked escape behaviour (Chatzigeorgiou et al. 2010; Wicks and Rankin 1996).

Wildtype worms were prodded with an eyebrow pick in two distinct locations: immediately posterior to the pharynx (to stimulate the anterior touch response) and immediately anterior to the anus (to stimulate the posterior touch response). Each nematode was tested five times anteriorly and five times posteriorly and the percentage of touches responded to – by moving towards or away from the pick – was recorded. Young adult (D1) worms cultivated on the EM responded to 63% ( $\pm 3\%$ ) of gentle touches, which fell to 49% ( $\pm 3\%$ ) by D11 (Figure 4.3A). Similarly, OP50-fed controls' responsiveness declined from 60% ( $\pm 2\%$ ) on D1 to 45% ( $\pm 3\%$ ) on D11. No difference in touch responsiveness was seen between feeding conditions on D1 ( $p = 0.957$ ), D4 ( $p = 0.974$ ), D7 ( $p = 0.908$ ), or D11 ( $p = 0.940$ ), suggesting that the EM does not adversely affect mechanosensory function in gentle touch receptor neurons throughout age.

#### 4.2.3. Experimental microbiome does not alter mechanosensory neuron morphology

We sought to support this functional data with morphological data obtained through fluorescent microscopy. Like in human ageing, *C. elegans* neurons do not undergo cell death and axons do not disintegrate (Herndon et al. 2002). Fluorescence and electron microscopy have revealed that the ageing *C. elegans* nervous system instead undergoes neuron-specific structural regrowth and synaptic deterioration (Toth et al. 2012). We documented structural changes occurring with age in two gentle touch receptor neurons

per transgenic (*zdfs5(p<sub>mec-4</sub>::GFP)*) animal: the ALM, positioned anteriorly, and the PLM, positioned posteriorly (Figure 4.3B). We counted the occurrence of three distinct morphological abnormalities in the somas and neurites of each ALM and PLM neuron as previously described (Chew et al. 2013; Chen et al. 2013; Toth et al. 2012). This included triangle-shaped protrusions along the neurite giving the appearance of “blebs,” bending of the neurite giving the appearance of “waves,” and novel outgrowths emanating from either somata or neurites with the appearance of “branches.” In both ALM and PLM neurons, we found no observable differences in the frequency of blebbing events between controls and EM worms on D1 (ALM  $p = 0.624$ , PLM  $p = 0.903$ ), D4 (ALM  $p > 0.999$ , PLM  $p = 0.999$ ), or D7 (ALM  $p = 0.193$ , PLM  $p = 0.173$ ) of adulthood (Figure 4.3E,H). Similarly, the number of aberrant branches in ALM or PLM neurons was comparable between feeding conditions on D1 (ALM  $p = 0.624$ , PLM  $p > 0.999$ ), D4 (ALM  $p > 0.999$ , PLM  $p = 0.847$ ), and D7 (ALM  $p = 0.193$ , PLM  $p = 0.058$ ) (Figure 4.3G,J). It was only in D7 ALM neurons that a reduced frequency of waving events was seen in EM-fed worms, though this effect was found to be mild ( $p = 0.02$ ) (Figure 4.3F).

Considering the results obtained in both ALM and PLM mechanosensory neurons across three age-associated features, we conclude that cultivation on the EM does not significantly alter the morphology of mechanosensory neurons, whether in early or mid-late adulthood.

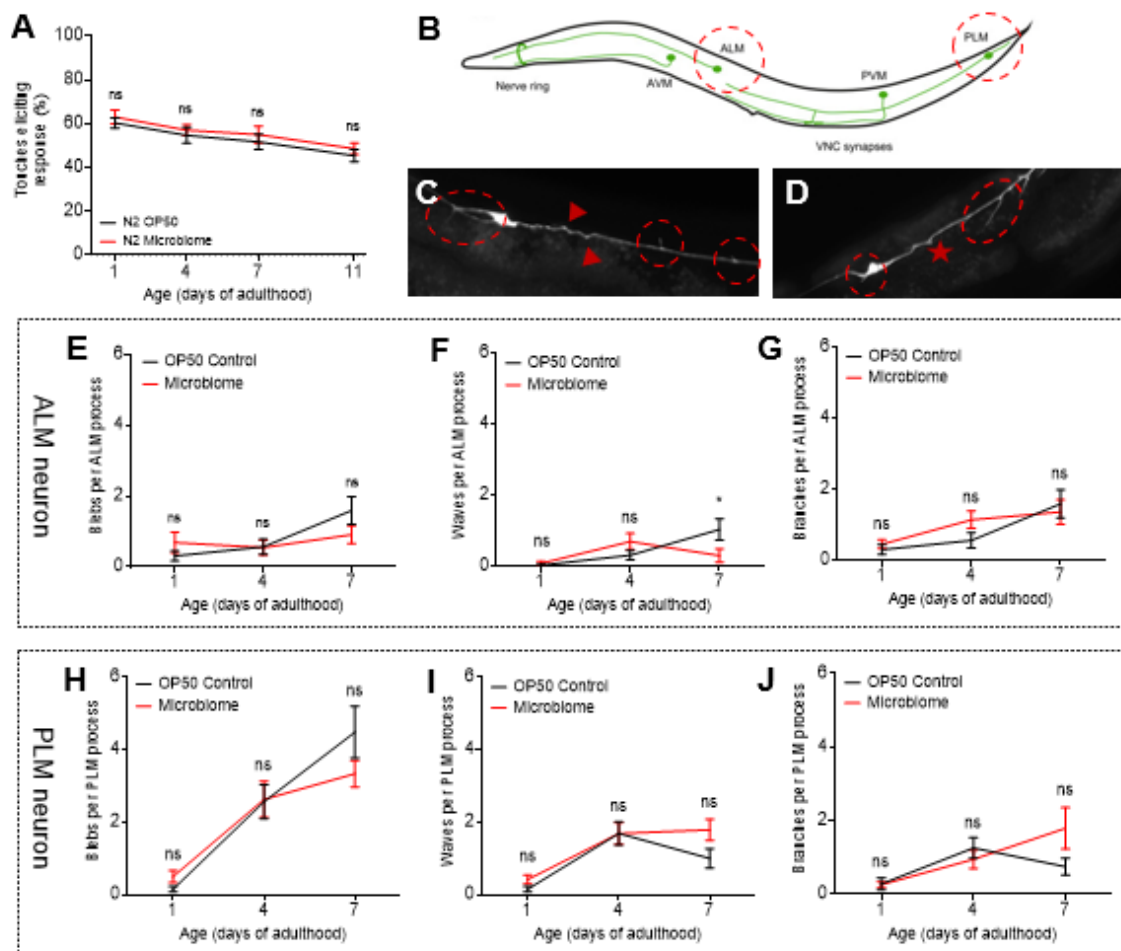


**Figure 4.3. EM does not alter mechanosensation in *C. elegans*.** (A) No difference in gentle touch responsiveness was observed between EM-fed worms and OP50-fed controls on D1, D4, D7, or D11 of adulthood. Data represents means of three independent trials ( $n = 10$  animals per trial)  $\pm$  SEM. Statistical analysis by two-way ANOVA ( $ns$   $p > 0.05$ ). Data provided by AK. (B) Schematic diagram of gentle touch receptor neurons in *C. elegans*, lateral view. For simplicity, only one of each bilateral neuron is shown. Broken circles indicate neurons imaged in following panels. Diagram adapted from Chen et al. 2013. (C) Representative image of ALM neuron in D7 OP50-fed worm. Triangles indicate "wave" events. Broken circles indicate novel "branches." (D) Representative image of ALM neuron in D7 EM-fed worm. Star indicates "blebbing." (E-G) Frequency of morphological abnormalities in soma and neurites of ALM neuron. No difference seen between feeding conditions except for an increase in mean wave frequency in OP50 controls on D7. Statistical analysis by two-way ANOVA ( $*p = 0.02$ ,  $ns$   $p > 0.05$ ). Data represents means of three independent trials ( $n \geq 12$  animals per trial)  $\pm$  SEM. (H-J) Frequency of morphological abnormalities in soma and neurites of PLM neuron. No difference seen between feeding conditions for all events counted. Statistical analysis by two-way ANOVA ( $ns$   $p > 0.05$ ). Data represents means of three independent trials ( $n \geq 12$  animals per trial)  $\pm$  SEM.

#### 4.2.4. Experimental microbiome does not alter sarcomere integrity

We wanted to determine if structural differences in muscle fibre organisation were underlying the protective effect of the EM on late-life motility. We did so with the use of a *C. elegans* strain expressing a GFP-tagged MYO-3 protein under the control of its own promoter. *myo-3* encodes a myosin heavy chain protein which serves as the central component of the thick filaments in body wall muscle (Meissner et al. 2009; Miller et al. 1983). Our initial approach to assay muscular health was to devise a qualitative scoring system for muscle fibre organisation based on previous reports (Herndon et al. 2002). A single body wall muscle cell situated between the pharynx and vulva was imaged per worm via fluorescent microscopy. A score between 1 and 4 was assigned to each cell imaged, with level 1 sarcomeres arranged in parallel, symmetric rows with no gaps or bends and level 4 sarcomeres appearing broken and 'blurred' (Figure 4.4A). Using this qualitative paradigm, we compared OP50-cultivated controls against worms raised on the EM on D1, D4, and D7 of adulthood. No difference in sarcomere integrity was observed at any of the assessed timepoints ( $p > 0.05$ ). Surprisingly, we also did not observe an age-associated increase in sarcomere disorganisation within each of the conditions tested, though this was likely due to insufficient ageing of the test subjects. Previous studies that had reported a progressive loss of sarcomere integrity in  $p_{myo-3}MYO-3/GFP$  worms *C. elegans* had done so in far advanced age i.e., D18 of adulthood (Herndon et al. 2002). However, adhering to the parameters set by the results of our thrashing assays, we hereby conclude that the protective effect of the EM against age-associated motility decline is not due to differences in sarcomere integrity.

#### 4.2.5. Experimental microbiome suppresses age-associated decline of three-dimensional motility

Once we had established that the protective effect of the EM on late-life motility was occurring without major changes in muscular integrity, we used a burrowing assay to measure potential differences in muscular strength and function. The technique used was developed as a neuromuscular health assay that more accurately reflects the nematode's true behavioural conditions of burrowing in three dimensions (Lesanpezeshki et al. 2019). Nematodes were loaded onto the bottom of empty plates and the optically transparent and biocompatible Pluronic F-127 gel (Sigma) was cast above them and allowed to set at room temperature (Pluronic F-127 gel is in liquid-phase at 4°C). A small volume of OP50 or EM bacterial culture was loaded onto the solidified gel as a chemoattractant and the number of nematodes successfully reaching the selected food source was quantified every 15 minutes for a total of 120 minutes.

When nematodes were tested on D1 of adulthood, 32% fewer animals ( $p < 0.0001$ ) were identified in the EM bacterial lawn than in the OP50 control at the 120-minute mark, suggesting a reduced burrowing ability in EM-cultivated worms (Figure 4.4C). We did not detect this difference in neuromuscular function between feeding conditions on D4 ( $p = 0.327$ ) or D7 ( $p = 0.931$ ), where equivalent proportions of animals had reached the corresponding chemoattractant. When we tracked changes in burrowing ability *within* each feeding condition over time, we found that the mean proportion of OP50-fed control animals occupying the bacterial lawn fell from 83% ( $\pm 8\%$ ) on D1 to 37% ( $\pm 11\%$ ) on D7 of adulthood ( $p < 0.0001$ ). By contrast, no statistically significant difference was found in EM-fed animals reaching the chemoattractant between D1 and D7 ( $p = 0.571$ ) (Figure 4.4D). The results of the two distinct motility assays performed – assessing both two-dimensional and three-dimensional locomotion – thus corroborate one another. Though wildtype

nematodes cultivated on the EM exhibit reduced motility in early adulthood (10% lower swimming locomotion and 32% lower burrowing locomotion on D1), they do not display the same progressive decline in locomotion as controls on *E. coli* OP50. We therefore conclude, following the evaluation of locomotion in two distinct dimensionalities, that the EM is protective against age-associated motility decline.

#### 4.2.6. Experimental microbiome effects on motility are not due to alterations in neuromuscular transmission

*C. elegans* body wall muscles are often used as a model system for the study of neuromuscular transmission due to their functional comparability to vertebrate skeletal muscle (Gieseler, 2017). One class of ionotropic acetylcholine receptor (AChR) located in the nematode neuromuscular junction is the L-AChR, which transduces chemical signals from cholinergic motor neurons into the electrical signals underlying muscular contraction. L-AChRs are sensitive to the action of the pharmacological antagonist levamisole and wildtype *C. elegans* exposed to levamisole undergo time-dependent paralysis (Lewis et al. 1980). Altered sensitivity to levamisole-induced paralysis thus indicates potential defects in postsynaptic cholinergic signalling (Chaya et al. 2021). Following our observations that the EM alters both two-dimensional and three-dimensional locomotion in wildtype nematodes, we investigated the possibility of defective neuromuscular transmission.

To do so, we placed wildtype nematodes reared on either OP50 or the EM within a drop of levamisole and measured relative changes in body length due to muscular contraction. As the contraction of body wall muscle in *C. elegans* is dependent on the excitatory action

of acetylcholine at the neuromuscular junction, alterations in the relative magnitude of contraction served as a proxy for the efficacy of cholinergic transmission. Using an overhead camera (WormLab Imaging System, MBF Bioscience), worms were imaged before and after transfer from M9 buffer into 200  $\mu$ M levamisole. On D1 of adulthood, OP50-fed controls and EM-fed worms both underwent a comparable 14% ( $\pm 3\%$  and  $\pm 1\%$ , respectively) decrease in body length following transfer into levamisole ( $p = 0.984$ ) (Figure 4.4E). On D4, worms of both feeding conditions exhibited a 13% decrease in body length ( $p = 0.964$ ) while on D7, OP50 controls' body length was shortened by a mean of 12% while EM worms were shortened by 11% ( $p = 0.923$ ). With no significant differences in contractility at the same ages where we observed significant differences in motility, we hereby conclude that the locomotor effects of the EM – whether the reduced swimming and burrowing abilities on D1 of adulthood or the maintenance of young adult motility into D7 of adulthood – are not the result of altered cholinergic transmission in body wall muscle.

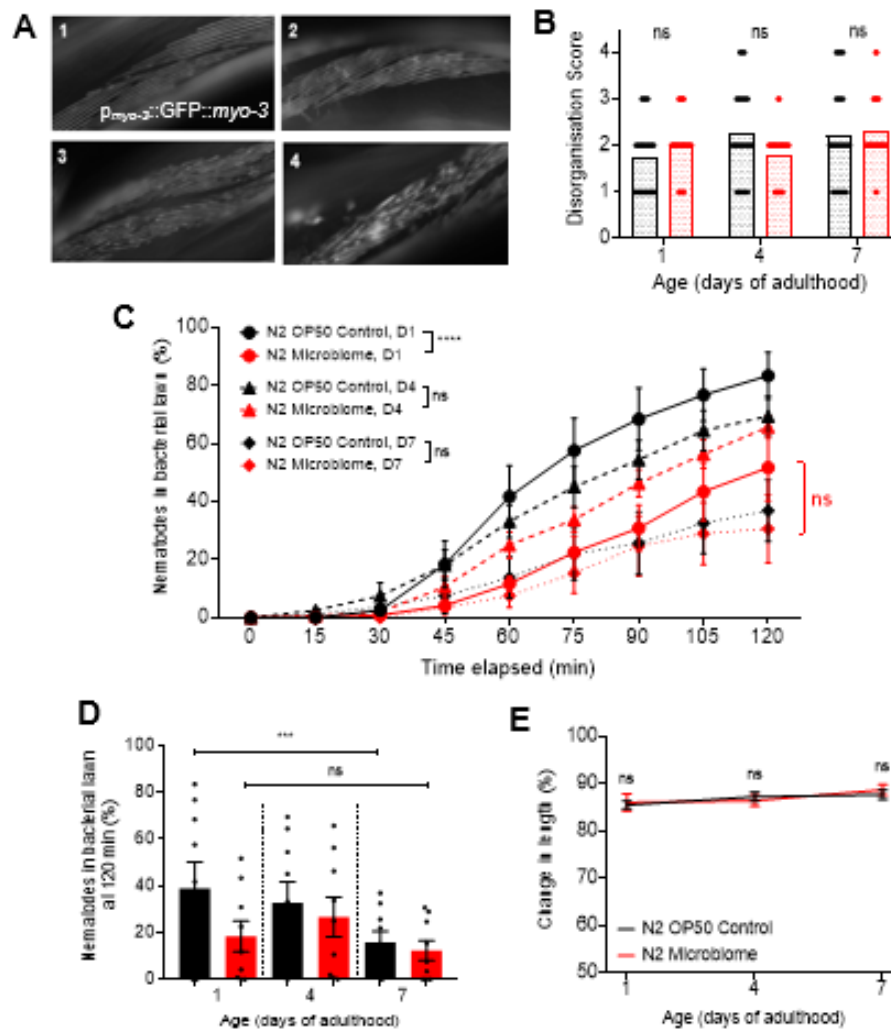


**Figure 4.4. EM does not adversely affect sarcomere integrity or muscle function.**

(A) Representative images of discrete numerical scores (1-4) describing muscle fibre organisation in the sarcomeres of  $p_{myo-3}::GFP::myo-3$  animals. One sarcomere located between head and vulva imaged per animal. 1 = Fibres arranged in parallel, symmetric rows; 2 = Fibres mainly parallel, containing some gaps; 3 = Fibres lie in same direction but contain gaps, bends, frayed; 4 = Fibres are broken and bent with a 'blurred' appearance. (B) No differences in muscle fibre organisation reported between OP50-fed controls and EM-fed worms on D1, D4, or D7 of adulthood. Statistical analysis by chi-square test ( $ns$   $p > 0.05$ ). Data points represent individual disorganisation scores per animal. Bars represent mean fragmentation scores per timepoint across three independent trials ( $n \geq 12$  animals per trial). (C-D) EM-fed worms exhibit reduced three-dimensional locomotion (burrowing ability to reach chemoattractant) on D1 of adulthood but are protected from age-associated decline ( $p = 0.571$ , EM D1 vs. D7). Statistical analysis by two-way ANOVA ( $****p < 0.0001$ ,  $***p < 0.001$ ,  $ns$   $p > 0.05$ ). Data represents mean proportions across three independent trials ( $n = 20$  animals per trial)  $\pm$  SEM. Data contributed by FX. (E) No differences in cholinergic transmission efficacy, as evidenced by percentage change in body length in 200  $\mu$ M levamisole, was found between OP50-fed controls and EM-fed worms. Statistical analysis by two-way ANOVA ( $ns$   $p > 0.05$ ). Data represents means of three independent trials ( $n = 10$  animals per trial)  $\pm$  SEM. Data contributed by FX.

#### 4.2.7 Experimental microbiome suppresses age-associated motility decline in a p38-dependent manner

The transcriptomic analysis we had performed to compare gene expression between feeding conditions (see section 3.2.3) revealed an EM-dependent enrichment of upregulated genes related to immune responses to pathogens. Noting that *C. elegans* innate immunity relies heavily on the p38 MAPK (PMK) signalling pathway, we probed its involvement in the EM effect on late-life motility. The lateral swimming (thrashing) assay was repeated using loss-of-function mutants for various components of the PMK signalling cascade. Each independent trial performed included four conditions: wildtype nematodes cultivated on OP50/EM and PMK pathway mutants cultivated on OP50/EM. We screened animals possessing null mutations in *tir-1*, *nsy-1*, *pmk-1*, and the transcription factor *atf-7* (Figure 4.5A) to identify if any PMK pathway components were required for the EM's protective effect on motility decline.

Motility in OP50-fed *tir-1* mutants was found to decline with age in a similar fashion to wildtype worms on the same food source: the thrashing rate of *tir-1*<sup>-/-</sup> mutants on OP50 is reduced by 47% from D1 to D7 of adulthood ( $p < 0.0001$ ; statistical significance applies to D1 vs. D7 values per condition). However, the protective effect of the EM which was observed in wildtype worms on D7 ( $p = 0.999$ ) was abrogated in *tir-1*<sup>-/-</sup> worms, which exhibited a 23% decline in thrashing rate by D7 ( $p = 0.002$ ) (Figure 4.5B). Similarly, *nsy-1*<sup>-/-</sup> worms lose the protective effect of the EM, with a 32% reduction in thrashing rate from D1 to D7 ( $p = 0.006$ ) – in contrast to the 6% increase in thrashing from D1 to D7 exhibited by EM-fed wildtype worms within the same trial ( $p = 0.803$ ) (Figure 4.5C). Taken together, these results indicate not only the requirement of the general PMK pathway in EM-mediated protection from motility decline but the involvement of upstream pathway

components *tir-1* and *nsy-1*. The involvement of downstream components *pmk-1* and *atf-7* in EM-mediated conservation of motility is less clear-cut. *pmk-1<sup>-/-</sup>* mutants cultivated on either OP50 or the EM behave in a similar fashion on D7 of adulthood, where the protective effect of the EM was lost and thrashing rates declined by 19% and 17%, respectively ( $p < 0.0001$ ). While this suggests a requirement for *pmk-1* expression in the protective effect of the EM, it is worth noting that wildtype EM-fed worms within this data set unexpectedly displayed a slight but significant decline in thrashing rate from D1 to D7 ( $p = 0.017$ ) (Figure 4.5D). As the wildtype controls included within this data set did not behave as anticipated based on previous trials, we are unable to draw a legitimate conclusion on the contribution of *pmk-1* expression to the EM's conservation of late-life motility. Interestingly, null mutants for the transcription factor-encoding *atf-7* gene behaved in the opposite fashion expected for their respective feeding conditions (Figure 4.5E). *atf-7<sup>-/-</sup>* worms reared on the EM exhibited a 19% decline in thrashing rate from D1 to D7 ( $p = 0.005$ ) while OP50-fed *atf-7<sup>-/-</sup>* worms maintained their motility ( $p = 0.592$ ). The loss of the protective effect of the EM in *atf-7* null mutant worms suggests a requirement for *atf-7* expression. However, the maintenance of motility in aged *atf-7<sup>-/-</sup>* worms on OP50 is unprecedented. Overall, the thrashing data sets involving null mutations in individual PMK pathway components indicate that the signalling pathway is required for the EM's capacity to preserve motility well into adulthood, with the most pronounced effects observed following the loss of the upstream kinases.

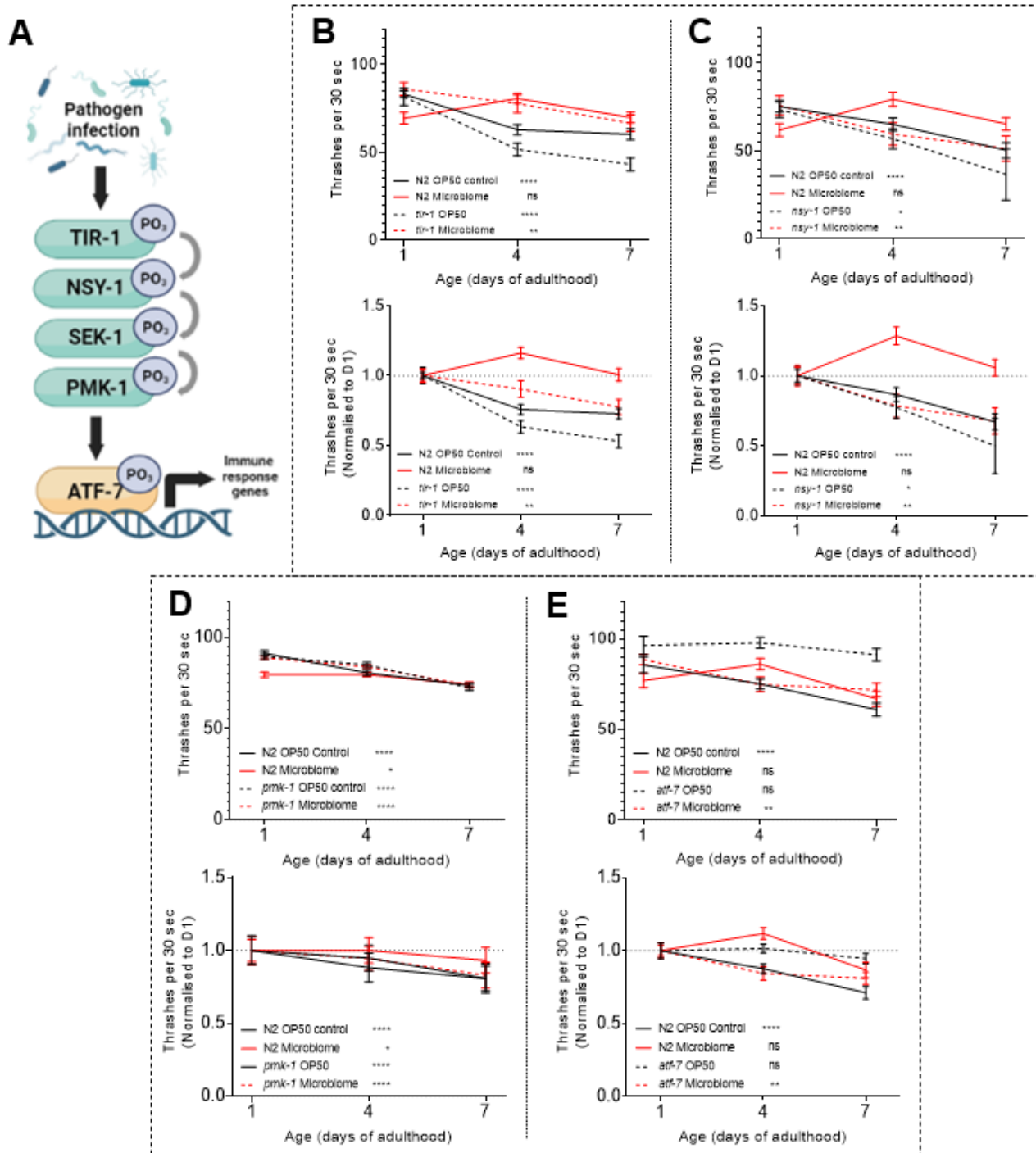


**Figure 4.5. The p38 MAPK (PMK) pathway is required for the protective effect of the EM against age-associated motility decline.** (A) Schematic diagram illustrating p38 MAPK signalling cascade. Activation of the PMK pathway via the TIR-1 receptor results in sequential phosphorylation of NSY-1, SEK-1, and PMK-1 at conserved residues. Active PMK-1 is translocated into the nucleus and phosphorylates the transcriptional repressor ATF-7, inducing expression of immune response genes. (B-E, above) Number of thrashes performed in physiological buffer following acclimation period. Statistical analyses by two-way ANOVA (\*\*\*\* $p < 0.0001$ , \*\* $p < 0.001$ , \* $p < 0.01$ , ns  $p > 0.05$ ). Statistical significance shown for each condition applies to D1 vs. D7 thrashing rates only. Data represent means of three independent trials ( $n = 10$  animals per trial)  $\pm$  SEM. (B-E, below) Thrashing rates per timepoint per condition normalised against D1 values. (B) Mutants deficient in *tir-1* expression lose the protective effect of the EM against motility decline at D7 ( $p = 0.002$ ). (C) Mutants deficient in *nsy-1* expression lose the protective effect of the EM against motility decline at D7 ( $p = 0.006$ ). (D) EM-fed mutants deficient in *pmk-1* expression exhibit motility decline as OP50-fed mutants do ( $p < 0.0001$ ), though no conclusions can be drawn due to mild decline in motility in EM-fed N2 controls ( $p = 0.017$ ). Data contributed by AK. (E) Mutants deficient in *atf-7* expression lose the protective effect of the EM against motility decline at D7 ( $p = 0.005$ ), but OP50-fed *atf-7* mutants maintain motility at D7 ( $p = 0.592$ ).

## 4.3 Discussion

### 4.3.1 Experimental microbiome protects against age-associated motility decline

Although evidence from human subjects and mammalian models has revealed the existence of a gut-muscle axis (Fielding et al. 2019; O'Toole and Jeffrey, 2015), little is known of the relationship between the microbiome and musculature in *C. elegans*. Dirksen et al. (2020) successfully colonised *C. elegans* with a complex and ecologically relevant microbiome, although the subsequently life history and healthspan metrics evaluated were limited. The work presented in this chapter continues to examine the effects of the EM on *C. elegans* physiology, now within the context of an age-associated phenotype. As in higher organisms, *C. elegans* exhibit a progressive deterioration of muscle structure and function that has been extensively documented via *in vivo* locomotory assays (Gieseler et al. 2016; Gaffney et al. 2014; Gaiser et al. 2011). As such, muscular health presents an attractive physiological domain from which to evaluate the influence of the EM on host fitness and identify motility-preserving interventions.

Young adult worms cultivated on the EM exhibited slightly reduced two-dimensional motility in liquid media in comparison to OP50-fed controls but preserve their thrashing rates into mid-adulthood, while OP50-fed controls exhibit progressive age-associated motility decline in accordance with published studies (Bansal et al. 2015; Glenn et al. 2004; Huang et al. 2004). EM-fed animals also exhibit a characteristic increase in thrashing rate from D1 to D4 of adulthood. The same phenotype was observed when three-dimensional motility was assessed via a burrowing assay, suggesting that the protective effect of the EM against motility decline can be extended to locomotor behaviour in native

environments. Cultivation on the EM is thus protective against the decline in motility associated with advanced age.

#### 4.3.2 Experimental microbiome protects against locomotor decline without altering muscular structure or function

We considered that the preservation of movement capacity by the EM may be due to the high viscosity of the EM lawn compared to *E. coli* OP50, subjecting worms to mechanical stress that improves muscle strength and function with time. Indeed, the implementation of exercise protocols in *C. elegans* have been shown to improve locomotory performance and extend the functional longevity of muscle (Laranjeiro et al. 2019). When sarcomere structure in the body wall muscle of OP50-fed versus EM-fed worms was compared, no difference in myosin organisation was found thereby suggesting that the preservation of motility by the EM is not due to induced changes in muscular integrity. Interestingly, we did not observe any decline in myosin organisation from early- to late-adulthood in either feeding condition. Even OP50-fed animals, which display significant reductions in thrashing rate by D7, showed no accompanying change in sarcomere disorganisation score. We considered that the qualitative scoring paradigm used may be of insufficient precision to detect differences in sarcomere integrity. Experiments quantifying gaps in thick myosin filaments using confocal microscopy are currently underway. The preliminary quantitative results obtained at higher magnification featuring compiled Z-stacks so far corroborate the results of our discrete scoring system and indicate no differences in sarcomere integrity between OP50-fed and EM-fed animals up to D7 of adulthood. It is likely that the conspicuous deterioration of *C. elegans* sarcomere organisation occurs far into adulthood, beyond the D7 cutoff selected for the scope of this project. Studies utilising the same transgenic reporter strain, for example, reported disorganised and irregular

myosin filament orientation at D18 of adulthood (Herndon et al. 2002). However, as significant differences in motility between OP50- and EM-fed animals are evident as early as D1 of adulthood, we next assessed whether alterations in muscle function – rather than structural integrity – underlie the suppression of motility decline by the EM.

The efficacy of neuromuscular transmission was compared in OP50- and EM-reared nematodes through changes in body length induced by levamisole, a nicotinic agonist (Chaya et al. 2021; Glenn et al. 2004). No differences in muscle contractibility were observed between feeding conditions, including on D7 of adulthood where thrashing rates in EM-fed animals were significantly higher than controls. We further examined neurotransmission through an aspect of neuronal signalling distinct from motor programmes: mechanosensation. OP50-fed and EM-fed nematodes demonstrated equivalent responsiveness to gentle touch stimulation from early- to late-adulthood. This finding was supported by morphological data obtained in two of the six neurons mediating gentle touch sensation, where no significant change in the occurrence of morphological abnormalities was reported. It is worth noting that as small novel branches would have been overlooked at the 630x magnification used, branching events are likely to be underestimated for both feeding conditions (Toth et al. 2012) – although the frequency of conspicuous blebbing or waving events were also unchanged in EM-fed animals. In the preceding chapter examining EM effects on nematode healthspan, defecation rate in wildtype worms was measured as an indicator of digestive health (Liu and Thomas, 1994) despite its additional utility as a model for synaptic transmission (Nagy et al. 2015; Mahoney et al. 2008; Peters et al. 2007). With no discernible EM-induced differences in DMP frequency from early- to late-adulthood, defecation data supports the conclusion that neuronal signalling is unaffected on the EM. Altogether, functional and morphological data

suggest that neuromuscular transmission and mechanosensation are not altered by cultivation on the EM, although it should be noted that the approaches taken to assess neuronal signalling were not exhaustive. Responsiveness to harsh body touch, for example, which is mediated by an independent network of 14 mechanosensory neurons (Li et al. 2011; Way and Chalfie 1989) was not evaluated within this project, therefore the effects of the EM on total mechanosensation are yet undetermined.

An indication of muscle function was also provided in the preceding chapter via feeding and defecation data. Food intake in *C. elegans* is controlled by the pumping action of the pharyngeal muscles, while defecation is mediated by alternating contractions in the posterior and anterior body wall muscles. The elevated pharyngeal pumping rate displayed by EM-reared worms suggested some nutritional deficit in the EM compared to *E. coli* OP50, but was also found to deteriorate over time in a similar fashion to OP50-reared controls (D1 to D7  $p < 0.0001$ ), suggesting that the EM does not preserve motility across the whole *C. elegans* body plan. Moreover, although the DMP is controlled by the action of body wall muscles, defecation rates were comparable in OP50- and EM-fed worms at all timepoints tested. Our findings indicate that the protective effects of the EM against motility decline apply only to directed locomotion.

The work presented in this chapter demonstrates that members of the native *C. elegans* microbiome suppress age-related locomotor decline without gross alterations to muscular structure or function. Although this hypothesis has been supported by various approaches, we cannot exclude that differences in muscular strength may underlie EM-mediated effects on late-life motility. Recent developments in microfluidics-based systems that

measure deflection in the experimental environment to assess muscle strength would benefit our investigation and provide a more complete profile of locomotion on the EM (Rahman et al. 2018; Johari et al. 2013). Taken together, our results have important implications for the gut-muscle axis in *C. elegans* as they suggest cross-talk between microbiota and motor programmes but call into question how these interactions may occur without fundamentally affecting muscle structure or function.

#### 4.3.3 Experimental microbiome protects from locomotory decline via the p38 MAPK pathway

With no apparent muscular differences to account for the enhanced locomotor capacity seen in aged EM-fed nematodes, we sought out an alternative mechanistic explanation with the use of loss-of-function mutants. In a previous chapter, we showed that rearing on the EM upregulates transcription of gene sets mediating host immune responses to pathogens, in agreement with published studies utilising bacterial strains included in our EM (Dirksen et al. 2020; Yang et al. 2019). We showed that the protective effect of the EM on locomotion relies on the p38 MAPK (PMK) signalling pathway, as EM-fed PMK pathway null mutants display age-associated decline in thrashing rate akin to OP50-fed controls. The protective effect of the EM is most notably abrogated in *tir-1* and *nsy-1* mutants lacking the upstream kinase components of the PMK pathway, while the effect is less pronounced in *pmk-1* mutants lacking a downstream kinase. These findings suggest that some PMK pathway functionality is retained following *pmk-1* knockout but is severely diminished by knockout of the upstream kinases, in agreement with Kamaladevi and Balamurugan (2015) who reported greater susceptibility to *Klebsiella pneumoniae* infection in *sek-1* mutants compared to *pmk-1* mutants.

A role for PMK pathway components in the EM's effects on motility also implies activation of the innate immune system by our microbial assembly. Several groups have documented innate immunosenescence – the progressive decline in innate immune function with age – underpinned by a decline in PMK pathway activity (Portal-Celhay et al. 2012; Youngman et al. 2011). Further investigation is required to evaluate whether innate immune function in EM-fed worms is resistant to age-associated decline in the same manner as locomotor function, and whether this serves as a contributor to the disparate age-associated phenotypes displayed by EM-fed animals versus OP50-fed controls. Although this was not studied within this project, *Pseudomonas aeruginosa* infection assays are currently underway to assess immune capacity in EM-fed worms.

## 5. Experimental microbiome (EM) effects on mitochondrial homeostasis

### 5.1 Introduction

#### 5.1.1 Mitochondria and the microbiome

Mitochondria are double-membraned organelles responsible for the production of 90% of the cell's chemical energy requirements via cellular respiration in the form of adenosine triphosphate (ATP) (Castellani et al. 2020). The endosymbiotic theory of mitochondrial origin posits that the organelles originated from eubacterial ancestors that survived endocytosis by proteobacteria, eventually becoming irreversibly incorporated into the cytoplasm (Gray et al. 2001; Sagan, 1967). Although the theory has been subject to several revisions, the likely evolutionary scenario suggests mitochondria are descended from the primordial aerobic *Rickettsia* that had entered into a mutualistic relationship with the ancient anaerobic *Archaea* (reviewed in Martin et al. 2015). Throughout evolution, mitochondria became integrated organelles in close communication with other cellular compartments. As a result of this integration, mitochondrial proteins are encoded by two independent genomes: nuclear DNA and mitochondrial DNA (mtDNA). While mtDNA encodes 13 proteins constituting the oxidative phosphorylation complexes, the remaining mitochondrial proteins are encoded in the nucleus and imported into the organelle through the cytoplasm. The newly assimilated mitochondria provided their hosts with energy provision in both the presence and absence of oxygen, along with the additional advantages of calcium regulation and the biosynthesis/metabolism of amino acids (Castellani et al. 2020).

Considering the mitochondrion's endosymbiotic origins, it is plausible that an organism's microbiome – composed of *external* symbionts – directly interacts with mitochondria – the host's *internal* symbionts – through convergent signalling pathways. One candidate mechanism underlying such cross-talk is the production of reactive oxygen species (ROS) by mitochondria – a consequence of cellular respiration in oxygen-rich environments (Ballard and Towarnicki, 2020). ROS is the combined term describing the chemical species formed upon incomplete reduction of oxygen and includes both nonradical and free radical ROS. Mitochondrial genotype was found to influence gut microbiome diversity in mice, as mutations in genes altering mitochondrial function resulted in distinct microbiota profiles that were maintained even in pups fostered by non-mutant mothers (Yardeni et al. 2019). As species diversity was correlated with host nonradical ROS production, researchers manipulated ROS abundance via antioxidant treatment, subject age, or the expression of ROS scavenger catalases within the mitochondria. In all conditions, microbiota composition was significantly altered, suggesting a robust relationship between ROS abundance and species diversity.

In the reciprocal direction, microbially-produced metabolites and byproducts are also capable of regulating mitochondrial functions in both health and disease states (Weber-Stiehl et al. 2022). For example, the short-chain fatty acid (SCFA) butyrate, which can only be produced through the metabolic activity of the microbiota, has been shown to reduce pro-inflammatory immune responses by enhancing the mitochondria-dependent apoptosis of activated T-cells (Zimmerman et al. 2012). The microbiota is also responsible for metabolising amino acids such as the proteinogenic cysteine. As a component of the antioxidant glutathione, cysteine is instrumental in detoxifying mitochondrial ROS and is also metabolised into hydrogen sulphide. The microbial production of hydrogen sulphide benefits host intestinal health by priming function of the mucosal barrier and protective

immunity at micromolar concentrations, while initiating an inflammatory response at millimolar concentrations (Blachier et al. 2019). Mechanistically, hydrogen sulphide feeds into the mitochondrial electron transfer chain to introduce sulphur residues to ATPase and glycolytic enzymes, stimulating respiration (Bonifacio et al. 2021). Cysteine deprivation has been shown to induce mitochondrial dysfunction and, ultimately, mitochondria-dependent cell death (Gao et al. 2019). Butyrate production and cysteine metabolism illustrate the avenues of communication between microbiota and mitochondria, and the consequences of this communication for coordinated signalling cascades such as host immune responses. A niche has thus emerged for therapeutic strategies targeting microbiota-mitochondria interactions to restore normal mitochondrial function in various disease states (Weber-Stiehl et al. 2022).

#### 5.1.2 Mitochondrial dynamics: A balance of fission and fusion

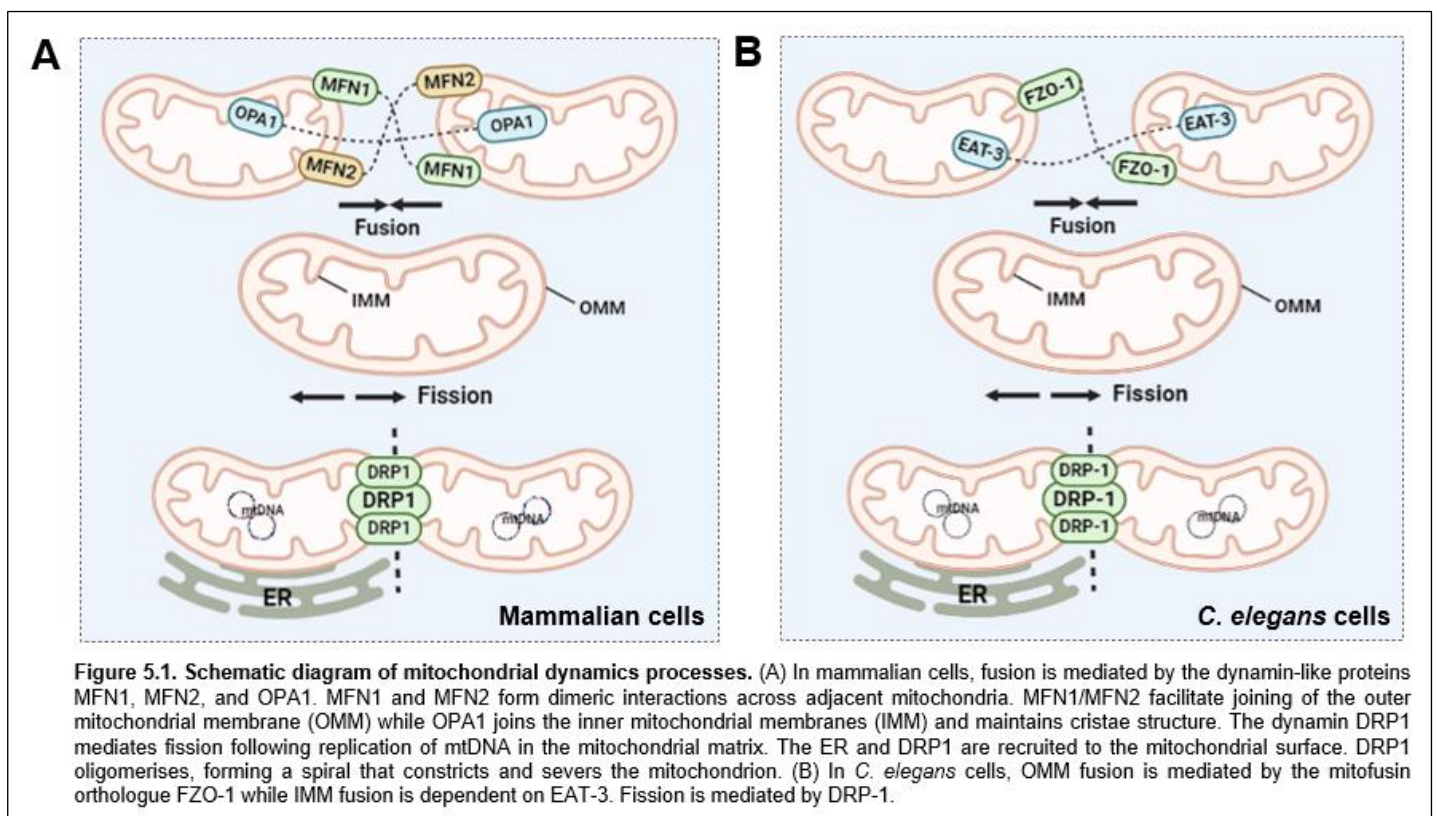
Mitochondria do not solely exist as isolated organelles but can also form highly interconnected networks. They are able to shift dynamically between these two states in response to environmental cues due to the opposing action of fission (one mitochondria separated into two) and fusion (the joining of adjacent mitochondria) forces permanently counterbalancing one another. Inactivating fission leads to the unopposed action of fusion – and vice versa – and the resultant imbalance dictates mitochondrial structure (Scorrano, 2013). Fusion allows damaged mitochondria to mitigate cellular stressors by combining their contents. This allows cellular stressors, such as accumulated mtDNA mutations and oxidised proteins, to be diluted within the cell while also providing a source of functional complementation in the form of shared solutes, metabolites, and proteins (reviewed in Liu et al. 2020; Ono et al. 2001). By contrast, fission aids damaged mitochondria by budding

off dysfunctional components for targeted breakdown via autophagy or mitophagy (Twig et al. 2008; Kim et al. 2007).

Mitochondrial network states are highly plastic and are able to respond not only to cellular stressors but to specific nutrient states. Elongated and hyperfused mitochondria are associated with starvation, presumably due to the increase in bioenergetics efficiency by mitochondrial fusion (Liesa and Shirihai, 2013; Tondera et al. 2009; Rossignol et al. 2004). This allows ATP production to be maintained regardless of nutrient availability (Rambold et al. 2011; Gomes et al. 2011). Fragmented mitochondrial networks, which are associated with increased oxidative stress, mitochondrial depolarisation, and reduced ATP production, tend to be observed in nutrient-rich environments (Jheng et al. 2012). Researchers theorise that the reduction in bioenergetics efficiency may be a protective mechanism against the detrimental effects of nutrient overload (Liesa and Shirihai, 2013).

In mammalian cells, mitochondrial fusion is mediated by three dynamin-like proteins - a subfamily of enzyme that catalyses the hydrolysis of guanosine triphosphate (GTP) – known as mitofusin 1 (MFN1), mitofusin 2 (MFN2), and optic atrophy 1 (OPA1). The mitofusins MFN1 and MFN2 are localised to the outer mitochondrial membrane (OMM) and possess catalytic GTP-binding domains at their N termini. The mitofusins form dimeric interactions across the OMMs of adjacent mitochondria, fusing them together by means of GTP hydrolysis which induces a conformational change that brings the opposing membranes in direct contact (Chandhok et al. 2018) (Figure 5.1A). OPA1 is essential for the fusion of the inner mitochondrial membrane (IMM) as well as maintenance of the internal cristae structure of the organelle (Chan, 2006; Olichon et al. 2003). By contrast, mitochondrial fission is mediated by another member of the dynamin family, DRP1. The process begins with the replication of mtDNA in the mitochondrial matrix, which recruits

the endoplasmic reticulum to specific mitochondria-ER contact sites. DRP1 is then recruited from the cytosol to the mitochondrial surface by a number of mitochondrial-bound proteins, where it begins to oligomerise due to GTP hydrolysis. The oligomerised DRP-1 forms a spiral around the mitochondrion which, along with the recruited ER, constricts and severs the inner and outer mitochondrial membranes (Osellame et al. 2016; Zhu et al. 2004).



There exists a large body of evidence linking aberrant mitochondrial dynamics with ageing-related cellular processes and several human diseases (reviewed in Liu et al. 2020). Charcot-Marie-Tooth Type 2A disease, for example, is caused by a mutation in mitochondrial fusion machinery (Chen et al. 2005; Vance, 2000). The inhibition of mitochondrial fusion prevents mtDNA integrity maintenance and leads to mtDNA

depletion, rendering neurons susceptible to death and causing late-onset peripheral neuropathy. Patients with dominant-negative mutations in fission machinery present fatal clinical abnormalities prenatally including microcephaly and optic atrophy – suggesting that functional mitochondrial fission may play a more crucial role in human health than mitochondrial fusion (Waterham et al. 2007). Abnormal, fragmented mitochondrial networks have also been implicated in human diseases that are not primarily caused by mutations in fusion or fission components. The loss of PTEN-induced kinase (PINK1) in patients with Parkinson's disease, for example, results in excessive mitochondrial fragmentation and the degeneration of dopaminergic neurons (Dagda et al. 2009; Lutz et al. 2009). Blocking the fission process is sufficient to ameliorate neural degeneration and restore striatal dopamine release in a PINK1 deletion mouse model, highlighting the significance of mitochondrial dynamics for PD prognosis (Rappold et al. 2014).

Despite the utility of investigating mitochondrial dynamics in order to improve human disease outcomes, many experiments probing the fundamental mechanisms of fission and fusion have been performed in animal models. As the intercellular signals determining mitochondrial function in mammalian cells are often lost *in vitro*, there is great experimental benefit in the use of whole organisms such as *Drosophila melanogaster* and *Caenorhabditis elegans* (McBride et al. 2006). Moreover, *C. elegans* is an attractive model to investigate mitochondrial dynamics and homeostasis due to the viability of mutants deficient in the fission/fusion proteins – an advantage that does not exist in mammals (Byrne et al. 2019). Mitochondrial fission and fusion processes are highly conserved between mammals and *C. elegans*, with fusion mediated by the OMM-anchored orthologue FZO-1 (in the place of both mitofusins) and the IMM-anchored EAT-3 (in the place of OPA1) (Liu et al. 2020; Kanazawa et al. 2008) (Figure 5.1B). Fission in *C. elegans*

is facilitated by the homonymous DRP-1, which is recruited to the mitochondrial surface by orthologous OMM-bound proteins.

Studies performed in *C. elegans* have greatly advanced the field's understanding of the link between mitochondrial dynamics and various aspects of longevity. Fragmentation of the mitochondrial network driven by fission forces is associated with advanced age in *C. elegans* and reduced respiratory function (Luz et al. 2015; Regmi et al. 2014; Houtkooper et al. 2013; Kanazawa et al. 2008). Although such studies reveal general associations between mitochondrial network states and organismal health, others underscore the inherent complexity these interactions. While severe disruption of mitochondrial dynamics has deleterious consequences, mild perturbations can delay age-related functional decline, demonstrating the concept of mitohormesis – in which a reduced amount of mitochondrial stress serves to improve health outcomes (Houtkooper et al. 2013; Lee et al. 2003).

### 5.1.3 The mitochondrial unfolded protein response (UPR<sup>mt</sup>)

In addition to altering the balance of fission and fusion, mitochondria possess other signalling cascades that facilitate responses to environmental stressors. The maintenance of protein homeostasis, termed 'proteostasis,' is essential to such responses, and involves all cellular pathways facilitating the production, folding, and degradation of proteins. The complex pathways that ensure proteostasis in specific subcellular compartments are referred to as the unfolded protein response (UPR) of that particular site, whether in the endoplasmic reticulum (UPR<sup>er</sup>), cytosol (heat shock response, HSR), or mitochondria (UPR<sup>mt</sup>). While the UPR<sup>er</sup> and HSR have been subjected to extensive study, the UPR<sup>mt</sup> was discovered more recently (reviewed in Jovaisaite et al. 2014; Martinus et al. 1996).

Each of these UPRs is tightly regulated by close communication between the subcellular compartment and the nucleus. In the case of the UPR<sup>mt</sup>, this stringent communication is essential due to the presence of both mtDNA and nuclear DNA. Mitochondrial homeostasis and the overall function of the organelle is therefore dependent on the coordinated transcription of both genomes which, when disrupted, results in protein aggregation associated with various age-related diseases (Couvillion et al. 2016; Wallace and Chalkia, 2013; Kikis et al. 2010). Furthermore, the UPR<sup>mt</sup> differs from those of the endoplasmic reticulum and cytosol as mitochondria are enclosed within a double membrane. While signalling proteins and molecular chaperones are capable of mediating communication between unfolded proteins and the nucleus in the HSR and UPR<sup>er</sup>, the UPR<sup>mt</sup> requires more elaborate targeting machinery to direct effectors to the appropriate mitochondrial loci (Neupert and Hermann, 2007). For example, unfolded precursor proteins are transported across mitochondrial membranes by the translocase of outer membrane (TOM) and translocase of inner membrane (TIM) complexes (Figure 5.1).

The UPR<sup>mt</sup> was first discovered in mammalian cells in response to mtDNA depletion by culture with ethidium bromide; however, most investigations elucidating the molecular mechanism of the UPR<sup>mt</sup> have been performed in *C. elegans* (Haynes et al. 2007; Martinus et al. 1996). During mitochondrial stress, misfolded proteins collect in the mitochondrial matrix where they overload the capacity of the mitochondrial chaperones HSP-6 and HSP-60 (homologues of the mammalian mtHSP70 and HSP-60, respectively) (Figure 5.2). In response, the accumulated proteins are digested by the CLPP-1 proteolytic complex, generating peptides between 6-30 amino acids in length (Haynes et al. 2007). These peptides are transported across the intermembrane space by the HAF-1 transporter, eventually diffusing into the cytoplasm (Haynes et al. 2010). The release of peptides

impairs the import of any effectors into the mitochondria, causing the leucine zipper transcription factor ATFS-1 to be translocated into the nucleus from the cytoplasm. ATFS-1 contains a nuclear localisation sequence (NLS) as well as a mitochondrial targeting sequence (MTS). Under basal conditions, the MTS of ATFS-1 directs its import into the mitochondria where it is degraded by the LON protease; however, in the event of proteotoxic stress, ATFS-1 is forced to translocate into the nucleus where it activates a protective transcriptional programme. Alongside ATFS-1, two additional proteins are translocated into the nucleus in the event of mitochondrial stress: the small ubiquitin-like protein UBL-5 and the homeodomain-containing transcription factor DVE-1 (Haynes et al. 2007; Benedetti et al. 2006). Within the nucleus, coregulators UBL-5 and DVE-1 form a complex that associates with the promoter region of the chaperone-encoding *hsp-60* gene to activate its transcription. Although the precise mechanism of the interaction remains elusive, the UBL-5/DVE-1 complex cooperates with ATFS-1 to drive transcription of UPR<sup>mt</sup>-related genes encoding mitochondrial chaperones and proteases (i.e., *hsp-60*, *hsp-6*, and *clpp-1*), proteins involved in mitochondrial import, and proteins involved in ROS detoxification (Figure 5.2). In addition, a set of glycolysis genes are upregulated by ATFS-1 binding, allowing the UPR<sup>mt</sup> to shift global cell metabolism from respiration to glycolysis (Nagrund et al. 2012). The UPR<sup>mt</sup> is initiated by a number of stressors including the impairment of the electron transport chain, the accumulation of unfolded proteins, alteration of mitochondrial dynamics, inhibition of mitochondrial chaperones and proteases, mtDNA deletions, and an increase in ROS levels (reviewed in Muñoz-Carvajal and Sanhueza, 2020).

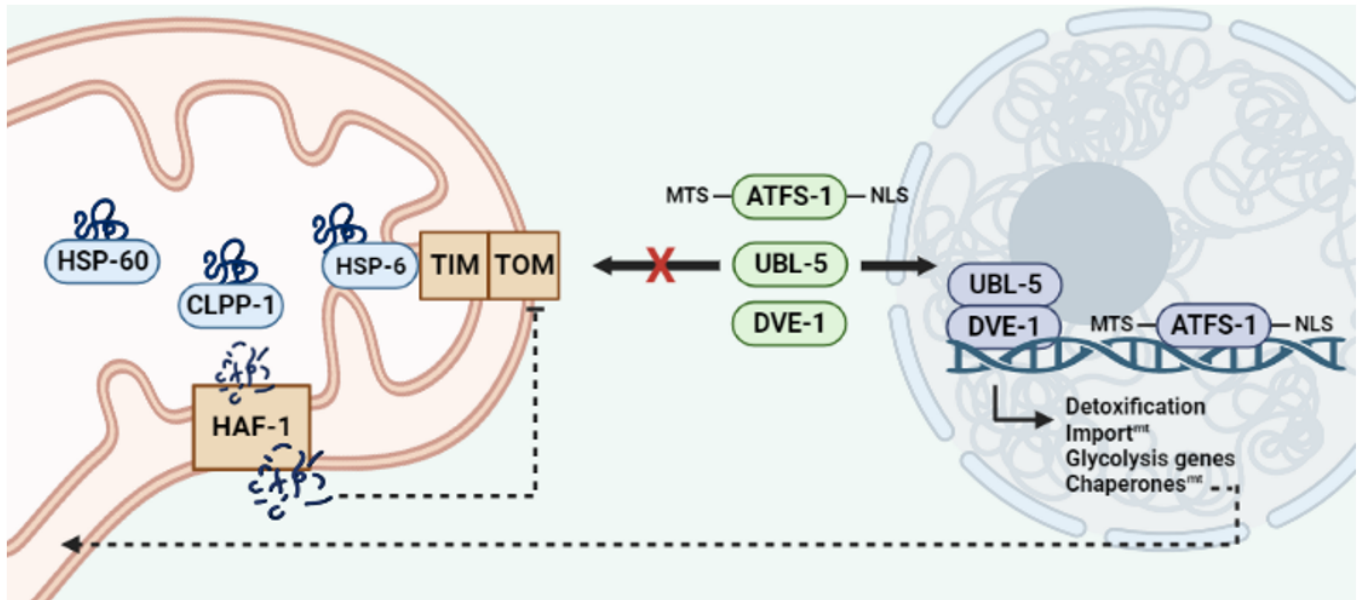


**Figure 5.2. Schematic diagram of the mitochondrial unfolded protein response (UPR<sup>mt</sup>).** (Left, mitochondrial matrix) Misfolded proteins accumulating in the mitochondrial matrix associate with chaperone proteins HSP-6 and HSP-60. When chaperones are overwhelmed, misfolded proteins are digested by CLPP-1 generating short peptides that are transported out of the organelle by HAF-1. (Centre, cytosol) The cytosolic peptides prevent subsequent translocation of proteins into the mitochondria by the TIM and TOM complexes. The transcription factor ATFS-1 possesses an MTS site that confers translocation into the mitochondria under basal conditions. (Right, nucleus) As it also possesses an NLS site, ATFS-1 is forced into the nucleus where – along with the UBL-5/DVE-1 coregulator complex – it drives transcription of UPR<sup>mt</sup>-related genes and activates a protective transcriptional response.

A direct link between mitochondrial dynamics and the UPR<sup>mt</sup> was proposed following studies in *C. elegans*, as loss-of-function mutations in *drp-1*, *eat-3*, and *fzo-1* are sufficient to induce the UPR<sup>mt</sup> (Zhang et al. 2018). Researchers foresee a role for altering the balance of mitochondrial fission and fusion to preserve mitochondrial protein homeostasis throughout age and extend healthspan in ageing animals (Liu et al. 2020).

#### 5.1.4 Mitochondria and ageing in *C. elegans*

A deterioration in mitochondrial function is one of the established hallmarks of ageing, characterised by diminished efficacy of the respiratory chain and reduced ATP generation (Lopez-Otin et al. 2013; Green et al. 2011). The qualities of specific *C. elegans* tissues

make them ideal candidates for studying mitochondrial biology, especially in the context of organismal ageing. The effects of advanced age on mitochondrial health have thus been documented in a range of cell and tissue types. *C. elegans* body wall muscle, for example, differs from that of higher animals as they lack satellite cells (muscle stem cells) and do not undergo muscle regeneration. The body wall muscles of adult nematodes are thus entirely post-mitotic, allowing researchers to utilise mtDNA copy number as a biomarker of mitochondrial function (Castellani et al. 2020; Gieseler et al. 2016). Much of what is known of mitochondrial ageing in the body wall muscle of *C. elegans* has been obtained using transgenic reporter strains expressing fluorescent protein tagged with a mitochondrial import signal (Benedetti et al. 2006). The body wall muscle of young *C. elegans* adults possesses a tubular/linear mitochondrial network that fragments with age, later adopting a globular/spherical morphology with a reduced volume (Regmi et al. 2014). In adult *C. elegans* neurons, mitochondria undergo three distinct phases of increase, maintenance, and decrease in mitochondrial size and density throughout age (Morsci et al. 2016). Early adulthood is characterised by an expansion of the mitochondrial network, evidenced by an increase in mitochondrial area and elongation of the organelle. Following the maintenance of this network state at mid-life, late adulthood is marked by a decline in mitochondrial area and sparse arrangement along the neuronal process. Across a variety of cell types, mitochondrial ageing in *C. elegans* involves restructuring of the network towards an increasingly fragmented morphology, driven by programmatic shifts in fission/fusion (Liu et al. 2020; Morsci et al. 2016; Regmi et al. 2014). Indeed, elevated mitochondrial fusion is associated with lifespan extension, and disruption of fusion causes deficits in muscular and neuronal function (Byrne et al. 2019; Chaudhari and Kipreos, 2017; Houtkooper et al. 2013). However, mitochondrial fusion is not a causative driver of longevity, but is required for the lifespan extension effect seen in diverse longevity pathways (Chaudhari and Kipreos, 2017; Regmi et al. 2014).

### 5.1.5 Investigating experimental microbiome effects on mitochondrial homeostasis

There is a need to understand the relationship between commensal microbes and host mitochondria and elucidate the mechanisms underpinning these interactions with the eventual aim of improving age-related decline. We anticipated a remodelling of mitochondrial networks in nematodes cultivated on the EM versus controls, in response to altered nutrient availability as well as the locomotor differences observed in the preceding chapter. A preservation of motor function in EM-fed animals may require restructuring of the mitochondrial network throughout age to meet altered energetic demands, presumably through initiation of mitochondrial fission and fusion processes. Having established that the EM inhibits age-associated motor decline, we hypothesised that the same may be true for mitochondria: that cultivation on the EM may retard mitochondrial network ageing. The following chapter aims to:

1. Assess the effects of the EM on mitochondrial network states in various cell types
2. Determine whether the EM induces activation of mitochondrial stress pathways
3. Assess whether physiological effects of EM (i.e., on motility) arise via action of mitochondrial signalling pathways
4. Identify molecular mechanisms underlying EM effects on mitochondrial homeostasis

## 5.2 Results

### 5.2.1 Experimental microbiome induces mitochondrial fragmentation in body wall muscle

Taking note of the various motility-related phenotypes induced by the EM but finding no alterations to muscular morphology or function, we redirected our focus to muscular

mitochondria networks. We utilised *zcls14(myo-3::GFP<sup>mit</sup>)*, an integrated transgenic *C. elegans* strain expressing a mitochondrially-localised GFP in body wall muscle (Benedetti et al. 2006; Labrousse et al. 1999). Building off of previous studies characterising mitochondrial morphology in body wall muscle, we devised a qualitative scoring system to classify animals based on the severity of mitochondrial fragmentation throughout adulthood (Figure 5.3A) (Min et al. 2020; Laranjeiro et al. 2019; Regmi et al. 2014). A single body wall muscle cell was imaged per animal, situated approximately halfway between the pharynx and vulva for consistency, and subsequently assigned a discrete numerical score from 0 to 4 (Figure 5.1A). Cells with an assigned score of 0 displayed hyperfusion, in which the majority of the cell is occupied by interconnected networks of mitochondria (Rolland et al. 2009; Tan et al. 2008). Cells with a score of 1 contain tubular mitochondria organised into the linear, parallel tracts associated with early adulthood (Regmi et al. 2014). Scores from 2-4 describe increasing degrees of mitochondrial fragmentation, differentiated by the proportion of the cell devoid of GFP signal. Body wall muscle cells with a score of 4 have severely fragmented mitochondria with a spherical/globular morphology (Figure 5.1A). A chi-square test was used to evaluate differences in mean fragmentation score per condition at each of the timepoints tested. As early as D1 of adulthood, the body wall muscle cells of EM-fed nematodes exhibit a 49% increase in mitochondrial fragmentation score with a mean score of 2.724 ( $\pm 0.156$ ) versus 1.833 ( $\pm 0.209$ ) in OP50-fed controls ( $p = 0.031$ ) (Figure 5.3B). The effect of the EM on mitochondrial morphology is also evident when the data is presented as proportions of each class observed, with a clear skew towards more severe fragmentation classes (Figure 5.3C). Enhanced mitochondrial fragmentation was also observed in EM animals on D4 ( $p = 0.015$ ) and D7 ( $p = 0.005$ ), but not on D11 of adulthood ( $p = 0.062$ ) (Figure 5.3B,C).

A previous study documenting age-related changes in mitochondrial homeostasis in mechanosensory neurons reported phasic patterns of mitochondrial maintenance (Morsci et al. 2016). Between D1 and D4 of adulthood they observed an increase in mitochondrial density as well as elongation, reflected by a greater aspect ratio (major/minor axis). This was followed by maintenance at midlife (D4-D8) and finally a decline in mitochondrial density and decreased aspect ratio (more spherical) from D11 onwards. Although described in another cell type, we saw similar phasic patterns of mitochondrial maintenance in body wall muscle mitochondria. Between D1 and D4, OP50-fed controls display a 21% decrease in mean mitochondrial fragmentation score while a 11% decrease is seen in EM-fed worms, indicating a tendency towards tubular/elongated mitochondrial morphology on D4. However, neither of the reductions in fragmentation score between D1 and D4 were found to be significant ( $p = 0.589$  for OP50,  $p = 0.746$  for EM) (Figure 5.1B). A 64% increase in fragmentation score was then observed from D4 to D11 in OP50-fed controls ( $p = 0.014$ ), in agreement with the altered mitochondrial aspect ratio seen in D11 mechanosensory neurons (Morsci et al. 2016). However, this increase in fragmentation severity from D4 to D11 of adulthood was not observed in EM-fed worms ( $p = 0.252$ ), suggesting a generalised fragmentation effect that outweighs the phasic patterns of mitochondrial homeostasis. This observation, along with the significantly higher fragmentation scores seen in EM-fed nematodes on D1 through D7, suggests that the EM induces alterations in mitochondrial network dynamics, and that the EM might result in mitochondrial stress pathways.

Once we had established an EM-mediated effects on mitochondria using a qualitative scoring paradigm, we determined whether this effect was maintained when the cells were evaluated using non-subjective quantitative analysis. The same epifluorescence images

used to qualitatively score individual body wall muscle cells were processed as previously described using the Mosaic Suite SQUASSH programme (Fiji, ImageJ Software) (Byrne et al. 2019; Rizk et al. 2014). In brief, background fluorescence was removed, objects within the selection – in this case, a single muscle cell – were separated and detected, and object characteristics including area and perimeter were computed (Figure 5.3D). For each muscle cell, a mean circularity value was calculated to describe all individual objects within the selection using the formula  $\text{Circularity} = (4 \times \pi) \times (\text{Area}/\text{Perimeter}^2)$ . Circularity is a two-dimensional measure of sphericity that fits objects to a perfect circle and measures their deviation, in which a measure of 1 describes a perfect circle and a measure of 0, a straight line. Contrary to the results of our qualitative analysis, we found no difference in mean circularity values between EM-fed nematodes and OP50-fed controls on D1 of adulthood ( $p = 0.918$ ). However, on D4 ( $p = 0.008$ ), D7 ( $p = 0.004$ ), and D11 ( $p = 0.009$ ), we observed a significant increase in circularity corroborating our previous findings. EM-cultivated worms displayed a 15% increase in circularity measures on D4, an 18% increase on D7, and a 13% increase on D11 in comparison to OP50-cultivated controls, indicating more spherical and therefore fragmented mitochondria occupying each cell, on average (Figure 5.3D, E). Our results suggest that the EM promotes mitochondrial fragmentation, particularly on D4 and D7 of adulthood, where the increases in mean fragmentation score and circularity values are significant in both data sets describing mitochondrial morphology.

Previous studies have demonstrated associations between mitochondrial fragmentation and increased oxidative stress, mitochondrial depolarisation, and reduced ATP production (Jheng et al. 2012). Moreover, a direct link between mitochondrial dynamics and mitochondrial stress pathways has been suggested as loss-of-function mutations in *drp-1*, *eat-3*, and *fzo-1* resulted in UPR<sup>mt</sup> induction (Zhang et al. 2018). With both qualitative

and quantitative results suggesting elevated mitochondrial fragmentation in EM-cultivated worms, our next series of experiments explored the possibility that the EM induces mitochondria-mediated stress responses.

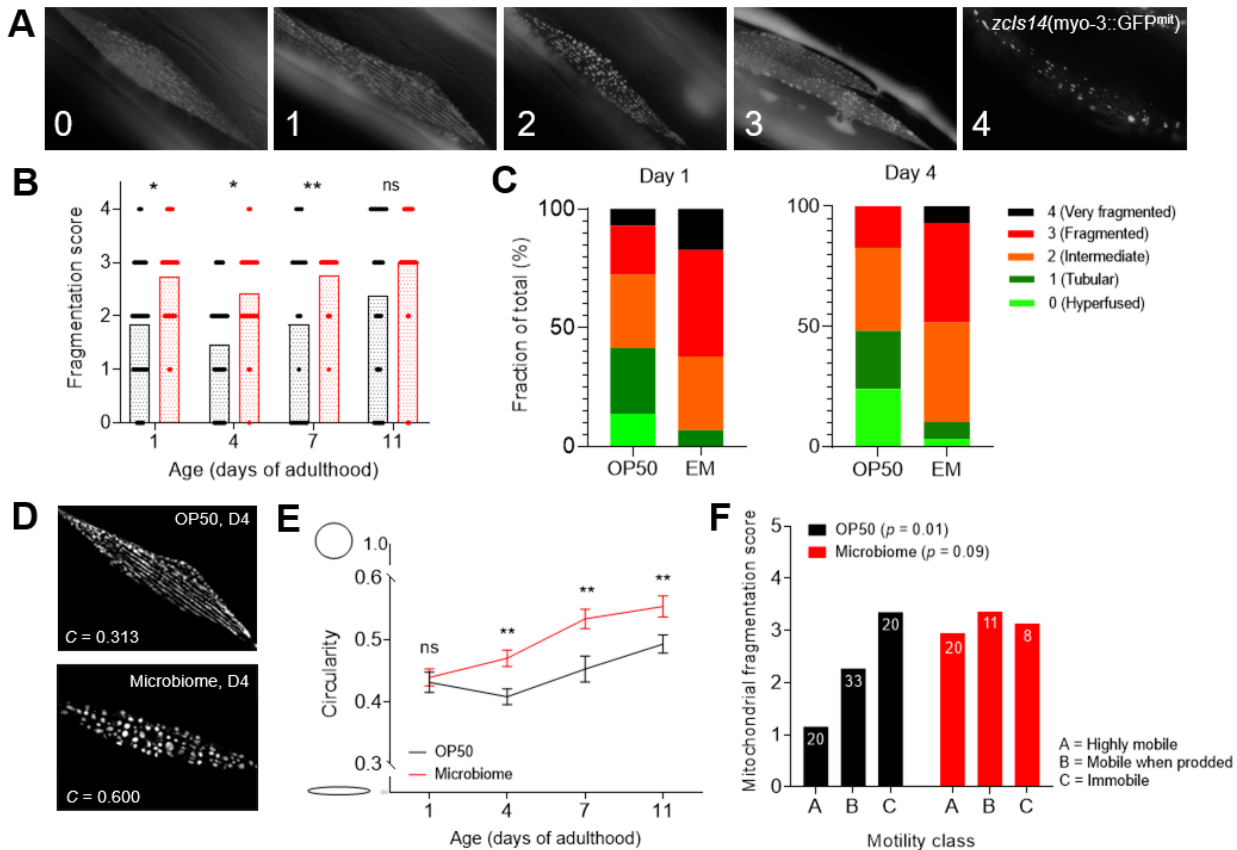


**Figure 5.3. The EM induces mitochondrial fragmentation in body wall muscle.** (A) Representative images of discrete numerical scores describing mitochondrial fragmentation in the sarcomeres of *zcls14(myo-3::GFP<sup>mt</sup>)* animals. 0 = Mitochondria are hyperfused; 1 = Mitochondria are tubular and organised into linear tracts; 2 = Mitochondria are intermediately fragmented, with both tubular and spherical morphologies present; 3 = Mitochondria are fragmented and primarily spherical; 4 = Mitochondria are highly fragmented, with most of sarcomere devoid of GFP signal. (B) EM-fed worms exhibit elevated mitochondrial fragmentation on D1, D4, and D7 of adulthood compared to OP50-fed controls. Statistical analysis by chi-square test (\*\* $p < 0.01$ , \* $p < 0.05$ , ns  $p > 0.05$ ). Data points represent individual fragmentation scores per animal. Bars represent mean fragmentation scores per timepoint across three independent trials ( $n \geq 12$  animals per trial). (C) EM-fed animals are skewed towards fragmented mitochondrial phenotypes. (D) Representative images of individual D4 sarcomeres and their respective mean circularity index ( $C$ ) values as calculated by the SQUASSH plugin (ImageJ Software). (E) EM-fed worms exhibit higher circularity indices on D4, D7, and D11 compared to OP50-fed controls, indicating spherical morphology and elevated mitochondrial fragmentation. Statistical analysis by two-way ANOVA (\*\* $p < 0.01$ , ns  $p > 0.05$ ). Data represent mean circularity values across three independent trials ( $n \geq 12$  animals per trial)  $\pm$  SEM. (F) Increased mitochondrial fragmentation scores are correlated with paralysis in aged OP50-fed worms ( $p = 0.01$ ). This correlation is lost in EM-fed worms ( $p = 0.09$ ), suggesting that measures of mitochondrial dynamics and muscle function are decoupled by EM. Statistical analysis by chi-square test assessing independence of fragmentation score and motility class. Bars represent mean fragmentation scores per motility class with numbers of animals per class indicated within ( $n = 112$  aged animals).

## 5.2.2 Relationship between muscular mitochondrial fragmentation and motility is lost in EM-fed worms

We asked whether mitochondrial morphology could serve as an indicator of fitness and addressed this by gauging a correlation between mitochondrial fragmentation and locomotion in control animals. Motility on solid agar plates was assessed in aged *zcls14(myo-3::GFP<sup>mt</sup>)* nematodes (D11-D16 of adulthood) by classification into motility classes as previously published (Herndon et al. 2002). Once worms were assigned to a motility class, they were mounted for epifluorescence imagery to determine the degree of mitochondrial fragmentation affecting their body wall muscle. OP50-fed controls that fell into motility class A (highly mobile, spontaneous sinusoidal locomotion) exhibited a mean fragmentation score of 1.15 ( $\pm 0.25$ ), those in class B (mobile only when prodded) a mean score of 2.27 ( $\pm 0.20$ ), and controls in class C (immobile even when prodded) a mean score of 3.35 ( $\pm 0.17$ ) (Figure 5.3F). A chi-square test for independence was performed to evaluate the relationship between motility class and mitochondrial fragmentation in OP50-fed controls, which was found to be statistically significant ( $p = 0.01$ ). Our results indicate that under control conditions, elevated mitochondrial fragmentation is correlated with motility decline – an expected relationship as both phenotypes have been reported in advanced age in *C. elegans* (Regmi et al. 2014). In nematodes cultivated on the EM, highly mobile class A worms displayed a mean fragmentation score of 2.95 ( $\pm 0.19$ ), class B a score of 3.36 ( $\pm 0.20$ ), and class C a score of 3.13 ( $\pm 0.52$ ). Contrary to the effect observed in OP50-fed controls, no significant association between motility class and mitochondrial fragmentation was found in EM-fed worms ( $p = 0.09$ ), suggesting that measures of mitochondrial dynamics using the *zcls14(myo-3::GFP<sup>mt</sup>)* reporter and muscular function are decoupled in this condition (Figure 5.3F). We interpreted this to suggest that the body wall muscle mitochondria in EM-cultivated worms may be subject

to basal levels of cellular stress that obscure a normal correlation between mitochondrial network state and locomotor capacity.

### 5.2.3 Experimental microbiome mildly induces mitochondrial fragmentation in mechanosensory neurons

We then asked whether the EM-mediated effects on mitochondrial fragmentation that we had observed in body wall muscle persisted in other cell types. Previous studies have documented non-linear phasic changes in mitochondrial homeostasis in ALM mechanosensory neurons using the transgenic *C. elegans* strain *jsIs609(p<sub>mec-7</sub>::GFP<sup>mt</sup>)*, expressing mitochondrial localisation signal-tagged GFP under the control of the *mec-7* promoter (Morsci et al. 2016; Fatouros et al. 2012) (Figure 5.4A). The gene *mec-7* encodes beta-tubulin and is responsible for generating the protofilament microtubules found in touch receptor neurons (Hamelin et al. 1992). In brief, adult neurons display three distinct stages of increase, maintenance, and decrease in mitochondrial size and density throughout age. From D1-D4, a dramatic increase in mitochondrial load (defined as summed mitochondrial area per 100  $\mu$ M process length) is seen, due to a combinatorial increase in mitochondrial size as well as density (defined as total number of mitochondria per 200  $\mu$ M process length). The increased mitochondrial size is primarily contributed by the elongation of mitochondria, evidenced by an increased aspect ratio (major axis/minor axis). From D4-D8, mitochondrial load, size, and density are maintained. From D11 onwards, however, a progressive decline in mitochondrial load is observed due to the combined effects of reduced size, number, and density.

Adapting the methodology of the study by Morsci et al. (2016), we documented mitochondrial size, shape, density, and overall load in the distal ALM process (extending from nerve ring to tip of nose, schematic in Figure 5.4A, representative image in Figure 5.4B) from D1-D11 of adulthood. We also scored mitochondrial fragmentation in the ALM cell body using a qualitative scoring paradigm (detailed in section 2.3.26 and Figure 5.4C). ALM somata with a score of 0 contain mitochondrial networks organised into a single filamentous loop localised around the perimeter of the soma. In somata with a score of 1, the mitochondrial loop is redistributed horizontally across the centre of the cell body. A score of 3 describes mitochondrial networks that are highly interconnected and redistributed to the polar ends of the soma. A score of 4 describes mitochondria at the poles of the soma that have begun to fragment, while a score of 5 indicates an elevated degree of fragmentation resulting in short, globular mitochondria located across the whole soma (Morsci et al. 2016).

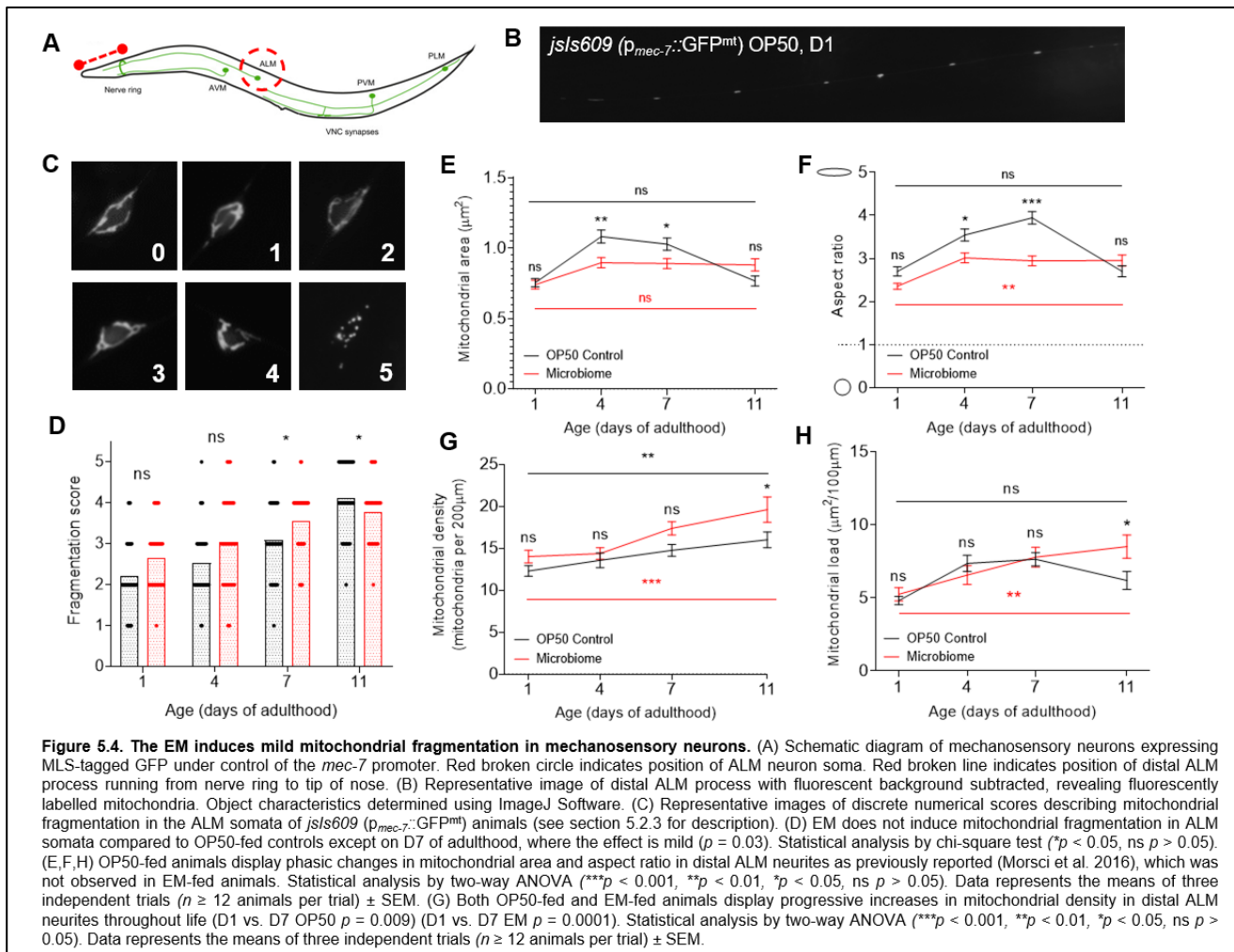
For both feeding conditions, the severity of mitochondrial fragmentation within the ALM soma increased progressively with age, as determined by a chi-square test. In OP50-fed animals, mean fragmentation score increased from 2.20 ( $\pm 0.14$ ) on D1 of adulthood to 4.12 ( $\pm 0.14$ ) on D11 ( $p < 0.0001$ ) (Figure 5.4D). In EM-fed worms, mean fragmentation score increased from 2.66 ( $\pm 0.14$ ) on D1 of adulthood to 3.76 ( $\pm 0.16$ ) on D11 ( $p = 0.001$ ) (Figure 5.4D). When statistical analysis was applied *between* feeding conditions at each time point, no significant differences in mean fragmentation score were observed on D1 ( $p = 0.432$ ) or D4 ( $p = 0.130$ ) of adulthood – opposing the results obtained when fragmentation was assessed in body wall muscle mitochondria. On D7 of adulthood, consistent with our observations in muscle, the EM was found to induce fragmentation of mitochondria in the ALM soma – though the reported effect was mild (15% greater than

OP50 control,  $p = 0.032$ ). On D11 of adulthood, a mildly reduced fragmentation score was observed in EM-fed worms (8% lower than OP50 control,  $p = 0.029$ ).

When we evaluated the various aspects of mitochondrial homeostasis covered by the Morsci et al. (2016) study in the mitochondria of distal ALM processes, we saw phasic changes that mirrored what was previously reported – particularly in mitochondrial size, shape, and load – in our OP50 controls (Figure 5.4E,F,H). From D1 to D4 of adulthood, mitochondrial size increased from  $0.76 \mu\text{m}^2 (\pm 0.03)$  to  $1.08 \mu\text{m}^2 (\pm 0.05)$  ( $p < 0.0001$ ) (Figure 5.4E). This was maintained through to D7 of adulthood ( $p = 0.768$ ), but followed by a significant decrease in area to  $0.77 \mu\text{m}^2 (\pm 0.04)$ ,  $p < 0.0001$  on D11. Similarly, mitochondrial aspect ratio (shape) in OP50-fed controls displayed a characteristic increase from D1 to D4 of adulthood of  $2.70 (\pm 0.11)$  to  $3.55 (\pm 0.14)$ , indicating an increasingly linear morphology ( $p = 0.0001$ ) (Figure 5.4F). Aspect ratio was maintained in controls from D4 to D7 ( $p = 0.112$ ), followed by a decrease to  $2.71 (\pm 0.13)$  on D11, indicating greater sphericity. Lastly, mitochondrial load exhibited the same phasic patterns of mitochondrial homeostasis in OP50-fed controls, increasing from  $4.81 \mu\text{m}^2/100 \mu\text{m}$  ( $\pm 0.29$ ) on D1 to  $7.35 \mu\text{m}^2/100 \mu\text{m}$  ( $\pm 0.55$ ) on D4 of adulthood ( $p = 0.0097$ ) (Figure 5.4H). Mitochondrial load was maintained through to D7 ( $p = 0.985$ ) followed by a decrease to  $6.178 \mu\text{m}^2/100 \mu\text{m}$  ( $\pm 0.29$ ) on D11. Only mitochondrial density, the total number of mitochondria per defined neurite length, did not adhere to the phasic patterns of increases and decreases reported previously. Instead, mitochondrial density in OP50-fed controls was found to progressively increase across the timepoints tested, from  $12.28$  mitochondria/ $200 \mu\text{m}$  ( $\pm 0.64$ ) on D1 to  $16.00$  mitochondria/ $200 \mu\text{m}$  ( $\pm 0.95$ ) on D11 of adulthood ( $p = 0.009$ ) (Figure 5.4G). Note that the ranges reported for each of these measurements are consistent with those reported in Morsci et al. (2016).

By contrast, *js/s609(p<sub>mec-7</sub>::GFP<sup>mt</sup>)* worms cultivated on the EM did not display phasic patterns of mitochondrial maintenance in the distal ALM process as previously described for any of the parameters assessed. EM-fed nematodes displayed a slight increase in mitochondrial area between D1 and D4 of adulthood, from 0.74  $\mu\text{m}^2$  ( $\pm 0.03$ ) to 0.90  $\mu\text{m}^2$  ( $\pm 0.04$ ) ( $p = 0.036$ ). This was maintained up until D11 of adulthood ( $p = 0.992$ ), with no characteristic decrease in mitochondrial area seen from D7 to D11 (Figure 5.4E). On both D4 ( $p = 0.006$ ) and D7 ( $p = 0.025$ ) of adulthood, EM-fed worms exhibited reduced mitochondrial size in the distal ALM process compared to OP50-fed controls, suggesting elevated fragmentation that is consistent from mid- to late-adulthood. This observation was supported by mitochondrial shape (aspect ratio) measurements in EM-fed worms, which were also found to be significantly lower (indicating greater sphericity) than controls on D4 ( $p = 0.017$ ) and D7 ( $p < 0.0001$ ) of adulthood. Just as we observed for mitochondrial size, EM-fed worms exhibited an increased mitochondrial aspect ratio from 2.36 ( $\pm 0.07$ ) on D1 to 3.015 ( $\pm 0.11$ ) on D4 ( $p = 0.002$ ) which was maintained up to D11 ( $p > 0.999$ ). No characteristic decrease from D7 to D11 was observed, resulting in an overall progressive increase in mitochondrial aspect ratio from D1 to D11 of adulthood ( $p = 0.0069$ ) (Figure 5.4F). Mitochondrial load in the distal ALM process of EM-fed animals followed the same pattern, progressively increasing from 5.24 mitochondria/200  $\mu\text{M}$  ( $\pm 0.46$ ) on D1 to 8.50 mitochondria/200  $\mu\text{M}$  ( $\pm 0.80$ ) on D11 of adulthood ( $p = 0.001$ ). Finally, as was observed in OP50-fed controls, mitochondrial density in the distal ALM processes of EM-fed animals does not follow the phasic pattern of maintenance but instead increases significantly from 14.02 mitochondria/200  $\mu\text{M}$  ( $\pm 0.76$ ) on D1 to 19.61 mitochondria/200  $\mu\text{M}$  ( $\pm 1.51$ ) on D11 of adulthood (Figure 5.4G). No significant differences in mitochondrial density were observed between feeding conditions on D1 ( $p = 0.480$ ), D4 ( $p = 0.948$ ), and D7 ( $p = 0.107$ ) of adulthood, with only a slightly elevated density in EM-fed worms on D11 ( $p = 0.019$ ).

The data obtained on mitochondria in the distal ALM process suggests a scenario in which the EM places mitochondria under stress, obscuring the phasic patterns of maintenance associated with normal ageing. Although the effects of the EM on mitochondrial homeostasis in mechanosensory neurons generally support our observations in body wall muscle, the effects are of reduced severity – perhaps highlighting the importance of proximity of the target cells to the intestinal microbiota.

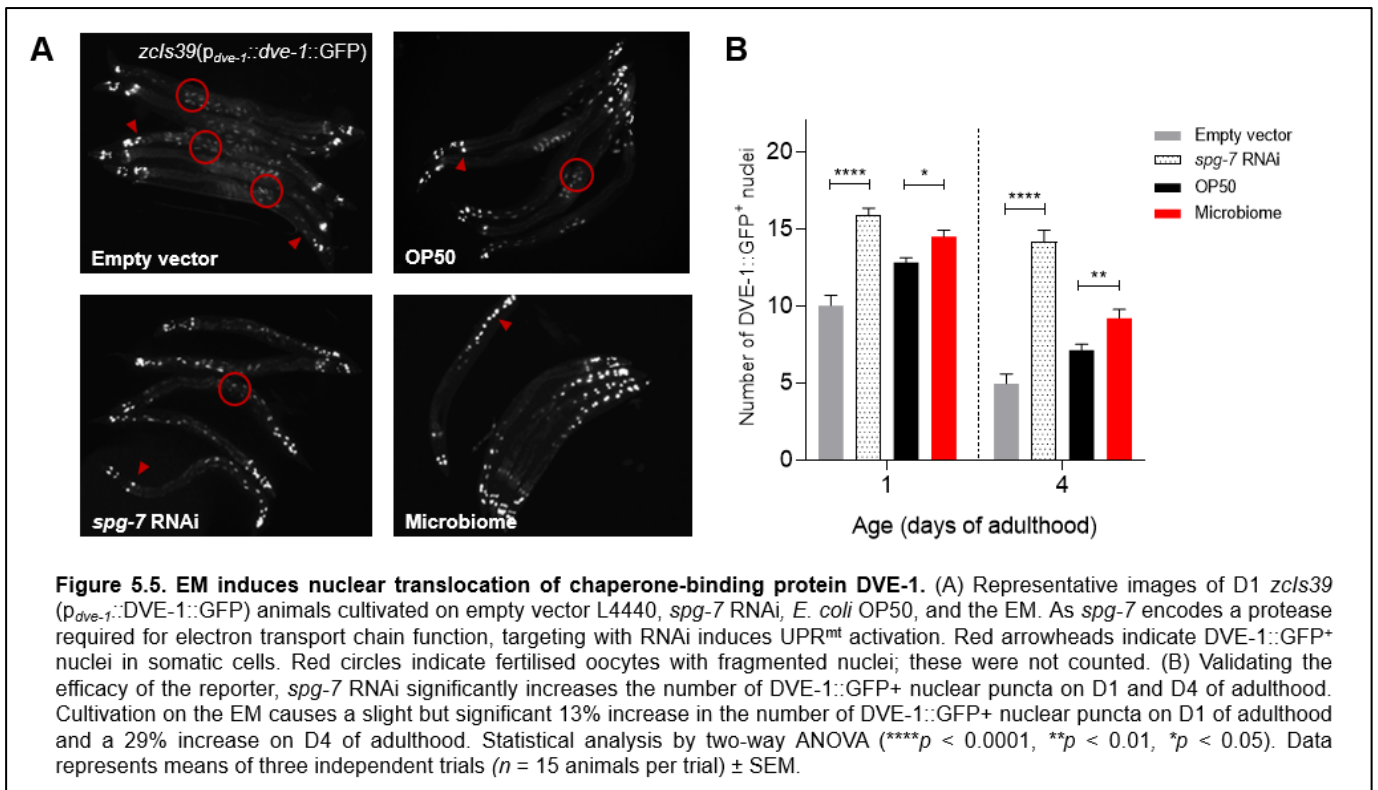


#### 5.2.4 Experimental microbiome induces nuclear localisation of DVE-1, a chaperone-binding protein involved in UPR<sup>mt</sup>

To evaluate whether the EM induces activation of the UPR<sup>mt</sup> in comparison to OP50-fed controls, thereby indicating a state of proteotoxic stress in the mitochondria, we utilised a fluorescent reporter of DVE-1 nuclear localisation. DVE-1 is a homeodomain-containing transcription factor that serves as a coregulator of the small ubiquitin-like protein UBL-5 (Haynes et al. 2007; Benedetti et al. 2006). Upon mitochondrial stress, cytosolic UBL-5 and DVE-1 form a complex that is translocated into the nucleus, cooperating with translocated ATFS-1 to activate transcription of stress response genes (Figure 5.1). The transgenic *C. elegans* strain *zcls39(p<sub>dve-1</sub>::DVE-1::GFP)* expresses GFP-tagged DVE-1 under the control of the *dve-1* promoter, providing a fluorescent readout of the transcription factor's subcellular location. The number of DVE-1::GFP<sup>+</sup> nuclei counted within the boundaries of each nematode body was thus used as a proxy for UPR<sup>mt</sup> induction (sample images provided in Figure 5.5A).

We first tested the efficacy of the reporter strain by comparing additional control conditions. RNAi against *spg-7*, encoding a mitochondrial protease required for electron transport chain quality control and mitochondrial ribosome biogenesis, was used as a positive control to induce the UPR<sup>mt</sup> (Nargund et al. 2012; Nolden et al. 2005). Indeed, we observed a 59% increase ( $p < 0.0001$ ) in the number of DVE::GFP<sup>+</sup> nuclear puncta in worms subjected to *spg-7* RNAi treatment compared to those cultivated on the standard empty vector L4440 on D1 of adulthood, with a mean of 16 puncta ( $\pm 2$ ) versus 10 ( $\pm 4$ ), respectively (Figure 5.4B). This effect was maintained at D4 of adulthood, where a dramatic 186% increase in DVE::GFP<sup>+</sup> nuclei was seen ( $p < 0.0001$ ) in *spg-7* RNAi

animals possessing a mean of 14 ( $\pm 4$ ) GFP<sup>+</sup> puncta compared to 5 ( $\pm 3$ ) in empty vector controls (data collected past D4 not shown). Confident in the utility of the fluorescent reporter strain up to D4 of adulthood, we compared nuclear puncta in EM-fed versus OP50-fed animals. EM-fed animals displayed a mild but significant 13% ( $p = 0.035$ ) increase in DVE-1::GFP<sup>+</sup> nuclei on D1 of adulthood, with a mean of 15 puncta ( $\pm 3$ ) compared to 9 ( $\pm 4$ ). This effect was more pronounced on D4, with a 29% increase in DVE-1::GFP<sup>+</sup> puncta in EM-fed worms than OP50-fed controls ( $p = 0.006$ ), with means of 9 puncta ( $\pm 4$ ) versus 7 ( $\pm 3$ ), respectively (Figure 5.5B). We conclude that the EM mildly induces translocation of DVE-1 into the nucleus on D1 and D4 of adulthood, suggesting mild induction of the UPR<sup>mt</sup> in early-/mid-life.



### 5.2.5 Experimental microbiome does not induce expression of *ubl-5*, encoding a ubiquitin-like protein involved in UPR<sup>mt</sup>

Given that translocated DVE-1 and UBL-5 operate as a complex when inducing transcription of UPR<sup>mt</sup> genes, we expected that the elevated nuclear localisation of DVE-1 by the EM would be mirrored in a reporter of *ubl-5* activity. We utilised the transgenic strain *zcls19(p<sub>ubl-5</sub>::ubl-5::GFP)* expressing GFP under the control of the *ubl-5* promoter and measured mean relative fluorescence within the boundaries of the worm body (representative images in Figure 5.6A) (Benedetti et al. 2006). Once again, *spg-7* RNAi was used to induce the UPR<sup>mt</sup> and served as a positive control condition. The relative fluorescence displayed by *spg-7* RNAi worms on D1 of adulthood was 22% higher than those of empty vector L4440 controls ( $p = 0.006$ ), validating the efficacy of the reporter (Figure 5.6B). Contrary to what we had expected based on the increased nuclear localisation of DVE-1, the EM was found to reduce GFP fluorescence by 18% compared to OP50-fed controls on D1 ( $p = 0.008$ ). On D4 of adulthood, no significant difference in relative fluorescence was observed between worms cultivated on the EM and worms cultivated on OP50 ( $p > 0.999$ ) – however, as *spg-7* RNAi was unable to elicit elevated *ubl-5* expression at this timepoint, it is difficult to draw a conclusion on the effect of the EM on UPR<sup>mt</sup> induction at D4. It is possible that the utility of the *zcls19(p<sub>ubl-5</sub>::ubl-5::GFP)* reporter is lost with advancing age and that alterations in whole-body fluorescence in this strain are undetectable in mid-/late-life.

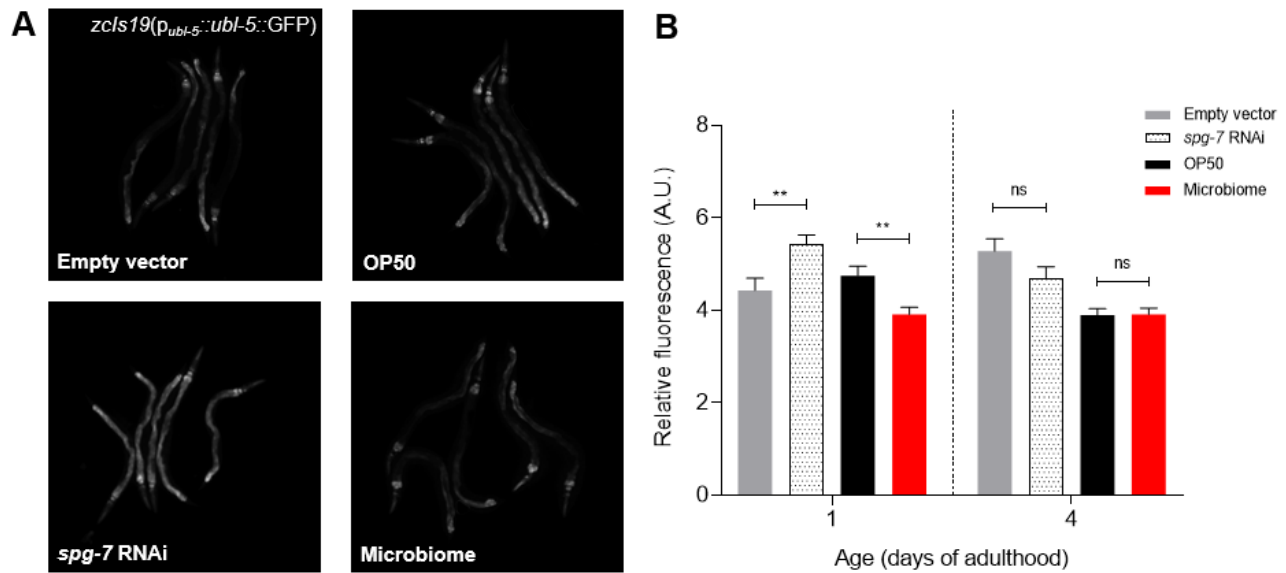


**Figure 5.6. EM does not induce expression of ubiquitin-like protein gene *ubl-5*.** (A) Representative images of D1 *zcls19(p<sub>ubl-5</sub>::ubl-5::GFP)* animals cultivated on empty vector L4440, *spg-7 RNAi*, *E. coli* OP50, and the EM. As *spg-7* encodes a protease required for electron transport chain function, targeting with RNAi induces UPR<sup>mt</sup> activation. (B) Validating the efficacy of the reporter in early-life, *spg-7 RNAi* increases *ubl-5::GFP* fluorescence on D1 of adulthood. However, as this effect was not observed on D4, no conclusions can be drawn past D1. Cultivation on the EM reduces *ubl-5::GFP* fluorescence by 18% on D1 of adulthood compared to OP50 controls. Statistical analysis by two-way ANOVA (\*\* $p < 0.01$ , ns  $p > 0.05$ ). Data represents the mean of three independent trials ( $n \geq 10$  animals per trial)  $\pm$  SEM.

### 5.2.6 Experimental microbiome effect on age-associated motility decline requires genes involved in UPR<sup>mt</sup>

Without a definitive conclusion on whether the EM induces the signalling cascade comprising the UPR<sup>mt</sup>, we decided on a different approach to address this question. We explored whether the protective effects of the EM on late-life motility decline (see section 4.2.1) required the expression of genes involved in the UPR<sup>mt</sup>, thereby linking the two phenotypes and providing a potential molecular mechanism for the EM's protective effect on motility.

We performed the lateral swimming (thrashing) assay using a set of mutants within the UPR<sup>mt</sup> cascade (Figure 5.7A). Each independent trial performed included four conditions: wildtype nematodes cultivated on OP50/EM and UPR<sup>mt</sup> mutants cultivated on OP50/EM. We screened animals possessing loss-/reduction-/gain-of-function mutations in *hsp-6*, *ubl-5*, and the transcription factor *atfs-1*. Nematodes possessing a viable reduction-of-function mutation in *hsp-6*, encoding a chaperone that binds to misfolded mitochondrial proteins, exhibit slow growth and a dramatically reduced thrashing rate compared to wildtype worms (Figure 5.7B, above) (Mao et al. 2019). We noted that the reduced fitness of this strain may confound any conclusions drawn on the involvement of *hsp-6* in the EM's protective effect on motility. However, we observed that the thrashing rates of *hsp-6* mutants cultivated on the EM were indiscernible from those cultivated on OP50 on D1 ( $p = 0.455$ ) and D4 ( $p = 0.547$ ) of adulthood. In addition, neither OP50-fed nor EM-fed *hsp-6* mutants exhibited an age-associated decline in motility between D1 and D7 ( $p = 0.865$ ,  $p = 0.052$ , respectively), suggesting the involvement of *hsp-6* expression in preserving motility regardless of feeding condition (Figure 5.7B). Motility in *ubl-5* null mutants was found to decline in a similar fashion in both OP50-fed and EM-fed animals between D1 and D7, falling to 81% ( $p = 0.003$ ) and 60% ( $p < 0.0001$ ) of their D1 values, respectively (Figure 5.7C). The loss of the protective effect of the EM in *ubl-5* mutants suggests that expression of the ubiquitin-like co-regulator is required for the phenotype. Loss-of-function mutants of the transcription factor-encoding gene *atfs-1* reared on OP50 exhibited a comparable decline in thrashing rate as OP50-fed wildtype worms ( $p = 0.182$ ), decreasing to 73% ( $p < 0.0001$ ) and 60% ( $p < 0.0001$ ) of their D1 thrashing rate by D7, respectively (Figure 5.7D). *atfs-1* loss-of-function mutants do not exhibit the characteristic increase in thrashing rate on D4 of adulthood seen in wildtypes; on D4, EM-fed *atfs-1* mutants decline to 75% of their D1 thrashing rate, comparable to OP50-fed mutants at the same timepoint ( $p = 0.862$ ). However, motility in EM-fed *atfs-1* mutants is recovered by D7 as evidenced

by an overall maintenance of thrashing rate from early to mid/late-adulthood ( $p = 0.261$ ) (Figure 5.7D). Taken together, this suggests some requirement for *atfs-1* expression in the protective effect of the EM against motility decline up to mid-adulthood, but that a compensatory mechanism recovers motility decline by D7. To further probe the contribution of *atfs-1* expression to the EM's effect on motility, we repeated the lateral swimming assay using a *C. elegans* strain possessing a gain-of-function mutation in *atfs-1*. These animals contain point mutations within the first six amino acids of ATFS-1 – specifically within the protein's MTS – resulting in persistent nuclear translocation of ATFS-1 and constitutive activation of the UPR<sup>mt</sup> (Rauthan et al. 2013). In gain-of-function *atfs-1* mutants with primed UPR<sup>mt</sup> induction, the protective effect of the EM was abrogated, with the thrashing rates of EM-fed mutants falling to 60% of D1 values by D7 of adulthood ( $p < 0.0001$ ) (Figure 5.7E). This result suggests that stringent control over *atfs-1* activity contributes more to the protective effect of the EM than its mere expression.

Altogether, the results of the lateral swimming (thrashing) assays in *hsp-6*, *ubl-5*, and *atfs-1* mutant worms suggest a more significant requirement for the upstream components of the UPR<sup>mt</sup> pathway rather than the downstream components – mirroring our findings in mutants of the PMK pathway of innate immunity (see Section 4.2.7).

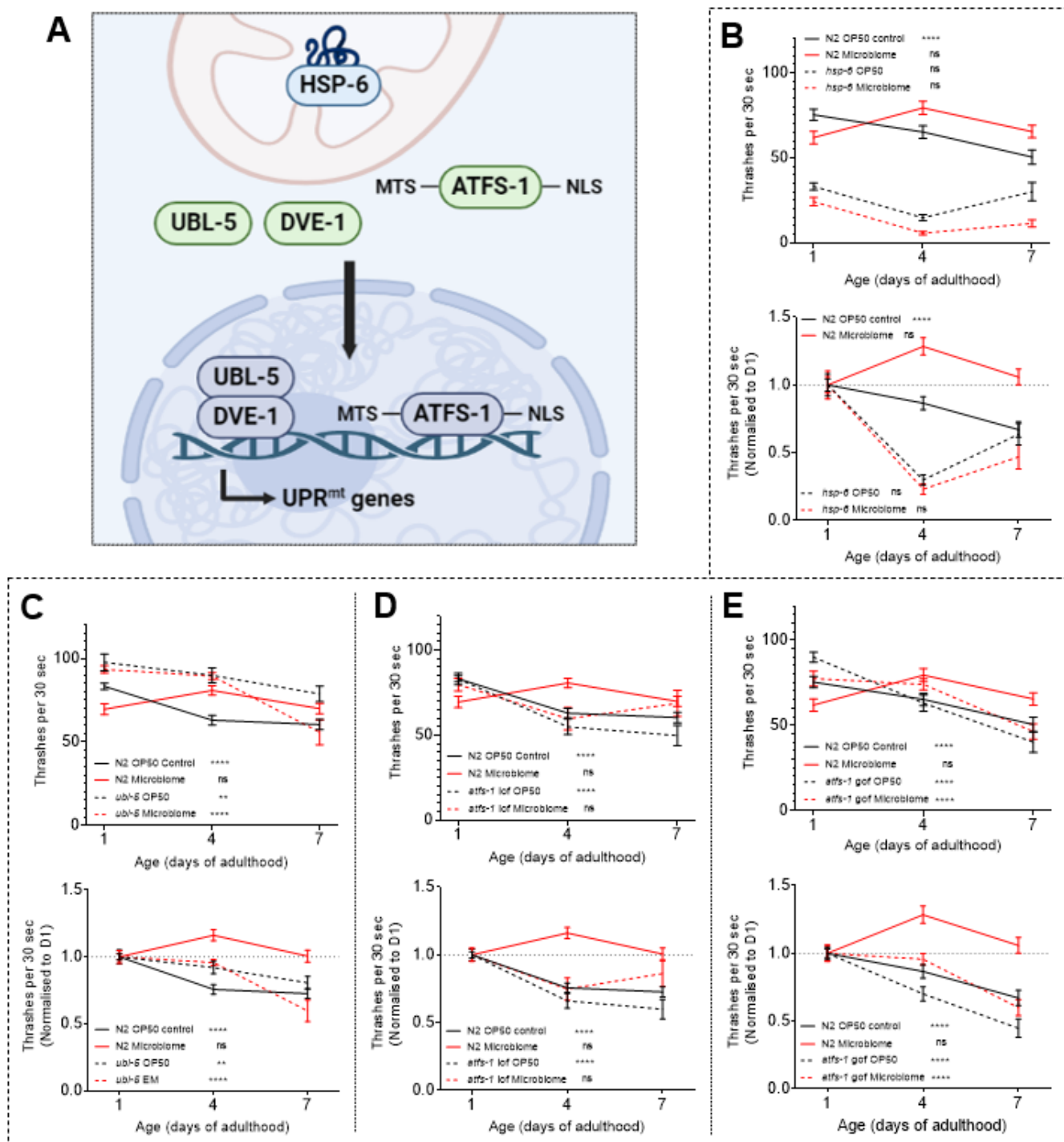


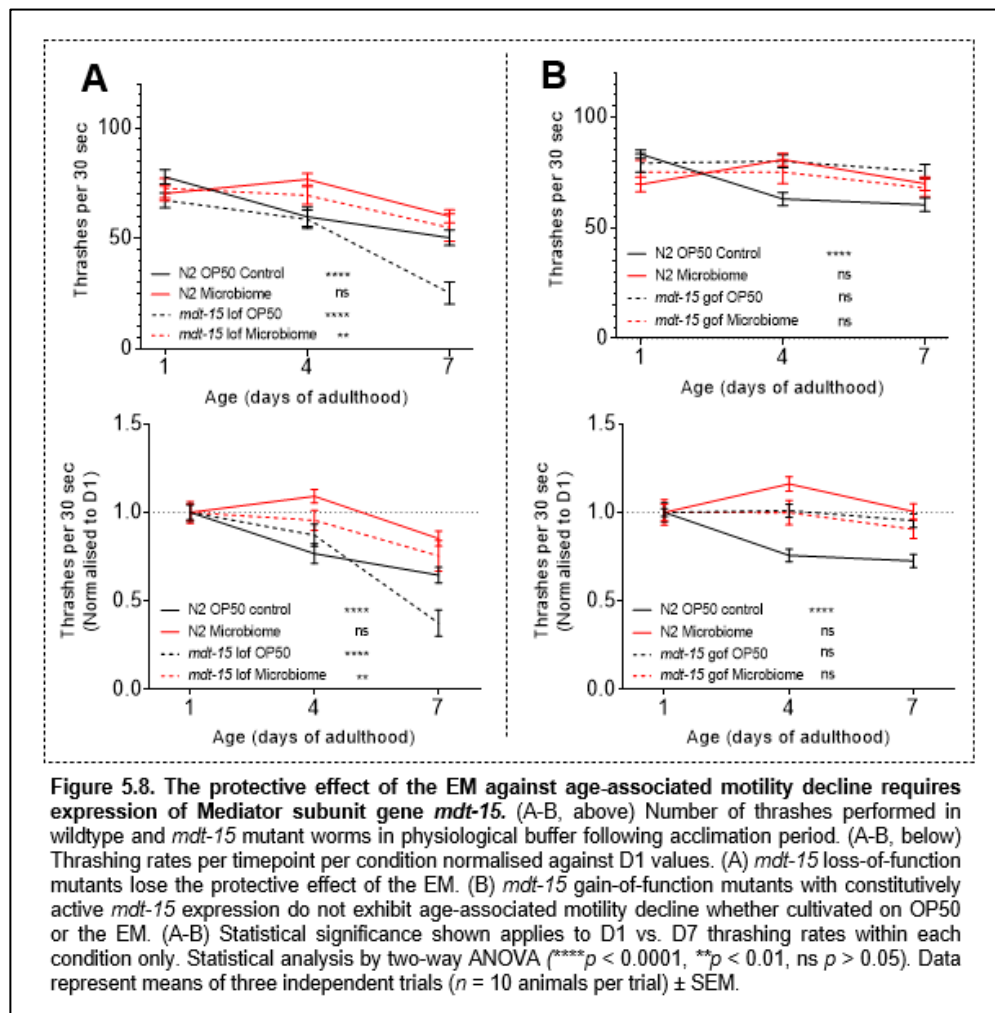
**Figure 5.7. Protective effect of EM against age-associated motility decline requires expression of UPR<sup>mt</sup> genes.** (A) Simplified schematic of the UPR<sup>mt</sup> highlighting mutants used in panels B-E. Misfolded proteins bind to chaperone HSP-6. During mitochondrial stress, UBL-5 and DVE-1 are translocated into nucleus, forming a complex that drives the expression of UPR<sup>mt</sup> genes along with translocated transcription factor ATFS-1. (B-E, above) Number of thrashes performed in physiological buffer following acclimation period. (B-E, below) Thrashing rates per timepoint per condition normalised against D1 values. (B) Mutants deficient in *hsp-6* expression did not exhibit a decline in thrashing rate between D1 and D7 regardless of feeding condition (OP50  $\rho = 0.87$ , EM  $\rho = 0.05$ ). Note that the reduced fitness of these mutants confounds any conclusions. (C) Mutants deficient in *ubl-5* expression lose the protective effect of the EM against motility decline at D7. (D) The protective effect of the EM is maintained in loss-of-function *atfs-1* mutants. (E) Thrashing rates of EM-fed gain-of-function *atfs-1* mutants decline from D1 to D7, suggesting that a fine balance of *atfs-1* expression is necessary for the EM effect on motility decline. (B-E) Statistical analysis by two-way ANOVA (\*\*\*\* $p < 0.0001$ , \*\*\* $p < 0.001$ , \*\* $p < 0.01$ , \* $p > 0.01$ , ns  $p > 0.05$ ). Statistical significance applies to D1 vs. D7 thrashing rates within each condition only. Data represent means of three independent trials ( $n = 10$  animals per trial)  $\pm$  SEM.

### 5.2.7 Experimental microbiome effect on age-associated motility requires expression of Mediator subunit gene *mdt-15*

We sought to expand our search for mitochondria-associated genes contributing to the EM's protective effect on late-life motility. A previous genetic screen in *C. elegans* for mutations constitutively activating the UPR<sup>mt</sup> identified *mdt-15*, encoding the Mediator component MDT-15. MDT-15 is a subunit of the evolutionarily conserved Mediator complex which is required for the oxidative stress response in nematodes. MDT-15 acts as a transcription factor from the upstream mitochondrial surveillance system to coordinate downstream detoxification responses (Mao et al. 2019; Goh et al. 2014). Noting the involvement of UPR<sup>mt</sup> components (see Section 5.2.6) in generating the motility phenotype seen in EM-fed nematodes, we performed the lateral swimming (thrashing) assay in two mutant strains for *mdt-15*. The protective effect of the EM against motility decline was lost in a loss-of-function *mdt-15* deletion mutant cultivated on the EM (Figure 5.8A). By D7 of adulthood, thrashing rate within this experimental condition declined to 75% of the D1 value ( $p = 0.009$ ), indicating a role for *mdt-15* expression in conserving motility via the EM.

We then repeated the assay using a gain-of-function mutant in which *mdt-15* is constitutively active (Mao et al. 2019). We observed that the difference in thrashing rate between OP50-fed and EM-fed conditions was lost at each of the tested timepoints (D1  $p = 0.886$ , D4  $p = 0.814$ , D7  $p = 0.526$ ) (Figure 5.8B). However, rather than both mutant conditions exhibiting significant decline in motility with advanced age as we had seen in other data sets, neither OP50-fed ( $p = 0.786$ ) nor EM-fed ( $p = 0.401$ ) gain-of-function *mdt-15* mutants exhibit any age-associated decline in thrashing rate between D1 and D7 of adulthood. This result indicates that constitutive *mdt-15* expression is sufficient to preserve

*C. elegans* motility in late-life regardless of the food course on which worms are cultivated. A previous study demonstrated that in response to bacterial pathogens, MDT-15 activates the transcription of mitochondrial detoxification and immune response genes (Mao et al. 2019). Broad protection against motility decline by overexpression of *mdt-15* highlights a potential mechanism by which EM-mediated protection may occur: by initiating a *mdt-15*-dependent detoxification programme in reaction to mitochondrial insult i.e., the presence of xenobiotic toxins.

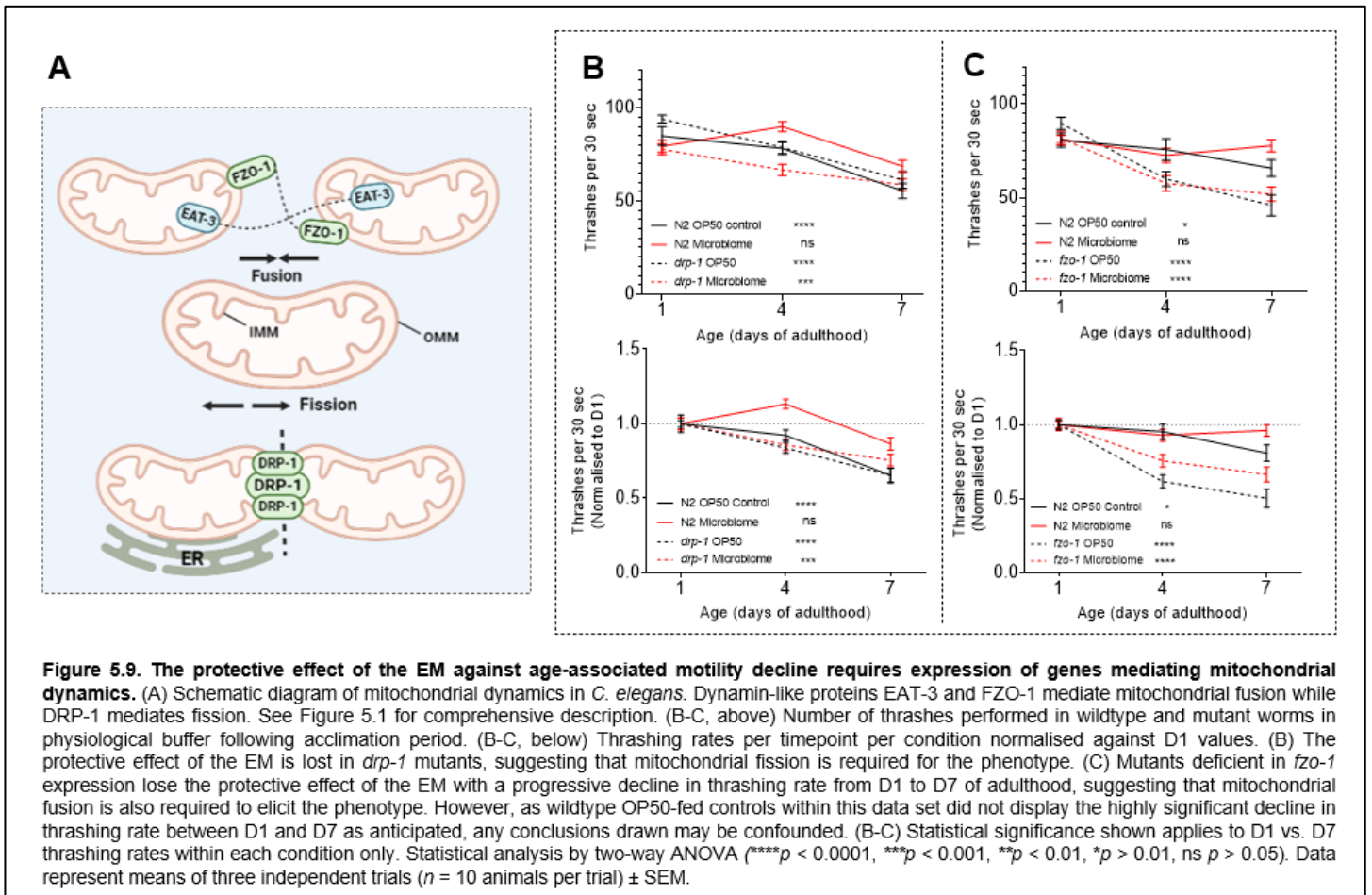


### 5.2.8 Experimental microbiome effect on age-associated motility decline requires genes mediating mitochondrial dynamics

Previous studies in *C. elegans* reported that deficiencies/losses in fusion proteins result in mitochondrial fragmentation (Ichishita et al. 2008; Kanazawa et al. 2008). The elevated fragmentation observed in the body wall muscle of EM-fed animals therefore implies a deficiency in the function of fusion proteins in this cell type. Noting this possibility, we asked whether mitochondrial dynamics genes were required for the EM's protective effect on locomotion in late life, thereby addressing whether the two main phenotypes of interest exhibited by EM-cultivated nematodes were linked.

Once more, we performed a set of lateral swimming (thrashing) assays using null mutants in mitochondrial dynamin genes: *drp-1*, encoding the fission-mediating protein DRP-1, and *fzo-1*, encoding the fusion-mediating FZO-1 (Breckenridge et al. 2008) (Figure 5.9A). Like wildtypes, *drp-1* mutants cultivated on OP50 exhibit age-associated motility decline, falling to 50% of their D1 thrashing rate by D7 of adulthood ( $p < 0.0001$ ) (Figure 5.9B). The protective effect of the EM against age-associated motility decline was lost in *drp-1* mutants, as we observed a 34% decline in thrashing rate from D1 to D7 ( $p = 0.0002$ ), suggesting that the phenotype requires mitochondrial fission to persist. Similarly, *fzo-1* null mutants deficient in mitochondrial fusion exhibited an age-associated motility decline not typically seen in the EM-fed condition, falling to 66% of their D1 thrashing rate on D7 ( $p < 0.0001$ ) and declining to a similar ( $p = 0.751$ ) extent as OP50-fed *fzo-1* mutants at the same timepoint (50% of D1 values) (Figure 5.9C). Although this suggests the involvement of *fzo-1* expression and mitochondrial fusion in EM-mediated protection against motility decline, note that wildtype OP50-fed controls within this data set did not display the dramatic decline in thrashing rate between D1 and D7 as anticipated – confounding

conclusions on the role of *fzo-1* – although the decline was yet significant ( $p = 0.02$ ). We hereby conclude that the protective effect of the EM requires the action of genes mediating mitochondrial dynamics, and that both fission and fusion processes are critical to this phenotype.



## 5.2.9 Experimental microbiome effect on mitochondrial fragmentation does not require *pmk-1* expression

Once we had observed that the EM's effect on *C. elegans* motility required mitochondrial fission and fusion processes, we next examined whether the inverse was true. Specifically, we asked whether the activity of the PMK pathway, which we had observed to be required for the EM effect on motility (see section 4.2.7), was also required to induce fragmentation of muscular mitochondria. We performed a genetic cross between *zcls(p<sub>myo-3</sub>::GFP<sup>mt</sup>)* animals with fluorescently labelled body wall muscle mitochondria and null mutants for *pmk-1*, encoding a kinase that phosphorylates the transcription factor ATF-7 to drive transcription of PMK immune response genes (Figure 4.5). The generated animals were cultivated on OP50 and the EM along with uncrossed *zcls(p<sub>myo-3</sub>::GFP<sup>mt</sup>)* animals as controls. The severity of muscular mitochondrial fragmentation – both qualitative and quantitative – was compared across feeding conditions as well as genotypes.

Comparing uncrossed *zcls(p<sub>myo-3</sub>::GFP<sup>mt</sup>)* worms, we observed a 49% increase in mitochondrial fragmentation score in those cultivated on the EM on D4 of adulthood compared to OP50-fed controls, consistent with our previous findings ( $p < 0.0001$ ) (see section 5.2.1). This was corroborated by circularity measures collected from the imaged sarcomeres, with a 20% increase in circularity in D4 EM-fed worms ( $p < 0.0001$ ). However, we did not observe the expected increase in fragmentation score on D1 ( $p = 0.981$ ) or in score *and* circularity on D7 (score  $p = 0.264$ , circularity  $p = 0.087$ ) and this must be considered when drawing conclusions within the associated data set (Figure 5.10A, Figure 5.10E).

Crossed animals possessing both a fluorescent mitochondrial reporter and a *pmk-1* deletion allele also showed elevated fragmentation on D4 of adulthood, with a 21% increase in fragmentation score ( $p = 0.027$ ) and a 14% increase in circularity ( $p = 0.002$ ) compared to OP50-fed controls (Figure 5.10B, Figure 5.10F). Circularity was also found to be elevated by 12% on D1 of adulthood in EM-fed crossed worms ( $p = 0.031$ ). When compared *within* feeding conditions, no significant differences were found in fragmentation score nor circularity between uncrossed and crossed genotypes ( $p > 0.05$ ) at each of the four timepoints tested (Figure 5.10C-D, Figure 5.10G-H). These results suggest that *pmk-1* expression is not required for the EM's effect on mitochondrial dynamics, as fragmentation persists in the absence of a functional *pmk-1* allele. However, as the magnitude of EM-induced fragmentation was greater in uncrossed *zcls(p<sub>myo-3</sub>::GFP<sup>mt</sup>)* D4 adults than the crossed genotype for both score (49% increase versus 21%,  $p < 0.0001$  versus  $p = 0.027$ , respectively) and circularity (20% increase versus 14%,  $p < 0.0001$  versus  $p = 0.002$ , respectively) we cannot discount the partial involvement of *pmk-1* and the PMK pathway in the alteration of mitochondrial dynamics by the EM.

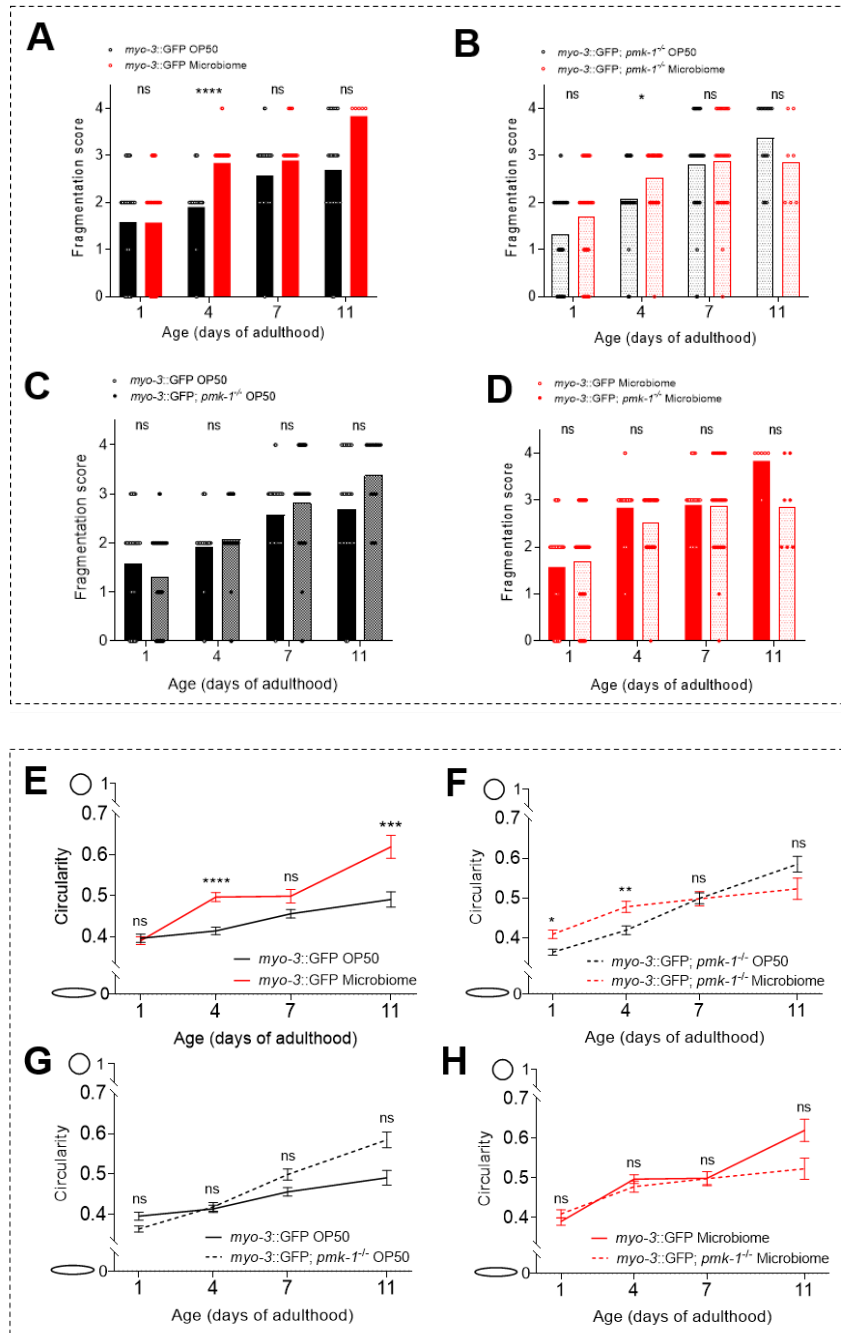


**Figure 5.10. The EM effect on mitochondrial dynamics in body wall muscle does not require *pmk-1* expression.** (A) Mean fragmentation scores in *zcls* ( $p_{myo-3}::GFP^{mt}$ ) worms cultivated on OP50 or the EM. EM elevates mitochondrial fragmentation on D4 of adulthood. (B) Mean fragmentation scores in *zcls* ( $p_{myo-3}::GFP^{mt}$ ) worms containing a *pmk-1* deletion cultivated on OP50 or the EM. The EM effect on mitochondrial fragmentation is maintained on D4 of adulthood, suggesting that the EM effect on mitochondrial dynamics does not require *pmk-1* expression. However, as EM-induced fragmentation is mild in crossed worms, partial involvement of *pmk-1* cannot be ruled out. (C) No difference in mean fragmentation score was detected between genotypes cultivated on OP50 at each of the timepoints tested. (D) No difference in mean fragmentation score was detected between genotypes cultivated on the EM at each of the timepoints tested. (A-D) Statistical analysis by chi-square test (\*\*\*\* $p < 0.0001$ , \*\* $p > 0.01$ , ns  $p > 0.05$ ). Data represents means of three independent trials ( $n = 12$  animals per trial). (E) Mean mitochondrial circularity in *zcls* ( $p_{myo-3}::GFP^{mt}$ ) worms cultivated on OP50 or the EM. EM elevates circularity on D4 of adulthood, indicating fragmented mitochondria. (F) Mean mitochondrial circularity in *zcls* ( $p_{myo-3}::GFP^{mt}$ ) worms containing a *pmk-1* deletion cultivated on OP50 or the EM. The EM mildly increases circularity on D1 and D4 of adulthood. (G) No difference in mean mitochondrial circularity was detected between genotypes cultivated on OP50 at each of the timepoints tested. (H) No difference in mean mitochondrial circularity was detected between genotypes cultivated on the EM at each of the timepoints tested. (E-H) Statistical analysis by two-way ANOVA (\*\*\*\* $p < 0.0001$ , \*\*\* $p < 0.001$ , \*\* $p < 0.01$ , \* $p > 0.01$ , ns  $p > 0.05$ ). Data represent means of three independent trials ( $n = 12$  animals per trial)  $\pm$  SEM.

## 5.3 Discussion

### 5.3.1 The experimental microbiome alters mitochondrial homeostasis

Mitochondrial ageing has been well documented in a variety of *C. elegans* tissue types and cellular conditions (Liu et al. 2020; Morsci et al. 2016; Regmi et al. 2014), but what is currently lacking is a profile of mitochondrial health in response to members of *C. elegans*' native microbiota (Dirksen et al. 2020; Yang et al. 2019). With a growing body of evidence linking the microbiome and signalling cascades in host mitochondria, there is obvious benefit in leveraging the nematode's tractability to expand the range of mitochondria-targeting interventions shown to improve ageing outcomes in other organisms (Weber-Stiehl et al. 2022).

We showed that cultivation on the EM induced mitochondrial fragmentation in body wall muscle, shifting the morphology of the mitochondrial network towards sparse, globular punctae typically associated with advanced age, oxidative stress, and even physical wounding (Fu et al. 2020; Regmi et al. 2014; Kanazawa et al. 2008). Mitochondrial fragmentation in EM-fed animals, which was first described qualitatively with the use of a scoring paradigm, was later verified by measuring mean circularity of discrete objects (i.e., mitochondria) within a defined region of interest (i.e., single sarcomere). This method was developed as a non-subjective means of quantifying mitochondrial morphology in *C. elegans* muscle and neuronal cells (Rizk et al. 2014) and reported higher circularity values following mitochondrial fission (Byrne et al. 2019).

Although both qualitative and quantitative data sets showed elevated mitochondrial fragmentation in EM-fed worms in mid-adulthood, fragmentation in early adulthood was

not reflected in our circularity measurements. It is likely that the object segmentation protocol developed by Rizk et al. (2014) is unsuitable for conditions where objects within the selection are merged, such as the 'hyperfused' mitochondrial phenotype. As this morphology is typically displayed in the muscle of young adult worms (Rolland et al. 2009; Tan et al. 2008), D1 circularity values may not be representative of the true mitochondrial network states of young adult worms. Another limitation of this study is that both fragmentation scores and circularity measurements were obtained from epifluorescence micrographs lacking depth information. Some sarcomeres exhibited multiple mitochondrial morphology scores within one cell depending on the depth of focus, while a single worm would often exhibit multiple scores depending on the location of the sarcomere within the body plan, consistent with previous studies showing differential rates of cellular deterioration across the worm (Bansal et al. 2015; Glenn et al. 2004; Herndon et al. 2002). We attempted to mitigate this by consistently imaging sarcomeres located midway between the pharynx and vulva. Confocal microscopy, utilising optical sectioning, would have generated a more accurate depiction of mitochondrial morphology via 3D reconstructions of whole sarcomeres and is worth utilising going forward. In ALM mechanosensory neurons, where epifluorescence microscopy was sufficient to capture mitochondrial properties, *OP50*-fed controls exhibited phasic patterns of mitochondrial homeostasis consistent with previous studies (Morsci et al. 2016). In early adulthood, mitochondrial load, area, and aspect ratio increase within the distal ALM process suggesting mitochondrial elongation. These metrics are maintained in mid-life followed by a decline in late-adulthood suggesting mitochondrial fragmentation. Unlike in body wall muscle where the incidence of mitochondrial fragmentation progressively increases with age (Regmi et al. 2014), mitochondrial load, area, and aspect ratio return to D1 levels by D11 of adulthood in the distal ALM neurite of *OP50*-fed controls. By contrast, *EM*-fed animals do not exhibit phasic patterns of mitochondrial homeostasis. Mitochondrial area

and aspect ratio are maintained from mid-adulthood onwards in EM-fed worms while mitochondrial density and load increase, suggesting that the ageing ALM neurite is progressively packed with small, spherical mitochondria – consistent with the occurrence of fragmentation. We interpreted this to show that cultivation on the EM overrides phasic patterns of normal mitochondrial homeostasis. In the ALM soma, the EM mildly induced mitochondrial fragmentation in mid-adulthood only. The reduced severity of this phenotype may suggest that neurons are less susceptible to EM-induced mitochondrial fragmentation than body wall muscle. Whether this variation is due to the proximity of body wall muscle to the intestine where EM microbiota proliferate or to tissue-specific physical characteristics (Byrne et al. 2019) is unknown. Neurons face exceptionally high energetic demands (Sheng, 2018) and may thus exhibit greater resistance to mitochondrial network remodelling in comparison to muscle cells.

### 5.3.2 Mitochondrial dynamics genes are required for experimental microbiome effects on locomotion

The effects of the EM on late-life motility shown in the preceding chapter appear to be dependent on genes mediating mitochondrial dynamics. Protection from locomotor decline was lost in EM-fed mutant worms lacking the fission protein-encoding *drp-1* and the fusion protein-encoding *fzo-1*. Even OP50-fed *fzo-1* mutants exhibited a greater decline in thrashing than OP50-fed wildtype controls, emphasising the critical role of mitochondrial fusion in late-life motility. Taken with the mitochondrial fragmentation shown in body wall muscle, these findings suggest a potential mechanism for the EM's effects on locomotion that does not involve alterations to muscular structure or function. Indeed, other EM-induced phenotypes are consistent with previous studies reporting the effects of disrupted mitochondrial dynamics. Mutations in the fusion protein-encoding gene *eat-3* have been

shown to reduce brood size (Kanazawa et al. 2008) – an effect that we also observe in EM-fed wildtype animals. There exist several mechanistic explanations for this effect, including inhibition of mitotic division by mutations in mitochondrial proteins through the actions of AMP kinase and cyclin E (Mandal et al. 2005) and reduced yolk availability due to the animal's altered metabolic state. The data suggests a potential link between mitochondrial dynamics and fecundity in EM-fed worms that merits further investigation.

What are the implications of altered mitochondrial homeostasis observed in EM-reared worms? The fragmentation phenotypes observed in body wall muscle and mechanosensory neurons, although associated with age, may not necessarily be indicative of accelerated ageing in EM-reared worms. Different mitochondrial network states correspond to specific nutrient states. Fragmented mitochondria are observed in nutrient-rich conditions while starvation is accompanied by mitochondrial elongation/hyperfusion to increase respiration efficiency (Liese and Shirihai, 2013; Jheng et al. 2012; Tondera et al. 2009; Rossignol et al. 2004). The mitochondrial state of EM-fed worms supports our previous claim that the EM is not an inferior food source compared to *E. coli* OP50 and does not induce signalling cascades associated with starvation. However, noting that mitochondrial fragmentation has also been documented following cellular damage and proteotoxic stress (Twig et al. 2008; Kim et al. 2007), we explored whether cultivation on the EM initiates mitochondrial stress-response signalling cascades.

### 5.3.3 Mitochondrial stress response genes are required for experimental microbiome effects on locomotion

Previous studies have shown that loss-of-function mutations in the mitochondrial dynamics-mediating genes *drp-1*, *eat-3*, *fzo-1* are sufficient to induce activation of the UPR<sup>mt</sup> (Zhang et al. 2018). Noting EM-induced changes in mitochondrial dynamics, we observed elevated nuclear localisation of the UPR<sup>mt</sup> transcription factor DVE-1 in EM-fed worms. Although this finding suggests that the EM induces activation of the UPR<sup>mt</sup> in early adulthood, this was contradicted by a reduction in *ubl-5::GFP* expression. As DVE-1 and UBL-5 function as a complex to drive UPR<sup>mt</sup> gene transcription, we anticipated parallel, rather than opposing, changes in expression. It is worth considering that expression of these coregulators was evaluated with different approaches: DVE-1::GFP<sup>+</sup> nuclei numbers and whole-worm relative fluorescence. Counting UBL-5::GFP<sup>+</sup> nuclei numbers, concurrently employing a DNA strain to delineate nuclei and circumvent the diffuse fluorescent *ubl-5* signal (Benedetti et al. 2006), may have been a more appropriate method of assessing *ubl-5* expression in the worm.

Further evidence of UPR<sup>mt</sup> activation by the EM was provided by the finding that UPR<sup>mt</sup> genes are required for EM-mediated protection against locomotor decline. Thrashing rates in EM-fed null mutants for the coregulator-encoding *ubl-5* gene declined with age indicating its involvement in the phenotype. Due to the unavailability of a mutant deficient in *dve-1* transcription, we were unable to determine if the same was true for UBL-5's associated coregulator. EM-mediated effects on thrashing rate were lost in *atfs-1* loss-of-function mutants on D4 but recovered by D7, perhaps in indication of a compensatory mechanism. Our findings suggest that the transcription of UPR<sup>mt</sup> components and, in turn, UPR<sup>mt</sup>-related genes underlie EM effects on locomotion – but that this dependence is

more complex than simple initiation of the transcriptional cascade. The loss of the locomotor effect in *atfs-1* gain-of-function mutants implies that expression of UPR<sup>mt</sup>-related genes must be tightly regulated in order to derive protection from the EM.

Our data provides another potential mechanism for the EM's effect on motility in addition to genes regulating mitochondrial dynamics, bolstering the hypothesis that mitochondrial signalling cascades underlie this effect. However, in the preceding chapter, we also established the PMK pathway of innate immunity as a vital contributor to the EM's effect on locomotion. We considered that these domains may be connected to one another, noting evidence linking mitochondria and innate immune activation (Chikka et al. 2016; West et al. 2011). Researchers hypothesise that mitochondria were incorporated into the innate immune pathway to facilitate the metabolic reprogramming required for its activation. Moreover, many intracellular pathogens directly modulate mitochondrial programmed cell death responses to benefit their survival and replication. Transgenic animals containing fluorescently-labelled body wall muscle mitochondria were crossed into a *pmk-1* null mutant background. When reared on the EM, crossed animals display the same degree of muscular mitochondrial fragmentation as their uncrossed counterparts, suggesting that EM-induced mitochondrial fragmentation is not dependent on *pmk-1* expression. Thus, the data undermines innate immune activation as a potential link between microbiota and altered mitochondrial dynamics. It should be noted, however, that *pmk-1* null mutants were selected for this cross due to their availability at the time of experimental design. We later determined that the loss of upstream components of the PMK pathway had more significant effects on locomotor decline than the downstream *pmk-1* – which may serve to explain the reduced degree of mitochondrial fragmentation in *pmk-1* mutants that was not entirely abrogated. A genetic cross using *tir-1* or *nsy-1* null

mutants would have been more definitive in establishing a role for the PMK pathway in EM-induced mitochondrial fragmentation. Alternatively, quantitative metrics of mitochondrial health – i.e., mtDNA copy number or ATP production – can be measured in wildtype worms versus PMK pathway mutants both reared on the EM to determine if any EM-induced effects are abrogated by the loss of PMK components.

Another significant finding of this chapter was the requirement of functional *mdt-15* expression, and presumably the subsequent MDT-15-mediated detoxification programme, for the EM effect on locomotor decline. This corroborates our transcriptomic data in which gene sets mediating detoxification were found to be upregulated by the EM. Interestingly, OP50-fed gain-of-function mutants with constitutively active *mdt-15* expression were completely protected from locomotor decline even without rearing on the EM. Hyperactivation of the mitochondrial oxidative stress surveillance system seems to mimic the effects of the EM on late-life motility, suggesting that the EM's effects on *C. elegans* physiology may function by initiating a detoxification programme in mitochondria triggered by the presence of external symbionts (Mao et al. 2019).

Overall, the findings outlined in this chapter provide evidence of communication between commensal microbes and host mitochondria through various pathways. However, the identification of additional mechanisms by which the EM exerts effects on *C. elegans* locomotion raises more questions. So far, the PMK pathway of innate immunity and various mitochondrial signalling cascades - including altered mitochondrial dynamics, the UPR<sup>mt</sup>, and detoxification responses - all contribute to the protective effect of the EM on *C. elegans* motility. Further investigation is required to understand if and how these

programmes are linked. Evidence indicating UPR<sup>mt</sup> activation in response to the EM is limited to DVE-1 nuclear localisation and *ubl-5* expression. Future work should examine expression of fluorescent reporters for mitochondrial chaperone-encoding *hsp-6* and *hsp-60* as readouts of EM-mediated UPR<sup>mt</sup> activation. The oxidative phosphorylation inhibitor antimycin A can serve as a positive control within this experiment (Bar-Ziv et al. 2020).

EM activation of cellular stress response pathways other than those localised to mitochondria should also be considered. Fluorescent transcriptional reporters are available for essential genes within these pathways. The UPR<sup>er</sup> is activated in response to misfolded protein accumulation in the endoplasmic reticulum (ER) and relies on the chaperone protein HSP-4. ER stress can thus be measured via *hsp-4p::GFP* transcription, using the N-linked glycosylation blocker tunicamycin as a positive control. By contrast, the heat-shock response (HSR) is activated following protein misfolding in the cytosol. Transcriptional reporters for the downstream targets of the master HSR regulator, HSF-1, have been synthesised, including *hsp-16.2p::GFP* and *hsp-70p::GFP*. A two-hour 34°C heat-shock serves as an appropriate positive control, robustly inducing transcription of HSR targets. For each of these strains, stress response activation can be assessed by microscopy or measured by large-particle flow cytometry (Bar-Ziv et al. 2020).

After measuring changes in fluorescence, the range of mutant strains utilised in the lateral swimming assay can be expanded to determine which cellular stress pathways are required for EM effects on motility. *hsp-60* null mutants were not included in our initial assessment. Considering the results obtained in other UPR<sup>mt</sup> null mutants (*hsp-6*, *ubl-5*, and *atfs-1*), we hypothesise that *hsp-60* expression will also be required for EM-mediated

protection from motor decline. Null mutants for *hsp-4* and *hsp-16.2* are available to assess the requirement of UPR<sup>er</sup> and HSR pathways in EM effects on motility, respectively (unfortunately, there is no available *hsp-70* mutant; *hsp-70* is typically targeted with RNAi which is incompatible with EM rearing). In addition, an interaction between the EM and these stress response pathways can be explored by measuring tolerance of organelle-specific stressors (i.e. paraquat for UPR<sup>mt</sup>, tunicamycin for UPR<sup>er</sup>, two-hour heat-shock for HSR) in EM-fed versus OP50-fed nematodes.

In chapter 4, we determined that the PMK pathway of innate immunity was required for EM-mediated protection from motility decline. However, we have not yet quantified PMK pathway activation following EM cultivation. To do so, we can utilise a transgenic fluorescent reporter strain showcasing expression of *C. elegans* open reading frame T24B8.5, a transcriptional target of the PMK pathway (Shivers et al. 2009). The innate immune response induces other cytoprotective pathways, including autophagy: a sequestration process that enables enzymatic degradation and recycling of cytosolic components. In *C. elegans*, the key transcriptional regulator HLH-30 modulates the expression of multiple autophagy-related and lysosomal genes (Lapierre et al. 2013). Experiments characterising autophagy activation in EM-fed animals versus OP50-fed controls are currently underway, using nuclear localisation of GFP-tagged HLH-30 as a readout. Lateral swimming assays featuring *hlh-30* null mutants are also in progress to determine whether autophagy contributes to EM effects on motility.

## 6. Experimental microbiome (EM) effects on amyloid beta (A $\beta$ )-associated toxicity

### 6.1 Introduction

#### 6.1.1 The microbiome and proteotoxic disease

Proteotoxicity – the impairment of cellular function due to protein misfolding and aggregation – is a major hallmark of ageing that has been extensively characterised (López-Otín et al. 2013). Some of the most devastating age-associated diseases are proteinopathic in nature. Parkinson’s disease (PD) affects 6.1 million individuals globally as of 2018 (Dorsey et al. 2018) and is a neurodegenerative disease involving the progressive loss of dopaminergic neurons resulting in motor and non-motor symptoms (Goya et al. 2019). The pathological hallmark of PD is the aggregation of alpha-synuclein ( $\alpha$  synuclein) proteins in filamentous assemblies known as Lewy bodies (Spillantini et al. 1997).  $\alpha$  synuclein acquires a neurotoxic character as these assemblies increase in size and form insoluble fibrils, with the magnitude of aggregation correlating with severity of PD symptoms (Stefanis, 2012). Although PD progression is localised to the central nervous system, a growing body of evidence suggests that pathological  $\alpha$ -synuclein accumulation begins in the gut (Rietdijk et al. 2017; Cersosimo and Bennaroch, 2012; Poewe, 2008; Braak, 2003). In a mouse model of PD overexpressing human  $\alpha$ -synuclein, motor deficits, neuroinflammation, and  $\alpha$ -synuclein inclusions were eliminated following depletion of gut bacteria with antibiotics, suggesting that microbiota are required to promote  $\alpha$ -synuclein-mediated pathophysiology (Sampson et al. 2016). The authors determined that administering bacterial metabolites, specifically the SCFAs butyrate, acetate, and propionate, to PD mice devoid of gut bacteria was sufficient to recapitulate disease features. In a *C. elegans* model of PD expressing  $\alpha$ -synuclein in muscle cells, a

probiotic strain of *Bacillus subtilis* was found to inhibit aggregation via the sphingolipid metabolism pathway (Goya et al. 2019). Unexpectedly, a *B. subtilis* feeding paradigm promoted clearance of existing  $\alpha$ -synuclein aggregates, most likely by activation of the lysosomal autophagy pathway, one of the main systems of  $\alpha$ -synuclein clearance in cells (Poewe et al. 2017; Levine and Kromer, 2008). Taken together, these findings demonstrate the microbiota's influence in PD pathophysiology as well as the therapeutic potential of microbiota-targeting interventions.

Alzheimer's disease (AD) is another progressive neurodegenerative disorder predominantly found in individuals above the age of 65 and affecting one in every six people over the age of 80 (National Health Service UK, 2021). Behaviourally, AD is characterised by a decline in cognition and memory, but its main pathological hallmark is the deposition of the amyloid beta ( $A\beta$ ) peptide in the form of neurotoxic senile plaques.  $A\beta$  peptides are derived from proteolytic cleavage of the transmembrane amyloid precursor protein (APP) first by the  $\alpha$ - or  $\beta$ -secretase enzymes, then finally by  $\gamma$ -secretase. In a healthy physiological state, APP is cleaved by  $\alpha$ -secretase, assigning the protein to a non-amyloidogenic cleavage pathway (Yan and Zhang, 2020). However, initial cleavage of APP by  $\beta$ -secretase enables the generation of  $\beta$ -pleated sheet amyloid structures measuring 40-42 amino acids in length. It is the hydrophobic 42-amino acid isoform,  $A\beta_{1-42}$ , that forms the central core of senile plaques (Zhao et al. 2015). Intraneuronal neurofibrillary tangles are another pathologic feature of AD, caused by hyperphosphorylation and polymerisation of the microtubule-associated protein, tau.

Though the specific agent initiating protein misfolding in AD is unknown, the polymerisation of amyloidogenic proteins is cooperative and can be accelerated by a cross-seeding process, in which aggregated amyloid influences the folding of adjacent peptides into  $\beta$ -pleated sheets (Hill and Lukiw, 2015). Functional amyloid secretion has been documented in several gram-negative bacterial genera including *Streptomyces*, *Bacillus*, *Pseudomonas*, and *Staphylococcus*, indicating that human hosts are exposed to a significant systemic amyloid burden, especially during ageing when the integrity of the gastrointestinal epithelium and blood-brain barrier are compromised (Friedland, 2015; Asti and Gioglio, 2014; Schwartz and Boles, 2013). It has thus been hypothesised that commensal bacteria may contribute to AD pathophysiology by amyloid cross-seeding.

Another mechanism by which microbes have been implicated in AD is through activation of the innate immune system thereby inducing neuroinflammation. Neuroinflammation has a major role in AD development and progression, mediated primarily by the actions of microglia (Lin et al. 2018). Under normal conditions, microglia bind to soluble A $\beta$  oligomers via cell-surface receptors, activating a proinflammatory microglial phenotype that leads to A $\beta$  clearance through phagocytosis (Heneka et al. 2015). Age-associated decline in microglial phagocytic capacity accompanied by insoluble A $\beta$  fibrils' resistance to degradation, however, permit A $\beta$  accumulation and induce a state of chronic inflammation (Lin et al. 2018; Hickman et al. 2008). Interestingly, the recognition of A $\beta$ <sub>1-42</sub> peptides induces an inflammatory gene expression pattern akin to that induced by bacterial lipopolysaccharide, an endotoxin found in the outer membrane of gram-negative bacteria (Ferrera et al. 2014; Colangelo et al. 2002). Endotoxin-mediated inflammation and the presence of bacteria have been found to enhance amyloid neurotoxicity (Hill and Lukiw, 2015; Dasari et al. 2011).

In a transgenic mouse model of amyloidosis, researchers observed a progressive shift away from wildtype microbiota as A $\beta$ -linked pathology worsened (Chen et al. 2020). Dysbiosis, hippocampal synaptic loss, and cognitive impairment were followed by an increase in proinflammatory microglia and infiltrating immune cells in the brain. Researchers hypothesise that AD-related gut dysbiosis stimulates peripheral immune cell entry into the central nervous system, thereby enhancing neuroinflammation and contributing to AD pathogenesis. Treatment of the AD mouse model with antibiotics yielded fewer activated microglia and infiltrating immune cells, supporting this microbiota-mediated mechanism of action. Gut dysbiosis was also reported in human AD patients. *Bifidobacterium* levels were reduced compared to age-matched controls and, importantly, were found to negatively correlate with A $\beta$ <sub>1-42</sub> concentrations in cerebrospinal fluid (Vogt et al. 2017). However, it is worth noting that despite similar reports of dysbiosis, the specific microbial populations altered in AD mice and humans were inconsistent. In transgenic AD mice, *Firmicutes* species were more abundant than *Bacteroidetes*, while the opposite was true in human subjects (Chen et al. 2020; Vogt et al. 2017). An overall reduction in taxonomic diversity was also observed in humans with AD that was not recapitulated in mice. Understanding the microbiome's role in AD pathophysiology would be benefitted by model systems in which amyloidosis can be modelled *in vivo* while maintaining a simplified microbial ecosystem.

### 6.1.2 Alzheimer's disease and iron homeostasis

The pathophysiology of AD is influenced by a range of genetic and environmental factors, allowing researchers to approach the disorder from various mechanistic and therapeutic perspectives. In addition to the microbiota-centric view, one perspective that has gained recent attention is the regulation of iron homeostasis. As iron is able to exist in two

oxidation states –  $\text{Fe}^{2+}$  and  $\text{Fe}^{3+}$  – it is able to readily donate and accept electrons to participate in the oxidation-reduction reactions involved in a range of biological processes (Andrews et al. 2003). For instance, iron serves as a component of haem enabling oxygen transport, as a cofactor of ribonucleotide reductase for DNA synthesis, and as an electron transport chain cofactor for ATP generation (reviewed in Yan and Zhang, 2020; Bogdan et al. 2016). The excessive accumulation of redox-active intracellular iron, however, is toxic to cells due to the generation of ROS and results in damage towards cellular lipids, proteins, and nucleic acids (Dev and Babitt, 2017; Ward et al. 2014). With both a high demand for dynamic energy metabolism and a low antioxidant defence system, the brain and its constituent neurons are especially susceptible to the oxidative damage caused by iron accumulation (Dringen, 2000). Iron homeostasis must therefore be tightly regulated through the processes of absorption, utilisation, recycling, and storage by a network of transport and storage proteins (Bogdan et al. 2016). One of such proteins is ferritin, a ubiquitous iron storage protein that sequesters iron in an inert form where it is unable to catalyse the formation of free radicals (Anderson and Leibold, 2014; Harrison and Arosio, 1996). Human ferritin is encoded by the ferritin heavy subunit (*FTH*) and ferritin light subunit (*FTL*) genes, together encoding 24 subunits forming a shell housing up to 4500 iron atoms (Theil, 2013). Given the fundamental nature of iron metabolism, ferritin is highly conserved across species and is encoded by two orthologues in the *C. elegans* genome: *ftn-1* and *ftn-2*. *ftn-1* is highly expressed in the *C. elegans* intestine while *ftn-2* is expressed in the pharynx, body wall muscle, hypodermis, and intestine (Kim et al. 2004; Gourley et al. 2003).

Several studies have linked dysregulated iron homeostasis with various facets of AD pathology. For instance, cortical iron levels were found to be positively correlated with the

rate of cognitive decline and disease progression in AD patients (Ayton et al. 2019; Derry and Kent, 2017; Ayton et al. 2017). Although the pathomechanism underlying this correlation is not fully understood, several studies have pointed towards direct interactions between iron availability and A $\beta$  production. Furin is a protease that plays a key role in mediating the proteolytic activation ratio of  $\alpha$ - versus  $\beta$ -secretase (Guillemot et al. 2013). Reduced concentrations of furin are associated with elevated  $\beta$ -secretase activity, resulting in enhanced cleavage of APP via the amyloidogenic pathway. Excessive concentrations of intracellular iron have been shown to reduce furin transcription, thereby reinforcing  $\beta$ -secretase activity and increasing A $\beta$  production (Ward et al. 2014). Another direct interaction between iron and A $\beta$  production is due to a feature of the A $\beta$  precursor itself, APP. APP mRNA features iron-responsive elements within its 5'-untranslated region (Rogers et al. 2008). Increased concentrations of intracellular iron upregulate APP translation, resulting in elevated generation of A $\beta$  and acceleration of cognitive impairment in AD mouse models (Peters et al. 2015; Becerril-Ortega et al. 2014).

X-ray spectromicroscopy has also indicated the presence of redox-active iron within sites of amyloid plaque formation in AD subjects, supporting the hypothesis that free radical generation in these plaques induces a form of cell-death known as ferroptosis (Everett et al. 2018). Ferroptosis is a form of programmed cell death that is morphologically, biochemically, and genetically distinct from other forms of death including apoptosis, autophagy, and necrosis (Yan and Zhang, 2020; Stockwell et al. 2017; Dixon et al. 2012). Iron-mediated lipid peroxidation and lethal ROS production, which in turn trigger cell death, are the defining features of ferroptosis, and are thought to contribute to the neuronal loss that accelerates AD progression. The recent development of selective Fe<sup>3+</sup>/Fe<sup>2+</sup> fluorescent imaging probes has enabled researchers to simultaneously monitor different

iron redox states in the AD mouse brain (Wu et al. 2023). These sensors have confirmed long-suspected differences in iron redox changes during AD: AD brains exhibited significant increases in  $\text{Fe}^{3+}/\text{Fe}^{2+}$  ratios surrounding amyloid plaques. Coupled with a decreased  $\text{Fe}^{3+}/\text{Fe}^{2+}$  ratio observed following the induction of ferroptosis, the results suggest a correlation between amyloid plaque formation and the conversion of  $\text{Fe}^{2+}$  to the insoluble  $\text{Fe}^{3+}$ . More than ever, researchers are compelled to investigate the role of iron homeostasis and ferroptosis in AD pathology, as well as in other neurological disorders involving neuronal death (Alim et al. 2019; Kenny et al. 2019).

### 6.1.3 Investigating experimental microbiome effects in human disease models

Previous sections of this project examined EM effects in unchallenged genetic backgrounds modelling standard *C. elegans* ageing. However, as the ageing process is often accompanied by diseases of proteotoxicity, we probed the effects of our representative microbiome in a *C. elegans* proteotoxicity model with relevance to human ageing. Specifically, we utilized a transgenic *C. elegans* strain expressing the full-length human isoform of A $\beta$  that typically undergoes fibrillisation in neurons in AD, A $\beta_{1-42}$ . *C. elegans* expresses an APP orthologue, Amyloid Precursor-Like-1 (APL-1), although the protein lacks sites for  $\beta$ -secretase binding. In addition, the *C. elegans* genome does not encode a  $\beta$ -secretase orthologue and no endogenous A $\beta$ -like peptide has yet been detected in the nematode (McColl et al. 2009). In the transgenic *C. elegans* AD model, A $\beta_{1-42}$  is instead expressed within body wall muscle under control of the *unc-54* promoter, encoding a heavy chain muscle myosin, resulting in whole-body paralysis when animals are cultured at 25°C (McColl et al. 2012). An easily scored *in vivo* phenotype such as paralysis, requiring only a dissection microscope to evaluate pathological protein misfolding, is a disease-relevant complement to traditional AD models that permits quick

screening of interventions ameliorating A $\beta$  toxicity. We hypothesised that commensal microbes may improve the nematode's resistance to proteotoxic stresses, perhaps by initiating systemic immune activation as has been suggested in the preceding chapters. Although we primarily assessed outcomes in response to A $\beta_{1-42}$  aggregation, we expected that EM rearing would improve outcomes in various proteotoxicity models. We explored the following aims:

1. Assess the effects of the EM in a model of age-associated proteotoxicity
2. Identify molecular mechanisms underlying EM effects on A $\beta$ -associated toxicity

## 6.2 Results

### 6.2.1 Experimental microbiome suppresses A $\beta_{1-42}$ -associated toxicity

Transgenic nematodes of the genotype *dvl100*(*p<sub>unc-54</sub>::A $\beta_{1-42}$*  + *p<sub>mtl-2</sub>::GFP*), expressing full-length human A $\beta_{1-42}$  under control of the muscular *unc-54* promoter (McColl et al. 2012), were age-synchronised and cultivated on either *E. coli* OP50 or the EM from egg stage at 20°C. At the L4 stage immediately preceding complete development of the hermaphrodite vulva, nematodes were shifted to 25° to initiate transcription of A $\beta_{1-42}$ . The proportion of the surviving population displaying whole-body paralysis was recorded over the course of four days with the original population transferred daily to avoid overcrowding.

*dvl100*(*p<sub>unc-54</sub>::A $\beta_{1-42}$*  + *p<sub>mtl-2</sub>::GFP*), worms cultivated on OP50 exhibit a rapid increase in the incidence of paralysis, with 27% ( $\pm 8\%$ ) of the population already paralysed on D1 of adulthood, 24 hours after transfer into the non-permissive 25°C (Figure 6.1A). This

increases to 88% ( $\pm 2\%$ ) on D2, 99% ( $\pm 1\%$ ) on D3, and paralysis of the total population by D4 of adulthood. By contrast, paralysis is not detected in EM-fed nematodes until D2 of adulthood and is significantly suppressed in comparison to age-matched OP50-fed animals ( $p < 0.0001$ ) with 17% ( $\pm 3\%$ ) paralysed. By D3, this increased to 52% ( $\pm 8\%$ ) of the population – once again significantly lower than D3 paralysis incidence in OP50 controls ( $p < 0.0001$ ) followed by 96% ( $\pm 1\%$ ) on D4 of adulthood, where a statistical difference between feeding conditions was no longer detected ( $p = 0.954$ ). The marked delay in paralysis onset in *dvIs100(p<sub>unc-54</sub>::A $\beta$ <sub>1-42</sub> + p<sub>mtl-2</sub>::GFP)* nematodes cultivated on the EM indicates a protective effect against A $\beta$ <sub>1-42</sub>-associated toxicity.

As the EM is comprised of 11 distinct bacterial species, we asked whether suppression of paralysis was due to a community effect or to the contributions of particular member species. We once again performed the paralysis assay using *dvIs100(p<sub>unc-54</sub>::A $\beta$ <sub>1-42</sub> + p<sub>mtl-2</sub>::GFP)* worms reared on OP50, the EM, or individual microbial constituents of the EM. For the purpose of clarity, the comparisons described here refer to statistical significance on D2 of adulthood – where the effects of the EM are most pronounced – as determined by two-way ANOVA. Species MYb9 was found to inhibit paralysis, with 45% fewer paralysed D2 adults than the OP50 control condition ( $p = 0.008$ ) (Figure 6.1B). No significant difference in paralysis proportion was identified between MYb9-fed and EM-fed animals on D2 ( $p = 0.693$ ), suggesting that MYb9 is a contributor to the EM effect on A $\beta$ <sub>1-42</sub>-associated paralysis. Similar efficacy was observed with MYb10, with 41% fewer paralysed animals on D2 compared to OP50 controls ( $p = 0.0035$ ) and no significant difference from the EM condition ( $p = 0.457$ ) (Figure 6.1C). The same was true for MYb11, exhibiting 66% fewer paralysed animals on D2 compared to OP50 controls ( $p < 0.0001$ ) and almost no discernible difference from the EM condition ( $p > 0.9999$ ) (Figure 6.1D).

However, it is worth noting that worms cultivated on MYb11 display slow growth and a reduced body size compared to other feeding conditions, confounding conclusions on the contribution of MYb11 to the EM effect (data not shown). No difference was observed between paralysed proportions of OP50-fed and MYb27-fed worms on D2 ( $p = 0.234$ ), suggesting that MYb27 is not a significant contributor to the EM's protective effect (Figure 6.1E). MYb45 was found to significantly inhibit paralysis, with 74% fewer paralysed animals on D2 than OP50-fed controls ( $p < 0.0001$ ) (Figure 6.1F) – although this result was obtained from three technical repeats within one biological replicate due to persistent contamination of MYb45 stocks. MYb56 provides mild protection against  $A\beta_{1-42}$ -associated paralysis ( $p = 0.015$ ), with 38% fewer paralysed animals on D2 than the OP50 condition (Figure 6.1G). There was no statistically significant difference between paralysis outcomes in MYb57-reared and OP50-reared worms on D2 ( $p = 0.887$ ), suggesting that live MYb57 bacteria does not contribute to the EM effect (Figure 6.1H). MYb71 bacteria was found to significantly inhibit paralysis, with 56% fewer paralysed D2 animals than OP50 controls ( $p < 0.0001$ ), statistically indistinguishable from the EM at the same timepoint ( $p = 0.999$ ) (Figure 6.1I). A similar effect was seen in worms reared on MYb83, with 50% less of the population paralysed on D2 compared to OP50 controls ( $p < 0.0001$ ) (Figure 6.1J). However, neither of the final two EM member strains – MYb120 and MYb218 – exhibited any protective effect against paralysis compared to controls, with both indistinguishable from OP50 results on D2 of the assay ( $p > 0.999$ ) (Figure 6.1K,L). Altogether, these results indicate that the individual bacterial strains comprising the EM exert varied effects against  $A\beta_{1-42}$ -associated toxicity and that it is unlikely a single species is responsible for the total effect of the EM. In addition, the aforementioned series of paralysis assays solely probed the effects of individual strains and does not account for the community effects of multiple EM species interacting with one another.

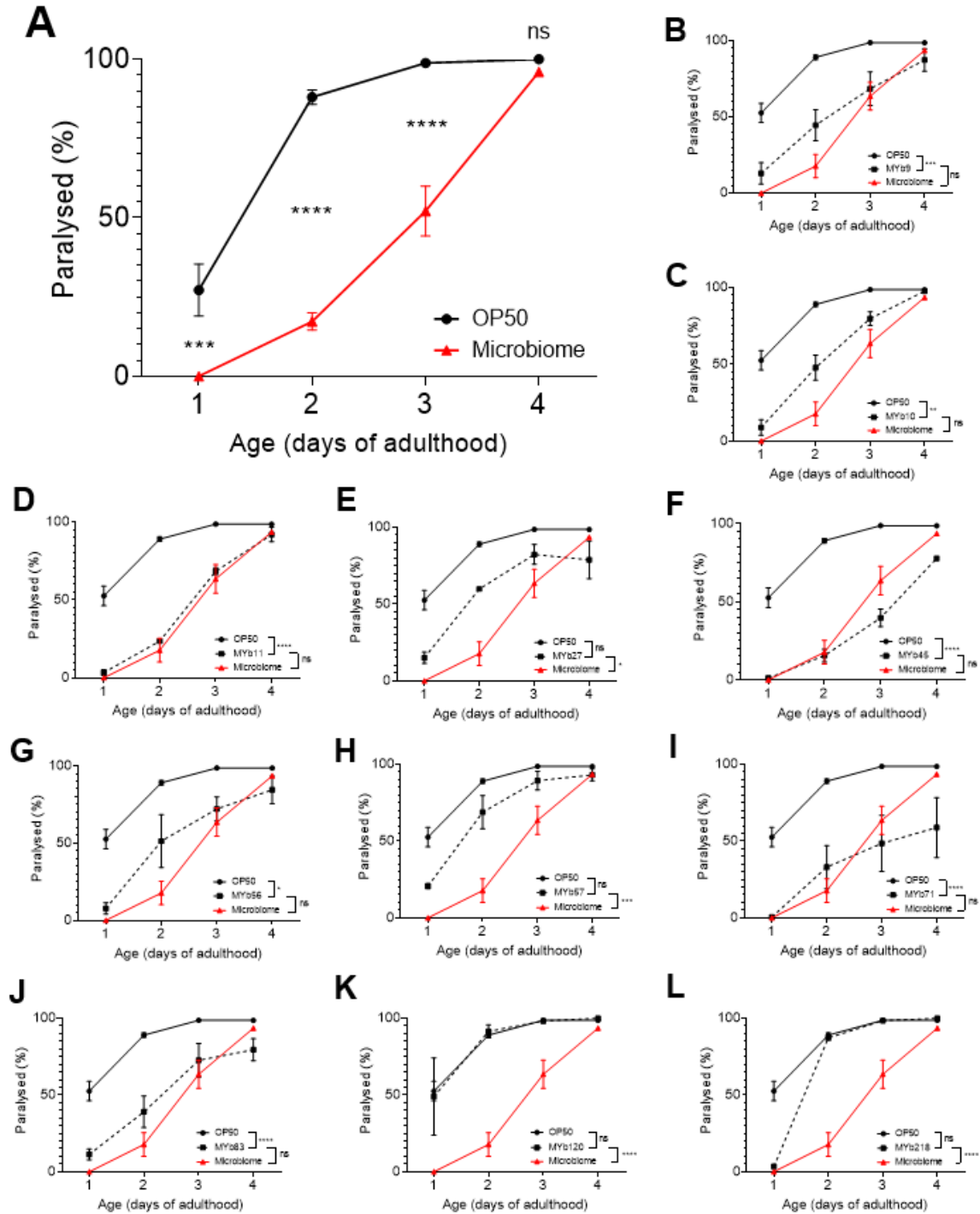


**Figure 6.1. Experimental microbiome suppresses A $\beta$ <sub>1-42</sub>-associated toxicity.** (A) *dvl100(p<sub>unc-54</sub>::A $\beta$ <sub>1-42</sub> + p<sub>mtl-2</sub>::GFP)* animals expressing human A $\beta$ <sub>1-42</sub> in body wall muscle undergo paralysis when shifted to 25°C. Cultivation on the EM significantly suppresses paralysis onset on D1, D2, and D3 versus OP50-fed controls. Statistical analysis by two-way ANOVA (\*\*\*\**p* < 0.0001, \*\*\**p* < 0.001, ns *p* > 0.05). Data represents means of seven independent trials (*n* = 100 animals per trial) ± SEM. (B-L) Live bacterial lawns from each of the 11 EM member strains exert varied effects on A $\beta$ -associated paralysis. Statistical analysis by two-way ANOVA (\*\*\*\**p* < 0.0001, \*\*\**p* < 0.001, \*\**p* < 0.01, \**p* > 0.01, ns *p* > 0.05). Statistical significance refers to paralysis proportions on D2 of adulthood only. Data represent means of at least three independent trials (*n* = 100 animals per trial) ± SEM, except in case of MYb45 (F) where only one biological repeat was performed due to persistent contamination.

### 6.2.2 Cell-free media from experimental microbiome partially suppresses A $\beta$ <sub>1-42</sub>-associated toxicity

We sought to determine whether the protective effect of the EM against paralysis onset was specifically contributed by live microbiota. Several attempts to kill the EM bacterial lawn were made with the use of heat treatment, UV crosslinking, and various antibiotics. However, administration of each of these techniques proved unsuccessful as novel colony forming units (CFUs) persisted following overnight incubation of the treated plates. The disparate morphology of these CFUs in comparison to the EM lawn suggested that certain species were more susceptible to killing while others were more robust – though none of the treatments applied were effective at eliminating CFUs from all 11 species (data not shown).

Our next aim was to determine whether extracellular material produced by EM strains contributed to the anti-paralysis effect. EM bacterial cells were separated from their cell-free suspension following combination of the species in liquid culture, prior to seeding of NGM plates (see section 2.3.4 for detailed protocol). Mixed bacterial cells were pelleted by centrifugation, the supernatant was filter-sterilised, and the resultant cell-free media (CFM) was pipetted onto a thickened OP50 lawn. We repeated the paralysis assay as previously described including OP50+CFM as an additional condition, permitting nematodes' access to extracellular material produced by the EM without the inclusion of live bacterial cells. Nematodes reared on OP50 once again exhibited paralysis as early as D1 of adulthood with 9% ( $\pm 1\%$ ) of the population affected. This proportion increased to 86% ( $\pm 4\%$ ) on D2 followed by 98% ( $\pm 1\%$ ) on D3, and finally complete paralysis of the total population by D4 of adulthood (Figure 6.2A). As expected, EM-fed nematodes did not exhibit any A $\beta$ -dependent paralysis on D1 of adulthood. On D2 and D3, paralysis was

reported in 17% ( $\pm 13\%$ ) and 56% ( $\pm 16\%$ ) of the EM-fed population, respectively – both significantly lower proportions in comparison to OP50 controls at the same timepoints ( $p < 0.0001$ ). By D4, nearly the total population of EM-fed nematodes was affected by paralysis at 95% ( $\pm 2\%$ ).

Interestingly, A $\beta$ -associated paralysis was partially abrogated in nematodes cultivated on the OP50+CFM condition, with the proportion of the population affected falling between OP50-fed and EM-fed values at each of the timepoints tested (Figure 6.2A). On D1 of adulthood, a mere 3% ( $\pm 3\%$ ) of the OP50+CFM-reared population was affected by paralysis, increasing to 54% ( $\pm 1\%$ ) on D2, 77% ( $\pm 2\%$ ) on D3, and 80% ( $\pm 14\%$ ) on D4 of adulthood. The protective effect of the EM against A $\beta$ -associated toxicity is most evident on D2 of adulthood where it reduces incidence of paralysis by 68% ( $p < 0.0001$ ) compared to OP50 controls within this data set. At the same timepoint, OP50+CFM reduces paralysis by 32% - a milder protective effect but still exhibiting statistical significance ( $p = 0.002$ ). The results not only highlight the protective effect of EM extracellular material against A $\beta$ -associated toxicity but also suggest that the effects of the CFM on *C. elegans* physiology can be dissociated from those of live EM bacteria. Considering the reduced magnitude of protection provided by CFM compared to live EM bacteria, we surmised two possibilities on their respective mechanisms: (1) live EM bacteria and CFM possess the same mechanism of action operating in a concentration-dependent manner, or (2) live EM bacteria and CFM inhibit A $\beta$ -associated toxicity using disparate mechanisms of action.

We next assessed the contributions of member strains to the CFM effect by supplementing OP50 with CFM from individual species. Once again, statistical significance here as

determined by two-way ANOVA describes D2 animals across feeding conditions. No significant effect on paralysis was observed in worms raised on OP50+MYb9 CFM ( $p > 0.999$ ), suggesting that MYb9 CFM is not primarily responsible for the efficacy of EM CFM (Figure 6.2B). Similar results were obtained for OP50 supplemented with CFM from MYb10 ( $p > 0.999$ ), MYb11 ( $p > 0.999$ ), MYb27 ( $p = 0.874$ ), MYb45 ( $p > 0.999$ ), MYb56 ( $p = 0.982$ ), MYb71 ( $p > 0.999$ ), and MYb83 ( $p > 0.999$ ) (Figures 6.2C,D,E,F,G,I,J). In fact, only one CFM supplementation condition yielded significant reduction in A $\beta$ -associated paralysis: OP50+MYb57 CFM (Figure 6.3H). In this condition, 45% ( $\pm 0.5\%$ ) of the D2 population exhibited paralysis compared to 89% ( $\pm 2\%$ ) of OP50-fed controls ( $p = 0.001$ ). Paralysis proportions of D2 OP50+MYb57 CFM worms were indistinguishable from the D2 OP50+CFM condition ( $p > 0.9999$ ), suggesting – along with the absence of protection from any of the other bacterial CFM conditions tested – that MYb57 CFM is the main driver of the protective effect of the EM CFM against A $\beta$ -associated paralysis. Interestingly, live MYb57 bacteria did not have a protective effect on paralysis (Figure 6.1H), once again highlighting the dissociable effects of live bacteria and their extracellular compounds on proteotoxicity. The finding that MYb57 was only effective against A $\beta$ -associated paralysis in its CFM form was nonetheless unexpected; if the protection provided by active compounds was concentration-dependent, we would expect at least an equivalent degree of protection provided by live MYb57. The results suggest that, at least in the case of MYb57, live bacteria and extracellular material may have differing effects on A $\beta$  proteotoxicity, and that the beneficial effects of MYb57 CFM may be obscured by deleterious effects of live MYb57.

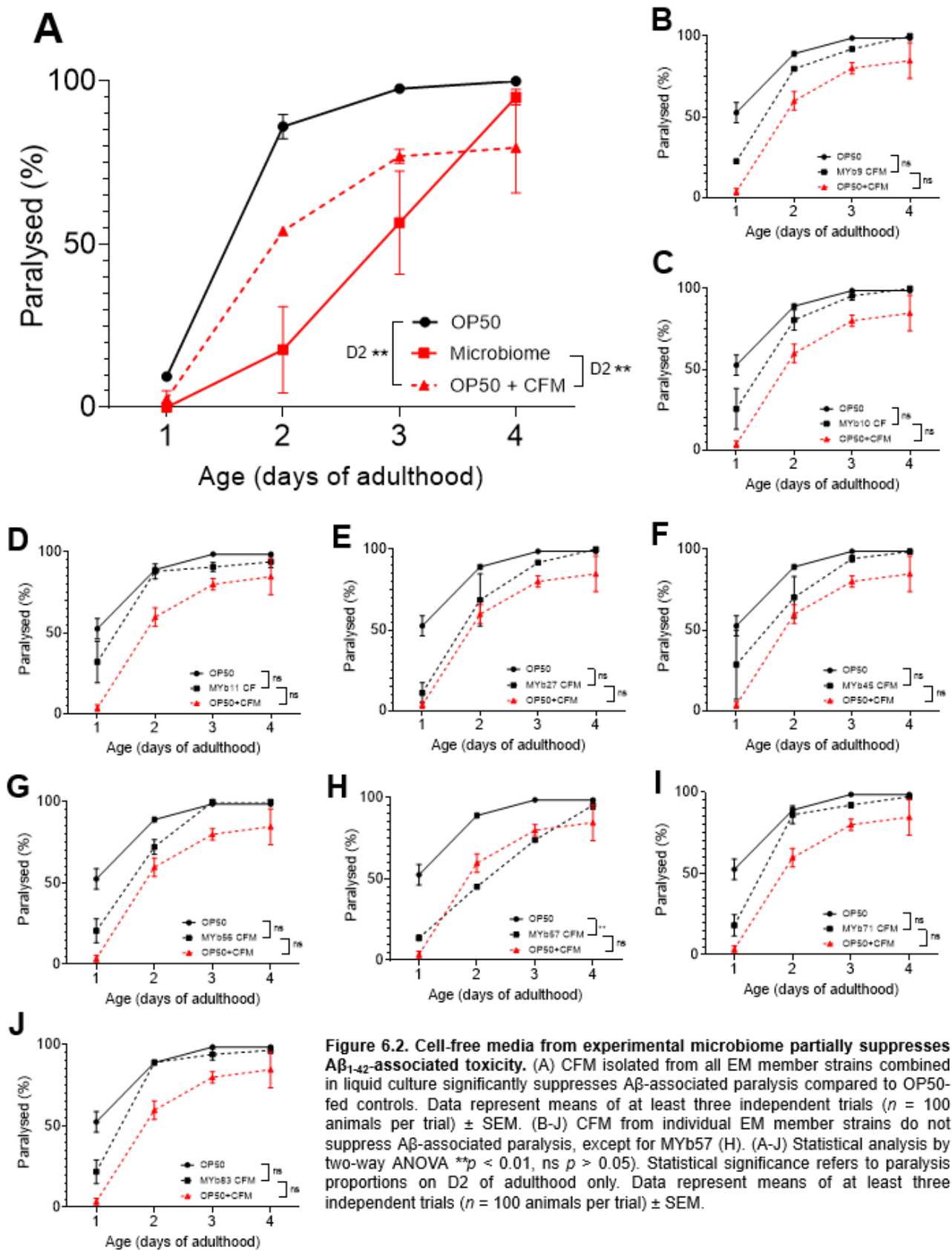


**Figure 6.2. Cell-free media from experimental microbiome partially suppresses A $\beta$ <sub>1-42</sub>-associated toxicity.** (A) CFM isolated from all EM member strains combined in liquid culture significantly suppresses A $\beta$ -associated paralysis compared to OP50-fed controls. Data represent means of at least three independent trials ( $n = 100$  animals per trial)  $\pm$  SEM. (B-J) CFM from individual EM member strains do not suppress A $\beta$ -associated paralysis, except for MYb57 (H). (A-J) Statistical analysis by two-way ANOVA  $**p < 0.01$ ,  $ns p > 0.05$ ). Statistical significance refers to paralysis proportions on D2 of adulthood only. Data represent means of at least three independent trials ( $n = 100$  animals per trial)  $\pm$  SEM.

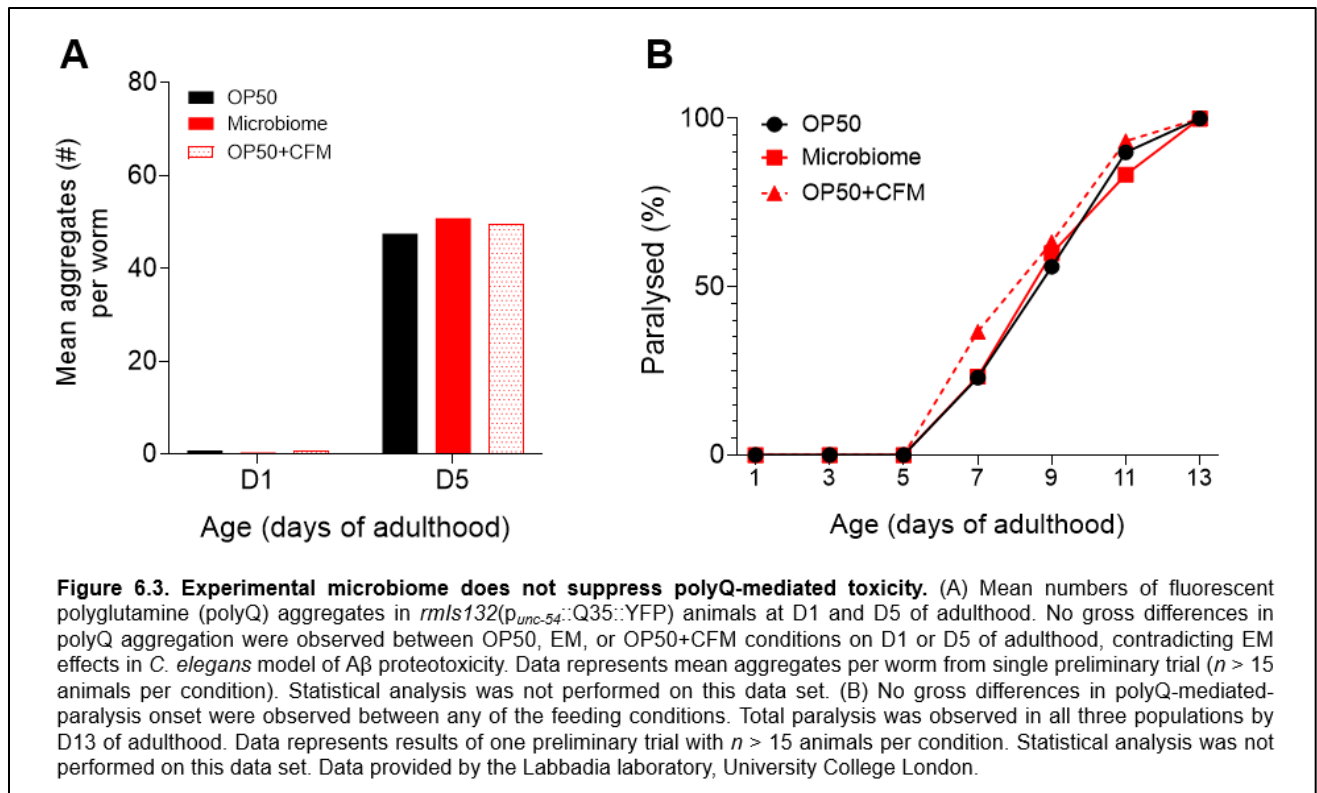
### 6.2.3 Experimental microbiome does not suppress polyQ-mediated toxicity

We asked whether the effects of the EM and CFM isolated from the microbiome were restricted to amyloid aggregation or if they persisted in other models of proteotoxicity. We were assisted by the Labbadia laboratory (University College London) in performing a single preliminary trial using a *C. elegans* model of Huntington's disease – a neurodegenerative disorder characterised by the expansion of polyglutamine (polyQ) repeats within the Huntingtin protein (reviewed in Gusella and MacDonald, 2000). The transgenic *C. elegans* strain *rmls132(p<sub>unc-54</sub>::Q35::YFP)* expresses yellow fluorescent protein (YFP) fused to a 35-glutamine repeat (Q35) (Morley et al. 2002). In these worms, Q35 YFP aggregates gradually become more visible from young adulthood in a subset of muscle cells and is accompanied by a progressive loss of motility (Nollen et al. 2004; Morley et al. 2002).

To assess the effects of the EM and CFM on polyQ toxicity, the Labbadia laboratory quantified polyQ aggregates in *rmls132(p<sub>unc-54</sub>::Q35::YFP)* worms on D1 and D5 of adulthood, as well as paralysis onset up to D13. On D1 of adulthood, worms reared on OP50 displayed a mean of 0.9 Q35 YFP aggregates while those reared on EM a mean of 0.5 and those on OP50 supplemented with CFM a mean of 0.8 aggregates. No gross differences in aggregate numbers were observed between OP50 and EM conditions nor between OP50 and OP50+CFM (Figure 6.3A). This was an anticipated result as previous studies have documented diffuse YFP staining patterns from hatching up to the onset of adulthood, with Q35 aggregation following later in the life cycle (Nollen et al. 2004). As expected, a notable increase in mean aggregate number was observed on D5 of adulthood for all conditions tested. OP50-fed nematodes displayed a mean of 47.6 aggregates per worm with 50.8 in EM-fed worms and 49.7 in those cultivated on

OP50+CFM. No gross difference in aggregate number was observed between OP50 and OP50+CFM, suggesting that the active extracellular compounds ameliorating amyloid-mediated toxicity are ineffective against polyQ-mediated aggregation. Whether this is a result of the compounds' specificity or that a concentration threshold has not been met has yet to be determined. Note that statistical analyses were not performed on this data set as only one preliminary trial had been completed.

The functional consequences of polyQ aggregation were then evaluated via paralysis onset in OP50-, EM-, and OP50+CFM-fed worms from D1 to D13 of adulthood. No gross differences in paralysed proportions were detected at any of the timepoints tested between all experimental conditions, indicating that neither the EM nor its sterile supernatant improve polyQ toxicity outcomes (Figure 6.3B). As total paralysis was observed in all three experimental populations by D13, the results cannot be attributed to insufficient assay duration and incomplete penetrance of the polyQ phenotype. Once again, statistical analyses were not performed on data obtained in the single trial. Taken together with the results from sections 6.2.1 and 6.2.2, the preliminary data implies that the EM may ameliorate amyloid-associated toxicity via direct interactions with A $\beta$  peptides rather than improving the nematode's capacity to cope with general proteotoxic stress. To probe this mechanism further, we examined A $\beta$ <sub>1-42</sub> fibril formation *in vitro*.

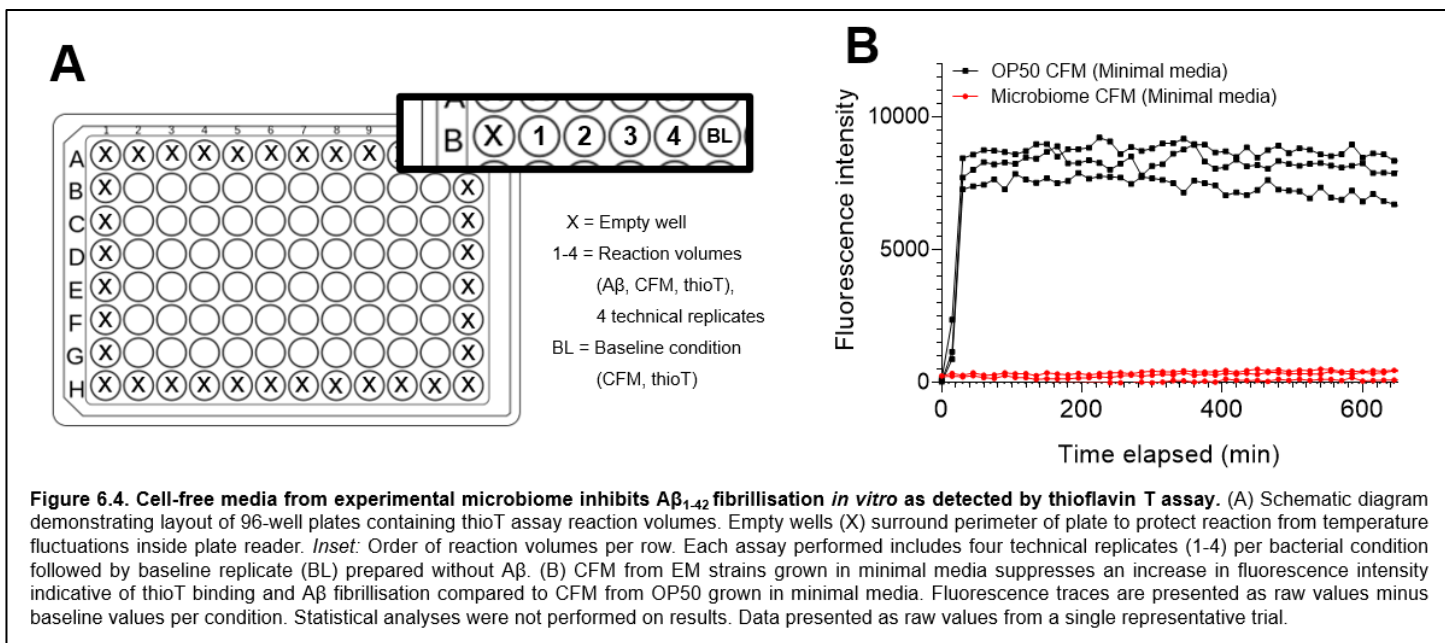


#### 6.2.4 Cell-free media from EM inhibits A $\beta$ <sub>1-42</sub> fibril formation *in vitro*

We observed partial suppression of A $\beta$ -dependent paralysis by sterile CFM isolated from the EM in liquid culture, suggesting the presence of active extracellular compounds with an undetermined mechanism of action. We hypothesised several scenarios by which CFM was inhibiting paralysis: by enhancing the nematode's resistance to A $\beta$  proteotoxicity, by impairing transcription of the A $\beta$  transgene, or by inhibiting the aggregation of A $\beta$  itself – or the concerted action of all three. We investigated the latter of these mechanisms by measuring A $\beta$ <sub>1-42</sub> fibril formation *in vitro* in combination with CFM isolated from the EM. With assistance from the Xue lab (University of Kent), monomeric recombinant A $\beta$ <sub>1-42</sub> was generated in pET Sac A $\beta$ <sub>1-42</sub> BL21 (DE3) *Escherichia coli* cells and purified by size exclusion (see section 2.3.33, 2.3.34 for detailed protocol). Reaction volumes containing

purified A $\beta$ <sub>1-42</sub> monomers, the CFM of interest, and thioflavin T (ThT) – a small molecule that produces strong fluorescence upon amyloid binding – were prepared in 96-well plates, allowing rapid detection of A $\beta$ <sub>1-42</sub> fibrillisation by UV-Vis spectrophotometer (Xue et al. 2017; LeVine, 1999; Naiki et al. 1989). Only CFM from the community/strain of interest was used in the reaction volume as live bacterial cells were found to interfere with fluorescence detection (see section 2.3.35 for formulation). As the nutrient-rich LB medium in which EM member strains were grown was also sufficient to obscure fluorescence detection, bacteria were instead grown in minimal media for 72h. Data from previous laboratory members demonstrated that EM member strains grown in minimal media maintained their efficacy in suppressing A $\beta$ -associated paralysis, although to a reduced extent (Appendix, Figure 8.1).

Each ThT assay performed featured four technical replicates per bacterial condition and a single baseline replicate that is not induced for luminescent signal (Figure 6.4A). The baseline control condition was prepared in the same manner as experimental conditions without the addition of recombinant amyloid. The resultant ‘background signal’ was subtracted from each technical replicate to generate four independent noise-free readings per condition per trial. In a trial including minimal media-grown OP50 CFM (as a control condition), all traces increased to a fluorescence intensity range between 7200 and 8500 A.U. within 30 minutes from initiation of the assay (Figure 6.4B). By contrast, no traces obtained from reaction volumes containing minimal media-grown EM CFM surpassed a fluorescence intensity of 650 A.U. over the full course of the assay, suggesting that EM CFM suppresses A $\beta$  fibrillisation *in vitro*.



We then performed the ThT assay using minimal media-grown CFM from individual EM member strains to assess the contribution of individual species to the community effect seen in Figure 6.4B. For each assay performed, reaction volumes containing A $\beta$ <sub>1-42</sub>, ThT, and minimal media were included as controls. For the purpose of clarity, Figure 6.5A-K features representative traces from one trial demonstrating effects consistent across two biological replicates (all trials included in Appendix, Figures 8.2 and 8.3). At the assay's completion at 10 hours (600 minutes), MYb9 CFM grown in minimal media suppressed fluorescence intensity to approximately 40% of the minimal media control (Figure 6.5A). At the same timepoint, MYb10 CFM fluorescence intensity was approximately 80% of the control signal (Figure 6.5B), MYb11 CFM approximately 10% (Figure 6.5C), MYb27 CFM approximately 4% (Figure 6.5D), MYb45 CFM approximately 80% (Figure 6.5E), MYb56 CFM approximately 50% (Figure 6.5F), MYb57 CFM approximately 4% (Figure 6.5G), MYb71 CFM approximately 80% (Figure 6.5H), MYb83 CFM approximately 1% (Figure 6.5I), MYb120 CFM approximately 40% (Figure 6.5J), and MYb218 CFM approximately

70% of the minimal media control signal (Figure 6.5K). The EM member strains displaying the lowest inhibitory effects on A $\beta$  fibrillisation *in vitro* were thus MYb10, MYb45, and MYb71 – corroborating the results of the paralysis assay featuring CFM from individual EM member strains (Figure 6.2C,F,I). Notably, CFM isolated from these species were found to be ineffective at suppressing A $\beta$ -associated paralysis (MYb10  $p > 0.9999$  vs. OP50, D2) (MYb45  $p = 0.9997$  vs. OP50, D2) (MYb71  $p > 0.9999$  vs. OP50, D2). By contrast, the EM member strains showing the greatest inhibitory effects on A $\beta$  fibrillisation *in vitro* were MYb11, MYb27, MYb57, and MYb83. Out of these CFM sources, only MYb57 CFM was found to inhibit A $\beta$ -associated paralysis ( $p = 0.0011$  vs. OP50, D2). Taken together, the data suggests that CFM isolated from the EM inhibits A $\beta_{1-42}$  fibrillisation *in vitro*, suggesting that suppression of A $\beta$ -associated paralysis by CFM is at least partially due to direct inhibition of A $\beta$  aggregation. Moreover, individual EM member strains displayed varying degrees of inhibition of A $\beta_{1-42}$  fibrillisation. Whether the total effect of EM CFM is due to a community effect from multiple bacterial strains or a single predominating bacterium is undetermined.

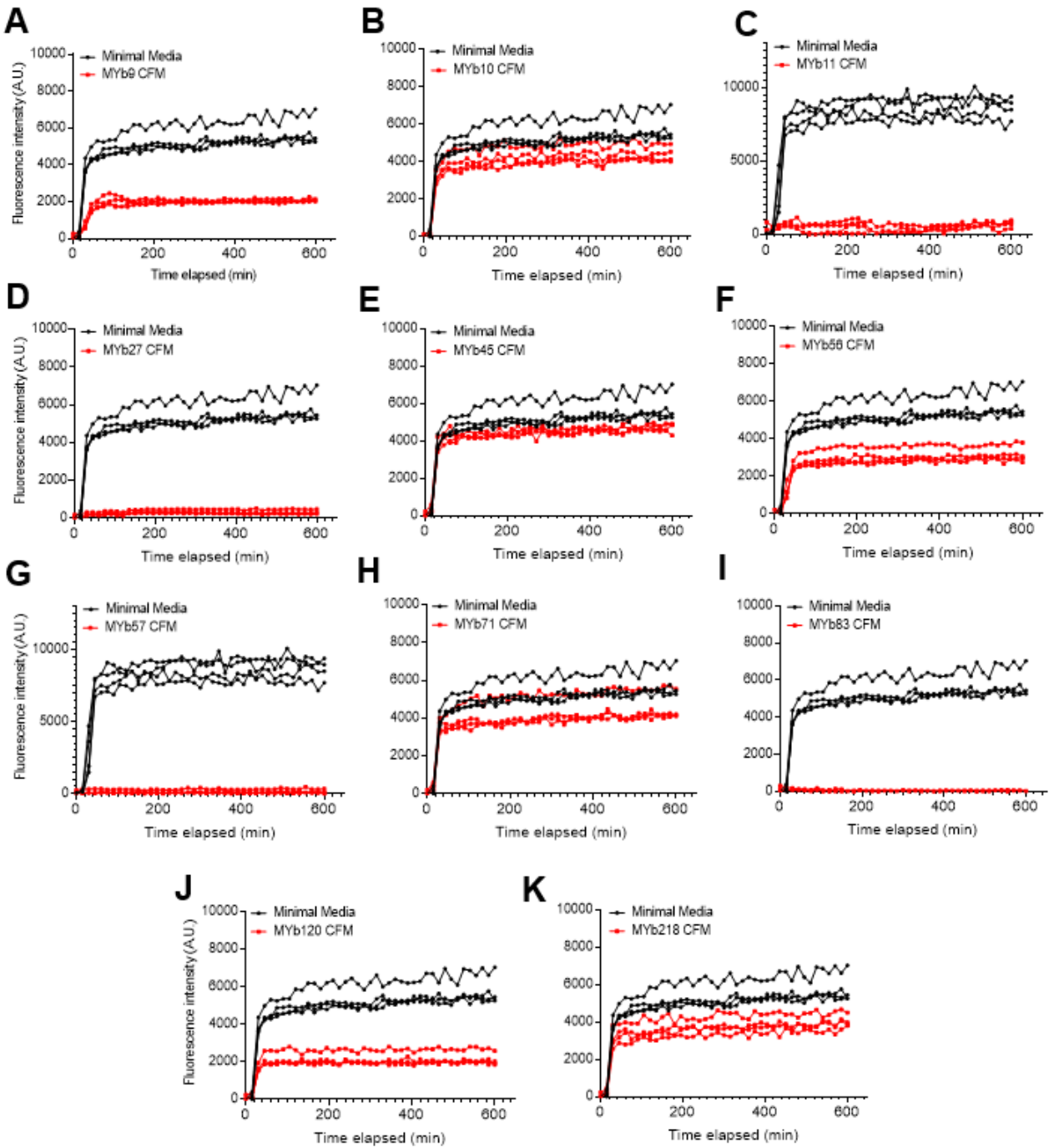


**Figure 6.5. Cell-free media from individual experimental microbiome member strains differentially inhibit A $\beta$  fibrillation *in vitro*.** (A-K) ThioT reaction volumes were prepared with CFM isolated from EM member strains grown in minimal media. Sterile minimal media was included in each trial as a control condition. Fluorescence traces are presented as raw values minus baseline values per condition. Statistical analyses were not performed on results. Data presented as raw values from a single representative trial.

### 6.2.5 Active compound(s) in MYb57 extracellular material cannot be extracted into volatile solvents

Following the results of our ThT assay, our next aim was to identify any compound(s) in bacterial CFM that were inhibiting  $A\beta_{1-42}$  toxicity. To reduce the number of potential candidates and simplify the process of identification, we selected a single bacterial strain that met two defined criteria: (1) the strain's CFM was capable of delaying the onset of  $A\beta$ -mediated paralysis, and (2) the strain's CFM inhibited  $A\beta_{1-42}$  fibrillisation *in vitro* as shown by ThT assay. In consideration of these criteria, we selected MYb57 CFM for closer analysis (Figure 6.2H and Figure 6.3H). In addition, MYb57 was the only member strain found to be efficacious against  $A\beta$ -mediated paralysis as a supernatant but not in its live bacterial form (Figure 6.1H and Figure 6.2H), further justifying its selection as a candidate for further analysis. We sought to identify an organic solvent into which the protective compound(s) could be extracted while preserving their efficacy. The properties of the effective extractant would, in turn, indicate the properties of the active compound(s) i.e., polarity, solubility, and more.

Extraction of MYb57 extracellular material into various organic solvents was performed as advised by Dr. Matthew Jenner (University of Warwick) (schematic in Figure 6.6A). MYb57 bacterial lawns were grown on NGM plates for a minimum of 72 hours then scraped from agar. Agar was cut into 1-cm squares and submerged in one of three organic solvents – ethyl acetate, dichloromethane, or acetonitrile – for one hour. The subsequent extracts were distilled via vacuum centrifuge. Remaining solutes were resuspended in water, filter sterilised, and used to supplement OP50 lawns. The  $A\beta$ -associated paralysis assay described in Section 6.2.1 was then performed using the prepared plates, with OP50 lawns extracted into the equivalent solvents used as additional control conditions.

Once again, *dvIs100(p<sub>unc-54</sub>::A $\beta$ <sub>1-42</sub> + p<sub>mtl-2</sub>::GFP)* worms cultivated on OP50 displayed rapid onset of A $\beta$ -associated paralysis, increasing from 6% ( $\pm$ 2%) of the population affected on D1 of adulthood to 60% ( $\pm$ 6%) on D2, followed by 91% ( $\pm$ 2%) affected at the assay's completion on D3 (Figure 6.6B-D). OP50 supplemented with MYb57 CFM, prepared as previously described, was included as a positive control condition and demonstrated mild suppression of paralysis as expected, with 2% ( $\pm$ 2%) of the population affected on D1, increasing to 39% ( $\pm$ 6%) ( $p = 0.016$  on D2 vs. OP50) on D2, and finally 90% ( $\pm$ 3%) on D3.

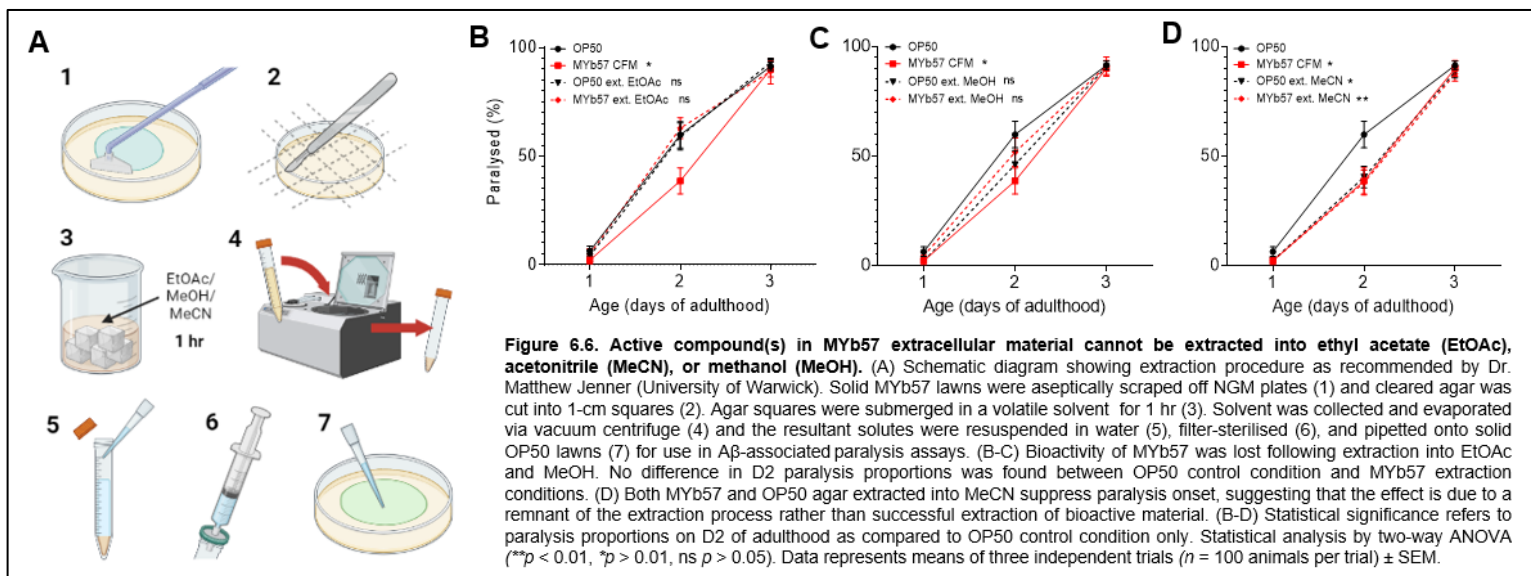
Worms reared on OP50 plates supplemented with OP50 agar extracted into ethyl acetate (Figure 6.5B, OP50 ext. EtOAc) behaved as standard OP50 controls, with 4% ( $\pm$ 1%) of the population paralysed on D1, 59% ( $\pm$ 6%) on D2, and 93% ( $\pm$ 2%) on D3. No differences were observed versus standard OP50 at any of the timepoints tested ( $p > 0.9999$ ), and a mild but significant difference from MYb57 CFM plates was observed on D2 ( $p = 0.024$ ). MYb57 agar extracted into ethyl acetate (MYb57 ext. EtOAc) did not exhibit a protective effect against paralysis, with no difference from OP50 values detected at any of the timepoints tested ( $p > 0.999$ ), and a significant difference from MYb57 CFM on D2 ( $p = 0.0029$ ). The data suggests that the bioactivity of MYb57 extracellular material is lost during the extraction process into ethyl acetate.

Worms reared on OP50 plates supplemented with OP50 agar extracted into methanol (Figure 6.6C, OP50 ext. MeOH) behaved as standard OP50 controls, with 2% ( $\pm$ 1%) of the population paralysed on D1, 46% ( $\pm$ 6%) on D2, and 91% ( $\pm$ 1%) on D3. No differences were observed versus standard OP50 at any of the timepoints tested ( $p = 0.995$  on D1,  $p$

= 0.254 on D2,  $p > 0.9999$  on D3). MYb57 agar extracted into methanol (MYb57 ext. MeOH) did not exhibit a protective effect against paralysis, with no difference from OP50 values detected at any of the timepoints tested ( $p > 0.9999$  on D1,  $p = 0.854$  on D2,  $p > 0.9999$ ), and a significant difference from MYb57 CFM on D2 ( $p = 0.396$ ). The data suggests that the bioactivity of MYb57 extracellular material is also lost during the extraction process into methanol.

Interestingly, extraction of MYb57 agar into acetonitrile (Figure 6.6D, MYb57 ext. MeCN) yielded significant suppression of A $\beta$ -paralysis in comparison to standard OP50-fed controls. Affected proportions increased from 2% ( $\pm 1\%$ ) of the population on D1, 38% ( $\pm 6\%$ ) on D2 ( $p = 0.0047$  on D2 vs. OP50), and 87% ( $\pm 3\%$ ) on D3. Moreover, no significant difference between paralysed proportions was detected between MYb57 extracted into acetonitrile and MYb57 CFM on D2 ( $p > 0.9999$ ). Together, these results seem to suggest that the active extracellular compounds protecting against A $\beta$  toxicity were successfully extracted into acetonitrile. However, OP50 agar extracted into acetonitrile (OP50 ext. MeCN) also exhibited a significant suppressive effect on paralysis in comparison to standard OP50-fed controls, with 2% ( $\pm 1\%$ ) of the population affected on D1, 40% ( $\pm 5\%$ ) on D2 ( $p = 0.02$  on D2 vs. OP50), and 88% ( $\pm 3\%$ ) on D3. No difference between OP50 extracted into acetonitrile and MYb57 CFM was detected ( $p > 0.9999$  on D2). These results suggest that the protective effect observed in Figure 6.5D may be a remnant of the extraction process into acetonitrile present in both conditions rather than the successful extraction of MYb57 material. Taken together, the results indicate that extraction of the active compound(s) present in MYb57 CFM into volatile organic solvents was unsuccessful. We suspect several potential sources of error, including but not limited to (1) failure of active products in MYb57 to be deposited in the NGM agar, (2) an

unsuccessful extraction procedure in general, (3) a loss of bioactivity following extraction, or (4) the concentration of active compound(s) required to induce a significant effect on paralysis was not reached. Further experiments are required to distinguish between each of these probabilities.



### 6.2.6 Siderophore supplementation does not suppress A $\beta$ <sub>1-42</sub>-associated toxicity

As our attempt to extract the protective compounds of MYb57 CFM into organic solvents while maintaining A $\beta$ -associated paralysis suppression was unsuccessful, we pursued a bioinformatics-based approach. The Antibiotics and Secondary Metabolite Analysis Shell (antiSMASH) is a software designed for the detection and characterisation of biosynthetic gene clusters within bacterial and fungal genomes (Medema et al. 2011). The pipeline identifies biosynthetic loci across the full range of known classes of secondary metabolites: low-molecular-mass natural products typically synthesised by microorganisms that are not essential to the organism's growth and reproduction but instead serve specialised

biological functions (Mosunova et al. 2021). The results of whole-genome sequencing of each of the 11 EM member strains were submitted for biosynthetic gene cluster detection into the antiSMASH software. For the majority of the EM member strains, sequence similarity to known biosynthetic clusters was relatively low, typically falling below 50% (results in Appendix, Figure 8.4). Complete (100%) sequence similarity to documented clusters was only found in MYb27 and MYb56 genomes, containing genomic regions encoding the siderophore molecules deferrioxamine and petrobactin, respectively. Siderophores are secondary metabolites that scavenge free iron from environmental sources by forming soluble  $\text{Fe}^{3+}$  complexes that are then taken up by specialised receptors (Kramer et al. 2019; Gueriot 1994). Environmental iron primarily exists as  $\text{Fe}^{3+}$  – its oxidised ferric state – which is largely insoluble at the neutral-basic pH levels of most organismal niches (Emerson et al. 2012). Microbial species thus evolved siderophore secretion to sequester iron as the element serves as enzymatic cofactor in fundamental cellular processes including respiration, DNA synthesis, and protection from ROS (Andrews et al. 2003).

Although live MYb56 bacteria only mildly delayed paralysis onset (Figure 6.1G,  $p = 0.015$ ) and neither MYb27 CFM nor MYb56 CFM displayed an effect (Figure 6.2E and 6.2G,  $p > 0.05$ ), we decided to explore siderophore production as a potential mechanism for suppression of  $\text{A}\beta$ -associated toxicity by the EM. Given the paucity of published information on MYb strains, we considered the possibility that biosynthetic clusters of EM member strains may yet be undocumented, leading to an underrepresentation of siderophore-encoding regions in our analyses. There is a growing body of evidence linking dysregulated iron homeostasis and ferroptosis to AD pathogenesis, suggesting iron chelation as a potential mechanism by which the EM's extracellular factors might operate

(reviewed in Yan and Zhang, 2020). In addition, altered mitochondrial morphology – a phenotype we had documented in animals cultivated on the EM – has been shown to accompany ferroptosis induction (Angeli et al. 2017; Stockwell et al. 2017). Researchers have reported diminished mitochondrial cristae, condensed mitochondrial membranes, and reduced mitochondrial volume in ferroptotic cells.

We broadly asked whether siderophores were produced by the EM via a chrome azurol S (CAS) siderophore detection assay. The CAS assay is a colorimetric method that detects siderophores independently of their species or structure (Himpsl and Mobley, 2019). In the presence of siderophores, iron is scavenged from a Fe-CAS-hexadecyltrimethylammonium bromide complex resulting in a colour change from blue to orange. Following overnight incubation on CAS agar plates, we qualitatively detected siderophores in EM liquid culture (Figure 6.5A top left) and, to a lesser extent, in MYb57 liquid culture (Figure 6.7A top right, B below), while no colour change was observed in OP50 (Figure 6.7A bottom left, B above). As a positive control, we included a 1 mM preparation of the stock siderophore deferrioxamine (Sigma) which induced an obvious colour change (Figure 6.7A, bottom right). Deferrioxamine is a high-affinity hydroxamate siderophore often administered as a therapeutic for iron overdose in human subjects (Kazantis, 2007). The iron-loaded form of deferrioxamine is ferrioxamine, which is water-soluble and easily expelled from the circulation (Llamas et al. 2006).

Noting siderophore production by the EM and MYb57, we next probed whether supplementation of an OP50 lawn with known siderophore sources was sufficient to recapitulate the protection provided by CFM in paralysis assays. In addition to OP50 and

OP50+CFM feeding conditions, OP50 lawns were seeded with 100  $\mu$ M ferrioxamine B (Sigma) in sterile water or CFM isolated from a liquid culture of *Pseudomonas aeruginosa* PA14. *P. aeruginosa* PA14 is a gram-negative proteobacterium known for causing opportunistic infections, stemming from its capacity to colonise various niches within host organisms (Cornelis and Dingemans, 2013). As sustaining opportunistic growth requires a consistent supply of iron, *P. aeruginosa* PA14 has evolved multiple iron uptake strategies including the secretion of two siderophores – pyoverdine and pyochelin – with high and low affinities for iron, respectively (Visca et al. 2007; Meyer, 2000; Cox et al. 1981). Under normal conditions, *P. aeruginosa* PA14 relies on pyochelin for iron uptake but switches to pyoverdine production in cases of low environmental iron concentrations (Dumas et al. 2013).

As in previous paralysis assays, OP50-fed control *dvl-100(p<sub>unc-54</sub>::A $\beta$ <sub>1-42</sub> + p<sub>mtl-2</sub>::GFP)* animals exhibited rapid onset of paralysis with 20% ( $\pm$ 3%) of the D1 population affected, increasing to 90% ( $\pm$ 1%) on D2 and 98% ( $\pm$ 1%) at the completion of the assay on D3 (Figure 6.7C). Paralysis was significantly suppressed in worms cultivated on OP50+CFM, with 5% ( $\pm$ 2%) of the population affected on D1, 71% ( $\pm$ 1%) affected on D2, and 94% ( $\pm$ 1%) affected on D3 (see Appendix, 8.1-8.34 for *p* values). Supplementation of OP50 lawns with 100  $\mu$ M ferrioxamine did not suppress paralysis progression in comparison to OP50-fed controls at any of the tested timepoints. Paralysis was elevated in D1 OP50+Ferrioxamine animals with 28% ( $\pm$ 5%) of the population affected, increasing to 85% ( $\pm$ 9%) on D2, and finally 98% ( $\pm$ 3%) on D3. By contrast, CFM isolated from a liquid culture of *P. aeruginosa* PA14 was found to suppress A $\beta$ -associated paralysis with the same efficacy as EM CFM. On D1 of adulthood, 6% ( $\pm$ 2%) of the population displays paralysis increasing to 72% ( $\pm$ 8%) on D2, and finally 96% ( $\pm$ 6%) on D3. The suppression of

paralysis by *P. aeruginosa* PA14 CFM supports the hypothesis that siderophore production and iron chelation mitigate A $\beta$ -associated toxicity and suggests a potential mechanism for the EM and its CFM. However, the absence of a protective effect by direct supplementation with the iron-loaded ferrioxamine B may suggest that the mechanism relies on high-affinity iron chelators. To address this, we performed another set of paralysis assays using OP50 plates supplemented with 1 mM deferrioxamine (Sigma) (Figure 6.7D). Within this data set, 26% ( $\pm 3\%$ ) of OP50-fed control animals exhibited paralysis on D1 of adulthood, increasing to 92% ( $\pm 1\%$ ) on D2 and 98% ( $\pm 1\%$ ) on D3. No difference in paralysis onset was observed following supplementation of OP50 lawns with deferrioxamine at any of the timepoints scored ( $p > 0.05$ , see Appendix 8.1-8.34 for specific  $p$  values). However, as paralysis suppression was not observed in the OP50+CFM positive control condition, caution must be exercised in drawing a conclusion cannot be drawn from the data set presented in Figure 6.7D. Taken together, the data suggests that administration of the siderophores deferrioxamine B or its iron-loaded form ferrioxamine have no effect on A $\beta$ -associated paralysis inhibition. We also considered the possibility that ferrioxamine B or deferrioxamine entry into cells was unsuccessful, as uptake was not assessed within the experiment.

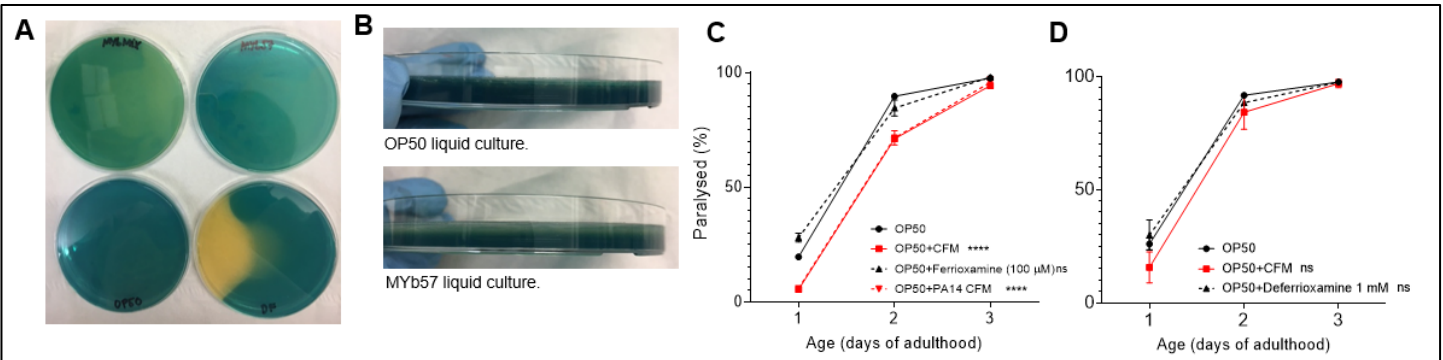


**Figure 6.7. Siderophore supplementation does not suppress A $\beta$ -associated paralysis.** (A) Blue to orange colorimetric change in CAS agar plates upon detection of siderophore species. (A, top left) EM liquid culture induces a colour change in CAS agar plates, suggesting presence of siderophore species. (A, bottom left and B, above) *E. coli* OP50 does not induce a colour change in CAS agar plates, suggesting absence of siderophore species. (A, top right and B, below) MYb57 liquid culture induces a mild colour change in CAS agar plates, suggesting the presence of siderophore species. (A, bottom right) A 1 mM solution of the siderophore deferrioxamine induces an intense colorimetric change in CAS agar plates. (C) Supplementation of OP50 plates with 100  $\mu$ M of the iron-loaded siderophore ferrioxamine B does not suppress A $\beta$ -associated paralysis. However, CFM isolated from the siderophore-producing *P. aeruginosa* PA14 is sufficient to inhibit paralysis. (D) Supplementation of OP50 plates with 1 mM of deferrioxamine does not suppress A $\beta$ -associated paralysis. However, note that OP50+CFM control condition does not inhibit paralysis as anticipated, preventing a conclusion on deferrioxamine efficacy from being drawn. (C-D) Statistical analysis by two-way ANOVA (\*\*\*\* $p$ , ns  $p > 0.05$ ). Statistical significance refers to D2 paralysis proportions as compared to OP50 control condition only. Data represents means of two independent trials ( $n = 100$  animals per trial)  $\pm$  SEM.

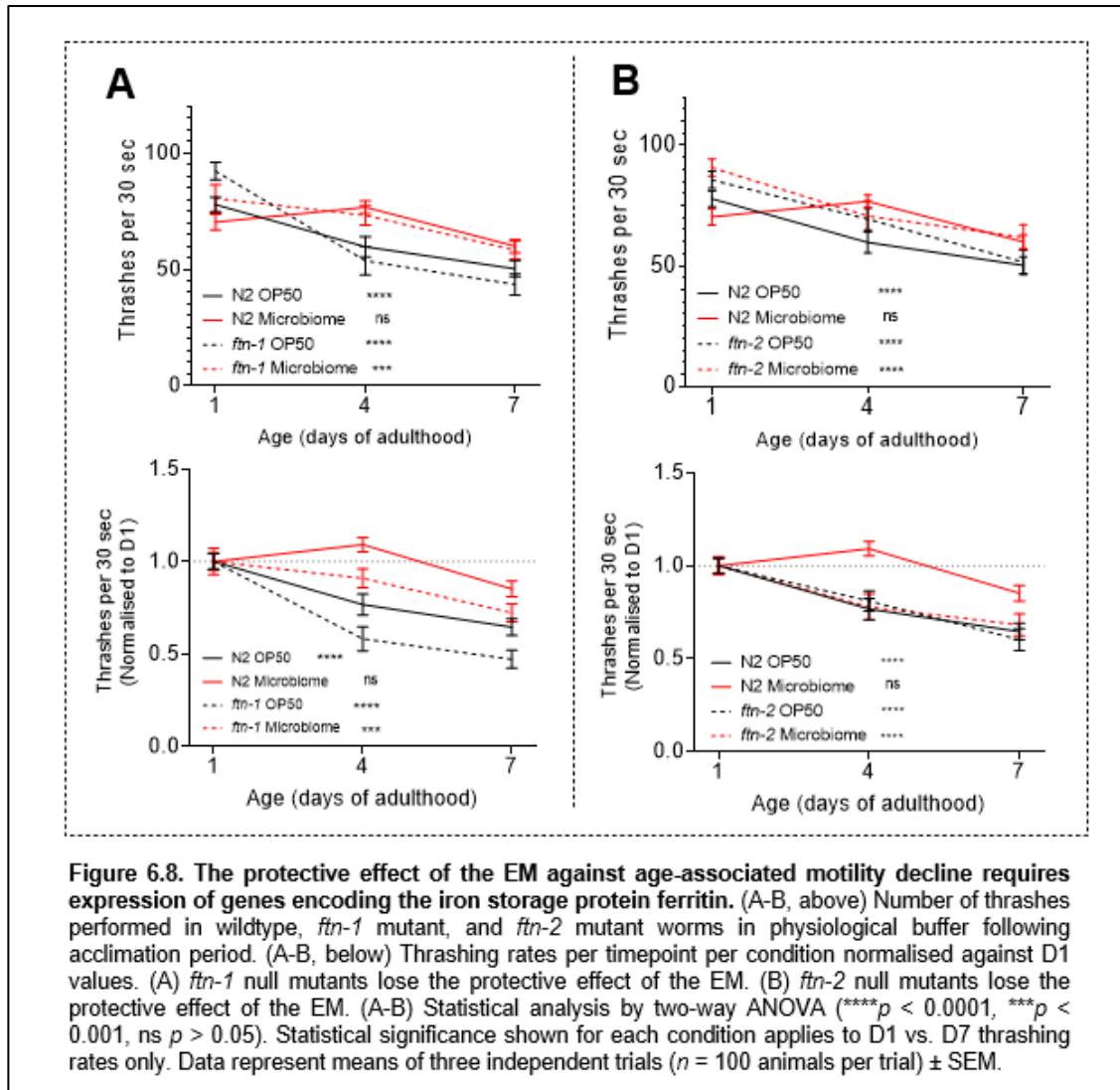
### 6.2.7 Suppression of late-life motility decline by the experimental microbiome involves genes encoding ferritin

With some indication that siderophore activity may contribute to EM effects on A $\beta$  associated toxicity, we sought to determine if iron chelation was involved in other EM-induced phenotypes we had observed. To probe this link, we tested whether the suppression of motility decline by the EM required genes encoding the iron storage protein ferritin. The *C. elegans* genome contains two such genes – *ftn-1* and *ftn-2* – that exhibit regional expression, with *ftn-1* highly expressed in the intestine and *ftn-2* in the pharynx, muscle, hypodermis, and at lower levels in the intestine (Kim et al. 2004; Gourley et al. 2003). Lateral swimming (thrashing) was measured in null mutants for *ftn-1* and *ftn-2* cultivated on OP50 or the EM, with wildtype animals on the same feeding conditions included as controls. As previously observed, wildtype nematodes reared on OP50 exhibited a 35% decline in thrashing rate between D1 and D7 of adulthood, from a mean rate of 77.83 ( $\pm$ 3.29) thrashes per 30 seconds to 50.30 ( $\pm$ 3.48) thrashes per 30 seconds

( $p < 0.0001$ ) (Figure 6.6A). By contrast, although wildtype nematodes cultivated on the EM thrash at a 15% lower rate on D7 compared to D1, falling from a mean rate of 70.38 ( $\pm 3.48$ ) thrashes per 30 seconds to 59.98 ( $\pm 2.98$ ) thrashes per 30 seconds, the decline in motility was not found to be significant ( $p = 0.122$ ). Motility in OP50-fed *ftn-1* null mutants was found to decline with age in a similar fashion as wildtype worms on the same food source, declining by 53% between D1 and D7 ( $p < 0.0001$ ). Unlike wildtype worms cultivated on the EM, EM-fed *ftn-1* mutant worms' thrashing rates decline by a significant 28% from D1 to D7 ( $p = 0.0009$ ), indicating that the protective effect of the EM is lost in animals lacking a functional *ftn-1* gene.

A similar effect was observed in *ftn-2* null mutants. *ftn-2* mutants reared on OP50 exhibited a 40% decline in thrashing rate from D1 to D7 ( $p < 0.0001$ ), while *ftn-2* mutants on the EM also exhibited a highly significant 32% decline in thrashing rate ( $p > 0.0001$ ) (Figure 6.6B). The protective effect of the EM against a decline in thrashing rate was thus lost in animals lacking a functional *ftn-2* gene. Taken together, the data suggests that ferritin expression is required for the EM effect on age-associated motility decline regardless of the tissue in which it is expressed. However, the magnitude of the motility decline in *ftn-1* null mutants, although significant, suggests that EM-mediated effects are not fully abolished by the gene knockout. On D4 of adulthood, EM-fed *ftn-1* mutants still thrash at a 36% greater rate than OP50-fed mutants ( $p = 0.0085$ ), and a 34% higher rate on D7 ( $p = 0.084$ , approaching significance) (Figure 6.8A). Conversely, the protective effect of the EM was completely abolished by *ftn-2* knockout, with OP50-fed and EM-fed *ftn-2* mutants exhibiting parallel declines in thrashing rate on both D4 ( $p = 0.997$ ) and D7 ( $p = 0.345$ ) of adulthood (Figure 6.8B). The results indicate that while general ferritin expression is required for EM-mediated suppression of motility decline with age, diffuse expression in various tissues (in

the pharynx, body wall muscle, and hypodermis) underlies this effect more critically than intestinal ferritin expression alone.



## 6.3 Discussion

### 6.3.1 Experimental microbiome suppresses A $\beta$ proteotoxicity

There is a large body of emerging evidence linking the progression of proteotoxic disease and gut microbiota. In this chapter, we examined the effects of cultivation on the EM in the context of a *C. elegans* model of age-associated proteotoxic disease. Transgenic *C. elegans* expressing the human isoform of amyloid beta (A $\beta$ ) characteristic of Alzheimer's disease, A $\beta$ <sub>1-42</sub>, undergo full-body paralysis in a non-permissive temperature. We showed that cultivation on the EM dramatically suppresses paralysis onset. The contributions of individual EM member strains to A $\beta$ <sub>1-42</sub> paralysis suppression were assessed through monoxenic rearing. Worms cultivated on individual member strains displayed varying paralysis severities, with the majority of species suppressing paralysis to an intermediate degree in comparison to the positive and negative EM and OP50 control conditions, respectively. MYb11 (*Pseudomonas lurida*) appeared to be the most efficacious bacterial species, with paralysis proportions indistinguishable from the EM condition at all timepoints tested. However, worms reared on MYb11 exhibited slow growth and a dramatically reduced body size. Although worms reared on the total EM also displayed a slight reduction in length, the timing of larval development was equal to that of OP50-fed controls, indicating that any deleterious effects of MYb11 rearing may have been overridden by the nutritional benefit of other EM member strains. Moreover, previous studies colonising worms using MYb11 reported an overall increase in fecundity that was inconsistent with our findings using the EM (Kissoyan et al. 2022). An elimination experiment in which the EM is prepared as normal with the exception of MYb11 would be valuable, where abrogation of paralysis suppression would serve as direct evidence of the species' involvement in the community effect. Conversely, other EM member strains such as MYb120 (*Chryseobacterium* sp. CHNTR56) and MYb218 (*Pseudomonas*

*tuomeurensis*), did not appear to contribute to paralysis suppression. Altogether, the data suggests that the benefit provided by the EM against A $\beta$ <sub>1-42</sub> toxicity is an emergent feature that relies on the interaction of multiple microbial species rather than the presence of any individual component. Our findings have important implications for understanding interactions between commensal microbes and amyloid proteotoxicity in *C. elegans*. As far as we know, our work represents the first evidence of a microbiome-based intervention to ameliorate phenotypes associated with A $\beta$ <sub>1-42</sub> aggregation in nematodes – although this relationship has been demonstrated in higher animal models and human subjects (Varesi et al. 2022; Chen et al. 2020; Vogt et al. 2017). This work highlights an opportunity to identify therapeutic interventions with the potential for translation into mammalian models, if a mechanistic basis for the effect can be identified.

Previous studies have implicated mitochondrial fragmentation as an important contributor to the pathogenesis of Alzheimer's disease (Liu et al. 2020). A $\beta$  deposition in neurons increases nitric oxide levels, activating the human orthologue of DRP-1, DRP1, via S-nitrosylation and inducing mitochondrial fission (Cho et al. 2009). Consistent with this observation, pharmacological inhibition of mitochondrial fission has been shown to alleviate A $\beta$ -dependent neuronal apoptosis (Kim et al. 2016). Collectively these data suggest restoration of mitochondrial homeostasis as a potential therapeutic strategy for the deleterious effects of A $\beta$  accumulation. Given that we observed EM-mediated protection from A $\beta$ -associated toxicity as well as altered mitochondrial homeostasis, we sought to determine whether these two phenotypes were linked by first assessing mitochondrial network states in paralysed versus motile animals. We attempted to cross transgenic animals expressing A $\beta$ <sub>1-42</sub> in body wall muscle with those possessing GFP-labelled body wall muscle mitochondria. Unfortunately, an intestinal GFP signal in the transgenic A $\beta$ -expressing strain obstructed successful completion of this genetic cross

(McColl et al. 2012). Additional methods of assessing mitochondrial health in EM-fed animals, including mtDNA copy number, ATP production, and oxygen consumption rate, are currently underway to characterising a more comprehensive profile of mitochondrial health in EM-fed worms.

### 6.3.2 Cell-free media from experimental microbiome inhibits A $\beta$ <sub>1-42</sub> aggregation

A $\beta$ <sub>1-42</sub>-associated paralysis was partially, but significantly, ameliorated when OP50 bacterial lawns were supplemented with cell-free media (CFM) isolated from the EM. This finding suggests that extracellular material produced by EM strains contributes, at least in part, to the overall protective effect. In the case of CFM, no single EM member strain suppressed paralysis aside from MYb57 (*Stenotrophomonas* sp. R-41388), which inhibited paralysis to an extent indistinguishable from combined CFM. We interpret this as an indication that either (1) the anti-paralysis effect of CFM is another emergent feature dependent on the concerted efficacies of several sub-threshold bacterial CFMs, or (2) that MYb57 is the primary contributor to the CFM effect. Once again, this project would be benefitted by an A $\beta$ <sub>1-42</sub>-associated paralysis assay using CFM prepared with standard procedure save for the omission of MYb57 CFM, to determine if the protective effect against paralysis is lost. Interestingly, live MYb57 bacteria was shown to have no significant effect on paralysis onset. We hypothesise that this may be due to mild pathogenicity of the live bacterium that does not persist in its extracellular material. The beneficial effects of MYb57 CFM against A $\beta$ <sub>1-42</sub>-associated toxicity may therefore be occluded by the detrimental effects of the bacterium in its live form – a plausible scenario given the reported pathogenicity of the opportunistic human pathogen *Stenotrophomonas maltophilia* (Trifonova and Strateva, 2018) and the phytopathogenicity of *Stenotrophomonas indologenes* (Ryan et al. 2009). As only ten *Stenotrophomonas*

species have been extensively described so far, the full profile of the genus' pathogenicity is yet undetermined (Alavi et al. 2014; Ryan et al. 2009). The finding that EM CFM protects against  $A\beta_{1-42}$ -associated toxicity implies that the effects of live EM bacteria and their extracellular compounds are dissociable, allowing for detailed study of each component individually. This is particularly useful for analyses such as the ThT assay described below, where the presence of bacterial cells interferes with fluorescence detection.

With the assistance of the Labbadia lab (University College London), we determined that the EM had no effect on polyglutamine (polyQ) aggregation associated with the human proteotoxic disorder Huntington's disease. This was validated by two approaches: by quantifying fluorescent Q35 aggregate numbers in D1 and D5 animals and through scoring of polyQ-associated paralysis up to D13 and. No difference in aggregation numbers nor in paralysis onset was identified between cultivation conditions, undermining the hypothesis that the EM and its CFM protect against general proteotoxicity. The results also served as an indication the EM may not exert benefit by improving the nematode's ability to cope with proteotoxic stress.

Noting the protective effect of EM CFM against  $A\beta_{1-42}$ -associated paralysis as well as the absence of such protection against polyQ toxicity, we asked whether CFM inhibited the aggregation of the  $A\beta_{1-42}$  peptide itself. Leveraging conformational changes in the benzothiazole dye thioflavin T (ThT) upon amyloid binding resulting in fluorescence emission, we determined that CFM isolated from minimal media-grown EM inhibited the fibrillisation of  $A\beta_{1-42}$  *in vitro*, with no fibril formation detected over the total duration of the

assay. In the minimal media-grown OP50 CFM control condition, A $\beta$ <sub>1-42</sub> fibrillisation was detected within 30 minutes from the assay's commencement.

We noted several instances where an EM member strain was shown to inhibit A $\beta$  fibril formation but did not have a corresponding effect on A $\beta$ -associated paralysis, such as MYb11 CFM, MYb27 CFM, and MYb83 CFM. This may point to a concentration-dependent effect, in which the A $\beta$ -inhibiting compounds present in the CFM of each of these member strains are sufficient to suppress fibrillisation *in vitro* but are at ineffective concentrations to elicit a phenotype *in vivo*. Paralysis in A $\beta$ -expressing worms is an easily recognisable phenotype that may permit rapid screening, but utilising a binary system (paralysed versus motile) to score proteotoxicity limits the sensitivity of detection. For instance, MYb27 (*Arthrobacter aureescens*) CFM was found to be one of the most potent inhibitors of A $\beta$  fibrillisation *in vitro*, although no effect on paralysis was reported on D2 of adulthood where the effect of EM CFM is most prominent. However, MYb27 CFM did exhibit an anti-paralysis effect on D1 of adulthood ( $p = 0.003$ ). Once again, the bioactivity of CFM in the A $\beta$  paralysis assay may be an emergent feature of multiple sub-threshold bacterial species converging to inhibit A $\beta$  fibril formation. We also considered the likely possibility that paralysis inhibition by EM CFM is due to multiple underlying mechanisms acting in concert, rather than the action of fibril-inhibiting compounds alone. Further research is required to distinguish between these probabilities, and to discount that fluorescence suppression was artefactual and due to indiscriminate binding of ThT to non-amyloid material. However, given the consistency of fluorescence signal increases in control conditions, it was concluded that the suppression of A $\beta$ -associated toxicity is contributed, albeit partially, by the inhibition of A $\beta$ <sub>1-42</sub> fibril formation. Our findings have

important implications for the identification of compounds capable of inhibiting A $\beta$ <sub>1-42</sub> aggregation as a potential therapeutic approach against amyloid diseases.

As we were unable to successfully extract the bioactive components of MYb57 extracellular material capable of ameliorating A $\beta$ -associated toxicity, no conclusions on the properties of these compounds, such as their polarity and solubility, can be drawn, although unpublished work carried out alongside this project determined that CFM retains its anti-paralysis effects after heat treatment at 95°C for one hour. We considered that the extracellular compounds shown to be efficacious in the preceding paralysis and ThT assays may have been degraded during the extraction process, or that post-extraction concentrations were sub-threshold and unable to mount an anti-paralysis effect. To increase sensitivity of detection, MYb57 extractions are currently underway to evaluate the effects of extracts on A $\beta$ <sub>1-42</sub> fibrillisation via ThT binding assay rather than A $\beta$ -associated paralysis.

### 6.3.3 Iron processing genes are required for experimental microbiome effects on locomotion

Microbial species are known to contribute greatly to iron homeostasis and processing in host organisms (Andrews et al. 2003). Some indication of a potential mechanistic basis for the beneficial effect of EM was provided by finding that the EM produces siderophores: organic ligands with an affinity for iron. These molecules scavenge iron from environmental stocks and deliver it to cells via specialised receptors. The significance of regulated iron processing in AD has been demonstrated by studies linking elevated iron concentrations with disease pathology (Ayton et al. 2019; Peters et al. 2015; Ward et al. 2014).

No effect on A $\beta$ -associated paralysis was observed following supplementation of OP50 lawns with the standard siderophore desferrioxamine or its iron-loaded form. However, A $\beta$ -associated paralysis suppression akin to that induced by CFM was observed following supplementation with CFM isolated from *Pseudomonas aeruginosa* PA14. *P. aeruginosa* PA14 produces two siderophores of varying iron affinities – pyoverdine and pyochelin – and primarily relies on the lower-affinity pyochelin until environmental iron is scarce (Dumas et al. 2013; Visca et al. 2007; Cox et al. 1981). While the lack of efficacy in the desferrioxamine and ferrioxamine conditions undermines the hypothesis that EM CFM ameliorates A $\beta$ -associated paralysis through iron chelation and siderophore production, the results of PA14 CFM supplementation suggest otherwise. It is possible that (1) the EM CFM effect relies on the action of particular siderophores, (2) the EM CFM effect relies on siderophores of specified iron affinities, or (3) uptake of stock siderophores desferrioxamine and ferrioxamine was unsuccessful. Moreover, *Pseudomonas aeruginosa* is a facultative pathogen capable of infecting *C. elegans* (Mahajan-Miklos et al. 1999). Although here only provided to nematodes in the form of CFM, *P. aeruginosa* PA14 produces three diffusible small molecules of the phenazine class that are toxic towards *C. elegans* (Cezairliyan et al. 2013). Kirienko et al. (2014) also demonstrated that high concentrations of pyoverdine were sufficient to induce a hypoxic response in the worm even in the absence of live bacteria. It is worth considering that the protection from A $\beta$ -associated paralysis provided by PA14 CFM may not be mediated by enhanced iron processing but by the activation of host immune pathways in response to extracellular virulence factors or stress pathways in response to hypoxia. Additional experiments supplementing OP50 lawns with various siderophores with wide-ranging iron affinities would help to clarify a role for iron chelation in mitigating A $\beta$ -associated paralysis.

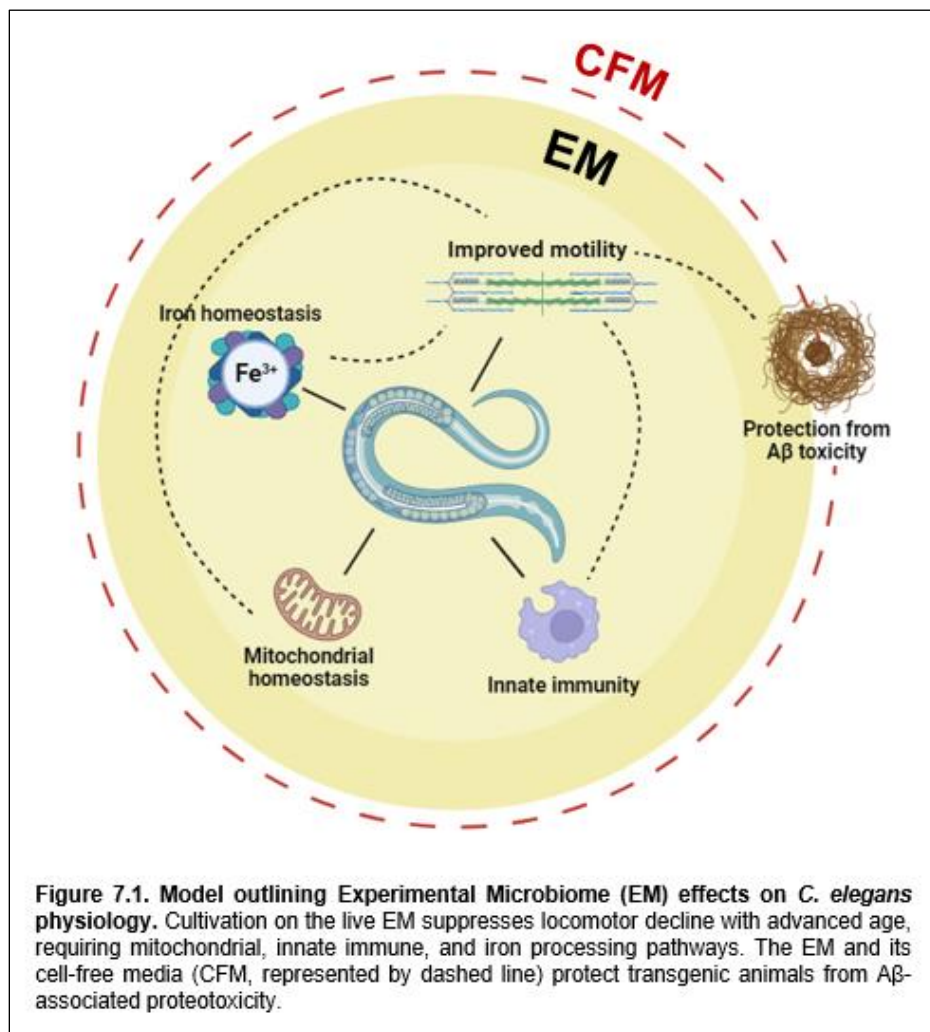
Even in the absence of a siderophore-mediated effect on A $\beta$ -associated paralysis, our findings suggest that iron homeostasis may have a role in certain EM-induced phenotypes. The suppression of locomotor decline by the EM (see Section 4.2.1) was lost in mutant animals deficient in the iron storage protein ferritin. A more severe abrogation was observed in mutants for *ftn-2* (expressed in various host tissues including the pharynx, muscle, and hypodermis) versus *ftn-1* (expressed in the intestine), suggesting that tissue-specific iron processing underlies EM effects on locomotion (Kim et al. 2004; Gourley et al. 2003). Previous studies have also shown that disrupting iron processing in the bacterial diet of *C. elegans* dysregulates mitochondrial function (Zhang et al. 2019). Iron homeostasis may therefore be a host-microbe interface where various EM-induced phenotypes converge, warranting further study.

## 7. Concluding remarks

Building on the characterisation of the nematode *C. elegans*' native microbiota (Dirksen et al. 2016; Berg et al. 2016; Samuel et al. 2016), this project aimed to uncover mechanisms by which age-associated phenotypes in the host could be altered by host-microbe interactions. An experimental microbiome was assembled, comprised of eleven bacterial species from highly enriched phylotypes identified in the native *C. elegans* intestine. The results of this project highlight the utility of using *C. elegans* as a model system to study host-microbe interactions, particularly using ecologically relevant microbial communities of moderate complexity. Previous studies featuring native microbiota members cultivated worms monoxenically, examining the effects of single bacterial species on host physiology (Kissoyan et al. 2022; Kissoyan et al. 2019; Yang et al. 2019). Although such studies have undoubtedly advanced our understanding of microbiome effects on host fecundity, susceptibility to infection, and transcription, there is a need to capture the complexity of interactions between microbiota members. Recent endeavours such as the CeMbio microbiome resource (Dirksen et al. 2020) include a microbial assembly similar to the Experimental Microbiome (EM) in breadth and specifications but have focused on developmental timing in the host, while ageing studies are limited. The work presented in this project serves as a proof-of-concept for supporting growth and development on a representative microbiome and expands the battery of healthspan metrics assessed in response.

The evidence presented here demonstrates that the EM colonises the *C. elegans* intestine, supports growth and development of the host and suppresses locomotor decline associated with age. The protective effect on motility is dependent on the p38 MAPK

pathway of innate immunity, iron processing by the storage protein ferritin, and mitochondrial homeostasis. Moreover, the EM induces rearrangement of mitochondrial networks, but additional study is necessary to determine whether mitochondrial function is subsequently affected. In addition to improving motility in wildtype animals, the EM also protects against paralysis in a *C. elegans* model of A $\beta$  proteotoxicity. A simplified overview of this model is presented in Figure 7.1.



Although this project has demonstrated the potential of microbiota to extend aspects of host healthspan, many questions remain unanswered. The protection from locomotory decline conferred by the EM requires functional expression of genes from various signalling cascades, suggesting that the underlying mechanisms involve multiple physiological systems. Innate immunity, mitochondrial dynamics and surveillance, and iron processing pathways are all involved in EM-mediated preservation of motility. What is still unknown is whether these pathways interact with one another, if activation of these pathways occurs sequentially, and what the underlying mechanism for this interaction may be. As a bacterivore, the nematode has evolved immune defence mechanisms within the intestinal epithelium that are initiated upon ingestion of microorganisms (Pukkila-Worley and Ausubel, 2012). We considered that innate immune activation may be the initial event driving the concerted response to the EM. We asked whether EM-induced mitochondrial fragmentation was abrogated in mutants deficient in the downstream MAP kinase-encoding *pmk-1* and observed persistent mitochondrial fragmentation in body wall muscle. While this finding suggests that *pmk-1* expression is not required for EM effects on mitochondrial dynamics, we previously noted that knockouts in the upstream PMK pathway components more severely abrogate the EM effect on locomotion. Evaluating mitochondrial fragmentation in *tir-1* or *nsy-1* mutants would therefore provide more definitive evidence of an association between innate immunity and mitochondrial network restructuring. An inverse mechanistic linkage – in which altered mitochondrial network states influence p38 MAPKK signalling – should also be investigated going forward. There is added benefit in expanding the list of cellular stress pathways investigated in response to cultivation on the EM beyond the PMK pathway of innate immunity and the UPR<sup>mt</sup>, including the cytosolic heat-shock response (HSR), the endoplasmic reticulum unfolded protein response (UPR<sup>er</sup>), and autophagy. Fluorescent transcriptional reporters are available for components of each of these pathways to first establish whether their

activation is altered by exposure to the EM. The availability of the corresponding null mutants for these components would also allow us to determine whether these pathways contribute to EM effects on motility.

Previous studies have demonstrated the efficacy of microbiota-based interventions against proteotoxic disease in higher animals (Varesi et al. 2022; Chen et al. 2020; Vogt et al. 2017) as well as nematodes (Goya et al. 2020). However, no published study in *C. elegans* has used this approach to target A $\beta$  proteotoxicity specifically. The EM significantly suppresses A $\beta$ -associated paralysis in transgenic nematodes, with dissociable effects contributed by live EM bacteria and their cell-free media (CFM). We also have yet to identify the compound(s) that ameliorate A $\beta$ -associated proteotoxicity, both in live EM as well as the assembly's cell-free supernatant. Perhaps a more fitting approach to identifying the beneficial compounds present in live EM bacteria is a series of elimination experiments in which the EM is prepared as normal with the omission of a single bacterial species. The loss of the protective effect against A $\beta$ -associated paralysis following the loss of one member species may be more revealing of the species' contributions than monoxenic feeding, as the method accounts for community interactions between remaining members. Another approach worth pursuing is crossing the transgenic strain expressing A $\beta$  in muscle into various mutant backgrounds. The loss of paralysis inhibition in this scenario would suggest genes and pathways required for the EM's effects on A $\beta$ -associated toxicity. Importantly, this would allow us to ascertain whether the cellular and molecular drivers of EM effects on age-dependent motor decline and A $\beta$ -associated paralysis converge, or if these mechanisms are dissociable.

This project also documented attempts to extract bio-active material from MYb57 CFM into various organic solvents, that proved ineffective. Attempts to characterise bio-active extracellular compounds in CFM, either from combined EM CFM or MYb57 CFM alone, have been made in parallel using a variety of techniques not detailed in this project. While nuclear magnetic resonance (NMR) spectroscopy and high-performance liquid chromatography (HPLC) analyses have indicated certain properties of CFM constituents, validating these findings through A $\beta$ -associated paralysis assays has been unsuccessful. We speculate that the bio-active components of CFM are degraded during extraction/distillation/fractionation processes inherent to these analyses or that the concentrations required to elicit detectable responses in the nematode are not reached. Going forward, these analyses should be replicated utilising a more sensitive final readout, such as inhibition of A $\beta$  fibrillisation via a ThT assay. However, this does not account for the possibility that the extracellular compounds inhibiting paralysis *in vivo* are distinct from those inhibiting aggregation *in vitro*. Experiments generating mutations in *Stenotrophomonas* species closely related to MYb57 are currently underway to determine whether the protective effect of the species' CFM against A $\beta$  proteotoxicity can be abrogated. Mapping of such mutations to biosynthetic gene clusters could help to reveal the identity of our compound(s) of interest.

There is great promise in identifying microbiota-based interventions to improve host health, particularly into advanced age. Our work demonstrates the utility of the combined system of *C. elegans* and a community of microbial symbionts and represents early steps towards understanding host-microbe interactions at different levels of granularity. Although establishing a native *C. elegans* microbiome in higher animals may not be viable, future work is directed at identifying the genetic and molecular drivers of the EM's impact

on *C. elegans* physiology. The beneficial phenotypes reported in this project following cultivation on the EM – suppression of motility decline and A $\beta$ -associated proteotoxicity – are both extremely relevant to human ageing, noting the prevalence of sarcopenia and proteinopathies such as AD and PD. Determining whether the mechanisms underlying EM effects are evolutionarily conserved will be instrumental in translating these findings to extend human healthspan.

## 8. Appendix

### 8.1-8.34 Statistical analyses for all relevant figures

Statistical analysis: Figure 3.1A. Two-way ANOVA.			
	Average CFUs per condition ( $\pm$ SEM)	<i>p</i> value	Significance
D1 OP50 vs. D1 EM	216.86 ( $\pm$ 28.40) vs. 2686.50 ( $\pm$ 540.47)	0.001	**
D7 OP50 vs. D7 EM	180 vs. 1533 ( $\pm$ 165.42)	0.789	ns
D1 OP50 vs. D7 OP50	216.86 ( $\pm$ 28.40) vs. 180	>0.999	ns
D1 EM vs. D7 EM	2686.50 ( $\pm$ 540.47) vs. 1533 ( $\pm$ 165.42)	0.434	ns

Statistical analysis: Figure 3.1B (NGM plates).		
	Average proportion (%) per species	SEM
MYb9	4.71	0.96
MYb10	38.98	6.42
MYb11	3.43	0.74
MYb27	0.07	0.02
MYb45	0.06	0.01
MYb56	5.22	3.68
MYb57	29.60	5.26
MYb71	1.91	0.77
MYb83	0.01	0.01
MYb120	11.45	3.16
MYb218	0.00	0.00

Statistical analysis: Figure 3.1C (Intestine).		
	Average proportion (%) per species	SEM
MYb9	6.51	0.92
MYb10	4.64	0.76
MYb11	5.41	0.89
MYb27	0.33	0.18
MYb45	1.10	0.59
MYb56	1.40	0.39
MYb57	38.06	5.06
MYb71	31.07	3.34
MYb83	0.01	0.01
MYb120	5.23	1.72
MYb218	0.00	0.00

Statistical analysis: Figure 3.2A.			
	Median lifespan (days)	<i>p</i> value (Log-Rank)	Significance
OP50	15.00	<0.0001	****
EM	12.00		

Statistical analysis: Figure 3.2B. Two-way ANOVA.			
	Average length per condition (pixels) ( $\pm$ SEM)	<i>p</i> value	Significance
D1 OP50 vs. D1. EM	134.11 ( $\pm$ 1.00) vs. 119.21 ( $\pm$ 1.62)	<0.0001	****
D4 OP50 vs. D4 EM	164.18 ( $\pm$ 1.22) vs. 138.94 ( $\pm$ 1.58)	<0.0001	****
D7 OP50 vs. D7 EM	175.39 ( $\pm$ 1.44) vs. 147.33 ( $\pm$ 2.27)	<0.0001	****
D1 OP50 vs. D7 OP50	134.11 ( $\pm$ 1.00) vs. 175.39 ( $\pm$ 1.44)	<0.0001	****
D1 EM vs. D7 EM	119.21 ( $\pm$ 1.62) vs. 147.33 ( $\pm$ 2.27)	<0.0001	****

Statistical analysis: Figure 3.2C, D. Chi-square test.			
	Average proportions (%) per stage ( $\pm$ SEM)	<i>p</i> value	Significance
L3 OP50 vs. L3 EM	5.90 ( $\pm$ 0.61) vs. 5.29 ( $\pm$ 1.59)	>0.999	ns
Early L4 OP50 vs. Early L4 EM	22.65 ( $\pm$ 4.97) vs. 24.84 ( $\pm$ 4.91)	0.997	ns
Late L4 OP50 vs. Late L4 EM	52.06 ( $\pm$ 3.90) vs. 42.31 ( $\pm$ 5.48)	0.551	ns
Adult OP50 vs. Adult EM	19.40 ( $\pm$ 9.34) vs. 27.56 ( $\pm$ 3.22)	0.698	ns

Statistical analysis: Figure 3.2E, F. Two-way ANOVA and Student's t-test for total size.			
	Average progeny number per condition ( $\pm$ SEM)	<i>p</i> value	Significance
D1 OP50 vs. D1 EM	32.61 ( $\pm$ 5.67) vs. 32.59 ( $\pm$ 3.90)	0.948	ns
D2 OP50 vs. D2 EM	129.48 ( $\pm$ 7.11) vs. 88.10 ( $\pm$ 7.72)	<0.0001	****
D3 OP50 vs. D3 EM	69.61 ( $\pm$ 6.04) vs. 28.41 ( $\pm$ 4.90)	<0.0001	****
D4 OP50 vs. D4 EM	13.57 ( $\pm$ 5.01) vs. 11.52 ( $\pm$ 2.65)	0.999	ns
D5 OP50 vs. D5 EM	1.52 ( $\pm$ 0.75) vs. 1.10 ( $\pm$ 0.51)	>0.999	ns
D6 OP50 vs. D6 EM	0.00 ( $\pm$ 0.00) vs. 0.12 ( $\pm$ 0.08)	>0.999	ns
Total OP50 vs. Total EM	246.59 ( $\pm$ 9.92) vs. 161.79 ( $\pm$ 7.76)	<0.0001	****

Statistical analysis: Figure 3.3A. Two-way ANOVA.			
	Average proportions per condition (%)	<i>p</i> value	Significance
On OP50 from OP50 vs. On EM from EM (familiar food source)	55.41 ( $\pm$ 3.23) vs. 61.01 ( $\pm$ 3.71)	0.605	ns
On EM from OP50 vs. On OP50 from EM (unfamiliar food source)	39.00 ( $\pm$ 4.27) vs. 36.28 ( $\pm$ 3.97)	0.909	ns

Statistical analysis: Figure 3.3B. Two-way ANOVA.			
	Average pharyngeal pumps per condition ( $\pm$ SEM)	<i>p</i> value	Significance
D1 OP50 vs. D1 EM	167.20 ( $\pm$ 4.13) vs. 191.85 ( $\pm$ 3.37)	<0.0001	****
D4 OP50 vs. D4 EM	140.60 ( $\pm$ 4.34) vs. 181.80 ( $\pm$ 2.81)	<0.0001	****
D7 OP50 vs. D7 EM	111.80 ( $\pm$ 4.40) vs. 124.20 ( $\pm$ 4.83)	0.114	ns
D1 OP50 vs. D7 OP50	167.20 ( $\pm$ 4.13) vs. 111.80 ( $\pm$ 4.40)	<0.0001	****
D1 EM vs. D7 EM	191.85 ( $\pm$ 3.37) vs. 124.20 ( $\pm$ 4.83)	<0.0001	****

Statistical analysis: Figure 3.3C,D. Two-way ANOVA.			
	Average DMPs per min per condition ( $\pm$ SEM)	<i>p</i> value	Significance
D1 OP50 vs. D1 EM	1.24 ( $\pm$ 0.10) vs. 1.30 ( $\pm$ 0.09)	0.945	ns
D4 OP50 vs. D4 EM	0.57 ( $\pm$ 0.07) vs. 0.63 ( $\pm$ 0.06)	0.921	ns
D7 OP50 vs. D7 EM	0.43 ( $\pm$ 0.07) vs. 0.34 ( $\pm$ 0.08)	0.783	ns
D1 OP50 vs. D7 OP50	1.24 ( $\pm$ 0.10) vs. 0.43 ( $\pm$ 0.07)	<0.0001	****
D1 EM vs. D7 EM	1.30 ( $\pm$ 0.09) vs. 0.34 ( $\pm$ 0.08)	<0.0001	****

Statistical analysis: Figure 4.2A. Two-way ANOVA.			
	Average thrashes per 30 sec per condition ( $\pm$ SEM)	<i>p</i> value	Significance
D1 OP50 vs. D1 EM	82.25 ( $\pm$ 1.34) vs. 73.72 ( $\pm$ 1.52)	0.0002	***
D4 OP50 vs. D4 EM	68.62 ( $\pm$ 1.64) vs. 81.53 ( $\pm$ 1.32)	<0.0001	****
D7 OP50 vs. D7 EM	56.95 ( $\pm$ 1.61) vs. 69.50 ( $\pm$ 1.45)	<0.0001	****
D1 OP50 vs. D4 OP50	82.25 ( $\pm$ 1.34) vs. 68.62 ( $\pm$ 1.64)	<0.0001	****
D4 OP50 vs. D7 OP50	68.62 ( $\pm$ 1.64) vs. 56.95 ( $\pm$ 1.61)	<0.0001	****
D1 OP50 vs. D7 OP50	82.25 ( $\pm$ 1.34) vs. 56.95 ( $\pm$ 1.61)	<0.0001	****
D1 EM vs. D4 EM	73.72 ( $\pm$ 1.52) vs. 81.53 ( $\pm$ 1.32)	0.0007	***
D4 EM vs. D7 EM	81.53 ( $\pm$ 1.32) vs. 69.50 ( $\pm$ 1.45)	<0.0001	****
D1 EM vs. D7 EM	73.72 ( $\pm$ 1.52) vs. 69.50 ( $\pm$ 1.45)	0.129	ns

Statistical analysis: Figure 4.3A. Two-way ANOVA.			
	Average touches eliciting response (%) per condition ( $\pm$ SEM)	<i>p</i> value	Significance
D1 OP50 vs. D1 EM	60.33 ( $\pm$ 2.38) vs. 63.00 ( $\pm$ 3.27)	0.999	ns
D4 OP50 vs. D4 EM	54.67 ( $\pm$ 3.64) vs. 57.00 ( $\pm$ 2.55)	0.953	ns
D7 OP50 vs. D7 EM	51.67 ( $\pm$ 3.53) vs. 55.00 ( $\pm$ 3.85)	0.877	ns
D11 OP50 vs. D11 EM	45.33 ( $\pm$ 2.78) vs. 48.57 ( $\pm$ 2.63)	0.912	ns
D1 OP50 vs. D11 OP50	60.33 ( $\pm$ 2.38) vs. 45.33 ( $\pm$ 2.78)	0.0045	**
D1 EM vs. D11 EM	63.00 ( $\pm$ 3.27) vs. 48.57 ( $\pm$ 2.63)	0.018	*

Statistical analysis: Figure 4.3E, F, G. Two-way ANOVA.			
	Average # morphological abnormalities per condition ( $\pm$ SEM)	<i>p</i> value	Significance
Blebs per ALM process			
D1 OP50 vs. D1 EM	0.30 ( $\pm$ 0.14) vs. 0.67 ( $\pm$ 0.29)	0.624	ns
D4 OP50 vs. D4 EM	0.56 ( $\pm$ 0.21) vs. 0.63 ( $\pm$ 0.21)	>0.999	ns
D7 OP50 vs. D7 EM	1.59 ( $\pm$ 0.39) vs. 0.91 ( $\pm$ 0.25)	0.198	ns
D1 OP50 vs. D7 OP50	0.30 ( $\pm$ 0.14) vs. 1.59 ( $\pm$ 0.39)	0.0023	**
D1 EM vs. D7 EM	0.67 ( $\pm$ 0.29) vs. 0.91 ( $\pm$ 0.25)	0.894	ns
Waves per ALM process			
D1 OP50 vs. D1 EM	0.03 ( $\pm$ 0.03) vs. 0.09 ( $\pm$ 0.06)	0.994	ns
D4 OP50 vs. D4 EM	0.31 ( $\pm$ 0.14) vs. 0.70 ( $\pm$ 0.23)	0.312	ns
D7 OP50 vs. D7 EM	1.04 ( $\pm$ 0.30) vs. 0.30 ( $\pm$ 0.19)	0.015	*
D1 OP50 vs. D7 OP50	0.03 ( $\pm$ 0.03) vs. 1.04 ( $\pm$ 0.30)	0.0004	***
D1 EM vs. D7 EM	0.09 ( $\pm$ 0.06) vs. 0.30 ( $\pm$ 0.19)	0.750	ns
Branches per ALM process			
D1 OP50 vs. D1 EM	0.30 ( $\pm$ 0.14) vs. 0.46 ( $\pm$ 0.13)	0.960	ns
D4 OP50 vs. D4 EM	0.56 ( $\pm$ 0.22) vs. 1.14 ( $\pm$ 0.25)	0.271	ns
D7 OP50 vs. D7 EM	1.59 ( $\pm$ 0.39) vs. 1.36 ( $\pm$ 0.34)	0.903	ns
D1 OP50 vs. D7 OP50	0.30 ( $\pm$ 0.14) vs. 1.59 ( $\pm$ 0.39)	0.002	**
D1 EM vs. D7 EM	0.46 ( $\pm$ 0.13) vs. 1.36 ( $\pm$ 0.34)	0.030	*

Statistical analysis: Figure 4.3H, I, J. Two-way ANOVA.			
	Average # morphological abnormalities per condition ( $\pm$ SEM)	p value	Significance
Blebs per PLM process			
D1 OP50 vs. D1 EM	0.15 ( $\pm$ 0.08) vs. 0.5 ( $\pm$ 0.16)	0.904	ns
D4 OP50 vs. D4 EM	2.56 ( $\pm$ 0.46) vs. 2.63 ( $\pm$ 0.50)	0.999	ns
D7 OP50 vs. D7 EM	4.48 ( $\pm$ 0.71) vs. 3.33 ( $\pm$ 0.37)	0.173	ns
D1 OP50 vs. D7 OP50	0.15 ( $\pm$ 0.08) vs. 4.48 ( $\pm$ 0.71)	<0.0001	****
D1 EM vs. D7 EM	0.5 ( $\pm$ 0.16) vs. 3.33 ( $\pm$ 0.37)	<0.0001	****
Waves per PLM process			
D1 OP50 vs. D1 EM	0.15 ( $\pm$ 0.08) vs. 0.42 ( $\pm$ 0.12)	0.824	ns
D4 OP50 vs. D4 EM	1.69 ( $\pm$ 0.32) vs. 1.69 ( $\pm$ 0.30)	>0.999	ns
D7 OP50 vs. D7 EM	1.00 ( $\pm$ 0.27) vs. 1.79 ( $\pm$ 0.29)	0.095	ns
D1 OP50 vs. D7 OP50	0.15 ( $\pm$ 0.08) vs. 1.00 ( $\pm$ 0.27)	0.063	ns
D1 EM vs. D7 EM	0.42 ( $\pm$ 0.12) vs. 1.79 ( $\pm$ 0.29)	0.003	***
Branches per PLM process			
D1 OP50 vs. D1 EM	0.27 ( $\pm$ 0.16) vs. 0.25 ( $\pm$ 0.08)	>0.999	ns
D4 OP50 vs. D4 EM	1.25 ( $\pm$ 0.28) vs. 0.94 ( $\pm$ 0.25)	0.847	ns
D7 OP50 vs. D7 EM	0.74 ( $\pm$ 0.22) vs. 1.79 ( $\pm$ 0.56)	0.058	ns
D1 OP50 vs. D7 OP50	0.27 ( $\pm$ 0.16) vs. 0.74 ( $\pm$ 0.22)	0.650	ns
D1 EM vs. D7 EM	0.25 ( $\pm$ 0.08) vs. 1.79 ( $\pm$ 0.56)	0.0009	***

Statistical analysis: Figure 4.4B. Chi-square test.			
	Average score per condition ( $\pm$ SEM)	p value	Significance
D1 OP50 vs. D1 EM	1.72 ( $\pm$ 0.15) vs. 2.00 ( $\pm$ 0.12)	0.128	ns
D4 OP50 vs. D4 EM	2.24 ( $\pm$ 0.19) vs. 1.80 ( $\pm$ 0.12)	0.091	ns
D7 OP50 vs. D7 EM	2.20 ( $\pm$ 0.21) vs. 2.28 ( $\pm$ 0.15)	0.176	ns
D1 OP50 vs. D7 OP50	1.72 ( $\pm$ 0.15) vs. 2.20 ( $\pm$ 0.21)	0.180	ns
D1 EM vs. D7 EM	2.00 ( $\pm$ 0.12) vs. 2.28 ( $\pm$ 0.21)	0.356	ns

Statistical analysis: Figure 4.4C,D. Two-way ANOVA.			
	Average proportion in lawn (%) per condition ( $\pm$ SEM)	p value	Significance
D1 OP50 vs. D1 EM (at 120 min)	83.33 ( $\pm$ 8.03) vs. 51.67 ( $\pm$ 11.45)	<0.0001	****
D4 OP50 vs. D4 EM (at 120 min)	69.38 ( $\pm$ 6.91) vs. 65.63 ( $\pm$ 3.83)	0.327	ns
D7 OP50 vs. D7 EM (at 120 min)	36.88 ( $\pm$ 10.65) vs. 30.63 ( $\pm$ 11.78)	0.921	ns
D1 OP50 vs. D7 OP50 (at 120 min)	83.33 ( $\pm$ 8.03) vs. 36.88 ( $\pm$ 10.65)	<0.0001	****
D1 EM vs. D7 EM (at 120 min)	51.67 ( $\pm$ 11.45) vs. 30.63 ( $\pm$ 11.78)	0.571	ns

Statistical analysis: Figure 4.4E. Two-way ANOVA.			
	Average change in length (%) per condition ( $\pm$ SEM)	p value	Significance
D1 OP50 vs. D1 EM	85.53 ( $\pm$ 0.83) vs. 86.05 ( $\pm$ 1.79)	0.986	ns
D4 OP50 vs. D4 EM	87.30 ( $\pm$ 0.90) vs. 86.46 ( $\pm$ 1.16)	0.946	ns
D7 OP50 vs. D7 EM	87.70 ( $\pm$ 0.97) vs. 88.77 ( $\pm$ 1.14)	0.904	ns
D1 OP50 vs. D7 OP50	85.53 ( $\pm$ 0.82) vs. 87.70 ( $\pm$ 0.97)	0.520	ns
D1 EM vs. D7 EM	86.05 ( $\pm$ 1.79) vs. 87.70 ( $\pm$ 0.97)	0.292	ns

Statistical analysis: Figure 4.5B, C, D, E. Two-way ANOVA.			
	Average thrashes per 30 sec per condition ( $\pm$ SEM)	p value	Significance
<i>tir-1</i> mutant			
N2 D1 OP50 vs. N2 D1 EM	83.22 ( $\pm$ 1.89) vs. 69.55 ( $\pm$ 3.32)	0.010	*
N2 D4 OP50 vs. N2 D4 EM	63.00 ( $\pm$ 2.95) vs. 80.77 ( $\pm$ 2.80)	0.0006	***
N2 D7 OP50 vs. N2 D7 EM	60.41 ( $\pm$ 3.11) vs. 69.94 ( $\pm$ 3.10)	0.119	ns
N2 D1 OP50 vs. N2 D7 OP50	83.22 ( $\pm$ 1.89) vs. 60.41 ( $\pm$ 3.11)	<0.0001	****
N2 D1 EM vs. N2 D7 EM	69.55 ( $\pm$ 3.32) vs. 69.94 ( $\pm$ 3.10)	0.996	ns
<i>tir-1</i> D1 OP50 vs. <i>tir-1</i> D1 EM	81.63 ( $\pm$ 4.87) vs. 86.17 ( $\pm$ 3.64)	0.852	ns
<i>tir-1</i> D4 OP50 vs. <i>tir-1</i> D4 EM	51.73 ( $\pm$ 3.68) vs. 77.83 ( $\pm$ 5.10)	<0.0001	****
<i>tir-1</i> D7 OP50 vs. <i>tir-1</i> D7 EM	43.33 ( $\pm$ 3.80) vs. 66.73 ( $\pm$ 4.76)	0.0002	***
<i>tir-1</i> D1 OP50 vs. <i>tir-1</i> D7 OP50	81.63 ( $\pm$ 4.87) vs. 43.33 ( $\pm$ 3.80)	<0.0001	****
<i>tir-1</i> D1 EM vs. <i>tir-1</i> D7 EM	86.17 ( $\pm$ 3.64) vs. 66.73 ( $\pm$ 4.76)	0.002	**
<i>nsy-1</i> mutant			
N2 D1 OP50 vs. N2 D1 EM	75.35 ( $\pm$ 3.38) vs. 61.88 ( $\pm$ 3.74)	0.083	ns
N2 D4 OP50 vs. N2 D4 EM	65.23 ( $\pm$ 3.69) vs. 79.45 ( $\pm$ 3.96)	0.060	ns
N2 D7 OP50 vs. N2 D7 EM	50.50 ( $\pm$ 4.26) vs. 65.45 ( $\pm$ 3.61)	0.043	*
N2 D1 OP50 vs. N2 D7 OP50	75.35 ( $\pm$ 3.38) vs. 50.50 ( $\pm$ 4.26)	<0.0001	****
N2 D1 EM vs. N2 D7 EM	61.88 ( $\pm$ 3.74) vs. 65.45 ( $\pm$ 3.61)	0.803	ns
<i>nsy-1</i> D1 OP50 vs. <i>nsy-1</i> D1 EM	73.50 ( $\pm$ 4.57) vs. 75.95 ( $\pm$ 5.55)	0.987	ns
<i>nsy-1</i> D4 OP50 vs. <i>nsy-1</i> D4 EM	56.93 ( $\pm$ 5.36) vs. 59.65 ( $\pm$ 6.43)	0.983	ns
<i>nsy-1</i> D7 OP50 vs. <i>nsy-1</i> D7 EM	36.67 ( $\pm$ 14.62) vs. 51.40 ( $\pm$ 7.07)	0.784	ns
<i>nsy-1</i> D1 OP50 vs. <i>nsy-1</i> D7 OP50	73.50 ( $\pm$ 4.57) vs. 36.67 ( $\pm$ 14.62)	0.045	*
<i>nsy-1</i> D1 EM vs. <i>nsy-1</i> D7 EM	75.95 ( $\pm$ 5.55) vs. 51.40 ( $\pm$ 7.07)	0.007	**
<i>pmk-1</i> mutant			
N2 D1 OP50 vs. N2 D1 EM	91.43 ( $\pm$ 1.45) vs. 79.67 ( $\pm$ 1.51)	<0.0001	****
N2 D4 OP50 vs. N2 D4 EM	80.73 ( $\pm$ 1.61) vs. 79.77 ( $\pm$ 1.26)	0.960	ns
N2 D7 OP50 vs. N2 D7 EM	73.77 ( $\pm$ 1.24) vs. 74.30 ( $\pm$ 1.27)	0.993	ns
N2 D1 OP50 vs. N2 D7 OP50	91.43 ( $\pm$ 1.45) vs. 73.77 ( $\pm$ 1.24)	<0.0001	****
N2 D1 EM vs. N2 D7 EM	79.67 ( $\pm$ 1.51) vs. 74.30 ( $\pm$ 1.27)	0.017	*
<i>pmk-1</i> D1 OP50 vs. <i>pmk-1</i> D1 EM	89.70 ( $\pm$ 1.68) vs. 88.93 ( $\pm$ 0.91)	0.979	ns
<i>pmk-1</i> D4 OP50 vs. <i>pmk-1</i> D4 EM	85.07 ( $\pm$ 1.27) vs. 84.07 ( $\pm$ 1.12)	0.955	ns
<i>pmk-1</i> D7 OP50 vs. <i>pmk-1</i> D7 EM	72.53 ( $\pm$ 1.64) vs. 73.90 ( $\pm$ 1.29)	0.895	ns
<i>pmk-1</i> D1 OP50 vs. <i>pmk-1</i> D7 OP50	89.70 ( $\pm$ 1.68) vs. 72.53 ( $\pm$ 1.64)	<0.0001	****
<i>pmk-1</i> D1 EM vs. <i>pmk-1</i> D7 EM	88.93 ( $\pm$ 0.91) vs. 73.90 ( $\pm$ 1.29)	<0.0001	****
<i>atf-7</i> mutant			
N2 D1 OP50 vs. N2 D1 EM	85.57 ( $\pm$ 4.54) vs. 76.97 ( $\pm$ 3.97)	0.358	ns
N2 D4 OP50 vs. N2 D4 EM	75.03 ( $\pm$ 2.79) vs. 86.03 ( $\pm$ 3.03)	0.151	ns
N2 D7 OP50 vs. N2 D7 EM	60.82 ( $\pm$ 3.71) vs. 66.79 ( $\pm$ 4.11)	0.690	ns
N2 D1 OP50 vs. N2 D7 OP50	85.57 ( $\pm$ 4.54) vs. 60.82 ( $\pm$ 3.71)	<0.0001	****
N2 D1 EM vs. N2 D7 EM	76.97 ( $\pm$ 3.97) vs. 66.79 ( $\pm$ 4.11)	0.134	ns
<i>atf-7</i> D1 OP50 vs. <i>atf-7</i> D1 EM	96.37 ( $\pm$ 5.03) vs. 88.50 ( $\pm$ 2.94)	0.447	ns
<i>atf-7</i> D4 OP50 vs. <i>atf-7</i> D4 EM	97.80 ( $\pm$ 2.93) vs. 74.73 ( $\pm$ 4.08)	0.0001	***
<i>atf-7</i> D7 OP50 vs. <i>atf-7</i> D7 EM	91.20 ( $\pm$ 3.36) vs. 71.80 ( $\pm$ 3.74)	0.002	**
<i>atf-7</i> D1 OP50 vs. <i>atf-7</i> D7 OP50	96.37 ( $\pm$ 5.03) vs. 91.20 ( $\pm$ 3.36)	0.592	ns
<i>atf-7</i> D1 EM vs. <i>atf-7</i> D7 EM	88.50 ( $\pm$ 2.94) vs. 71.80 ( $\pm$ 3.74)	0.0049	**

Statistical analysis: Figure 5.3B. Chi-square test.			
	Average score per condition ( $\pm$ SEM)	<i>p</i> value	Significance
D1 OP50 vs. D1 EM	1.83 ( $\pm$ 0.21) vs. 2.72 ( $\pm$ 0.16)	0.031	*
D4 OP50 vs. D4 EM	1.45 ( $\pm$ 0.20) vs. 2.41 ( $\pm$ 0.16)	0.015	*
D7 OP50 vs. D7 EM	1.84 ( $\pm$ 0.37) vs. 2.75 ( $\pm$ 0.12)	0.005	**
D11 OP50 vs. D11 EM	2.38 ( $\pm$ 0.29) vs. 3.00 ( $\pm$ 0.21)	0.062	ns
D1 OP50 vs. D4 OP50	1.83 ( $\pm$ 0.21) vs. 1.45 ( $\pm$ 0.20)	0.516	ns
D4 OP50 vs. D7 OP50	1.45 ( $\pm$ 0.20) vs. 1.84 ( $\pm$ 0.37)	0.023	*
D7 OP50 vs. D11 OP50	1.84 ( $\pm$ 0.37) vs. 2.38 ( $\pm$ 0.29)	0.465	ns
D1 EM vs. D4 EM	2.72 ( $\pm$ 0.16) vs. 2.41 ( $\pm$ 0.16)	0.600	ns
D4 EM vs. D7 EM	2.41 ( $\pm$ 0.16) vs. 2.75 ( $\pm$ 0.12)	0.095	ns
D7 EM vs. D11 EM	2.75 ( $\pm$ 0.12) vs. 3.00 ( $\pm$ 0.21)	0.030	*
D1 OP50 vs. D11 OP50	1.83 ( $\pm$ 0.21) vs. 2.38 ( $\pm$ 0.29)	0.041	*
D1 EM vs. D11 EM	2.72 ( $\pm$ 0.16) vs. 3.00 ( $\pm$ 0.21)	0.060	ns

Statistical analysis: Figure 5.3E. Two-way ANOVA.			
	Average circularity values per condition ( $\pm$ SEM)	<i>p</i> value	Significance
D1 OP50 vs. D1 EM	0.43 ( $\pm$ 0.02) vs. 0.44 ( $\pm$ 0.01)	0.919	ns
D4 OP50 vs. D4 EM	0.41 ( $\pm$ 0.01) vs. 0.47 ( $\pm$ 0.01)	0.008	**
D7 OP50 vs. D7 EM	0.45 ( $\pm$ 0.02) vs. 0.53 ( $\pm$ 0.02)	0.004	**
D11 OP50 vs. D11 EM	0.49 ( $\pm$ 0.02) vs. 0.55 ( $\pm$ 0.02)	0.009	**
D1 OP50 vs. D4 OP50	0.43 ( $\pm$ 0.02) vs. 0.41 ( $\pm$ 0.01)	0.672	ns
D4 OP50 vs. D7 OP50	0.41 ( $\pm$ 0.01) vs. 0.45 ( $\pm$ 0.02)	0.797	ns
D7 OP50 vs. D11 OP50	0.45 ( $\pm$ 0.02) vs. 0.49 ( $\pm$ 0.02)	0.309	ns
D1 EM vs. D4 EM	0.44 ( $\pm$ 0.01) vs. 0.47 ( $\pm$ 0.01)	0.434	ns
D4 EM vs. D7 EM	0.47 ( $\pm$ 0.01) vs. 0.53 ( $\pm$ 0.02)	0.030	*
D7 EM vs. D11 EM	0.53 ( $\pm$ 0.02) vs. 0.55 ( $\pm$ 0.02)	0.800	ns
D1 OP50 vs. D11 OP50	0.43 ( $\pm$ 0.02) vs. 0.49 ( $\pm$ 0.02)	0.016	*
D1 EM vs. D11 EM	0.44 ( $\pm$ 0.01) vs. 0.55 ( $\pm$ 0.02)	<0.0001	****

Statistical analysis: Figure 5.4D. Chi-square test.			
	Average score per condition ( $\pm$ SEM)	<i>p</i> value	Significance
D1 OP50 vs. D1 EM	2.20 ( $\pm$ 0.14) vs. 2.66 ( $\pm$ 0.14)	0.432	ns
D4 OP50 vs. D4 EM	2.53 ( $\pm$ 0.15) vs. 3.03 ( $\pm$ 0.19)	0.130	ns
D7 OP50 vs. D7 EM	3.08 ( $\pm$ 0.15) vs. 3.56 ( $\pm$ 0.13)	0.032	*
D11 OP50 vs. D11 EM	4.11 ( $\pm$ 0.14) vs. 3.76 ( $\pm$ 0.16)	0.029	*
D1 OP50 vs. D4 OP50	2.20 ( $\pm$ 0.14) vs. 2.53 ( $\pm$ 0.15)	0.432	ns
D4 OP50 vs. D7 OP50	2.53 ( $\pm$ 0.15) vs. 3.08 ( $\pm$ 0.15)	0.007	**
D7 OP50 vs. D11 OP50	3.08 ( $\pm$ 0.15) vs. 4.11 ( $\pm$ 0.14)	0.001	**
D1 EM vs. D4 EM	2.66 ( $\pm$ 0.14) vs. 3.03 ( $\pm$ 0.19)	0.130	ns
D4 EM vs. D7 EM	3.03 ( $\pm$ 0.19) vs. 3.56 ( $\pm$ 0.13)	0.044	*
D7 EM vs. D11 EM	3.56 ( $\pm$ 0.13) vs. 3.76 ( $\pm$ 0.16)	0.087	ns
D1 OP50 vs. D11 OP50	2.20 ( $\pm$ 0.14) vs. 4.11 ( $\pm$ 0.14)	<0.0001	****
D1 EM vs. D11 EM	2.66 ( $\pm$ 0.14) vs. 3.76 ( $\pm$ 0.16)	0.001	**

Statistical analysis: Figure 5.4E. Two-way ANOVA.			
	Average area per condition ( $\pm$ SEM)	<i>p</i> value	Significance
D1 OP50 vs. D1 EM	0.76 ( $\pm$ 0.03) vs. 0.74 ( $\pm$ 0.03)	0.999	ns
D4 OP50 vs. D4 EM	1.08 ( $\pm$ 0.05) vs. 0.90 ( $\pm$ 0.04)	0.055	**
D7 OP50 vs. D7 EM	1.03 ( $\pm$ 0.04) vs. 0.89 ( $\pm$ 0.04)	0.025	*
D11 OP50 vs. D11 EM	0.77 ( $\pm$ 0.04) vs. 0.88 ( $\pm$ 0.04)	0.121	ns
D1 OP50 vs. D4 OP50	0.76 ( $\pm$ 0.03) vs. 1.08 ( $\pm$ 0.05)	<0.0001	****
D4 OP50 vs. D7 OP50	1.08 ( $\pm$ 0.05) vs. 1.03 ( $\pm$ 0.04)	0.768	ns
D7 OP50 vs. D11 OP50	1.03 ( $\pm$ 0.04) vs. 0.77 ( $\pm$ 0.04)	<0.0001	****
D1 EM vs. D4 EM	0.74 ( $\pm$ 0.03) vs. 0.90 ( $\pm$ 0.04)	0.036	*
D4 EM vs. D7 EM	0.90 ( $\pm$ 0.04) vs. 0.89 ( $\pm$ 0.04)	0.999	ns
D7 EM vs. D11 EM	0.89 ( $\pm$ 0.04) vs. 0.88 ( $\pm$ 0.04)	0.998	ns
D1 OP50 vs. D11 OP50	0.76 ( $\pm$ 0.03) vs. 0.77 ( $\pm$ 0.04)	0.997	ns
D1 EM vs. D11 EM	0.74 ( $\pm$ 0.03) vs. 0.88 ( $\pm$ 0.04)	0.070	ns

Statistical analysis: Figure 5.4F. Two-way ANOVA.			
	Average aspect ratio per condition ( $\pm$ SEM)	<i>p</i> value	Significance
D1 OP50 vs. D1 EM	2.70 ( $\pm$ 0.11) vs. 2.36 ( $\pm$ 0.07)	0.275	ns
D4 OP50 vs. D4 EM	3.55 ( $\pm$ 0.14) vs. 3.02 ( $\pm$ 0.12)	0.017	*
D7 OP50 vs. D7 EM	3.95 ( $\pm$ 0.15) vs. 2.95 ( $\pm$ 0.11)	<0.0001	****
D11 OP50 vs. D11 EM	2.71 ( $\pm$ 0.13) vs. 2.95 ( $\pm$ 0.13)	0.459	ns
D1 OP50 vs. D4 OP50	2.70 ( $\pm$ 0.11) vs. 3.55 ( $\pm$ 0.14)	0.0001	***
D4 OP50 vs. D7 OP50	3.55 ( $\pm$ 0.14) vs. 3.95 ( $\pm$ 0.15)	0.112	ns
D7 OP50 vs. D11 OP50	3.95 ( $\pm$ 0.15) vs. 2.71 ( $\pm$ 0.13)	<0.0001	****
D1 EM vs. D4 EM	2.36 ( $\pm$ 0.07) vs. 3.02 ( $\pm$ 0.12)	0.002	**
D4 EM vs. D7 EM	3.02 ( $\pm$ 0.12) vs. 2.95 ( $\pm$ 0.11)	0.979	ns
D7 EM vs. D11 EM	2.95 ( $\pm$ 0.11) vs. 2.95 ( $\pm$ 0.13)	>0.999	ns
D1 OP50 vs. D11 OP50	2.70 ( $\pm$ 0.11) vs. 2.71 ( $\pm$ 0.13)	>0.999	ns
D1 EM vs. D11 EM	2.36 ( $\pm$ 0.07) vs. 2.95 ( $\pm$ 0.13)	0.006	**

Statistical analysis: Figure 5.4G. Two-way ANOVA.			
	Average density per condition ( $\pm$ SEM)	<i>p</i> value	Significance
D1 OP50 vs. D1 EM	12.28 ( $\pm$ 0.64) vs. 14.02 ( $\pm$ 0.76)	0.480	ns
D4 OP50 vs. D4 EM	13.57 ( $\pm$ 0.88) vs. 14.36 ( $\pm$ 0.69)	0.948	ns
D7 OP50 vs. D7 EM	14.75 ( $\pm$ 0.70) vs. 17.37 ( $\pm$ 0.79)	0.107	ns
D11 OP50 vs. D11 EM	16.00 ( $\pm$ 0.95) vs. 19.61 ( $\pm$ 1.51)	0.019	*
D1 OP50 vs. D4 OP50	12.28 ( $\pm$ 0.64) vs. 13.57 ( $\pm$ 0.88)	0.010	**
D4 OP50 vs. D7 OP50	13.57 ( $\pm$ 0.88) vs. 14.75 ( $\pm$ 0.70)	0.985	ns
D7 OP50 vs. D11 OP50	14.75 ( $\pm$ 0.70) vs. 16.00 ( $\pm$ 0.95)	0.230	ns
D1 EM vs. D4 EM	14.02 ( $\pm$ 0.76) vs. 14.36 ( $\pm$ 0.69)	0.357	ns
D4 EM vs. D7 EM	14.36 ( $\pm$ 0.69) vs. 17.37 ( $\pm$ 0.79)	0.423	ns
D7 EM vs. D11 EM	17.37 ( $\pm$ 0.79) vs. 19.61 ( $\pm$ 1.51)	0.832	ns
D1 OP50 vs. D11 OP50	12.28 ( $\pm$ 0.64) vs. 16.00 ( $\pm$ 0.95)	0.285	ns
D1 EM vs. D11 EM	14.02 ( $\pm$ 0.76) vs. 19.61 ( $\pm$ 1.51)	0.001	**

Statistical analysis: Figure 5.4H. Two-way ANOVA.			
	Average load per condition ( $\pm$ SEM)	p value	Significance
D1 OP50 vs. D1 EM	4.81 ( $\pm$ 0.29) vs. 5.24 ( $\pm$ 0.46)	0.971	ns
D4 OP50 vs. D4 EM	7.35 ( $\pm$ 0.56) vs. 6.56 ( $\pm$ 0.65)	0.805	ns
D7 OP50 vs. D7 EM	7.63 ( $\pm$ 0.45) vs. 7.78 ( $\pm$ 0.67)	0.999	ns
D11 OP50 vs. D11 EM	6.18 ( $\pm$ 0.62) vs. 8.50 ( $\pm$ 0.80)	0.023	*
D1 OP50 vs. D4 OP50	4.81 ( $\pm$ 0.29) vs. 7.35 ( $\pm$ 0.56)	0.010	**
D4 OP50 vs. D7 OP50	7.35 ( $\pm$ 0.56) vs. 7.63 ( $\pm$ 0.45)	0.985	ns
D7 OP50 vs. D11 OP50	7.63 ( $\pm$ 0.45) vs. 6.18 ( $\pm$ 0.62)	0.230	ns
D1 EM vs. D4 EM	5.24 ( $\pm$ 0.46) vs. 6.56 ( $\pm$ 0.65)	0.356	ns
D4 EM vs. D7 EM	6.56 ( $\pm$ 0.65) vs. 7.78 ( $\pm$ 0.67)	0.423	ns
D7 EM vs. D11 EM	7.78 ( $\pm$ 0.67) vs. 8.50 ( $\pm$ 0.80)	0.832	ns
D1 OP50 vs. D11 OP50	4.81 ( $\pm$ 0.29) vs. 6.18 ( $\pm$ 0.62)	0.285	ns
D1 EM vs. D11 EM	5.24 ( $\pm$ 0.46) vs. 8.50 ( $\pm$ 0.80)	0.001	**

Statistical analysis: Figure 5.5B. Two-way ANOVA.			
	Average # nuclei per condition ( $\pm$ SEM)	p value	Significance
D1 L4440 vs. D1 <i>spg-7</i> RNAi	10.03 ( $\pm$ 0.67) vs. 15.93 ( $\pm$ 0.41)	<0.0001	****
D1 L4440 vs. D1 OP50	10.03 ( $\pm$ 0.67) vs. 12.83 ( $\pm$ 0.30)	0.001	**
D1 L4440 vs. D1 EM	10.03 ( $\pm$ 0.67) vs. 14.50 ( $\pm$ 0.41)	<0.0001	****
D1 OP50 vs. D1 <i>spg-7</i> RNAi	12.83 ( $\pm$ 0.30) vs. 15.93 ( $\pm$ 0.41)	0.0002	***
D1 EM vs. D1 <i>spg-7</i> RNAi	14.50 ( $\pm$ 0.41) vs. 15.93 ( $\pm$ 0.41)	0.208	ns
D1 OP50 vs. D1 EM	12.83 ( $\pm$ 0.30) vs. 14.50 ( $\pm$ 0.41)	0.035	*
D4 L4440 vs. D4 <i>spg-7</i> RNAi	4.96 ( $\pm$ 0.63) vs. 14.19 ( $\pm$ 0.73)	<0.0001	****
D4 L4440 vs. D4 OP50	4.96 ( $\pm$ 0.63) vs. 7.13 ( $\pm$ 0.38)	0.026	*
D4 L4440 vs. D4 EM	4.96 ( $\pm$ 0.63) vs. 9.20 ( $\pm$ 0.57)	<0.0001	****
D4 OP50 vs. D4 <i>spg-7</i> RNAi	7.13 ( $\pm$ 0.38) vs. 14.19 ( $\pm$ 0.73)	<0.0001	****
D4 EM vs. D4 <i>spg-7</i> RNAi	9.20 ( $\pm$ 0.57) vs. 14.19 ( $\pm$ 0.73)	<0.0001	****
D4 OP50 vs. D4 EM	7.13 ( $\pm$ 0.38) vs. 9.20 ( $\pm$ 0.57)	0.006	**

Statistical analysis: Figure 5.6B. Two-way ANOVA.			
	Average fluorescence values per condition ( $\pm$ SEM)	p value	Significance
D1 L4440 vs. D1 <i>spg-7</i> RNAi	4.43 ( $\pm$ 0.26) vs. 5.42 ( $\pm$ 0.21)	0.006	**
D1 L4440 vs. D1 OP50	4.43 ( $\pm$ 0.26) vs. 4.74 ( $\pm$ 0.21)	0.666	ns
D1 L4440 vs. D1 EM	4.43 ( $\pm$ 0.26) vs. 3.91 ( $\pm$ 0.15)	0.250	ns
D1 OP50 vs. D1 <i>spg-7</i> RNAi	4.74 ( $\pm$ 0.21) vs. 5.42 ( $\pm$ 0.21)	0.081	ns
D1 EM vs. D1 <i>spg-7</i> RNAi	3.91 ( $\pm$ 0.15) vs. 5.42 ( $\pm$ 0.21)	<0.0001	****
D1 OP50 vs. D1 EM	4.74 ( $\pm$ 0.21) vs. 3.91 ( $\pm$ 0.15)	0.008	**
D4 L4440 vs. D4 <i>spg-7</i> RNAi	5.28 ( $\pm$ 0.27) vs. 4.69 ( $\pm$ 0.25)	0.250	ns
D4 L4440 vs. D4 OP50	5.28 ( $\pm$ 0.27) vs. 3.90 ( $\pm$ 0.14)	<0.0001	****
D4 L4440 vs. D4 EM	5.28 ( $\pm$ 0.27) vs. 3.91 ( $\pm$ 0.14)	<0.0001	****
D4 OP50 vs. D4 <i>spg-7</i> RNAi	3.90 ( $\pm$ 0.14) vs. 4.69 ( $\pm$ 0.25)	0.043	*
D4 EM vs. D4 <i>spg-7</i> RNAi	3.91 ( $\pm$ 0.14) vs. 4.69 ( $\pm$ 0.25)	0.044	*
D4 OP50 vs. D4 EM	3.90 ( $\pm$ 0.14) vs. 3.91 ( $\pm$ 0.14)	>0.999	ns

Statistical analysis: Figure 5.7B, C, D, E. Two-way ANOVA.			
	Average thrashes per 30 sec per condition ( $\pm$ SEM)	p value	Significance
<i>hsp-6</i> mutant			
N2 D1 OP50 vs. N2 D1 EM	75.35 ( $\pm$ 3.38) vs. 61.88 ( $\pm$ 3.74)	0.013	*
N2 D4 OP50 vs. N2 D4 EM	65.23 ( $\pm$ 3.69) vs. 79.45 ( $\pm$ 3.96)	0.007	**
N2 D7 OP50 vs. N2 D7 EM	50.50 ( $\pm$ 4.26) vs. 65.45 ( $\pm$ 3.61)	0.004	**
N2 D1 OP50 vs. N2 D7 OP50	75.35 ( $\pm$ 3.38) vs. 50.50 ( $\pm$ 4.26)	<0.0001	****
N2 D1 EM vs. N2 D7 EM	61.88 ( $\pm$ 3.74) vs. 65.45 ( $\pm$ 3.61)	0.696	ns
<i>hsp-6</i> D1 OP50 vs. <i>hsp-6</i> D1 EM	33.10 ( $\pm$ 2.69) vs. 24.20 ( $\pm$ 2.50)	0.298	ns
<i>hsp-6</i> D4 OP50 vs. <i>hsp-6</i> D4 EM	9.93 ( $\pm$ 1.24) vs. 5.60 ( $\pm$ 0.95)	0.829	ns
<i>hsp-6</i> D7 OP50 vs. <i>hsp-6</i> D7 EM	21.07 ( $\pm$ 2.65) vs. 11.37 ( $\pm$ 2.14)	0.226	ns
<i>hsp-6</i> D1 OP50 vs. <i>hsp-6</i> D7 OP50	33.10 ( $\pm$ 2.69) vs. 21.07 ( $\pm$ 2.65)	0.048	*
<i>hsp-6</i> D1 EM vs. <i>hsp-6</i> D7 EM	24.20 ( $\pm$ 2.50) vs. 11.37 ( $\pm$ 2.14)	0.032	*
<i>ubl-5</i> mutant			
N2 D1 OP50 vs. N2 D1 EM	83.22 ( $\pm$ 1.89) vs. 69.55 ( $\pm$ 3.32)	0.012	*
N2 D4 OP50 vs. N2 D4 EM	63.00 ( $\pm$ 2.95) vs. 80.77 ( $\pm$ 2.80)	0.0007	***
N2 D7 OP50 vs. N2 D7 EM	60.41 ( $\pm$ 3.11) vs. 69.94 ( $\pm$ 3.10)	0.126	ns
N2 D1 OP50 vs. N2 D7 OP50	83.22 ( $\pm$ 1.89) vs. 60.41 ( $\pm$ 3.11)	<0.0001	****
N2 D1 EM vs. N2 D7 EM	69.55 ( $\pm$ 3.32) vs. 69.94 ( $\pm$ 3.10)	0.996	ns
<i>ubl-5</i> D1 OP50 vs. <i>ubl-5</i> D1 EM	97.63 ( $\pm$ 5.04) vs. 93.43 ( $\pm$ 2.23)	0.882	ns
<i>ubl-5</i> D4 OP50 vs. <i>ubl-5</i> D4 EM	89.83 ( $\pm$ 4.46) vs. 89.43 ( $\pm$ 2.14)	0.999	ns
<i>ubl-5</i> D7 OP50 vs. <i>ubl-5</i> D7 EM	78.72 ( $\pm$ 4.65) vs. 55.77 ( $\pm$ 7.50)	0.0008	***
<i>ubl-5</i> D1 OP50 vs. <i>ubl-5</i> D7 OP50	97.63 ( $\pm$ 5.04) vs. 78.72 ( $\pm$ 4.65)	0.003	**
<i>ubl-5</i> D1 EM vs. <i>ubl-5</i> D7 EM	93.43 ( $\pm$ 2.23) vs. 55.77 ( $\pm$ 7.50)	<0.0001	****
<i>atfs-1</i> loss-of-function (lof) mutant			
N2 D1 OP50 vs. N2 D1 EM	83.22 ( $\pm$ 1.89) vs. 69.55 ( $\pm$ 3.32)	0.019	*
N2 D4 OP50 vs. N2 D4 EM	63.00 ( $\pm$ 2.95) vs. 80.77 ( $\pm$ 2.80)	0.002	**
N2 D7 OP50 vs. N2 D7 EM	60.41 ( $\pm$ 3.11) vs. 69.94 ( $\pm$ 3.10)	0.159	ns
N2 D1 OP50 vs. N2 D7 OP50	83.22 ( $\pm$ 1.89) vs. 60.41 ( $\pm$ 3.11)	<0.0001	****
N2 D1 EM vs. N2 D7 EM	69.55 ( $\pm$ 3.32) vs. 69.94 ( $\pm$ 3.10)	0.996	ns
<i>atfs-1</i> (lof) D1 OP50 vs. <i>atfs-1</i> (lof) D1 EM	83.10 ( $\pm$ 3.48) vs. 79.80 ( $\pm$ 3.74)	0.946	ns
<i>atfs-1</i> (lof) D4 OP50 vs. <i>atfs-1</i> (lof) D4 EM	54.90 ( $\pm$ 4.52) vs. 59.68 ( $\pm$ 6.52)	0.862	ns
<i>atfs-1</i> (lof) D7 OP50 vs. <i>atfs-1</i> (lof) D7 EM	49.80 ( $\pm$ 6.02) vs. 68.76 ( $\pm$ 7.68)	0.037	*
<i>atfs-1</i> (lof) D1 OP50 vs. <i>atfs-1</i> (lof) D7 OP50	83.10 ( $\pm$ 3.48) vs. 49.80 ( $\pm$ 6.02)	<0.0001	****
<i>atfs-1</i> (lof) D1 EM vs. <i>atfs-1</i> (lof) D7 EM	79.80 ( $\pm$ 3.74) vs. 68.76 ( $\pm$ 7.68)	0.261	ns
<i>atfs-1</i> gain-of-function (gof) mutant			
N2 D1 OP50 vs. N2 D1 EM	75.35 ( $\pm$ 3.38) vs. 61.88 ( $\pm$ 3.74)	0.058	ns
N2 D4 OP50 vs. N2 D4 EM	65.25 ( $\pm$ 3.69) vs. 79.45 ( $\pm$ 3.96)	0.040	*
N2 D7 OP50 vs. N2 D7 EM	50.50 ( $\pm$ 4.26) vs. 65.45 ( $\pm$ 3.61)	0.028	*
N2 D1 OP50 vs. N2 D7 OP50	75.35 ( $\pm$ 3.38) vs. 50.50 ( $\pm$ 4.26)	<0.0001	****
N2 D1 EM vs. N2 D7 EM	61.88 ( $\pm$ 3.74) vs. 65.45 ( $\pm$ 3.61)	0.782	ns
<i>atfs-1</i> (gof) D1 OP50 vs. <i>atfs-1</i> (gof) D1 EM	90.00 ( $\pm$ 2.92) vs. 77.43 ( $\pm$ 4.40)	0.176	ns
<i>atfs-1</i> (gof) D4 OP50 vs. <i>atfs-1</i> (gof) D4 EM	63.07 ( $\pm$ 4.72) vs. 74.03 ( $\pm$ 3.29)	0.286	ns
<i>atfs-1</i> (gof) D7 OP50 vs. <i>atfs-1</i> (gof) D7 EM	40.19 ( $\pm$ 6.09) vs. 46.37 ( $\pm$ 4.56)	0.028	*
<i>atfs-1</i> (gof) D1 OP50 vs. <i>atfs-1</i> (gof) D7 OP50	90.00 ( $\pm$ 2.92) vs. 40.19 ( $\pm$ 6.09)	<0.0001	****
<i>atfs-1</i> (gof) D1 EM vs. <i>atfs-1</i> (gof) D7 EM	77.43 ( $\pm$ 4.40) vs. 46.37 ( $\pm$ 4.56)	<0.0001	****

Statistical analysis: Figure 5.8. Two-way ANOVA.			
	Average thrashes per 30 sec per condition ( $\pm$ SEM)	p value	Significance
<i>mdt-15</i> loss-of-function (lof) mutant			
N2 D1 OP50 vs. N2 D1 EM	77.83 ( $\pm$ 3.29) vs. 70.38 ( $\pm$ 3.39)	0.491	ns
N2 D4 OP50 vs. N2 D4 EM	59.73 ( $\pm$ 4.42) vs. 76.80 ( $\pm$ 2.71)	0.007	**
N2 D7 OP50 vs. N2 D7 EM	50.30 ( $\pm$ 3.48) vs. 59.98 ( $\pm$ 2.98)	0.232	ns
N2 D1 OP50 vs. N2 D7 OP50	77.83 ( $\pm$ 3.29) vs. 50.30 ( $\pm$ 3.48)	<0.0001	****
N2 D1 EM vs. N2 D7 EM	70.38 ( $\pm$ 3.39) vs. 59.98 ( $\pm$ 2.98)	0.117	ns
<i>mdt-15</i> (lof) D1 OP50 vs. <i>mdt-15</i> (lof) D1 EM	67.23 ( $\pm$ 3.39) vs. 72.68 ( $\pm$ 3.98)	0.729	ns
<i>mdt-15</i> (lof) D4 OP50 vs. <i>mdt-15</i> (lof) D4 EM	58.60 ( $\pm$ 4.16) vs. 69.47 ( $\pm$ 4.04)	0.233	ns
<i>mdt-15</i> (lof) D7 OP50 vs. <i>mdt-15</i> (lof) D7 EM	25.21 ( $\pm$ 5.05) vs. 54.84 ( $\pm$ 6.23)	<0.0001	****
<i>mdt-15</i> (lof) D1 OP50 vs. <i>mdt-15</i> (lof) D7 OP50	67.23 ( $\pm$ 3.39) vs. 25.21 ( $\pm$ 5.05)	<0.0001	****
<i>mdt-15</i> (lof) D1 EM vs. <i>mdt-15</i> (lof) D7 EM	72.68 ( $\pm$ 3.98) vs. 54.84 ( $\pm$ 6.23)	0.009	**
<i>mdt-15</i> gain-of-function (gof) mutant			
N2 D1 OP50 vs. N2 D1 EM	83.22 ( $\pm$ 1.89) vs. 69.55 ( $\pm$ 3.32)	0.009	**
N2 D4 OP50 vs. N2 D4 EM	63.00 ( $\pm$ 2.95) vs. 80.77 ( $\pm$ 2.80)	0.0005	***
N2 D7 OP50 vs. N2 D7 EM	60.41 ( $\pm$ 3.11) vs. 69.94 ( $\pm$ 3.10)	0.111	ns
N2 D1 OP50 vs. N2 D7 OP50	83.22 ( $\pm$ 1.89) vs. 60.41 ( $\pm$ 3.11)	<0.0001	****
N2 D1 EM vs. N2 D7 EM	69.55 ( $\pm$ 3.32) vs. 69.94 ( $\pm$ 3.10)	0.996	ns
<i>mdt-15</i> (gof) D1 OP50 vs. <i>mdt-15</i> (gof) D1 EM	79.17 ( $\pm$ 4.13) vs. 75.13 ( $\pm$ 5.37)	0.886	ns
<i>mdt-15</i> (gof) D4 OP50 vs. <i>mdt-15</i> (gof) D4 EM	80.00 ( $\pm$ 2.94) vs. 75.10 ( $\pm$ 5.22)	0.814	ns
<i>mdt-15</i> (gof) D7 OP50 vs. <i>mdt-15</i> (gof) D7 EM	75.70 ( $\pm$ 3.03) vs. 67.97 ( $\pm$ 3.95)	0.527	ns
<i>mdt-15</i> (gof) D1 OP50 vs. <i>mdt-15</i> (gof) D7 OP50	79.17 ( $\pm$ 4.13) vs. 75.70 ( $\pm$ 3.03)	0.786	ns
<i>mdt-15</i> (gof) D1 EM vs. <i>mdt-15</i> (gof) D7 EM	75.13 ( $\pm$ 5.37) vs. 67.97 ( $\pm$ 3.95)	0.401	ns

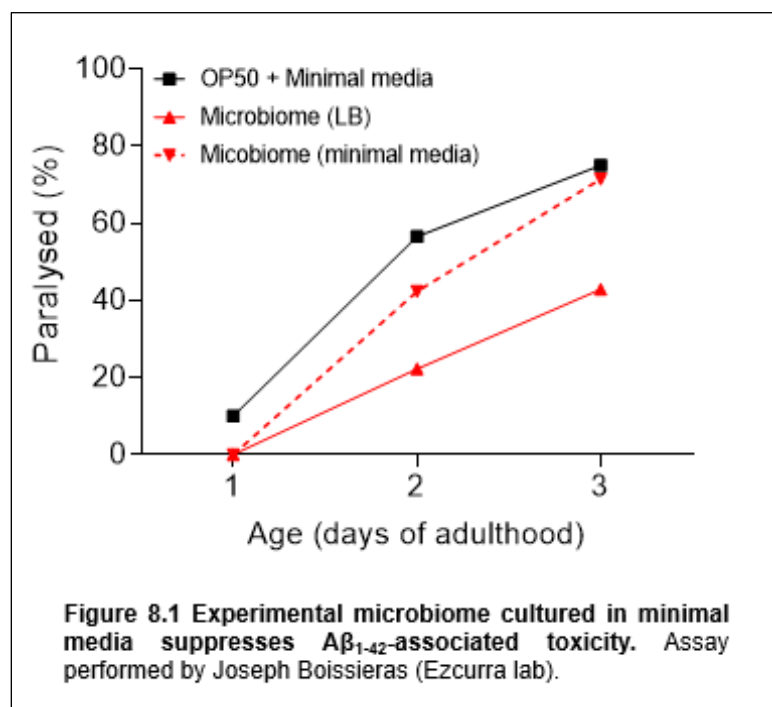
Statistical analysis: Figure 5.9. Two-way ANOVA.			
	Average thrashes per 30 sec per condition ( $\pm$ SEM)	p value	Significance
<i>drp-1</i> mutant			
N2 D1 OP50 vs. N2 D1 EM	84.96 ( $\pm$ 5.04) vs. 79.46 ( $\pm$ 3.32)	0.698	ns
N2 D4 OP50 vs. N2 D4 EM	78.34 ( $\pm$ 3.17) vs. 90.02 ( $\pm$ 2.62)	0.094	ns
N2 D7 OP50 vs. N2 D7 EM	55.56 ( $\pm$ 4.01) vs. 68.77 ( $\pm$ 3.30)	0.030	*
N2 D1 OP50 vs. N2 D7 OP50	84.96 ( $\pm$ 5.04) vs. 55.56 ( $\pm$ 4.01)	<0.0001	****
N2 D1 EM vs. N2 D7 EM	79.46 ( $\pm$ 3.32) vs. 68.77 ( $\pm$ 3.30)	0.053	ns
<i>drp-1</i> D1 OP50 vs. <i>drp-1</i> D1 EM	94.13 ( $\pm$ 2.11) vs. 77.88 ( $\pm$ 2.90)	0.004	ns
<i>drp-1</i> D4 OP50 vs. <i>drp-1</i> D4 EM	78.80 ( $\pm$ 3.44) vs. 66.78 ( $\pm$ 2.94)	0.055	ns
<i>drp-1</i> D7 OP50 vs. <i>drp-1</i> D7 EM	61.48 ( $\pm$ 4.64) vs. 58.85 ( $\pm$ 3.19)	0.945	ns
<i>drp-1</i> D1 OP50 vs. <i>drp-1</i> D7 OP50	94.13 ( $\pm$ 2.11) vs. 61.48 ( $\pm$ 4.64)	<0.0001	****
<i>drp-1</i> D1 EM vs. <i>drp-1</i> D7 EM	77.88 ( $\pm$ 2.90) vs. 58.85 ( $\pm$ 3.19)	0.0002	***
<i>fzo-1</i> mutant			
N2 D1 OP50 vs. N2 D1 EM	81.37 ( $\pm$ 2.63) vs. 80.97 ( $\pm$ 1.89)	0.999	ns
N2 D4 OP50 vs. N2 D4 EM	77.55 ( $\pm$ 4.20) vs. 75.17 ( $\pm$ 3.23)	0.958	ns
N2 D7 OP50 vs. N2 D7 EM	65.75 ( $\pm$ 4.45) vs. 77.85 ( $\pm$ 3.26)	0.121	ns
N2 D1 OP50 vs. N2 D7 OP50	81.37 ( $\pm$ 2.63) vs. 65.75 ( $\pm$ 4.45)	0.006	**
N2 D1 EM vs. N2 D7 EM	80.97 ( $\pm$ 1.89) vs. 77.85 ( $\pm$ 3.26)	0.821	ns
<i>fzo-1</i> D1 OP50 vs. <i>fzo-1</i> D1 EM	91.20 ( $\pm$ 2.31) vs. 78.03 ( $\pm$ 3.26)	0.028	*
<i>fzo-1</i> D4 OP50 vs. <i>fzo-1</i> D4 EM	56.20 ( $\pm$ 4.14) vs. 59.03 ( $\pm$ 3.33)	0.932	ns
<i>fzo-1</i> D7 OP50 vs. <i>fzo-1</i> D7 EM	45.95 ( $\pm$ 5.63) vs. 51.84 ( $\pm$ 3.86)	0.746	ns
<i>fzo-1</i> D1 OP50 vs. <i>fzo-1</i> D7 OP50	91.20 ( $\pm$ 2.31) vs. 45.95 ( $\pm$ 5.63)	<0.0001	****
<i>fzo-1</i> D1 EM vs. <i>fzo-1</i> D7 EM	78.03 ( $\pm$ 3.26) vs. 51.84 ( $\pm$ 3.86)	<0.0001	****

Statistical analysis: Figure 5.10A, B, C, D. Chi-square test.			
	Average score per condition ( $\pm$ SEM)	<i>p</i> value	Significance
<i>myo-3::GFP</i> (OP50 vs. EM)			
D1 OP50 vs. D1 EM	1.59 ( $\pm$ 0.16) vs. 1.58 ( $\pm$ 0.16)	0.981	ns
D4 OP50 vs. D4 EM	1.91 ( $\pm$ 0.11) vs. 2.84 ( $\pm$ 0.09)	<0.0001	****
D7 OP50 vs. D7 EM	2.58 ( $\pm$ 0.11) vs. 2.90 ( $\pm$ 0.12)	0.264	ns
D11 OP50 vs. D11 EM	2.69 ( $\pm$ 0.21) vs. 3.83 ( $\pm$ 0.17)	0.069	ns
<i>myo-3::GFP; pmk-1<sup>-/-</sup></i> (OP50 vs. EM)			
D1 OP50 vs. D1 EM	1.32 ( $\pm$ 0.15) vs. 1.69 ( $\pm$ 0.16)	0.107	ns
D4 OP50 vs. D4 EM	2.08 ( $\pm$ 0.12) vs. 2.52 ( $\pm$ 0.10)	0.027	*
D7 OP50 vs. D7 EM	2.81 ( $\pm$ 0.17) vs. 2.88 ( $\pm$ 0.18)	0.849	ns
D11 OP50 vs. D11 EM	3.38 ( $\pm$ 0.20) vs. 2.86 ( $\pm$ 0.34)	0.389	ns
<i>myo-3::GFP</i> OP50 vs. <i>myo-3::GFP; pmk-1<sup>-/-</sup></i> OP50			
D1	1.59 ( $\pm$ 0.16) vs. 1.32 ( $\pm$ 0.15)	0.349	ns
D4	1.91 ( $\pm$ 0.11) vs. 2.08 ( $\pm$ 0.12)	0.361	ns
D7	2.58 ( $\pm$ 0.11) vs. 2.81 ( $\pm$ 0.17)	0.067	ns
D11	2.69 ( $\pm$ 0.21) vs. 3.38 ( $\pm$ 0.20)	0.204	ns
<i>myo-3::GFP</i> EM vs. <i>myo-3::GFP; pmk-1<sup>-/-</sup></i> EM			
D1	1.58 ( $\pm$ 0.16) vs. 1.69 ( $\pm$ 0.16)	0.662	ns
D4	2.84 ( $\pm$ 0.09) vs. 2.08 ( $\pm$ 0.12)	0.054	ns
D7	2.90 ( $\pm$ 0.12) vs. 2.81 ( $\pm$ 0.17)	0.341	ns
D11	3.83 ( $\pm$ 0.17) vs. 2.86 ( $\pm$ 0.34)	0.102	ns

Statistical analysis: Figure 5.10E, F, G, H. Two-way ANOVA.			
	Average circularity per condition ( $\pm$ SEM)	<i>p</i> value	Significance
<i>myo-3::GFP</i> (OP50 vs. EM)			
D1 OP50 vs. D1 EM	0.40 ( $\pm$ 0.01) vs. 0.39 ( $\pm$ 0.01)	0.939	ns
D4 OP50 vs. D4 EM	0.41 ( $\pm$ 0.01) vs. 0.50 ( $\pm$ 0.01)	<0.0001	****
D7 OP50 vs. D7 EM	0.46 ( $\pm$ 0.01) vs. 0.50 ( $\pm$ 0.02)	0.087	ns
D11 OP50 vs. D11 EM	0.49 ( $\pm$ 0.02) vs. 0.62 ( $\pm$ 0.03)	0.0008	***
<i>myo-3::GFP; pmk-1<sup>-/-</sup></i> (OP50 vs. EM)			
D1 OP50 vs. D1 EM	0.36 ( $\pm$ 0.01) vs. 0.41 ( $\pm$ 0.01)	0.031	*
D4 OP50 vs. D4 EM	0.42 ( $\pm$ 0.01) vs. 0.48 ( $\pm$ 0.01)	0.002	**
D7 OP50 vs. D7 EM	0.50 ( $\pm$ 0.01) vs. 0.50 ( $\pm$ 0.02)	>0.999	ns
D11 OP50 vs. D11 EM	0.59 ( $\pm$ 0.02) vs. 0.52 ( $\pm$ 0.03)	0.261	ns
<i>myo-3::GFP</i> OP50 vs. <i>myo-3::GFP; pmk-1<sup>-/-</sup></i> OP50			
D1	0.40 ( $\pm$ 0.01) vs. 0.36 ( $\pm$ 0.01)	0.209	ns
D4	0.41 ( $\pm$ 0.01) vs. 0.42 ( $\pm$ 0.01)	0.991	ns
D7	0.46 ( $\pm$ 0.01) vs. 0.50 ( $\pm$ 0.01)	0.058	ns
D11	0.49 ( $\pm$ 0.02) vs. 0.59 ( $\pm$ 0.02)	0.0004	***
<i>myo-3::GFP</i> EM vs. <i>myo-3::GFP; pmk-1<sup>-/-</sup></i> EM			
D1	0.39 ( $\pm$ 0.01) vs. 0.41 ( $\pm$ 0.01)	0.659	ns
D4	0.50 ( $\pm$ 0.01) vs. 0.48 ( $\pm$ 0.01)	0.673	ns
D7	0.50 ( $\pm$ 0.02) vs. 0.50 ( $\pm$ 0.02)	>0.999	ns
D11	0.62 ( $\pm$ 0.03) vs. 0.52 ( $\pm$ 0.03)	0.762	ns

Statistical analysis: Figure 6.1A-L. Two-way ANOVA.			
	Percentage paralysed per condition ( $\pm$ SEM)	p value	Significance
EM			
D1 OP50 vs. D1 EM	27.18 ( $\pm$ 8.27) vs. 0.00 ( $\pm$ 0.00)	0.0003	***
D2 OP50 vs. D2 EM	88.04 ( $\pm$ 2.29) vs. 17.29 ( $\pm$ 2.72)	<0.0001	****
D3 OP50 vs. D3 EM	98.80 ( $\pm$ 0.52) vs. 52.12 ( $\pm$ 7.85)	<0.0001	****
D4 OP50 vs. D4 EM	100.00 ( $\pm$ 0.00) vs. 96.06 ( $\pm$ 1.32)	0.955	ns
MYb9			
D1 OP50 vs. D1 MYb9	52.61 ( $\pm$ 6.29) vs. 12.99 ( $\pm$ 6.94)	0.007	**
D2 OP50 vs. D2 MYb9	89.10 ( $\pm$ 1.48) vs. 44.56 ( $\pm$ 10.09)	0.0008	***
D3 OP50 vs. D3 MYb9	98.73 ( $\pm$ 0.51) vs. 68.46 ( $\pm$ 11.00)	0.180	ns
D4 OP50 vs. D4 MYb9	98.61 ( $\pm$ 0.89) vs. 87.30 ( $\pm$ 7.33)	>0.999	ns
MYb10			
D1 OP50 vs. D1 MYb10	52.61 ( $\pm$ 6.29) vs. 8.89 ( $\pm$ 5.13)	0.001	**
D2 OP50 vs. D2 MYb10	89.10 ( $\pm$ 1.48) vs. 47.85 ( $\pm$ 8.18)	0.004	**
D3 OP50 vs. D3 MYb10	98.73 ( $\pm$ 0.51) vs. 79.83 ( $\pm$ 4.43)	0.938	ns
D4 OP50 vs. D4 MYb10	98.61 ( $\pm$ 0.89) vs. 97.73 ( $\pm$ 1.31)	>0.999	ns
MYb11			
D1 OP50 vs. D1 MYb11	52.61 ( $\pm$ 6.29) vs. 3.34 ( $\pm$ 1.93)	<0.0001	****
D2 OP50 vs. D2 MYb11	89.10 ( $\pm$ 1.48) vs. 23.57 ( $\pm$ 0.69)	<0.0001	****
D3 OP50 vs. D3 MYb11	98.73 ( $\pm$ 0.51) vs. 68.44 ( $\pm$ 2.19)	0.179	ns
D4 OP50 vs. D4 MYb11	98.61 ( $\pm$ 0.89) vs. 91.98 ( $\pm$ 4.63)	>0.999	ns
MYb27			
D1 OP50 vs. D1 MYb27	52.61 ( $\pm$ 6.29) vs. 15.02 ( $\pm$ 3.65)	0.016	*
D2 OP50 vs. D2 MYb27	89.10 ( $\pm$ 1.48) vs. 59.89 ( $\pm$ 1.24)	0.236	ns
D3 OP50 vs. D3 MYb27	98.73 ( $\pm$ 0.51) vs. 82.35 ( $\pm$ 6.45)	0.987	ns
D4 OP50 vs. D4 MYb27	98.61 ( $\pm$ 0.89) vs. 78.85 ( $\pm$ 12.21)	0.907	ns
MYb45			
D1 OP50 vs. D1 MYb45	52.61 ( $\pm$ 6.29) vs. 1.18 ( $\pm$ 1.15)	0.006	**
D2 OP50 vs. D2 MYb45	89.10 ( $\pm$ 1.48) vs. 15.58 ( $\pm$ 4.05)	<0.0001	****
D3 OP50 vs. D3 MYb45	98.73 ( $\pm$ 0.51) vs. 39.73 ( $\pm$ 5.55)	0.0004	***
D4 OP50 vs. D4 MYb45	98.61 ( $\pm$ 0.89) vs. 77.78 ( $\pm$ 1.16)	0.989	ns
MYb56			
D1 OP50 vs. D1 MYb9	52.61 ( $\pm$ 6.29) vs. 7.69 ( $\pm$ 3.72)	0.0006	***
D2 OP50 vs. D2 MYb9	89.10 ( $\pm$ 1.48) vs. 51.35 ( $\pm$ 17.21)	0.015	*
D3 OP50 vs. D3 MYb9	98.73 ( $\pm$ 0.51) vs. 72.17 ( $\pm$ 7.82)	0.419	ns
D4 OP50 vs. D4 MYb9	98.61 ( $\pm$ 0.89) vs. 84.53 ( $\pm$ 8.93)	0.998	ns
MYb57			
D1 OP50 vs. D1 MYb9	52.61 ( $\pm$ 6.29) vs. 20.66 ( $\pm$ 1.66)	0.112	ns
D2 OP50 vs. D2 MYb9	89.10 ( $\pm$ 1.48) vs. 68.90 ( $\pm$ 10.91)	0.888	ns
D3 OP50 vs. D3 MYb9	98.73 ( $\pm$ 0.51) vs. 89.94 ( $\pm$ 6.12)	>0.999	ns
D4 OP50 vs. D4 MYb9	98.61 ( $\pm$ 0.89) vs. 93.14 ( $\pm$ 3.96)	>0.999	ns
MYb71			
D1 OP50 vs. D1 MYb9	52.61 ( $\pm$ 6.29) vs. 0.54 ( $\pm$ 0.54)	<0.0001	****
D2 OP50 vs. D2 MYb9	89.10 ( $\pm$ 1.48) vs. 33.08 ( $\pm$ 14.04)	<0.0001	****
D3 OP50 vs. D3 MYb9	98.73 ( $\pm$ 0.51) vs. 48.58 ( $\pm$ 18.22)	<0.0001	****
D4 OP50 vs. D4 MYb9	98.61 ( $\pm$ 0.89) vs. 58.86 ( $\pm$ 19.59)	0.007	**
MYb83			
D1 OP50 vs. D1 MYb9	52.61 ( $\pm$ 6.29) vs. 11.34 ( $\pm$ 3.50)	0.0003	***
D2 OP50 vs. D2 MYb9	89.10 ( $\pm$ 1.48) vs. 39.05 ( $\pm$ 10.21)	<0.0001	****
D3 OP50 vs. D3 MYb9	98.73 ( $\pm$ 0.51) vs. 72.63 ( $\pm$ 10.91)	0.214	ns
D4 OP50 vs. D4 MYb9	98.61 ( $\pm$ 0.89) vs. 79.51 ( $\pm$ 7.20)	0.806	ns
MYb120			
D1 OP50 vs. D1 MYb9	52.61 ( $\pm$ 6.29) vs. 49.05 ( $\pm$ 25.25)	>0.999	ns
D2 OP50 vs. D2 MYb9	89.10 ( $\pm$ 1.48) vs. 91.52 ( $\pm$ 4.26)	>0.999	ns
D3 OP50 vs. D3 MYb9	98.73 ( $\pm$ 0.51) vs. 98.24 ( $\pm$ 0.05)	>0.999	ns
D4 OP50 vs. D4 MYb9	98.61 ( $\pm$ 0.89) vs. 100 ( $\pm$ 0.00)	>0.999	ns
MYb218			
D1 OP50 vs. D1 MYb9	52.61 ( $\pm$ 6.29) vs. 3.43 ( $\pm$ 0.01)	<0.0001	****
D2 OP50 vs. D2 MYb9	89.10 ( $\pm$ 1.48) vs. 87.18 ( $\pm$ 1.48)	>0.999	ns
D3 OP50 vs. D3 MYb9	98.73 ( $\pm$ 0.51) vs. 98.44 ( $\pm$ 0.90)	>0.999	ns
D4 OP50 vs. D4 MYb9	98.61 ( $\pm$ 0.89) vs. 100.00 ( $\pm$ 0.00)	>0.999	ns

Statistical analysis: Figure 6.2A-J. Two-way ANOVA.			
	Percentage paralysed per condition ( $\pm$ SEM)	p value	Significance
OP50 vs. EM			
D1 OP50 vs. D1 EM	9.48 ( $\pm$ 0.90) vs. 0.00 ( $\pm$ 0.00)	0.496	ns
D2 OP50 vs. D2 EM	86.13 ( $\pm$ 3.71) vs. 17.69 ( $\pm$ 13.24)	<0.0001	****
D3 OP50 vs. D3 EM	97.71 ( $\pm$ 0.97) vs. 56.63 ( $\pm$ 15.84)	<0.0001	****
D4 OP50 vs. D4 EM	100.00 ( $\pm$ 0.00) vs. 95.14 ( $\pm$ 2.44)	0.829	ns
OP50 vs. CFM			
D1 OP50 vs. D1 CFM	9.48 ( $\pm$ 0.90) vs. 2.56 ( $\pm$ 2.56)	0.685	ns
D2 OP50 vs. D2 CFM	86.13 ( $\pm$ 3.71) vs. 54.14 ( $\pm$ 1.23)	0.002	**
D3 OP50 vs. D3 CFM	97.71 ( $\pm$ 0.97) vs. 77.00 ( $\pm$ 2.19)	0.046	*
D4 OP50 vs. D4 CFM	100.00 ( $\pm$ 0.00) vs. 79.63 ( $\pm$ 13.86)	0.050	ns
CFM vs. EM			
D1 CFM vs. D1 EM	2.56 ( $\pm$ 2.56) vs. 0.00 ( $\pm$ 0.00)	0.959	ns
D2 CFM vs. D2 EM	54.14 ( $\pm$ 1.23) vs. 17.69 ( $\pm$ 13.24)	0.001	**
D3 CFM vs. D3 EM	77.00 ( $\pm$ 2.19) vs. 56.63 ( $\pm$ 15.84)	0.087	ns
D4 CFM vs. D4 EM	79.63 ( $\pm$ 13.86) vs. 95.14 ( $\pm$ 2.44)	0.232	ns
MYb9 CFM			
D1 OP50 vs. D1 MYb9 CFM	52.61 ( $\pm$ 6.29) vs. 22.39 ( $\pm$ 9.35)	0.054	ns
D2 OP50 vs. D2 MYb9 CFM	89.10 ( $\pm$ 1.48) vs. 79.64 ( $\pm$ 8.02)	>0.999	ns
D3 OP50 vs. D3 MYb9 CFM	98.73 ( $\pm$ 0.51) vs. 92.00 ( $\pm$ 4.62)	>0.999	ns
D4 OP50 vs. D4 MYb9 CFM	98.61 ( $\pm$ 0.89) vs. 100.00 ( $\pm$ 0.00)	>0.999	ns
MYb10 CFM			
D1 OP50 vs. D1 MYb10 CFM	52.61 ( $\pm$ 6.29) vs. 25.49 ( $\pm$ 12.55)	0.158	ns
D2 OP50 vs. D2 MYb10 CFM	89.10 ( $\pm$ 1.48) vs. 80.56 ( $\pm$ 6.21)	>0.999	ns
D3 OP50 vs. D3 MYb10 CFM	98.73 ( $\pm$ 0.51) vs. 95.45 ( $\pm$ 2.63)	>0.999	ns
D4 OP50 vs. D4 MYb10 CFM	98.61 ( $\pm$ 0.89) vs. 100.00 ( $\pm$ 0.00)	>0.999	ns
MYb11 CFM			
D1 OP50 vs. D1 MYb11 CFM	52.61 ( $\pm$ 6.29) vs. 32.12 ( $\pm$ 12.81)	0.693	ns
D2 OP50 vs. D2 MYb11 CFM	89.10 ( $\pm$ 1.48) vs. 88.03 ( $\pm$ 4.63)	>0.999	ns
D3 OP50 vs. D3 MYb11 CFM	98.73 ( $\pm$ 0.51) vs. 90.71 ( $\pm$ 2.73)	>0.999	ns
D4 OP50 vs. D4 MYb11 CFM	98.61 ( $\pm$ 0.89) vs. 93.94 ( $\pm$ 3.50)	>0.999	ns
MYb27 CFM			
D1 OP50 vs. D1 MYb27 CFM	52.61 ( $\pm$ 6.29) vs. 11.11 ( $\pm$ 6.41)	0.003	**
D2 OP50 vs. D2 MYb27 CFM	89.10 ( $\pm$ 1.48) vs. 68.65 ( $\pm$ 16.11)	0.875	ns
D3 OP50 vs. D3 MYb27 CFM	98.73 ( $\pm$ 0.51) vs. 91.67 ( $\pm$ 0.69)	>0.999	ns
D4 OP50 vs. D4 MYb27 CFM	98.61 ( $\pm$ 0.89) vs. 100.00 ( $\pm$ 0.00)	>0.999	ns
MYb45 CFM			
D1 OP50 vs. D1 MYb45 CFM	52.61 ( $\pm$ 6.29) vs. 28.57 ( $\pm$ 21.43)	0.992	ns
D2 OP50 vs. D2 MYb45 CFM	89.10 ( $\pm$ 1.48) vs. 70.13 ( $\pm$ 12.99)	0.999	ns
D3 OP50 vs. D3 MYb45 CFM	98.73 ( $\pm$ 0.51) vs. 94.16 ( $\pm$ 1.99)	>0.999	ns
D4 OP50 vs. D4 MYb45 CFM	98.61 ( $\pm$ 0.89) vs. 98.53 ( $\pm$ 1.47)	>0.999	ns
MYb56 CFM			
D1 OP50 vs. D1 MYb56 CFM	52.61 ( $\pm$ 6.29) vs. 20.67 ( $\pm$ 7.31)	0.112	ns
D2 OP50 vs. D2 MYb56 CFM	89.10 ( $\pm$ 1.48) vs. 72.26 ( $\pm$ 4.47)	0.982	ns
D3 OP50 vs. D3 MYb56 CFM	98.73 ( $\pm$ 0.51) vs. 100.00 ( $\pm$ 0.00)	>0.999	ns
D4 OP50 vs. D4 MYb56 CFM	98.61 ( $\pm$ 0.89) vs. 100.00 ( $\pm$ 0.00)	>0.999	ns
MYb57 CFM			
D1 OP50 vs. D1 MYb57 CFM	52.61 ( $\pm$ 6.29) vs. 13.69 ( $\pm$ 1.72)	0.009	**
D2 OP50 vs. D2 MYb57 CFM	89.10 ( $\pm$ 1.48) vs. 45.30 ( $\pm$ 0.49)	0.001	**
D3 OP50 vs. D3 MYb57 CFM	98.73 ( $\pm$ 0.51) vs. 74.02 ( $\pm$ 0.57)	0.571	ns
D4 OP50 vs. D4 MYb57 CFM	98.61 ( $\pm$ 0.89) vs. 95.46 ( $\pm$ 2.62)	>0.999	ns
MYb71 CFM			
D1 OP50 vs. D1 MYb71 CFM	52.61 ( $\pm$ 6.29) vs. 18.15 ( $\pm$ 6.63)	0.050	ns
D2 OP50 vs. D2 MYb71 CFM	89.10 ( $\pm$ 1.48) vs. 86.16 ( $\pm$ 5.48)	>0.999	ns
D3 OP50 vs. D3 MYb71 CFM	98.73 ( $\pm$ 0.51) vs. 92.15 ( $\pm$ 1.65)	>0.999	ns
D4 OP50 vs. D4 MYb71 CFM	98.61 ( $\pm$ 0.89) vs. 97.37 ( $\pm$ 1.52)	>0.999	ns
MYb83 CFM			
D1 OP50 vs. D1 MYb83 CFM	52.61 ( $\pm$ 6.29) vs. 21.93 ( $\pm$ 7.25)	0.161	ns
D2 OP50 vs. D2 MYb83 CFM	89.10 ( $\pm$ 1.48) vs. 89.17 ( $\pm$ 1.44)	>0.999	ns
D3 OP50 vs. D3 MYb83 CFM	98.73 ( $\pm$ 0.51) vs. 94.12 ( $\pm$ 3.39)	>0.999	ns
D4 OP50 vs. D4 MYb83 CFM	98.61 ( $\pm$ 0.89) vs. 96.67 ( $\pm$ 1.93)	>0.999	ns



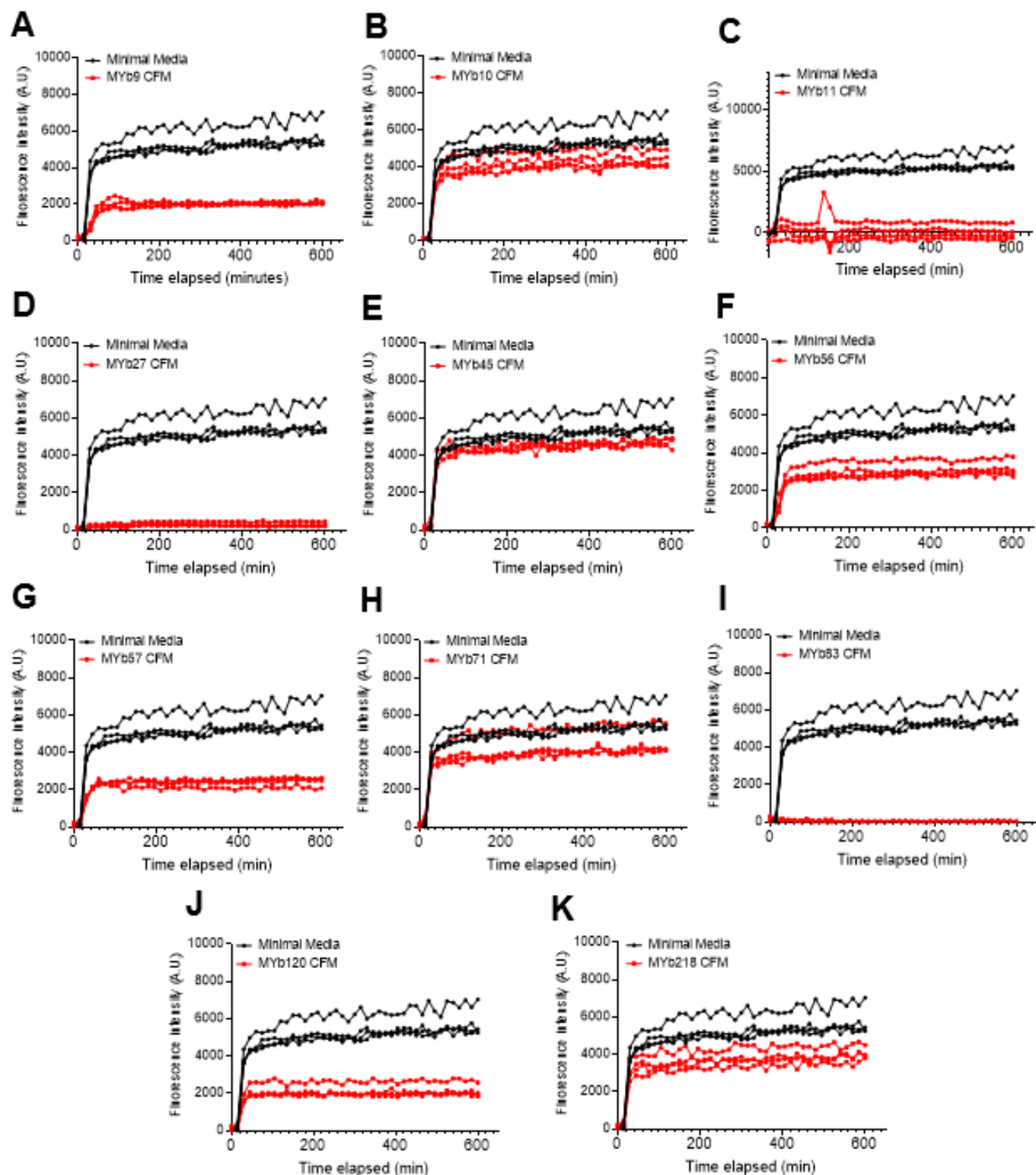
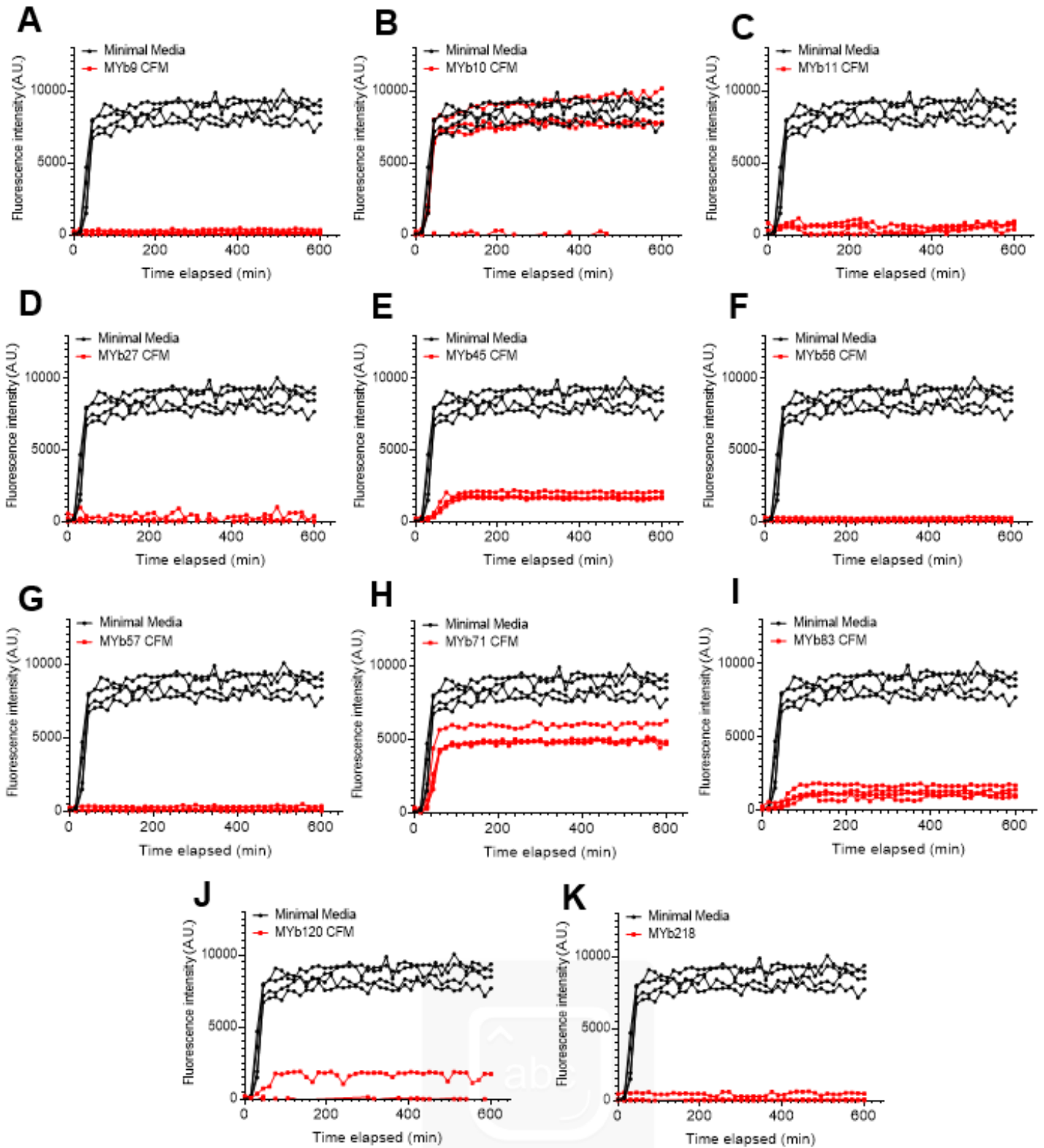


Figure 8.2 Fluorescence intensity traces from thioflavin T assay biological replicate #1.



**Figure 8.3** Fluorescence intensity traces from thioflavin T assay biological replicate #2.

Identified secondary metabolite regions					
Region	Type	From	To	Most similar known cluster	Similarity
Region 1.1	terpene <i>cf.</i>	292,623	314,333		
Region 3.1	betalactone <i>cf.</i>	332,940	355,524		
Region 4.3	phenazine <i>cf.</i>	85,661	106,089		
Region 4.2	betalactone <i>cf.</i>	109,347	142,060		
Region 7.1	NRPS <i>cf.</i>	76,841	155,389	Serobactins <i>cf.</i>	NRPS 69%
Region 9.1	NRPS-like <i>cf.</i>	923	44,921		
Region 13.1	resorcinol <i>cf.</i>	74,100	116,034		
Region 14.1	T1PKS <i>cf.</i>	31,503	79,122	Capular polysaccharide <i>cf.</i>	saccharide 33%
Region 17.1	transAT-PKS <i>cf.</i>	44,888	113,627	Lagrimide <i>cf.</i>	polyketide 9%
Region 18.1	ectoine <i>cf.</i>	50,623	61,027	Ectoine <i>cf.</i>	other 75%
Region 20.1	arylpolyene <i>cf.</i>	30,989	74,600	APE Ec <i>cf.</i>	other 31%

MYb9 (*Achromobacter* sp. F32) antiSMASH results.

Identified secondary metabolite regions using strictness 'relaxed'					
Region	Type	From	To	Most similar known cluster	Similarity
Region 2.1	bacteriocin <i>cf.</i>	576,615	587,460		
Region 7.1	arylpolyene <i>cf.</i>	1	38,094	APE VI <i>cf.</i>	Other 45%
Region 8.1	bacteriocin <i>cf.</i>	196,102	206,980		
Region 9.1	NRPS <i>cf.</i>	37,084	144,600	viscosin <i>cf.</i>	NRP 100%
Region 12.1	NRPS <i>cf.</i>	36,312	82,533	lipoasin I / lipoasin F <i>cf.</i>	NRP-Lipopeptide 60%
Region 13.1	NRPS <i>cf.</i>	105,262	158,140	gyroverdin <i>cf.</i>	NRP 9%
Region 14.1	bacteriocin <i>cf.</i>	172,324	183,148		
Region 15.1	ectoine <i>cf.</i>	66,074	76,460		
Region 20.1	NRPS-like <i>cf.</i>	1	30,651	L-2-amino-4-methoxy-trans-3-butenoic acid <i>cf.</i>	NRP 40%
Region 27.1	betalactone <i>cf.</i>	13,634	36,789	fengycin <i>cf.</i>	NRP 13%
Region 30.1	NAGGN <i>cf.</i>	36,438	50,623		

MYb11 (*Pseudomonas lurida*) antiSMASH results.

Identified secondary metabolite regions					
Region	Type	From	To	Most similar known cluster	Similarity
Region 4.1	T3PKS <i>cf.</i> , betalactone <i>cf.</i>	17,573	63,246	Streptomycin <i>cf.</i>	saccharide 2%
Region 18.1	NRPS-like <i>cf.</i>	52,086	84,833		
Region 24.1	bacteriocin <i>cf.</i>	20,729	31,049		
Region 39.1	terpene <i>cf.</i>	1	11,963	Carotenoid <i>cf.</i>	terpene 26%

MYb45 (*Microbacterium oxydans*) antiSMASH results.

Identified secondary metabolite regions using strictness 'relaxed'					
NZ_CP023271.1 ( <i>Stenotrophomonas</i> sp. MYb57)					
Region	Type	From	To	Most similar known cluster	Similarity
Region 1	RIPP-like <i>cf.</i>	1,228,400	1,237,975		
Region 2	RIPP-like <i>cf.</i>	1,632,628	1,643,503		
Region 3	NRPS <i>cf.</i>	2,692,883	2,736,781	myxochelin A / myxochelin B <i>cf.</i>	NRP 25%
Region 4	arylpolyene <i>cf.</i>	4,500,391	4,543,999	APE VI <i>cf.</i>	Other 35%

MYb57 (*Stenotrophomonas* sp. R-41388) antiSMASH results.

Identified secondary metabolite regions					
Region	Type	From	To	Most similar known cluster	Similarity
Region 1.1	acyl_ amino_ acids <i>cf.</i>	10,217	70,963	Ambactin <i>cf.</i>	NRPS 25%
Region 5.1	terpene <i>cf.</i>	89,374	110,207		
Region 5.2	arylpolyene <i>cf.</i>	116,269	157,450		
Region 10.1	betalactone <i>cf.</i>	88,906	116,755	Fengycin <i>cf.</i>	other-nrps 13%
Region 13.1	NAGGN <i>cf.</i>	91,231	112,128		
Region 528.1	terpene <i>cf.</i>	1	1,235		

MYb83 (*Leuconostoc pseudomesenteroides*) antiSMASH results.

Identified secondary metabolite regions using strictness 'relaxed'					
Region	Type	From	To	Most similar known cluster	Similarity
Region 14.1	NRPS-like <i>cf.</i>	52,086	84,855		
Region 26.1	T3PKS <i>cf.</i>	17,582	51,386		
Region 68.1	terpene <i>cf.</i>	5,095	17,050	carotenoid <i>cf.</i>	Terpene 28%
Region 659.1	terpene <i>cf.</i>	1	1,395		

MYb218 (*Pseudomonas tuomuerensis*) antiSMASH results.

Identified secondary metabolite regions					
Region	Type	From	To	Most similar known cluster	Similarity
Region 1.1	siderophore <i>cf.</i>	234,586	249,197	Acinetolemin <i>cf.</i>	NRPS 70%
Region 1.2	siderophore <i>cf.</i>	966,521	984,308	Acinetolemin <i>cf.</i>	NRPS 40%
Region 2.1	bacteriocin <i>cf.</i>	748,152	759,015		
Region 2.2	arylpolyene <i>cf.</i>	836,842	876,074	Bemisinamycin <i>cf.</i>	other 26%
Region 3.1	arylpolyene <i>cf.</i>	197,604	241,199	APE VI <i>cf.</i>	other 45%

MYb10 (*Acinetobacter* sp. LB BR12338) antiSMASH results.

Identified secondary metabolite regions					
Region	Type	From	To	Most similar known cluster	Similarity
Region 2.1	NRPS <i>cf.</i>	183,247	233,824	Galbonolides <i>cf.</i>	tlpk 6%
Region 4.1	T3PKS <i>cf.</i>	89,728	130,852	SW-163 <i>cf.</i>	NRPS 7%
Region 10.1	siderophore <i>cf.</i>	51,363	63,204	Desferrioxamine <i>cf.</i>	other 100%
Region 10.2	terpene <i>cf.</i>	110,648	131,583	Carotenoid <i>cf.</i>	terpene 28%
Region 11.1	NRPS-like <i>cf.</i>	87,774	130,359	Streptomycin <i>cf.</i>	saccharide 16%
Region 13.1	betalactone <i>cf.</i>	46,631	73,899	Microasamycin <i>cf.</i>	polyketide 7%
Region 18.1	ectoine <i>cf.</i>	6,993	17,370	Showdomycin <i>cf.</i>	other 17%

MYb27 (*Arthrobacter aureus*) antiSMASH results.

Identified secondary metabolite regions					
Region	Type	From	To	Most similar known cluster	Similarity
Region 2.1	lassopeptide <i>cf.</i>	327,592	351,509	Paenidin <i>cf.</i>	other 100%
Region 3.1	bacteriocin <i>cf.</i> , LAP <i>cf.</i>	100,883	124,417		
Region 6.1	NRPS <i>cf.</i>	114,595	164,323	Bacillibactin <i>cf.</i>	NRPS 46%
Region 6.2	bacteriocin <i>cf.</i>	198,704	208,997		
Region 7.1	terpene <i>cf.</i>	69,924	120,777		
Region 12.1	siderophore <i>cf.</i>	116,285	130,002	Petrobactin <i>cf.</i>	other 100%
Region 15.1	betalactone <i>cf.</i>	41,677	66,915	Fengycin <i>cf.</i>	other-nrps 40%
Region 19.1	NRPS <i>cf.</i>	1	28,773		
Region 19.2	bacteriocin <i>cf.</i>	52,621	63,096		
Region 33.1	NRPS <i>cf.</i> , T1PKS <i>cf.</i>	1	50,611	Paenitanin <i>cf.</i>	nps-tlpks 35%
Region 33.1	NRPS <i>cf.</i>	1	47,897		

MYb56 (*Bacillus* sp. SG20) antiSMASH results.

Identified secondary metabolite regions					
Region	Type	From	To	Most similar known cluster	Similarity
Region 1.1	acyl_ amino_ acids <i>cf.</i>	10,217	70,963	Ambactin <i>cf.</i>	NRPS 25%
Region 5.1	terpene <i>cf.</i>	89,374	110,207		
Region 5.2	arylpolyene <i>cf.</i>	116,269	157,450		
Region 11.1	betalactone <i>cf.</i>	38,651	66,500	Fengycin <i>cf.</i>	other-nrps 13%
Region 14.1	NAGGN <i>cf.</i>	10,084	30,981		

MYb71 (*Ochrobacterum* sp. R-26465) antiSMASH results.

Identified secondary metabolite regions					
Region	Type	From	To	Most similar known cluster	Similarity
Region 1.1	siderophore <i>cf.</i>	590,224	605,758	Desferrioxamine <i>cf.</i>	other 50%
Region 1.2	hgE-KS <i>cf.</i> , T1PKS <i>cf.</i>	648,708	699,962		
Region 2.1	arylpolyene <i>cf.</i> , resorcinol <i>cf.</i>	608,160	933,745	Flexubin <i>cf.</i>	polyketide 77%

MYb120 (*Chryseobacterium* sp. CHNTR56) antiSMASH results.

Figure 8.4 Secondary metabolite-encoding cluster similarity per EM member strain, as identified via antiSMASH software.

## 9. Bibliography

- Alavi, P. *et al.* Stenotrophomonas comparative genomics reveals genes and functions that differentiate beneficial and pathogenic bacteria. *BMC Genomics* **15**, 482 (2014).
- Alim, I. *et al.* Selenium Drives a Transcriptional Adaptive Program to Block Ferroptosis and Treat Stroke. *Cell* **177**, 1262-1279.e25 (2019).
- Amrit, F. R. G., Ratnappan, R., Keith, S. A. & Ghazi, A. The *C. elegans* lifespan assay toolkit. *Methods* **68**, 465–475 (2014).
- Anderson, C. P. & Leibold, E. A. Mechanisms of iron metabolism in *Caenorhabditis elegans*. *Front Pharmacol* **5**, (2014).
- Andrews, S. C., Robinson, A. K. & Rodríguez-Quiriones, F. Bacterial iron homeostasis. *FEMS Microbiol Rev* **27**, 215–237 (2003).
- Angeli, J. P. F., Shah, R., Pratt, D. A. & Conrad, M. Ferroptosis Inhibition: Mechanisms and Opportunities. *Trends Pharmacol Sci* **38**, 489–498 (2017).
- Armanios, M. & Blackburn, E. H. The telomere syndromes. *Nat Rev Genet* **13**, 693–704 (2012).
- Armanios, M. *et al.* Short Telomeres are Sufficient to Cause the Degenerative Defects Associated with Aging. *The American Journal of Human Genetics* **85**, 823–832 (2009).
- Arumugam, M. *et al.* Enterotypes of the human gut microbiome. *Nature* **473**, 174–180 (2011).
- Asai, T. *et al.* MAP kinase signalling cascade in Arabidopsis innate immunity. *Nature* **415**, 977–983 (2002).
- Ashburner, M. *et al.* Gene Ontology: tool for the unification of biology. *Nat Genet* **25**, 25–29 (2000).
- Asti, A. & Gioglio, L. Can a Bacterial Endotoxin be a Key Factor in the Kinetics of Amyloid Fibril Formation? *Journal of Alzheimer's Disease* **39**, 169–179 (2014).
- Avery, L. & Horvitz, H. R. Effects of starvation and neuroactive drugs on feeding in *Caenorhabditis elegans*. *Journal of Experimental Zoology* **253**, 263–270 (1990).
- Ayton, S. *et al.* Brain iron is associated with accelerated cognitive decline in people with Alzheimer pathology. *Mol Psychiatry* **25**, 2932–2941 (2020).
- Ayton, S. *et al.* Cerebral quantitative susceptibility mapping predicts amyloid- $\beta$ -related cognitive decline. *Brain* **140**, 2112–2119 (2017).
- Bäckhed, F., Manchester, J. K., Semenkovich, C. F. & Gordon, J. I. Mechanisms underlying the resistance to diet-induced obesity in germ-free mice. *Proc Natl Acad Sci U S A* **104**, 979–84 (2007).
- Ballard, J. W. O. & Towarnicki, S. G. Mitochondria, the gut microbiome and ROS. *Cell Signal* **75**, 109737 (2020).
- Bansal, A., Zhu, L. J., Yen, K. & Tissenbaum, H. A. Uncoupling lifespan and healthspan in *Caenorhabditis elegans* longevity mutants. *Proceedings of the National Academy of Sciences* **112**, (2015).
- Bar-Ziv, R., Frakes, A. E., Higuchi-Sanabria, R., Bolas, T., Frankino, P. A., Gildea, H. K., Metcalf, M. G., & Dillin, A. Measurements of Physiological Stress Responses in *C. Elegans*; *Journal of Visualized Experiments*, **159**, (2020).

- Bean, J. F. *et al.* A comparison of leg power and leg strength within the InCHIANTI study: which influences mobility more? *J Gerontol A Biol Sci Med Sci* **58**, 728–33 (2003).
- Benedetti, C., Haynes, C. M., Yang, Y., Harding, H. P. & Ron, D. Ubiquitin-Like Protein 5 Positively Regulates Chaperone Gene Expression in the Mitochondrial Unfolded Protein Response. *Genetics* **174**, 229–239 (2006).
- Beron, C. *et al.* The burrowing behavior of the nematode *Caenorhabditis elegans*: a new assay for the study of neuromuscular disorders. *Genes Brain Behav* **14**, 357–368 (2015).
- Bervoets, L. *et al.* Differences in gut microbiota composition between obese and lean children: a cross-sectional study. *Gut Pathog* **5**, 10 (2013).
- Biagi, E. *et al.* Through Ageing, and Beyond: Gut Microbiota and Inflammatory Status in Seniors and Centenarians. *PLoS One* **5**, e10667 (2010).
- Biesalski, H. K. Nutrition meets the microbiome: micronutrients and the microbiota. *Ann N Y Acad Sci* **1372**, 53–64 (2016).
- Blackburn, E. H. Telomeres and telomerase: their mechanisms of action and the effects of altering their functions. *FEBS Lett* **579**, 859–862 (2005).
- Bogdan, A. R., Miyazawa, M., Hashimoto, K. & Tsuji, Y. Regulators of Iron Homeostasis: New Players in Metabolism, Cell Death, and Disease. *Trends Biochem Sci* **41**, 274–286 (2016).
- Bonifácio, V. D. B., Pereira, S. A., Serpa, J. & Vicente, J. B. Cysteine metabolic circuitries: druggable targets in cancer. *Br J Cancer* **124**, 862–879 (2021).
- Bouskra, D. *et al.* Lymphoid tissue genesis induced by commensals through NOD1 regulates intestinal homeostasis. *Nature* **456**, 507–510 (2008).
- Byerly, L., Cassada, R. C. & Russell, R. L. The life cycle of the nematode *Caenorhabditis elegans*. *Dev Biol* **51**, 23–33 (1976).
- Byrne, J. J. *et al.* Disruption of mitochondrial dynamics affects behaviour and lifespan in *Caenorhabditis elegans*. *Cellular and Molecular Life Sciences* **76**, 1967–1985 (2019).
- Cabreiro, F. & Gems, D. Worms need microbes too: microbiota, health and aging in *Caenorhabditis elegans*. *EMBO Mol Med* **5**, 1300–1310 (2013).
- Campisi, J. Aging, Cellular Senescence, and Cancer. *Annu Rev Physiol* **75**, 685–705 (2013).
- Caporaso, J. G. *et al.* Global patterns of 16S rRNA diversity at a depth of millions of sequences per sample. *Proceedings of the National Academy of Sciences* **108**, 4516–4522 (2011).
- Carone, G. *et al.* The economic impact of ageing populations in the EU25 Member States. *Directorate-General for Economic and Financial Affairs* (2005).
- Cary, M., Podshivalova, K. & Kenyon, C. Application of Transcriptional Gene Modules to Analysis of *Caenorhabditis elegans* ' Gene Expression Data. *G3 Genes/Genomes/Genetics* **10**, 3623–3638 (2020).
- Cassada, R. C. & Russell, R. L. The dauerlarva, a post-embryonic developmental variant of the nematode *Caenorhabditis elegans*. *Dev Biol* **46**, 326–342 (1975).
- Castellani, C. A., Longchamps, R. J., Sun, J., Guallar, E. & Arking, D. E. Thinking outside the nucleus: Mitochondrial DNA copy number in health and disease. *Mitochondrion* **53**, 214–223 (2020).

- Cersosimo, M. G. & Benarroch, E. E. Pathological correlates of gastrointestinal dysfunction in Parkinson's disease. *Neurobiol Dis* **46**, 559–564 (2012).
- Cezairliyan, B., Vinayavekhin, N., Grenfell-Lee, D., Yuen, G. J., Saghatelian, A., & Ausubel, F. M. Identification of *Pseudomonas aeruginosa* Phenazines that Kill *Caenorhabditis elegans*. *PLoS Pathogens*, *9*(1), e1003101. (2013).
- Chakkalakal, J. V., Jones, K. M., Basson, M. A. & Brack, A. S. The aged niche disrupts muscle stem cell quiescence. *Nature* **490**, 355–360 (2012).
- Chalfie, M. Assaying mechanosensation. *WormBook* 1–13 (2014) doi:10.1895/wormbook.1.172.1.
- Chalfie, M. *et al.* The neural circuit for touch sensitivity in *Caenorhabditis elegans*. *The Journal of Neuroscience* **5**, 956–964 (1985).
- Chan, D. C. Mitochondrial Fusion and Fission in Mammals. *Annu Rev Cell Dev Biol* **22**, 79–99 (2006).
- Chandhok, G., Lazarou, M. & Neumann, B. Structure, function, and regulation of mitofusin-2 in health and disease. *Biological Reviews* **93**, 933–949 (2018).
- Chatzigeorgiou, M. *et al.* Spatial Asymmetry in the Mechanosensory Phenotypes of the *C. elegans* DEG/ENaC Gene *mec-10*. *J Neurophysiol* **104**, 3334–3344 (2010).
- Chaudhari, S. N. & Kipreos, E. T. Increased mitochondrial fusion allows the survival of older animals in diverse *C. elegans* longevity pathways. *Nat Commun* **8**, 182 (2017).
- Chaya, T. *et al.* A *C. elegans* genome-wide RNAi screen for altered levamisole sensitivity identifies genes required for muscle function. *G3 Genes/Genomes/Genetics* **11**, (2021).
- Cheesman, H. K. *et al.* Aberrant Activation of p38 MAP Kinase-Dependent Innate Immune Responses Is Toxic to *Caenorhabditis elegans*. *G3 Genes/Genomes/Genetics* **6**, 541–549 (2016).
- Chen, C. *et al.* Gut dysbiosis contributes to amyloid pathology, associated with C/EBP $\beta$ /AEP signaling activation in Alzheimer's disease mouse model. *Sci Adv* **6**, (2020).
- Chen, C.-H., Chen, Y.-C., Jiang, H.-C., Chen, C.-K. & Pan, C.-L. Neuronal aging: learning from *C. elegans*. *J Mol Signal* **8**, 14 (2013).
- Chen, H., Chomyn, A. & Chan, D. C. Disruption of Fusion Results in Mitochondrial Heterogeneity and Dysfunction. *Journal of Biological Chemistry* **280**, 26185–26192 (2005).
- Chikka, M. R., Anbalagan, C., Dvorak, K., Dombeck, K., & Prahlad, V. The Mitochondria-Regulated Immune Pathway Activated in the *C. elegans* Intestine Is Neuroprotective. *Cell Reports*, *16*(9), 2399–2414. (2016).
- Cho, I. & Blaser, M. J. The human microbiome: at the interface of health and disease. *Nat Rev Genet* **13**, 260–270 (2012).
- Cho, D.-H., Nakamura, T., Fang, J., Cieplak, P., Godzik, A., Gu, Z., & Lipton, S. A. S-Nitrosylation of Drp1 Mediates  $\beta$ -Amyloid-Related Mitochondrial Fission and Neuronal Injury. *Science*, *324*(5923), 102–105. (2009).
- Chow, D., Glenn, C., Johnston, J., Goldberg, I. & Wolkow, C. Sarcopenia in the *Caenorhabditis elegans* pharynx correlates with muscle contraction rate over lifespan. *Exp Gerontol* **41**, 252–260 (2006).
- Claesson, M. J. *et al.* Composition, variability, and temporal stability of the intestinal microbiota of the elderly. *Proceedings of the National Academy of Sciences* **108**, 4586–4591 (2011).

- Clarke, S. F. *et al.* Exercise and associated dietary extremes impact on gut microbial diversity. *Gut* **63**, 1913–1920 (2014).
- Colangelo, V. *et al.* Gene expression profiling of 12633 genes in Alzheimer hippocampal CA1: Transcription and neurotrophic factor down-regulation and up-regulation of apoptotic and pro-inflammatory signaling. *J Neurosci Res* **70**, 462–473 (2002).
- Colman, R. J. *et al.* Caloric Restriction Delays Disease Onset and Mortality in Rhesus Monkeys. *Science (1979)* **325**, 201–204 (2009).
- Consortium HMP. Data Analysis and Coordination Center (DACC). *Human Microbiome Project (HMP)* (2012).
- Coolon, J. D., Jones, K. L., Todd, T. C., Carr, B. C. & Herman, M. A. *Caenorhabditis elegans* Genomic Response to Soil Bacteria Predicts Environment-Specific Genetic Effects on Life History Traits. *PLoS Genet* **5**, e1000503 (2009). Cornelis, P. & Dingemans, J. *Pseudomonas aeruginosa* adapts its iron uptake strategies in function of the type of infections. *Front Cell Infect Microbiol* **3**, (2013).
- Cotter, P. D., Stanton, C., Ross, R. P. & Hill, C. The impact of antibiotics on the gut microbiota as revealed by high throughput DNA sequencing. *Discov Med* **13**, 193–9 (2012).
- Couvillion, M. T., Soto, I. C., Shipkovenska, G. & Churchman, L. S. Synchronized mitochondrial and cytosolic translation programs. *Nature* **533**, 499–503 (2016).
- Cox, M. A. *et al.* Short-chain fatty acids act as antiinflammatory mediators by regulating prostaglandin E(2) and cytokines. *World J Gastroenterol* **15**, 5549–57 (2009).
- Crimmins, E. M. & Beltran-Sanchez, H. Mortality and Morbidity Trends: Is There Compression of Morbidity? *J Gerontol B Psychol Sci Soc Sci* **66B**, 75–86 (2011).
- Cryan, J. F. & Dinan, T. G. Mind-altering microorganisms: the impact of the gut microbiota on brain and behaviour. *Nat Rev Neurosci* **13**, 701–712 (2012).
- Dagda, R. K. *et al.* Loss of PINK1 Function Promotes Mitophagy through Effects on Oxidative Stress and Mitochondrial Fission. *Journal of Biological Chemistry* **284**, 13843–13855 (2009).
- Darby, C. Interactions with microbial pathogens. *WormBook* (2005) doi:10.1895/wormbook.1.21.1.
- Dasari, M. *et al.* Bacterial Inclusion Bodies of Alzheimer's Disease  $\beta$ -Amyloid Peptides Can Be Employed To Study Native-Like Aggregation Intermediate States. *ChemBioChem* **12**, 407–423 (2011).
- De Angelis, M. *et al.* Fecal Microbiota and Metabolome of Children with Autism and Pervasive Developmental Disorder Not Otherwise Specified. *PLoS One* **8**, e76993 (2013).
- Derry, P. J. & Kent, T. A. Correlating quantitative susceptibility mapping with cognitive decline in Alzheimer's disease. *Brain* **140**, 2069–2072 (2017).
- Dev, S. & Babitt, J. L. Overview of iron metabolism in health and disease. *Hemodialysis International* **21**, S6–S20 (2017).
- DiLoreto, R. & Murphy, C. T. The cell biology of aging. *Mol Biol Cell* **26**, 4524–4531 (2015).
- Dirksen, P. *et al.* CeMbio - The *Caenorhabditis elegans* Microbiome Resource. *G3 Genes/Genomes/Genetics* **10**, 3025–3039 (2020).
- Dixon, S. J. *et al.* Ferroptosis: An Iron-Dependent Form of Nonapoptotic Cell Death. *Cell* **149**, 1060–1072 (2012).

- Dobin, A., Davis, C. A., Schlesinger, F., Drenkow, J., Zaleski, C., Jha, S., Batut, P., Chaisson, M., & Gingeras, T. R. STAR: ultrafast universal RNA-seq aligner. *Bioinformatics*, **29**(1), 15–21. (2013).
- Doles, J., Storer, M., Cozzuto, L., Roma, G. & Keyes, W. M. Age-associated inflammation inhibits epidermal stem cell function. *Genes Dev* **26**, 2144–2153 (2012).
- Doonan, R., McElwee, J. J., Matthijssens, F., Walker, G. A., Houthoofd, K., Back, P., Matscheski, A., Vanfleteren, J. R., & Gems, D. (2008). Against the oxidative damage theory of aging: superoxide dismutases protect against oxidative stress but have little or no effect on life span in *Caenorhabditis elegans*. *Genes & Development*, **22**(23), 3236–3241.
- Dong, C., Davis, R. J. & Flavell, R. A. MAP Kinases in the Immune Response. *Annu Rev Immunol* **20**, 55–72 (2002).
- Dorsey, E. R. *et al.* Global, regional, and national burden of Parkinson's disease, 1990–2016: a systematic analysis for the Global Burden of Disease Study 2016. *Lancet Neurol* **17**, 939–953 (2018).
- Dringen, R. Metabolism and functions of glutathione in brain. *Prog Neurobiol* **62**, 649–671 (2000).
- Dumas, Z., Ross-Gillespie, A. & Kümmerli, R. Switching between apparently redundant iron-uptake mechanisms benefits bacteria in changeable environments. *Proceedings of the Royal Society B: Biological Sciences* **280**, 20131055 (2013).
- Duranti, S. *et al.* Maternal inheritance of bifidobacterial communities and bifidophages in infants through vertical transmission. *Microbiome* **5**, 66 (2017).
- Durieux, J., Wolff, S. & Dillin, A. The Cell-Non-Autonomous Nature of Electron Transport Chain-Mediated Longevity. *Cell* **144**, 79–91 (2011).
- Ekmekciu, I. *et al.* Fecal Microbiota Transplantation, Commensal *Escherichia coli* and *Lactobacillus johnsonii* Strains Differentially Restore Intestinal and Systemic Adaptive Immune Cell Populations Following Broad-spectrum Antibiotic Treatment. *Front Microbiol* **8**, (2017).
- Emerson, D., Roden, E. & Twining, B. S. The microbial ferrous wheel: iron cycling in terrestrial, freshwater, and marine environments. *Front Microbiol* **3**, (2012).
- Ezcurra, M. Dissecting cause and effect in host-microbiome interactions using the combined worm-bug model system. *Biogerontology* **19**, 567–578 (2018).
- Fatouros, C. *et al.* Inhibition of tau aggregation in a novel *Caenorhabditis elegans* model of tauopathy mitigates proteotoxicity. *Hum Mol Genet* **21**, 3587–3603 (2012).
- Ferrera, D., Mazzaro, N., Canale, C. & Gasparini, L. Resting microglia react to A $\beta$ 42 fibrils but do not detect oligomers or oligomer-induced neuronal damage. *Neurobiol Aging* **35**, 2444–2457 (2014).
- Finegold, S. M. *et al.* Pyrosequencing study of fecal microflora of autistic and control children. *Anaerobe* **16**, 444–453 (2010).
- Fischbach, M. A. Microbiome: Focus on Causation and Mechanism. *Cell* **174**, 785–790 (2018).
- Fischer, K. E. *et al.* A cross-sectional study of male and female C57BL/6Nia mice suggests lifespan and healthspan are not necessarily correlated. *Aging* **8**, 2370–2391 (2016).
- Flores, I., Cayuela, M. L. & Blasco, M. A. Effects of Telomerase and Telomere Length on Epidermal Stem Cell Behavior. *Science (1979)* **309**, 1253–1256 (2005).

- Fontana, L., Partridge, L. & Longo, V. D. Extending Healthy Life Span—From Yeast to Humans. *Science* (1979) **328**, 321–326 (2010).fs
- Frézal, L. & Félix, M.-A. C. elegans outside the Petri dish. *Elife* **4**, (2015).
- Friedland, R. P. Mechanisms of Molecular Mimicry Involving the Microbiota in Neurodegeneration. *Journal of Alzheimer's Disease* **45**, 349–362 (2015).
- Fu, H. *et al.* Wounding triggers MIRO-1 dependent mitochondrial fragmentation that accelerates epidermal wound closure through oxidative signaling. *Nat Commun* **11**, 1050 (2020).
- Gaffney, C. J., Bass, J. J., Barratt, T. F. & Szewczyk, N. J. Methods to Assess Subcellular Compartments of Muscle in *C. elegans*; *Journal of Visualized Experiments* (2014) doi:10.3791/52043.
- Gaiser, A. M., Kaiser, C. J. O., Haslbeck, V. & Richter, K. Downregulation of the Hsp90 System Causes Defects in Muscle Cells of *Caenorhabditis Elegans*. *PLoS One* **6**, e25485 (2011).
- Gao, M. *et al.* Role of Mitochondria in Ferroptosis. *Mol Cell* **73**, 354-363.e3 (2019).
- Gems, D. The aging-disease false dichotomy: understanding senescence as pathology. *Front Genet* **6**, (2015).
- Gieseler, K. Development, structure, and maintenance of *C. elegans* body wall muscle. *WormBook* 1–59 (2017) doi:10.1895/wormbook.1.81.2.
- Gill, S. R. *et al.* Metagenomic Analysis of the Human Distal Gut Microbiome. *Science* (1979) **312**, 1355–1359 (2006).
- Glenn, C. F. *et al.* Behavioral Deficits During Early Stages of Aging in *Caenorhabditis elegans* Result From Locomotory Deficits Possibly Linked to Muscle Frailty. *J Gerontol A Biol Sci Med Sci* **59**, 1251–1260 (2004).
- Goh, G. Y. S. *et al.* The conserved Mediator subunit MDT-15 is required for oxidative stress responses in *Caenorhabditis elegans*. *Aging Cell* **13**, 70–79 (2014).
- Gomes, L. C., Benedetto, G. Di & Scorrano, L. During autophagy mitochondria elongate, are spared from degradation and sustain cell viability. *Nat Cell Biol* **13**, 589–598 (2011).
- Gourley, B. L., Parker, S. B., Jones, B. J., Zumbrennen, K. B. & Leibold, E. A. Cytosolic Aconitase and Ferritin Are Regulated by Iron in *Caenorhabditis elegans*. *Journal of Biological Chemistry* **278**, 3227–3234 (2003).
- Goya, M. E. *et al.* Probiotic *Bacillus subtilis* Protects against  $\alpha$ -Synuclein Aggregation in *C. elegans*. *Cell Rep* **30**, 367-380.e7 (2020).
- Gray, M. W., Burger, G. & Lang, B. F. The origin and early evolution of mitochondria. *Genome Biol* **2**, reviews1018.1 (2001).
- Green, D. R., Galluzzi, L. & Kroemer, G. Mitochondria and the Autophagy–Inflammation–Cell Death Axis in Organismal Aging. *Science* (1979) **333**, 1109–1112 (2011).
- Grewal, P. S. Relative contribution of nematodes (*Caenorhabditis elegans*) and bacteria towards the disruption of flushing patterns and losses in yield and quality of mushrooms (*Agaricus bisporus*). *Annals of Applied Biology* **119**, 483–499 (1991).
- Guerinot, M. Lou. Microbial Iron Transport. *Annu Rev Microbiol* **48**, 743–772 (1994).

- Guilloteau, P. *et al.* From the gut to the peripheral tissues: the multiple effects of butyrate. *Nutr Res Rev* **23**, 366–384 (2010).
- Gusella, J. F. & MacDonald, M. E. Molecular genetics: Unmasking polyglutamine triggers in neurodegenerative disease. *Nat Rev Neurosci* **1**, 109–115 (2000).
- Haigis, M. C. & Yankner, B. A. The Aging Stress Response. *Mol Cell* **40**, 333–344 (2010).
- Hamelin, M., Scott, I. M., Way, J. C. & Culotti, J. G. The mec-7 beta-tubulin gene of *Caenorhabditis elegans* is expressed primarily in the touch receptor neurons. *EMBO J* **11**, 2885–2893 (1992).
- Harman, D. The Free Radical Theory of Aging: Effect of Age on Serum Copper Levels. *Journal of Gerontology*, *20*(2), 151–153. (1965).
- Harrison, P. M. & Arosio, P. The ferritins: molecular properties, iron storage function and cellular regulation. *Biochimica et Biophysica Acta (BBA) - Bioenergetics* **1275**, 161–203 (1996).
- Hartl, F. U., Bracher, A. & Hayer-Hartl, M. Molecular chaperones in protein folding and proteostasis. *Nature* **475**, 324–332 (2011).
- Hayashi, H., Sakamoto, M., Kitahara, M. & Benno, Y. Molecular Analysis of Fecal Microbiota in Elderly Individuals Using 16S rDNA Library and T-RFLP. *Microbiol Immunol* **47**, 557–570 (2003).
- Haynes, C. M. & Ron, D. The mitochondrial UPR – protecting organelle protein homeostasis. *J Cell Sci* **123**, 3849–3855 (2010).
- Haynes, C. M., Petrova, K., Benedetti, C., Yang, Y. & Ron, D. ClpP Mediates Activation of a Mitochondrial Unfolded Protein Response in *C. elegans*. *Dev Cell* **13**, 467–480 (2007).
- Heneka, M. T. *et al.* Neuroinflammation in Alzheimer’s disease. *Lancet Neurol* **14**, 388–405 (2015).
- Herndon, L. A. *et al.* Stochastic and genetic factors influence tissue-specific decline in ageing *C. elegans*. *Nature* **419**, 808–814 (2002).
- Hertweck, M. *C. elegans*, a model for aging with high-throughput capacity. *Exp Gerontol* **38**, 345–346 (2003).
- Hickman, S. E., Allison, E. K. & El Khoury, J. Microglial Dysfunction and Defective  $\beta$ -Amyloid Clearance Pathways in Aging Alzheimer’s Disease Mice. *The Journal of Neuroscience* **28**, 8354–8360 (2008).
- Hill, J. M. & Lukiw, W. J. Microbial-generated amyloids and Alzheimer’s disease (AD). *Front Aging Neurosci* **7**, (2015).
- Himpsl, S. D. & Mobley, H. L. T. Siderophore Detection Using Chrome Azurol S and Cross-Feeding Assays. in 97–108 (2019). doi:10.1007/978-1-4939-9601-8\_10.
- Hosono, R., Sato, Y., Aizawa, S.-I. & Mitsui, Y. Age-dependent changes in mobility and separation of the nematode *Caenorhabditis elegans*. *Exp Gerontol* **15**, 285–289 (1980).
- Houtkooper, R. H. *et al.* Mitonuclear protein imbalance as a conserved longevity mechanism. *Nature* **497**, 451–457 (2013).
- Huang, C., Xiong, C. & Kornfeld, K. Measurements of age-related changes of physiological processes that predict lifespan of *Caenorhabditis elegans*. *Proceedings of the National Academy of Sciences* **101**, 8084–8089 (2004).

- Huffman, D. M. *et al.* Evaluating Health Span in Preclinical Models of Aging and Disease: Guidelines, Challenges, and Opportunities for Geroscience. *J Gerontol A Biol Sci Med Sci* **71**, 1395–1406 (2016).
- Hughes, S. E., Evason, K., Xiong, C. & Kornfeld, K. Genetic and Pharmacological Factors That Influence Reproductive Aging in Nematodes. *PLoS Genet* **3**, e25 (2007).
- Inoue, H. *et al.* The *C. elegans* p38 MAPK pathway regulates nuclear localization of the transcription factor SKN-1 in oxidative stress response. *Genes Dev* **19**, 2278–2283 (2005).
- Jheng, H.-F. *et al.* Mitochondrial Fission Contributes to Mitochondrial Dysfunction and Insulin Resistance in Skeletal Muscle. *Mol Cell Biol* **32**, 309–319 (2012).
- Johari, S., Nock, V., Alkaisi, M. M. & Wang, W. On-chip analysis of *C. elegans* muscular forces and locomotion patterns in microstructured environments. *Lab Chip* **13**, 1699 (2013).
- Jovaisaite, V., Mouchiroud, L. & Auwerx, J. The mitochondrial unfolded protein response, a conserved stress response pathway with implications in health and disease. *Journal of Experimental Biology* **217**, 137–143 (2014).
- Kamada, C. *et al.* Optimal energy distribution of carbohydrate intake for Japanese elderly patients with type 2 diabetes: The Japanese Elderly Intervention Trial. *Geriatr Gerontol Int* **12**, 41–49 (2012).
- Kamaladevi, A. & Balamurugan, K. Role of PMK-1/p38 MAPK defense in *Caenorhabditis elegans* against *Klebsiella pneumoniae* infection during host–pathogen interaction. *Pathog Dis* **73**, (2015).
- Kamath, R. S., Martinez-Campos, M., Zipperlen, P., Fraser, A. G. & Ahringer, J. Effectiveness of specific RNA-mediated interference through ingested double-stranded RNA in *Caenorhabditis elegans*. *Genome Biol* **2**, research0002.1 (2000).
- Kanazawa, T. *et al.* The *C. elegans* Opa1 Homologue EAT-3 Is Essential for Resistance to Free Radicals. *PLoS Genet* **4**, e1000022 (2008).
- Kanfi, Y. *et al.* The sirtuin SIRT6 regulates lifespan in male mice. *Nature* **483**, 218–221 (2012).
- Kapahi, P. *et al.* With TOR, Less Is More: A Key Role for the Conserved Nutrient-Sensing TOR Pathway in Aging. *Cell Metab* **11**, 453–465 (2010).
- Kazantzi, G. Diagnosis and Treatment of Metal Poisoning—General Aspects. in *Handbook on the Toxicology of Metals* 303–317 (Elsevier, 2007).
- Kennedy, B. K. *et al.* Geroscience: Linking Aging to Chronic Disease. *Cell* **159**, 709–713 (2014).
- Kenny, E. M. *et al.* Ferroptosis Contributes to Neuronal Death and Functional Outcome After Traumatic Brain Injury\*. *Crit Care Med* **47**, 410–418 (2019).
- Kenyon, C. J. The genetics of ageing. *Nature* **464**, 504–512 (2010).
- Kenyon, C., Chang, J., Gensch, E., Rudner, A. & Tabtiang, R. A *C. elegans* mutant that lives twice as long as wild type. *Nature* **366**, 461–464 (1993).
- Kikis, E. A., Gidalevitz, T. & Morimoto, R. I. Protein Homeostasis in Models of Aging and Age-Related Conformational Disease. in 138–159 (2010).
- Kim, D. I., Lee, K. H., Gabr, A. A., Choi, G. E., Kim, J. S., Ko, S. H., & Han, H. J. A $\beta$ -Induced Drp1 phosphorylation through Akt activation promotes excessive mitochondrial fission leading to neuronal apoptosis. *Biochimica et Biophysica Acta (BBA) - Molecular Cell Research*, 1863(11), 2820–2834. (2016).

- Kim, D. H. Bacteria and the Aging and Longevity of *Caenorhabditis elegans*. *Annu Rev Genet* **47**, 233–246 (2013).
- Kim, D. H. *et al.* Integration of *Caenorhabditis elegans* MAPK pathways mediating immunity and stress resistance by MEK-1 MAPK kinase and VHP-1 MAPK phosphatase. *Proceedings of the National Academy of Sciences* **101**, 10990–10994 (2004).
- Kim, E. B. *et al.* Genome sequencing reveals insights into physiology and longevity of the naked mole rat. *Nature* **479**, 223–227 (2011).
- Kim, I., Rodriguez-Enriquez, S. & Lemasters, J. J. Selective degradation of mitochondria by mitophagy. *Arch Biochem Biophys* **462**, 245–253 (2007).
- Kim, S., Covington, A. & Pamer, E. G. The intestinal microbiota: Antibiotics, colonization resistance, and enteric pathogens. *Immunol Rev* **279**, 90–105 (2017).
- Kim, Y.-I., Cho, J. H., Yoo, O. J. & Ahnn, J. Transcriptional Regulation and Life-span Modulation of Cytosolic Aconitase and Ferritin Genes in *C.elegans*. *J Mol Biol* **342**, 421–433 (2004).
- Kinnebrew, M. A. & Pamer, E. G. Innate immune signaling in defense against intestinal microbes. *Immunol Rev* **245**, 113–131 (2012).
- Kirienko, N. V. *et al.* *Pseudomonas aeruginosa* Disrupts *Caenorhabditis elegans* Iron Homeostasis, Causing a Hypoxic Response and Death. *Cell Host Microbe* **13**, 406–416 (2013).
- Kissoyan, K. A. B., Peters, L., Giez, C., Michels, J., Pees, B., Hamerich, I. K., Schulenburg, H., & Dierking, K. Exploring Effects of *C. elegans* Protective Natural Microbiota on Host Physiology. *Frontiers in Cellular and Infection Microbiology*, 12. (2022).
- Kissoyan, K. A. B., Drechsler, M., Stange, E.-L., Zimmermann, J., Kaleta, C., Bode, H. B., & Dierking, K. Natural *C. elegans* Microbiota Protects against Infection via Production of a Cyclic Lipopeptide of the Viscosin Group. *Current Biology*, 29(6), 1030-1037.e5. (2019).
- Koga, H., Kaushik, S. & Cuervo, A. M. Protein homeostasis and aging: The importance of exquisite quality control. *Ageing Res Rev* **10**, 205–215 (2011).
- Kontis, V. *et al.* Future life expectancy in 35 industrialised countries: projections with a Bayesian model ensemble. *The Lancet* **389**, 1323–1335 (2017).
- Kramer, J., Özkaya, Ö. & Kümmerli, R. Bacterial siderophores in community and host interactions. *Nat Rev Microbiol* **18**, 152–163 (2020).
- Kramer, J., Özkaya, Ö. & Kümmerli, R. Bacterial siderophores in community and host interactions. *Nat Rev Microbiol* **18**, 152–163 (2020).
- Kuilman, T., Michaloglou, C., Mooi, W. J. & Peeper, D. S. The essence of senescence. *Genes Dev* **24**, 2463–2479 (2010).
- Kujoth, G. C., Hiona, A., Pugh, T. D., Someya, S., Panzer, K., Wohlgemuth, S. E., Hofer, T., Seo, A. Y., Sullivan, R., Jobling, W. A., Morrow, J. D., van Remmen, H., Sedivy, J. M., Yamasoba, T., Tanokura, M., Weindruch, R., Leeuwenburgh, C., & Prolla, T. A. Mitochondrial DNA Mutations, Oxidative Stress, and Apoptosis in Mammalian Aging. *Science*, 309(5733), 481–484. (2005).
- Labrousse, A. M., Zappaterra, M. D., Rube, D. A. & van der Bliek, A. M. *C. elegans* Dynamin-Related Protein DRP-1 Controls Severing of the Mitochondrial Outer Membrane. *Mol Cell* **4**, 815–826 (1999).

- Lapierre, L. R., de Magalhaes Filho, C. D., McQuary, P. R., Chu, C.-C., Visvikis, O., Chang, J. T., Gelino, S., Ong, B., Davis, A. E., Irazoqui, J. E., Dillin, A., & Hansen, M. The TFEB orthologue HLH-30 regulates autophagy and modulates longevity in *Caenorhabditis elegans*. *Nature Communications*, **4**(1), 2267. (2013).
- Laranjeiro, R. *et al.* Swim exercise in *Caenorhabditis elegans* extends neuromuscular and gut healthspan, enhances learning ability, and protects against neurodegeneration. *Proceedings of the National Academy of Sciences* **116**, 23829–23839 (2019).
- Lee, T. Y., Yoon, K. & Lee, J. II. NGT-3D: a simple nematode cultivation system to study *Caenorhabditis elegans* biology in 3D. *Biol Open* **5**, 529–534 (2016).
- Lesanpezeshki, L. *et al.* Pluronic gel-based burrowing assay for rapid assessment of neuromuscular health in *C. elegans*. *Sci Rep* **9**, 15246 (2019).
- Levine, B. & Kroemer, G. Autophagy in the Pathogenesis of Disease. *Cell* **132**, 27–42 (2008).
- LeVine, H. Quantification of  $\beta$ -sheet amyloid fibril structures with thioflavin T. in 274–284 (1999). doi:10.1016/S0076-6879(99)09020-5.
- Lewis, J. A., Wu, C.-H., Berg, H. & Levine, J. H. The genetics of levamisole resistance in the nematode *Caenorhabditis elegans*. *Genetics* **95**, 905–928 (1980).
- Ley, R. E. *et al.* Obesity alters gut microbial ecology. *Proceedings of the National Academy of Sciences* **102**, 11070–11075 (2005).
- Ley, R. E., Turnbaugh, P. J., Klein, S. & Gordon, J. I. Human gut microbes associated with obesity. *Nature* **444**, 1022–1023 (2006).
- Li, W., Kang, L., Piggott, B. J., Feng, Z. & Xu, X. Z. S. The neural circuits and sensory channels mediating harsh touch sensation in *Caenorhabditis elegans*. *Nat Commun* **2**, 315 (2011).
- Lian Chew, Y., Fan, X., Götz, J. & Nicholas, H. R. Aging in the nervous system of *Caenorhabditis elegans*. *Commun Integr Biol* **6**, e25288 (2013).
- Liao Y, Smyth GK, and Shi W. featureCounts: an efficient general purpose program for assigning sequence reads to genomic features. *Bioinformatics*, **30**(7):923-30. (2014).
- Lieber, R. L., Roberts, T. J., Blemker, S. S., Lee, S. S. M. & Herzog, W. Skeletal muscle mechanics, energetics and plasticity. *J Neuroeng Rehabil* **14**, 108 (2017).
- Liesa, M. & Shirihai, O. S. Mitochondrial Dynamics in the Regulation of Nutrient Utilization and Energy Expenditure. *Cell Metab* **17**, 491–506 (2013).
- Lin, L., Zheng, L. J. & Zhang, L. J. Neuroinflammation, Gut Microbiome, and Alzheimer's Disease. *Mol Neurobiol* **55**, 8243–8250 (2018).
- Liu, D. & Thomas, J. Regulation of a periodic motor program in *C. elegans*. *The Journal of Neuroscience* **14**, 1953–1962 (1994).
- Liu, Y. J., McIntyre, R. L., Janssens, G. E. & Houtkooper, R. H. Mitochondrial fission and fusion: A dynamic role in aging and potential target for age-related disease. *Mech Ageing Dev* **186**, 111212 (2020).
- Llamas, M. A. *et al.* The Heterologous Siderophores Ferrioxamine B and Ferrichrome Activate Signaling Pathways in *Pseudomonas aeruginosa*. *J Bacteriol* **188**, 1882–1891 (2006).

- Lloyd-Price, J., Abu-Ali, G. & Huttenhower, C. The healthy human microbiome. *Genome Med* **8**, 51 (2016).
- López-Otín, C., Blasco, M. A., Partridge, L., Serrano, M. & Kroemer, G. The Hallmarks of Aging. *Cell* **153**, 1194–1217 (2013).
- Love, M.I., Huber, W. & Anders, S. Moderated estimation of fold change and dispersion for RNA-seq data with DESeq2. *Genome Biol* **15**, 550. (2014).
- Lutz, A. K. *et al.* Loss of parkin or PINK1 function increases Drp1-dependent mitochondrial fragmentation. *J Biol Chem* **284**, 22938–51 (2009).
- Luz, A. L. *et al.* Mitochondrial Morphology and Fundamental Parameters of the Mitochondrial Respiratory Chain Are Altered in *Caenorhabditis elegans* Strains Deficient in Mitochondrial Dynamics and Homeostasis Processes. *PLoS One* **10**, e0130940 (2015).
- Machiela, E. *et al.* The Interaction of Aging and Cellular Stress Contributes to Pathogenesis in Mouse and Human Huntington Disease Neurons. *Front Aging Neurosci* **12**, (2020).
- MacNeil, L. T., Watson, E., Arda, H. E., Zhu, L. J. & Walhout, A. J. M. Diet-Induced Developmental Acceleration Independent of TOR and Insulin in *C. elegans*. *Cell* **153**, 240–252 (2013).
- Macpherson, A. J. & Harris, N. L. Interactions between commensal intestinal bacteria and the immune system. *Nat Rev Immunol* **4**, 478–485 (2004).
- Mahajan-Miklos, S., Tan, M.-W., Rahme, L. G. & Ausubel, F. M. Molecular Mechanisms of Bacterial Virulence Elucidated Using a *Pseudomonas aeruginosa*–*Caenorhabditis elegans* Pathogenesis Model. *Cell* **96**, 47–56 (1999).
- Mahoney, T. R. *et al.* Intestinal signaling to GABAergic neurons regulates a rhythmic behavior in *Caenorhabditis elegans*. *Proceedings of the National Academy of Sciences* **105**, 16350–16355 (2008).
- Mao, K. *et al.* Mitochondrial Dysfunction in *C. elegans* Activates Mitochondrial Relocalization and Nuclear Hormone Receptor-Dependent Detoxification Genes. *Cell Metab* **29**, 1182-1191.e4 (2019).
- Mariat, D. *et al.* The Firmicutes/Bacteroidetes ratio of the human microbiota changes with age. *BMC Microbiol* **9**, 123 (2009).
- Martín, R., Bermúdez-Humarán, L. G. & Langella, P. Gnotobiotic Rodents: An In Vivo Model for the Study of Microbe–Microbe Interactions. *Front Microbiol* **7**, (2016).
- Martin, W. F., Garg, S. & Zimorski, V. Endosymbiotic theories for eukaryote origin. *Philosophical Transactions of the Royal Society B: Biological Sciences* **370**, 20140330 (2015).
- Martinus, R. D. *et al.* Selective Induction of Mitochondrial Chaperones in Response to Loss of the Mitochondrial Genome. *Eur J Biochem* **240**, 98–103 (1996).
- McBride, H. M., Neuspiel, M. & Wasiak, S. Mitochondria: More Than Just a Powerhouse. *Current Biology* **16**, R551–R560 (2006).
- McColl, G. *et al.* The *Caenorhabditis elegans* A $\beta$ 1–42 Model of Alzheimer Disease Predominantly Expresses A $\beta$ 3–42. *Journal of Biological Chemistry* **284**, 22697–22702 (2009).
- Medema, M. H. *et al.* antiSMASH: rapid identification, annotation and analysis of secondary metabolite biosynthesis gene clusters in bacterial and fungal genome sequences. *Nucleic Acids Res* **39**, W339–W346 (2011).

- Meissner, B. *et al.* An Integrated Strategy to Study Muscle Development and Myofilament Structure in *Caenorhabditis elegans*. *PLoS Genet* **5**, e1000537 (2009)
- Mesquita, A., Weinberger, M., Silva, A., Sampaio-Marques, B., Almeida, B., Leão, C., Costa, V., Rodrigues, F., Burhans, W. C., & Ludovico, P. Caloric restriction or catalase inactivation extends yeast chronological lifespan by inducing H<sub>2</sub>O<sub>2</sub> and superoxide dismutase activity. *Proceedings of the National Academy of Sciences*, *107*(34). (2010).
- Meyer, J. M. Pyoverdines: pigments, siderophores and potential taxonomic markers of fluorescent *Pseudomonas* species. *Arch Microbiol* **174**, 135–42 (2000).
- Miller, D. M., Ortiz, I., Berliner, G. C. & Epstein, H. F. Differential localization of two myosins within nematode thick filaments. *Cell* **34**, 477–490 (1983).
- Mok, D. Z. L., Sternberg, P. W. & Inoue, T. Morphologically defined sub-stages of *C. elegans* vulval development in the fourth larval stage. *BMC Dev Biol* **15**, 26 (2015).
- Montalvo-Katz, S., Huang, H., Appel, M. D., Berg, M. & Shapira, M. Association with Soil Bacteria Enhances p38-Dependent Infection Resistance in *Caenorhabditis elegans*. *Infect Immun* **81**, 514–520 (2013).
- Moreau, M. C., Ducluzeau, R., Guy-Grand, D. & Muller, M. C. Increase in the Population of Duodenal Immunoglobulin A Plasmocytes in Axenic Mice Associated with Different Living or Dead Bacterial Strains of Intestinal Origin. *Infect Immun* **21**, 532–539 (1978).
- Morley, J. F., Brignull, H. R., Weyers, J. J. & Morimoto, R. I. The threshold for polyglutamine-expansion protein aggregation and cellular toxicity is dynamic and influenced by aging in *Caenorhabditis elegans*. *Proceedings of the National Academy of Sciences* **99**, 10417–10422 (2002).
- Morley, J. F., Brignull, H. R., Weyers, J. J. & Morimoto, R. I. The threshold for polyglutamine-expansion protein aggregation and cellular toxicity is dynamic and influenced by aging in *Caenorhabditis elegans*. *Proceedings of the National Academy of Sciences* **99**, 10417–10422 (2002).
- Morrow, G., Samson, M., Michaud, S. & M. Tanguay, R. Overexpression of the small mitochondrial Hsp22 extends *Drosophila* life span and increases resistance to oxidative stress. *The FASEB Journal* **18**, 598–599 (2004).
- Morsci, N. S., Hall, D. H., Driscoll, M. & Sheng, Z.-H. Age-Related Phasic Patterns of Mitochondrial Maintenance in Adult *Caenorhabditis elegans* Neurons. *The Journal of Neuroscience* **36**, 1373–1385 (2016).
- Mostoslavsky, R. *et al.* Genomic Instability and Aging-like Phenotype in the Absence of Mammalian SIRT6. *Cell* **124**, 315–329 (2006).
- Mosunova, O., Navarro-Muñoz, J. C. & Collemare, J. The Biosynthesis of Fungal Secondary Metabolites: From Fundamentals to Biotechnological Applications. in *Encyclopedia of Mycology* 458–476 (Elsevier, 2021). doi:10.1016/B978-0-12-809633-8.21072-8.
- Muñoz-Carvajal, F. & Sanhueza, M. The Mitochondrial Unfolded Protein Response: A Hinge Between Healthy and Pathological Aging. *Front Aging Neurosci* **12**, (2020).
- Nagy, S., Huang, Y.-C., Alkema, M. J. & Biron, D. *Caenorhabditis elegans* exhibit a coupling between the defecation motor program and directed locomotion. *Sci Rep* **5**, 17174 (2015).
- Nargund, A. M., Pellegrino, M. W., Fiorese, C. J., Baker, B. M. & Haynes, C. M. Mitochondrial Import Efficiency of ATFS-1 Regulates Mitochondrial UPR Activation. *Science* (1979) **337**, 587–590 (2012).

- National Health Service, U. Alzheimer's disease. (2021).
- Nelson, G. *et al.* A senescent cell bystander effect: senescence-induced senescence. *Aging Cell* **11**, 345–349 (2012).
- Neupert, W. & Herrmann, J. M. Translocation of Proteins into Mitochondria. *Annu Rev Biochem* **76**, 723–749 (2007).
- Nolden, M. *et al.* The m-AAA Protease Defective in Hereditary Spastic Paraplegia Controls Ribosome Assembly in Mitochondria. *Cell* **123**, 277–289 (2005).
- Norvaisas, P. & Cabreiro, F. Pharmacology in the age of the holobiont. *Curr Opin Syst Biol* **10**, 34–42 (2018).
- Nowak, K., McCullagh, K., Poon, E. & Davies, K. E. Muscular dystrophies related to the cytoskeleton/nuclear envelope. *Novartis Found Symp* **264**, 98–111; discussion 112–7, 227–30 (2005).
- O'Hara, A. M. & Shanahan, F. The gut flora as a forgotten organ. *EMBO Rep* **7**, 688–693 (2006).
- O'Toole, P. W. & Jeffery, I. B. Gut microbiota and aging. *Science* (1979) **350**, 1214–1215 (2015).
- Olichon, A. *et al.* Loss of OPA1 Perturbates the Mitochondrial Inner Membrane Structure and Integrity, Leading to Cytochrome c Release and Apoptosis. *Journal of Biological Chemistry* **278**, 7743–7746 (2003).
- Olshansky, S. J., Rudberg, M. A., Carnes, B. A., Cassel, C. K. & Brody, J. A. Trading Off Longer Life for Worsening Health. *J Aging Health* **3**, 194–216 (1991).
- Onken, B. & Driscoll, M. Metformin Induces a Dietary Restriction–Like State and the Oxidative Stress Response to Extend *C. elegans* Healthspan via AMPK, LKB1, and SKN-1. *PLoS One* **5**, e8758 (2010).
- Ono, T., Isobe, K., Nakada, K. & Hayashi, J.-I. Human cells are protected from mitochondrial dysfunction by complementation of DNA products in fused mitochondria. *Nat Genet* **28**, 272–275 (2001).
- Osellame, L. D. *et al.* Cooperative and independent roles of Drp1 adaptors Mff and MiD49/51 in mitochondrial fission. *J Cell Sci* (2016) doi:10.1242/jcs.185165.
- Padmanabhan, V. *et al.* Locomotion of *C. elegans*: A Piecewise-Harmonic Curvature Representation of Nematode Behavior. *PLoS One* **7**, e40121 (2012).
- Palikaras, K., Lionaki, E., & Tavernarakis, N. Coordination of mitophagy and mitochondrial biogenesis during ageing in *C. elegans*. *Nature*, *521*(7553), 525–528. (2015).
- Park, H.-E. H., Jung, Y. & Lee, S.-J. V. Survival assays using *Caenorhabditis elegans*. *Mol Cells* **40**, 90–99 (2017).
- Parracho, H. M., Bingham, M. O., Gibson, G. R. & McCartney, A. L. Differences between the gut microflora of children with autistic spectrum disorders and that of healthy children. *J Med Microbiol* **54**, 987–991 (2005).
- Pasparakis, M. Regulation of tissue homeostasis by NF- $\kappa$ B signalling: implications for inflammatory diseases. *Nat Rev Immunol* **9**, 778–788 (2009).
- Patel, J. 16S rRNA gene sequencing for bacterial pathogen identification in the clinical laboratory. *Molecular Diagnosis* **6**, 313–321 (2001).

- Pedersen, B. K. & Febbraio, M. A. Muscle as an endocrine organ: focus on muscle-derived interleukin-6. *Physiol Rev* **88**, 1379–406 (2008).
- Pédron, T. & Sansonetti, P. Commensals, Bacterial Pathogens and Intestinal Inflammation: An Intriguing Ménage à Trois. *Cell Host Microbe* **3**, 344–347 (2008).
- Peng, L., Li, Z.-R., Green, R. S., Holzman, I. R. & Lin, J. Butyrate enhances the intestinal barrier by facilitating tight junction assembly via activation of AMP-activated protein kinase in Caco-2 cell monolayers. *J Nutr* **139**, 1619–25 (2009).
- Peters, M. A., Teramoto, T., White, J. Q., Iwasaki, K. & Jorgensen, E. M. A Calcium Wave Mediated by Gap Junctions Coordinates a Rhythmic Behavior in *C. elegans*. *Current Biology* **17**, 1601–1608 (2007).
- Pham, L. N., Kanther, M., Semova, I. & Rawls, J. F. Methods for generating and colonizing gnotobiotic zebrafish. *Nat Protoc* **3**, 1862–1875 (2008).
- Podbilewicz, B. Cell fusion. *WormBook* (2006) doi:10.1895/wormbook.1.52.1.
- Poewe, W. *et al.* Parkinson disease. *Nat Rev Dis Primers* **3**, 17013 (2017).
- Poewe, W. Non-motor symptoms in Parkinson's disease. *Eur J Neurol* **15**, 14–20 (2008).
- Portal-Celhay, C. & Blaser, M. J. Competition and Resilience between Founder and Introduced Bacteria in the *Caenorhabditis elegans* Gut. *Infect Immun* **80**, 1288–1299 (2012).
- Pukkila-Worley, R. & Ausubel, F. M. Immune defense mechanisms in the *Caenorhabditis elegans* intestinal epithelium. *Curr Opin Immunol* **24**, 3–9 (2012).
- Pukkila-Worley, R., Ausubel, F. M. & Mylonakis, E. *Candida albicans* Infection of *Caenorhabditis elegans* Induces Antifungal Immune Defenses. *PLoS Pathog* **7**, e1002074 (2011).
- Qin, J. *et al.* A human gut microbial gene catalogue established by metagenomic sequencing. *Nature* **464**, 59–65 (2010).
- Qin, J. *et al.* A metagenome-wide association study of gut microbiota in type 2 diabetes. *Nature* **490**, 55–60 (2012).
- Rae, R., Witte, H., Rödelberger, C. & Sommer, R. J. The importance of being regular: *Caenorhabditis elegans* and *Pristionchus pacificus* defecation mutants are hypersusceptible to bacterial pathogens. *Int J Parasitol* **42**, 747–753 (2012).
- Rahman, M. *et al.* NemaFlex: a microfluidics-based technology for standardized measurement of muscular strength of *C. elegans*. *Lab Chip* **18**, 2187–2201 (2018).
- Rambold, A. S., Kostecky, B., Elia, N. & Lippincott-Schwartz, J. Tubular network formation protects mitochondria from autophagosomal degradation during nutrient starvation. *Proceedings of the National Academy of Sciences* **108**, 10190–10195 (2011).
- Rauthan, M., Ranji, P., Aguilera Pradenas, N., Pitot, C. & Pilon, M. The mitochondrial unfolded protein response activator ATFS-1 protects cells from inhibition of the mevalonate pathway. *Proceedings of the National Academy of Sciences* **110**, 5981–5986 (2013).
- Regmi, S. G., Rolland, S. G. & Conradt, B. Age-dependent changes in mitochondrial morphology and volume are not predictors of lifespan. *Aging* **6**, 118–130 (2014).

- Reid, K. F., Naumova, E. N., Carabello, R. J., Phillips, E. M. & Fielding, R. A. Lower extremity muscle mass predicts functional performance in mobility-limited elders. *J Nutr Health Aging* **12**, 493–8 (2008).
- Rera, M. *et al.* Modulation of Longevity and Tissue Homeostasis by the *Drosophila* PGC-1 Homolog. *Cell Metab* **14**, 623–634 (2011).
- Restif, C. *et al.* CeleST: Computer Vision Software for Quantitative Analysis of *C. elegans* Swim Behavior Reveals Novel Features of Locomotion. *PLoS Comput Biol* **10**, e1003702 (2014).
- Riddle, D. L., Blumenthal, T., Meyer, B. J. & Priess, J. R. *C. elegans II*. vol. 33 (Cold Spring Harbor, 1997).
- Rietdijk, C. D., Perez-Pardo, P., Garssen, J., van Wezel, R. J. A. & Kraneveld, A. D. Exploring Braak's Hypothesis of Parkinson's Disease. *Front Neurol* **8**, (2017).
- Rizk, A. *et al.* Segmentation and quantification of subcellular structures in fluorescence microscopy images using Squassh. *Nat Protoc* **9**, 586–596 (2014).
- Rolland, S. G., Lu, Y., David, C. N. & Conradt, B. The BCL-2-like protein CED-9 of *C. elegans* promotes FZO-1/Mfn1,2- and EAT-3/Opa1-dependent mitochondrial fusion. *Journal of Cell Biology* **186**, 525–540 (2009).
- Rossi, D. J. *et al.* Deficiencies in DNA damage repair limit the function of haematopoietic stem cells with age. *Nature* **447**, 725–729 (2007).
- Rossignol, R. *et al.* Energy Substrate Modulates Mitochondrial Structure and Oxidative Capacity in Cancer Cells. *Cancer Res* **64**, 985–993 (2004).
- Round, J. L. & Mazmanian, S. K. The gut microbiota shapes intestinal immune responses during health and disease. *Nat Rev Immunol* **9**, 313–323 (2009).
- Rual, J.-F. *et al.* Toward Improving *Caenorhabditis elegans* Phenome Mapping With an ORFeome-Based RNAi Library. *Genome Res* **14**, 2162–2168 (2004).
- Rubinsztein, D. C., Mariño, G. & Kroemer, G. Autophagy and Aging. *Cell* **146**, 682–695 (2011).
- Ryan, R. P. *et al.* The versatility and adaptation of bacteria from the genus *Stenotrophomonas*. *Nat Rev Microbiol* **7**, 514–525 (2009).
- Sackton, T. B. *et al.* Dynamic evolution of the innate immune system in *Drosophila*. *Nat Genet* **39**, 1461–1468 (2007).
- Sampson, T. R. *et al.* Gut Microbiota Regulate Motor Deficits and Neuroinflammation in a Model of Parkinson's Disease. *Cell* **167**, 1469-1480.e12 (2016).
- Schafer, W. R. Mechanosensory molecules and circuits in *C. elegans*. *Pflugers Arch* **467**, 39–48 (2015).
- Schaffitzel, E. & Hertweck, M. Recent aging research in *Caenorhabditis elegans*. *Exp Gerontol* **41**, 557–563 (2006).
- Schumacker, S. T., Chidester, C. A. M., Enke, R. A. & Marcello, M. R. RNA sequencing dataset characterizing transcriptomic responses to dietary changes in *Caenorhabditis elegans*. *Data Brief* **25**, 104006 (2019).
- Schwartz, K. & Boles, B. R. Microbial amyloids – functions and interactions within the host. *Curr Opin Microbiol* **16**, 93–99 (2013).

- Scorrano, L. Keeping mitochondria in shape: a matter of life and death. *Eur J Clin Invest* **43**, 886–893 (2013).
- Sender, R., Fuchs, S. & Milo, R. Revised Estimates for the Number of Human and Bacteria Cells in the Body. *PLoS Biol* **14**, e1002533 (2016).
- Sharon, G., Sampson, T. R., Geschwind, D. H. & Mazmanian, S. K. The Central Nervous System and the Gut Microbiome. *Cell* **167**, 915–932 (2016).
- Sheng, Z.-H. The Interplay of Axonal Energy Homeostasis and Mitochondrial Trafficking and Anchoring. *Trends Cell Biol* **27**, 403–416 (2017).
- Shimizu, K. *et al.* Normalization of Reproductive Function in Germfree Mice Following Bacterial Contamination. *Exp Anim* **47**, 151–158 (1998)
- Shivers, R. P., Kooistra, T., Chu, S. W., Pagano, D. J., & Kim, D. H. Tissue-Specific Activities of an Immune Signaling Module Regulate Physiological Responses to Pathogenic and Nutritional Bacteria in *C. elegans*. *Cell Host & Microbe*, *6*(4), 321–330. (2009).
- Shivers, R. P. *et al.* Phosphorylation of the Conserved Transcription Factor ATF-7 by PMK-1 p38 MAPK Regulates Innate Immunity in *Caenorhabditis elegans*. *PLoS Genet* **6**, e1000892 (2010).
- Shtonda, B. B. & Avery, L. Dietary choice behavior in *Caenorhabditis elegans*. *Journal of Experimental Biology* **209**, 89–102 (2006).
- Smith, P. *et al.* Regulation of life span by the gut microbiota in the short-lived African turquoise killifish. *Elife* **6**, (2017).
- Sommer, F. & Bäckhed, F. The gut microbiota — masters of host development and physiology. *Nat Rev Microbiol* **11**, 227–238 (2013).
- Spillantini, M. G. *et al.*  $\alpha$ -Synuclein in Lewy bodies. *Nature* **388**, 839–840 (1997).
- Spillantini, M. G. *et al.*  $\alpha$ -Synuclein in Lewy bodies. *Nature* **388**, 839–840 (1997).
- Stefanis, L.  $\alpha$ -Synuclein in Parkinson's Disease. *Cold Spring Harb Perspect Med* **2**, a009399–a009399 (2012).
- Stiernagle, T. Maintenance of *C. elegans*. *WormBook* (2006) doi:10.1895/wormbook.1.101.1.
- Stockwell, B. R. *et al.* Ferroptosis: A Regulated Cell Death Nexus Linking Metabolism, Redox Biology, and Disease. *Cell* **171**, 273–285 (2017).
- Stuhr, N. L. & Curran, S. P. Bacterial diets differentially alter lifespan and healthspan trajectories in *C. elegans*. *Commun Biol* **3**, 653 (2020).
- Tan, F. J. *et al.* CED-9 and mitochondrial homeostasis in *C. elegans* muscle. *J Cell Sci* **121**, 3373–3382 (2008).
- Tan, M.-W., Mahajan-Miklos, S. & Ausubel, F. M. Killing of *Caenorhabditis elegans* by *Pseudomonas aeruginosa* used to model mammalian bacterial pathogenesis. *Proceedings of the National Academy of Sciences* **96**, 715–720 (1999).
- Tan, M.-W., Mahajan-Miklos, S. & Ausubel, F. M. Killing of *Caenorhabditis elegans* by *Pseudomonas aeruginosa* used to model mammalian bacterial pathogenesis. *Proceedings of the National Academy of Sciences* **96**, 715–720 (1999).
- Tang, W. H. W., Kitai, T. & Hazen, S. L. Gut Microbiota in Cardiovascular Health and Disease. *Circ Res* **120**, 1183–1196 (2017).

- Tap, J. *et al.* Towards the human intestinal microbiota phylogenetic core. *Environ Microbiol* **11**, 2574–2584 (2009).
- Theil, E. C. Ferritin: The Protein Nanocage and Iron Biomineral in Health and in Disease. *Inorg Chem* **52**, 12223–12233 (2013).
- Tomaru, U. *et al.* Decreased Proteasomal Activity Causes Age-Related Phenotypes and Promotes the Development of Metabolic Abnormalities. *Am J Pathol* **180**, 963–972 (2012).
- Tondera, D. *et al.* SLP-2 is required for stress-induced mitochondrial hyperfusion. *EMBO J* **28**, 1589–1600 (2009).
- Toth, M. L. *et al.* Neurite Sprouting and Synapse Deterioration in the Aging *Caenorhabditis elegans* Nervous System. *Journal of Neuroscience* **32**, 8778–8790 (2012).
- Trifonova, A. & Strateva, T. *Stenotrophomonas maltophilia*— a low-grade pathogen with numerous virulence factors. *Infect Dis* **51**, 168–178 (2019).
- Trifunovic, A., Wredenberg, A., Falkenberg, M., Spelbrink, J. N., Rovio, A. T., Bruder, C. E., Bohlooly-Y, M., Gidlöf, S., Oldfors, A., Wibom, R., Törnell, J., Jacobs, H. T., & Larsson, N.-G. Premature ageing in mice expressing defective mitochondrial DNA polymerase. *Nature*, 429(6990), 417–423. (2004).
- Tringe, S. G., & Hugenholtz, P. A renaissance for the pioneering 16S rRNA gene. *Current Opinion in Microbiology*, 11(5), 442–446. (2008).
- Troemel, E. R. *et al.* p38 MAPK Regulates Expression of Immune Response Genes and Contributes to Longevity in *C. elegans*. *PLoS Genet* **2**, e183 (2006).
- Twig, G. *et al.* Fission and selective fusion govern mitochondrial segregation and elimination by autophagy. *EMBO J* **27**, 433–446 (2008).
- Valles-Colomer, M. *et al.* The neuroactive potential of the human gut microbiota in quality of life and depression. *Nat Microbiol* **4**, 623–632 (2019).
- van Tongeren, S. P., Slaets, J. P. J., Harmsen, H. J. M. & Welling, G. W. Fecal microbiota composition and frailty. *Appl Environ Microbiol* **71**, 6438–42 (2005).
- Vance, J. M. The Many Faces of Charcot-Marie-Tooth Disease. *Arch Neurol* **57**, 638 (2000).
- Vandeputte, D. *et al.* Quantitative microbiome profiling links gut community variation to microbial load. *Nature* **551**, 507–511 (2017).
- Varesi, A. *et al.* The Potential Role of Gut Microbiota in Alzheimer’s Disease: From Diagnosis to Treatment. *Nutrients* **14**, 668 (2022).
- Venette, R. C. & Ferris, H. Influence of bacterial type and density on population growth of bacterial-feeding nematodes. *Soil Biol Biochem* **30**, 949–960 (1998).
- Verbrugge, L. M. Longer life but worsening health? Trends in health and mortality of middle-aged and older persons. *Milbank Memorial Fund Quarterly* **62**, 475–519 (1984).
- Villanueva-Millán, M. J., Pérez-Matute, P. & Oteo, J. A. Gut microbiota: a key player in health and disease. A review focused on obesity. *J Physiol Biochem* **71**, 509–525 (2015).
- Visca, P., Imperi, F. & Lamont, I. L. Pyoverdine siderophores: from biogenesis to biosignificance. *Trends Microbiol* **15**, 22–30 (2007).
- Vogt, N. M. *et al.* Gut microbiome alterations in Alzheimer’s disease. *Sci Rep* **7**, 13537 (2017).

- Volkers, R. J. *et al.* Gene-environment and protein-degradation signatures characterize genomic and phenotypic diversity in wild *Caenorhabditis elegans* populations. *BMC Biol* **11**, 93 (2013).
- Walker, G. A. & Lithgow, G. J. Lifespan extension in *C. elegans* by a molecular chaperone dependent upon insulin-like signals. *Aging Cell* **2**, 131–139 (2003).
- Wallace, D. C. & Chalkia, D. Mitochondrial DNA Genetics and the Heteroplasmy Conundrum in Evolution and Disease. *Cold Spring Harb Perspect Biol* **5**, a021220–a021220 (2013).
- Ward, R. J., Zucca, F. A., Duyn, J. H., Crichton, R. R. & Zecca, L. The role of iron in brain ageing and neurodegenerative disorders. *Lancet Neurol* **13**, 1045–1060 (2014).
- Way, J. C. & Chalfie, M. The *mec-3* gene of *Caenorhabditis elegans* requires its own product for maintained expression and is expressed in three neuronal cell types. *Genes Dev* **3**, 1823–1833 (1989).
- Weber-Stiehl, S., Järke, L., Castrillón-Betancur, J. C., Gilbert, F. & Sommer, F. Mitochondrial Function and Microbial Metabolites as Central Regulators of Intestinal Immune Responses and Cancer. *Front Microbiol* **13**, (2022).
- West, A. P., Shadel, G. S. & Ghosh, S. Mitochondria in innate immune responses. *Nat Rev Immunol* **11**, 389–402 (2011).
- Wicks, S. R. & Rankin, C. H. The integration of antagonistic reflexes revealed by laser ablation of identified neurons determines habituation kinetics of the *Caenorhabditis elegans* tap withdrawal response. *Journal of Comparative Physiology A* **179**, 675–685 (1996).
- Wikoff, W. R. *et al.* Metabolomics analysis reveals large effects of gut microflora on mammalian blood metabolites. *Proceedings of the National Academy of Sciences* **106**, 3698–3703 (2009).
- Wilmoth, J. R. Demography of longevity: past, present, and future trends. *Exp Gerontol* **35**, 1111–1129 (2000).
- Woese, C. R. Bacterial evolution. *Microbiol Rev* **51**, 221–271 (1987).
- Wu, X. *et al.* Molecular Characterisation of the Faecal Microbiota in Patients with Type II Diabetes. *Curr Microbiol* **61**, 69–78 (2010).
- Wu, Y. *et al.* Simultaneous Fe<sup>2+</sup>/Fe<sup>3+</sup> imaging shows Fe<sup>3+</sup> over Fe<sup>2+</sup>-enrichment in Alzheimer's disease mouse brain. *Sci Adv* **9**, (2023).
- Xue, C., Lin, T. Y., Chang, D. & Guo, Z. Thioflavin T as an amyloid dye: fibril quantification, optimal concentration and effect on aggregation. *R Soc Open Sci* **4**, 160696 (2017).
- Xue, C., Lin, T. Y., Chang, D. & Guo, Z. Thioflavin T as an amyloid dye: fibril quantification, optimal concentration and effect on aggregation. *R Soc Open Sci* **4**, 160696 (2017).
- Yan, N. & Zhang, J. Iron Metabolism, Ferroptosis, and the Links With Alzheimer's Disease. *Front Neurosci* **13**, (2020).
- Yang, W. *et al.* The Inducible Response of the Nematode *Caenorhabditis elegans* to Members of Its Natural Microbiota Across Development and Adult Life. *Front Microbiol* **10**, (2019).
- Yardeni, T. *et al.* Host mitochondria influence gut microbiome diversity: A role for ROS. *Sci Signal* **12**, (2019).
- You, Y., Kim, J., Raizen, D. M. & Avery, L. Insulin, cGMP, and TGF- $\beta$  Signals Regulate Food Intake and Quiescence in *C. elegans*: A Model for Satiety. *Cell Metab* **7**, 249–257 (2008).

- You, Y., Kim, J., Raizen, D. M. & Avery, L. Insulin, cGMP, and TGF- $\beta$  Signals Regulate Food Intake and Quiescence in *C. elegans*: A Model for Satiety. *Cell Metab* **7**, 249–257 (2008).
- Youngman, M. J., Rogers, Z. N. & Kim, D. H. A Decline in p38 MAPK Signaling Underlies Immunosenescence in *Caenorhabditis elegans*. *PLoS Genet* **7**, e1002082 (2011).
- Youssef, N. *et al.* Comparison of Species Richness Estimates Obtained Using Nearly Complete Fragments and Simulated Pyrosequencing-Generated Fragments in 16S rRNA Gene-Based Environmental Surveys. *Appl Environ Microbiol* **75**, 5227–5236 (2009).
- Zembroń-Łacny, A., Dzuibek, W., Rogowski, Ł., Skorupka, E. & Dabrowska, G. Sarcopenia: Monitoring, Molecular Mechanisms, and Physical Intervention. *Physiol Res* 683–691 (2014) doi:10.33549/physiolres.932692.
- Zhang, Y., Ikeno, Y., Qi, W., Chaudhuri, A., Li, Y., Bokov, A., Thorpe, S. R., Baynes, J. W., Epstein, C., Richardson, A., & van Remmen, H. Mice Deficient in Both Mn Superoxide Dismutase and Glutathione Peroxidase-1 Have Increased Oxidative Damage and a Greater Incidence of Pathology but No Reduction in Longevity. *The Journals of Gerontology Series A: Biological Sciences and Medical Sciences*, 64A(12),. (2009).
- Zhang, J. *et al.* A Delicate Balance between Bacterial Iron and Reactive Oxygen Species Supports Optimal *C. elegans* Development. *Cell Host Microbe* **26**, 400-411.e3 (2019).
- Zhang, S., Li, F., Zhou, T., Wang, G. & Li, Z. *Caenorhabditis elegans* as a Useful Model for Studying Aging Mutations. *Front Endocrinol (Lausanne)* **11**, (2020).
- Zhao, Y. *et al.* Beta-Amyloid Precursor Protein ( $\beta$ APP) Processing in Alzheimer's Disease (AD) and Age-Related Macular Degeneration (AMD). *Mol Neurobiol* **52**, 533–544 (2015).
- Zhu, P.-P. *et al.* Intra- and Intermolecular Domain Interactions of the C-terminal GTPase Effector Domain of the Multimeric Dynamin-like GTPase Drp1. *Journal of Biological Chemistry* **279**, 35967–35974 (2004).
- Zilber-Rosenberg, I. & Rosenberg, E. Role of microorganisms in the evolution of animals and plants: the hologenome theory of evolution. *FEMS Microbiol Rev* **32**, 723–735 (2008).